SULFUR POISONING AND TOLERANCE OF HIGH PERMEANCE Pd/Cu ALLOY MEMBRANES FOR HYDROGEN SEPARATION

By

Natalie Pomerantz

A PhD thesis

Submitted to the faculty of the

Worcester Polytechnic Institute

In fulfillment of the requirement for the

Degree of Doctor of Philosophy

In Chemical Engineering

By

_____

August 2010

APPROVED BY:

_____ _____

Dr. Yi Hua Ma, Adviser Dr. David DiBiasio, Head of Department

_____ _____

Dr. Satya Shivkumar, Committee Member Dr. Richard Sisson, Committee Member

_____

Dr. Nikoloas Kazantzis, Committee Member

for my family

Acknowledgements

Firstly to my advisor Prof. Yi Hua Ma, thank you for the many opportunities that you gave me. I am especially thankful for the independence given me in conducting my research thus allowing me to learn from both my mistakes and successes. I'm grateful for the opportunity to present my own work at conferences which enabled me to build confidence in myself and my work and also to meet other researchers in fields both similar to and vastly different from mine. Travelling to both MIT and ORNL afforded me the chance to work side by side with many experts in various fields and use instrumentation that I would not normally have access to. I appreciate you working tirelessly to provide funding for our lab which allowed all of us to devote our time and effort towards research and conduct experiments with great freedom. I'm thankful for your availability and willingness to discuss my research whenever I had the need, your patience during disagreements, and your support for my ideas.

To my committee members: Prof. Sisson, Prof. Shivkumar and Prof. Kazantzis thank you for the advice, suggestions and encouragement given along the way. The insight given from your respective areas of expertise not directly related to the membrane field added a valuable dimension to my research.

I'm grateful for Dr. Ivan Mardilovich for taking the time to train me in the various methods of making Pd membranes which were developed in the lab, for his input and his knowledge of "tricks" to solve all sorts of tiny problems that popped up. I'm thankful to Dr. Erik Engwall, Dr. Federico Guazzone, Dr. M. Engin Ayturk, Dr. Rajkumar Bhandari,

Diana Otalvaro, Alpna Saini, Chao-Huang Chen, Alex Augustine, Reyyan Koc and Pei-Shan Yen for being both friends and colleagues and for the discussions which ranged from science to religion to history to politics and to food! We had a lot of fun together and I'll miss you guys.

Thanks to Doug White and Jack Ferraro for the technical help and support, without which building and troubleshooting my system would have taken much longer, and for the discussions on where George Lucas went horribly wrong. To Paula Moravek, Felicia Vidito and Tiffany Royale thank you for the administrative support and occasional book recommendations, and to the entire Chemical Engineering Department for helping to make my experience at WPI a more rewarding one.

Thanks to Dr. E. Andrew Payzant and Dr. Harry Meyer III for their help, guidance and expertise during my stay at Oak Ridge and conducting the HT-XRD and XPS experiments. Thanks to Elizabeth Shaw for her help with the XPS and Don Pellegrino for his help with the AAS.

Much appreciation is expressed to the U.S. Department of Energy (DOE) University Coal Research Program for the financial support which was supported by U.S. DOE Award No. DE-FG26-04NT42194 under project manager Dr. Arun Bose, and for the additional support of U.S. DOE Hydrogen Pathway Award No. DE-FC26-07NT43058 under project managers Jason Hissam and Dr. Dan Driscoll. The research at the Oak Ridge National Laboratory's High Temperature Materials Laboratory was sponsored by the U.S. OE, Office of Energy Efficiency and Renewable Energy, Vehicle Technologies Program.

I would like to extend a special thanks to the faculty of Ben Gurion University, and especially to Prof. Jaime Wisniak, Prof. Moshe Gottlieb and Prof. Moti Herskowitz who gave me such a solid base and fundamental understanding of the principles of chemical engineering, without which continuing on to graduate school would have been infinitely more difficult. Another thanks to Prof. Jack Gilron for advising my senior project and enabling me to be a part of his research which is now at the very exciting stage of the construction of two desalination pilot plants. They were all excellent teachers who were very much dedicated to the education of their students. I miss them all and wish them success and in the case of Prof. Wisniak, a happy retirement.

I would like to dedicate this work to my husband, Hanan, whose love, support and encouragement helped me through these years. It's not easy being married to a graduate student. To my parents for their support and especially my mother for babysitting when needed. And to my daughter Naomi, whose smiling face never failed to turn the worst of days around. I love you all.

Abstract

This work investigated the long-term stability of sulfur tolerant Pd/Cu alloy membranes for hydrogen separation by performing characterizations lasting several thousand hours in H_2, He and H_2S/H_2 atmospheres ranging in concentration from 0.2 – 50 ppm and temperatures ranging from 250 - 500ºC. Two methods were used for fabricating the Pd/Cu membranes so that the sulfur tolerant fcc alloy would remain on the surface and minimize the decrease in hydrogen permeance inherent with fcc Pd/Cu alloys. The first method consisted of annealing a Pd/Cu bi-layer at high-temperatures and the second consisted of depositing a Pd/Cu/Pd tri-layer with an ultra-thin surface alloy. High temperature X-ray diffraction (HT-XRD) was employed to study the kinetics of the annealing process and atomic adsorption spectroscopy (AAS) was used to investigate the kinetics of the Cu deposition and Pd displacement of Cu.

Upon the introduction of H_2S, the permeance decrease observed was dependent upon the H_2S feed concentration, and not the time of poisoning. However, after the recovery in pure H_2 there was a portion of the permeance which could not be recovered due to adsorbed sulfur blocking H_2 adsorption sites. The amount of recoverable permeance was dependent on the time of exposure to H_2S and reached a limiting value which decreased with temperature. X-ray photoemission spectroscopy (XPS) was used to investigate poisoned samples and it was observed that the permeance not recovered at a given temperature in H_2 was caused mostly by Cu sulfides.

Both bi-layer and tri-layer membranes had hydrogen permeances which were higher than homogeneous Pd/Cu membranes of the same surface concentration. However, the tri-layer membranes performed as well as Pd membranes thus eliminating the disadvantage of alloying Pd with Cu without sacrificing sulfur tolerance.

Executive Summary

Hydrogen selective Pd membranes can improve the efficiency and cost effectiveness of the coal gasification process by recovering high purity hydrogen from the syngas, producing high pressure CO_2 in the retentate stream for carbon capture and sequestration, and by increasing the reaction conversion by removing the limitations of temperature dependent equilibrium. However, small quantities of H_2S present in the gas stream poison Pd membranes and reduce the hydrogen permeance by either adsorbing on the membrane surface or forming a bulk sulfide scale (McKinley, 1967, Kajiwara et al., 1999). Pd/Cu alloy membranes have engendered much research due to their greater H_2S tolerance than Pd membranes (Morreale et al., 2004). However, the sulfur tolerant fcc phase has a low hydrogen permeability in comparison to Pd membranes (McKinley, 1969, Subramanian and Laughlin, 1991).

This work describes two novel techniques for obtaining both H_2S resistance and a high hydrogen permeance in Pd/Cu alloy membranes by limiting the sulfur tolerant fcc alloy to the top layer of the membrane, with the Cu forming a gradient within the Pd layer. Furthermore, the membranes were tested extensively in a shell and tube apparatus in H_2, He and H_2S/H_2 atmospheres ranging from 0.2 – 50 ppm and between the temperatures of 250 - 500ºC.

The first technique involved using the electroless deposition method to deposit a bi-layer of Pd and Cu on oxidized porous metal supports graded with Al_2O_3 particles and a porous Pd/Ag barrier. The long-term characterizations of the bi-layer Pd/Cu membranes that were performed for over 1500 h between the temperatures of 250 - 500ºC in He and

H_2 atmospheres showed a stable hydrogen permeance over the time period tested and a decrease in the ideal H_2/He separation factor from infinity to 300. The permeabilities of the membranes ranged from 45 – 65% of the permeabilities of Pd foils of the same thickness (Guazzone, 2006, Ayturk, 2007) which was less than pure Pd membranes made with the same method of support modification (79 – 101%) but much more than homogeneous Pd/Cu membranes of the same surface concentration (McKinley, 1967). The activation energies of the bi-layer membranes ranged between 15 – 20 kJ/mol which was higher than Pd membranes fabricated with the same grading method (10 – 15 kJ/mol).

To determine the time and temperature needed for fabricating membranes with the first technique, the kinetics of the fcc alloy formation from Pd/Cu bi-layers in a H_2 atmosphere was investigated with HT-XRD by monitoring the fcc phase while annealing Pd/Cu bi-layers in H_2 between the temperatures of 500 - 600ºC. The good fit of the Avrami model for nucleation and growth (Hulbert, 1969) to the data yielded that the fcc alloy formation from Pd/Cu bi-layers was a one dimensional diffusion controlled process and that temperatures as high as 600ºC were needed in order to complete the alloy formation in a timely fashion (10 h) which would cause great damage to the selectivity of a membrane. Lower temperatures at 500ºC would require 225 h, reducing the cost effectiveness of the fabrication process.

The second technique for fabricating Pd/Cu membranes with the fcc alloy on the top layer was by depositing an ultra-thin Cu layer on an already dense Pd membrane, and displacing part of the Cu layer with Pd forming a Pd/Cu/Pd tri-layer. The plating and displacement baths were agitated to form more uniform layers with evenly dispersed particles and the deposition kinetics were studied with AAS to enable consistent

thicknesses to be obtained. Annealing studies showed that only 36 h at 450ºC were needed to complete the fcc alloy formation on the surface.

Characterizations of the tri-layer membranes lasted roughly 200 h and yielded activation energies of roughly 13 kJ/mol which was well within the range of Pd membranes fabricated with the same support modification (9 – 15 kJ/mol). Furthermore, the hydrogen permeances of the membranes were 81 and 93% of pure Pd foils of the same thickness, also within the range of Pd membranes (79 – 101%), showing a vast improvement over the first method of Pd/Cu membrane fabrication and that sulfur tolerant Pd/Cu membranes could indeed be fabricated without the permeance loss inherent in fcc Pd/Cu alloys.

Both bi-layer and tri-layer membranes were poisoned with H_2S concentrations ranging between 0.2 – 50 ppm and recovered in H_2, the total testing time lasting for as long as several thousand hours. All membranes suffered from a decrease in permeance which ranged from small (25% at 0.2 ppm) to more severe (80% at 50 ppm) with increased H_2S concentration due to the dissociative chemisorption of H_2S on the Pd/Cu surface. However, the permeance stabilized immediately upon introduction of the H_2S and remained stable for the duration of the poisoning.

Tolerance to H_2S increased with temperature due to the exothermic nature of H_2S adsorption on metals. The extent of permeance decrease lessened with increased temperature, more permeance was recovered in H_2 at higher temperatures and the time needed for recovery decreased with increasing temperature. After recovery in pure H_2, a portion of the membrane permeance was not recoverable at a given temperature. The amount of irrecoverable permeance increased with exposure time to H_2S, reaching a limiting value which increased with decreasing temperature.

While the amount of recoverable permeance between the bi-layer and tri-layer membranes was the same at any given temperature, the permeance decline suffered by the bi-layer membranes was slightly larger than that of the tri-layer membranes. The reason could be because of residual bcc phase patches on the bi-layer membrane surface which had not completely annealed, that would not be present on the tri-layer membrane due to the difference in the Cu profile during annealing. The bi-layer membrane would have the highest Cu concentration on the surface and the tri-layer membrane would have the highest Cu concentration below the surface.

XPS studies showed that the Cu sulfides served for the majority of the adsorption sites for sulfur at smaller H_2S concentrations (< 5 ppm), while Pd sulfides formed in a fraction more conducive to the surface alloy composition at higher H_2S concentrations (50 ppm). Furthermore, the permeance not recovered was caused mostly by Cu surface sulfides as the majority of the Pd surface sulfides were able to be reduced in H_2, showing that the Cu adsorption sites were more energetically favorable for sulfur adsorption than the Pd sites.

The sulfur poisoning was deemed to stem solely from the formation of surface sulfides caused by the dissociative chemisorption of H_2S on the Pd/Cu surface. All membranes continued to have linear Sieverts' plots, showing that the mechanism of hydrogen mass transfer was governed by the one dimensional diffusion through the hydrogen selective layer. Furthermore, the activation energies of the Pd/Cu membranes were nearly the same both before the start of the poisoning experiments and after the recoveries. The lack of change in activation energy showed that there was no change to the membrane structure and that the decrease in permeance seen from poisoning was due to the reduction of the effective membrane area for H_2 adsorption.

Table of Contents

List of Figures

List of Tables

1. Introduction

Hydrogen has many uses today, and given the potential of being a sustainable, "emissions free" energy carrier, could be much more valuable in the future. Currently, hydrogen is mainly used by the petrochemical industry for the processing of fossil fuels, and in the production of ammonia for fertilizers. It is also a hydrogenating agent for fats and oils, used for methanol and hydrochloric acid production, and a reducer of metallic ores. Hydrogen powered fuel cells and turbines could provide clean energy for the gamut of human needs ranging from small batteries to everyday transportation to large industrial plants. Currently, hydrogen is used as a fuel in space shuttles, internal combustion engines of specially designed BMW's and bus lines located in Iceland, and hydrogen fuel stations are available in several cities in Europe and California. In addition, hydrogen could be used as an energy source in nuclear fusion power plants, enabling an enormous amount of energy to be produced.

The recent international concern with regards to climate change has prompted carbon cap and trade agreements and sparked interest in emission free energy production. Clean and sustainable processes for hydrogen production are currently being researched such as the extraction of H_2 from biomass and the electrolysis of water by solar, wind and nuclear power[*]. But until these technologies are profitable enough to be implemented on a large industrial scale, steam reforming and coal gasification can serve as a bridge to

[*] Nuclear energy is considered to be sustainable because several thousand years are required to deplete raw materials needed for fission at the current global energy consumption (Kessler, 2002).

establishing the infrastructure and consumer dependence required for a hydrogen economy.

As of now, steam reforming is the most common method of producing hydrogen on an industrial scale. Natural gas and naphtha are generally employed as raw materials. Utilizing coal for hydrogen production through coal gasification is predicted to be inexpensive in comparison to steam reforming of natural gas and has the advantage of convenience for countries which would otherwise have to import natural gas. However, the carbon dioxide emissions from burning fossil fuels necessitate CO_2 capture and sequestration.

H_2 production on an industrial scale can be made more efficient with the use of Pd membrane reactors. Separating hydrogen from CO_2 and other steam reforming by-products is currently done by pressure swing adsorption (PSA), but membrane reactors equipped with hydrogen selective Pd membranes have the potential to produce high purity hydrogen at lower temperatures by extracting the H_2 simultaneously with H_2 production, thus greatly reducing the energy expended in reaching a high conversion. Tokyo Gas is currently producing 40 Nm^3/h of 99.99% pure H_2 with a membrane reformer system with an efficiency of 70% (Shirasaki et al, 2009).

Integrated gasification combined cycle (IGCC) plants use coal, petroleum residue and biomass to produce electricity from syngas powered turbines. Membrane reactors with hydrogen selective Pd membranes can improve the efficiency and cost effectiveness of the coal gasification process by recovering high purity hydrogen from the syngas. Also, the high pressure CO_2 in the retentate reduces the cost of carbon capture required

for carbon sequestration by lessening the amount of energy required for the pressurizing stage (Bredesen et al., 2004).

Asymmetric composite Pd and Pd-alloy membranes deposited on porous metal supports are especially well-suited for industrial applications due to the strength and structural integrity of the metal supports and the simplicity of module construction. In addition, similar coefficients of thermal expansion between the Pd layer and the support ensure stability during temperature cycling. Electroless deposition is an advantageous method of depositing the Pd due to the hardness of the deposited film, the ease of scale-up, and the uniform deposition on complex shapes. The resultant hydrogen selective layer has good adhesion to the support and is thin, ensuring a high hydrogen permeance and low Pd cost.

However, the use of Pd membranes is not without disadvantages. Small quantities of H_2S present in the gas stream poison the Pd membrane and can drastically reduce the hydrogen permeance or cause irreparable damage to the membrane (McKinley, 1967, Mundshau et al., 2006, Kajiwara et al., 1999, Kuprathipanja et al., 2005). Pd/Cu alloys have generated much research, not only because they do not exhibit hydrogen embrittlement even at room temperature (Uemiya et al., 1991) but also because Pd/Cu alloys are more resistant to H_2S poisoning than pure Pd when the Cu composition is in the fcc region of the Pd/Cu phase diagram (Morreale et al., 2004, McKinley, 1967, Mundschau et al., 2006, Kulprathipanja et al., 2005, see Figure 1-1). The disadvantage of fcc Pd/Cu membranes is their low permeance in comparison to Pd and other Pd alloys (McKinley, 1966, Knapton, 1977, Grashoff et al., 1983). The relative permeability of Pd/Cu membranes as a function of Cu content is overlaid on the phase diagram in Figure

1-1. As can be seen, increasing Cu content in a Pd/Cu alloy membrane causes the overall permeability to decrease while in the fcc phase.

The fabrication of Pd/Cu alloy membranes is problematic in that the Cu concentration range in which the permeability increase occurs is extremely narrow and requires a very accurate method of determining alloy composition. However, as stated earlier, the permeability increase is accompanied by a loss in the sulfur resistance. The sulfur resistant fcc phase has a relatively low permeability but since H_2S poisoning happens near the surface of the membrane, an fcc alloy on the top layer of the Pd membrane would protect the surface of the membrane without greatly reducing the permeance. In addition, a thin top fcc layer would preclude the need to form a homogeneous alloy which, in the absence of an adequate co-deposition bath, required temperatures as high as 600°C (Ma et al., 2004a) in order for the Pd and Cu layers to completely diffuse into each other.

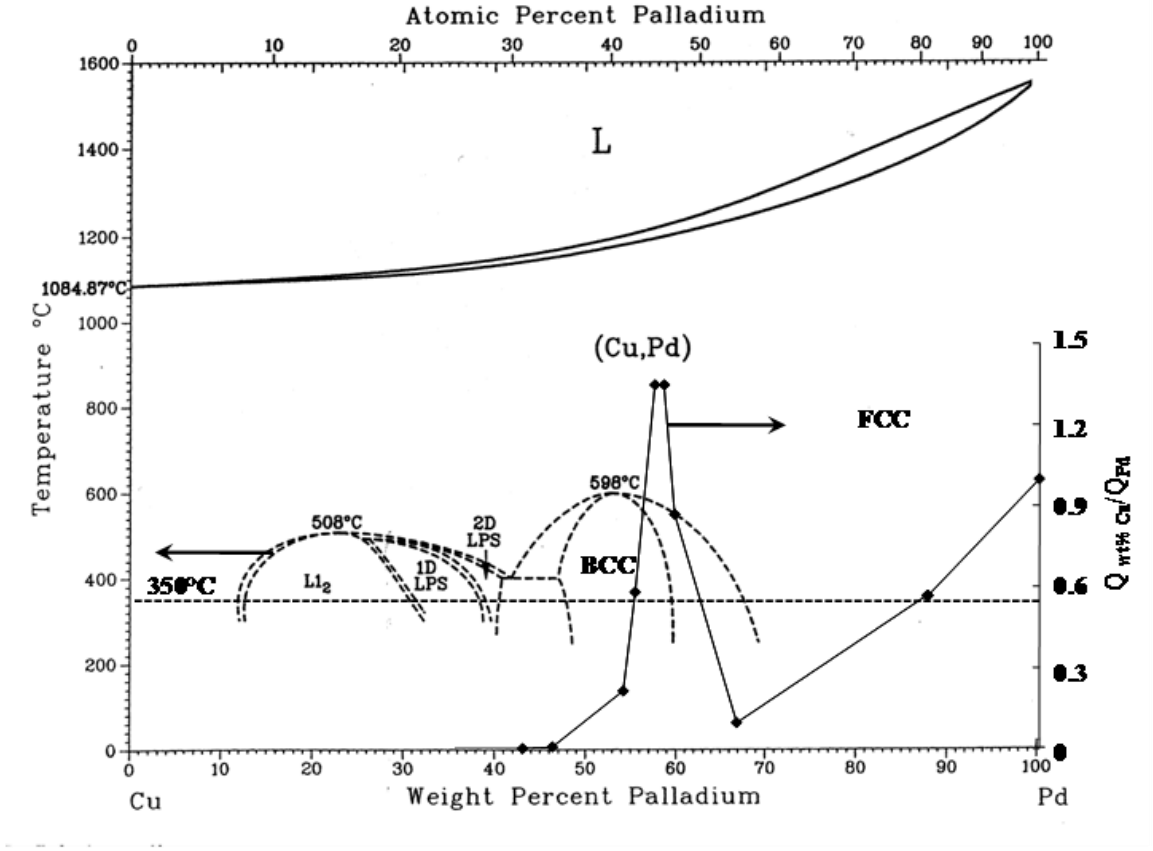

Figure 1-1 Pd – Cu phase diagram (Subramanian and Laughlin, 1991) overlaid with the relative permeability of Pd/Cu membranes as a function of Cu content at 350°C.[*]

[*] The graph was adapted from the data collected from McKinley (1966) for Pd and Pd/Cu foils of 1 mm thickness. The line is for guiding the eye.

The main objective of this research was to understand the fundamental principles involved in the fabrication, the H_2 permeation characteristics, the long term stability and the effect of H_2S on Pd and Pd/Cu alloy membranes synthesized by the electroless plating method on porous metal supports. Specifically, the specific objectives of this research were to:

(1) Understand the kinetics of the Pd/Cu alloy phase transformation and the annealing conditions required to fabricate Pd/Cu alloy membranes with the top layer in the sulfur tolerant fcc phase.

(2) Understand and characterize the hydrogen transport mechanism through Pd/Cu membranes.

(3) Understand the permeation characteristics and investigate the long-term stability of Pd and Pd/Cu alloy membranes in H_2 and He atmospheres.

(4) Understand the permeation characteristics of Pd/Cu alloy membranes and investigate the long-term stability during H_2S poisoning and recovery in pure H_2.

(5) Understand how H_2S composition in the feed gas affects the degree of H_2S poisoning.

(6) Understand how H_2S bonds to the surface of Pd and Pd/Cu alloy membranes.

(7) Understand the effect of bath agitation on Cu plating kinetics, deposition morphology, membrane fabrication and membrane performance.

(8) Understand the effect of bath agitation on Pd displacement kinetics, deposition morphology, membrane fabrication and membrane performance.

2. Literature Review

2.1 Pd – H System

Hydrogen is unique among the elements in that it has the ability to permeate through solid Pd. The hydrogen permeation phenomenon through Pd was discovered by Graham (1866) after a previous study (Deville, 1864) had shown that metals such as platinum and iron were permeable to hydrogen. Deville (1864) theorized that the H_2 permeability through seemingly dense metal was from "an intermolecular porosity due entirely to dilatation.[*]" Today, it is known that hydrogen atoms occupy interstitial sites within the Pd lattice and act as local dilatation centers, causing the lattice to expand in their near vicinity (Alefeld and Volkl, 1978).

The discovery of hydrogen permeability in Pd aroused interest in the Pd – H system. In Figure 2-1, the molar H/Pd ratio (n) is shown as a function of hydrogen pressure with each line representing a different temperature (isotherms). Isotherms were generally constructed by measuring weight gain (Lewis, 1967). Frieske and Wicke (1973) achieved more accurate isotherms with the use of magnetic susceptibility. More recently, Latyshev and Gur'yanov (1988) used the dilatometric method to determine the isotherms.

Hydrogen occupying interstitial sites within Pd in the α phase causes the lattice parameter to increase from 3.891 E to 3.894 E[**] (Alefeld and Volkl, 1978). At the saturation point of the α phase, the lattice parameter undergoes a non-continuous jump to

[*] As translated from French by Graham (1866).

[**] At room temperature.

4.026 Å** (Alefeld and Volkl, 1978) marking the onset of the β phase in the miscibility gap.

Frieske and Wicke (1973) measured the critical temperature of the phase transition to be 291°C. Latyshev and Gur'yanov (1988) determined the critical temperature to be 299°C, the critical molar H/Pd ratio to be 0.292 and the critical pressure to be 21.5 bar.

The α ↔ β phase transformation causes hydrogen embrittlement which deforms the Pd metal to relieve the lattice strain (Lewis, 1967). Bryden and Ying (1995) exposed sputtered Pd films to hydrogen at room temperature and found that after exposure, the films delaminated since the attachment to supports constrained the Pd films and prevented them from deforming. Hydrogen embrittlement would drastically reduce the selective properties of pure Pd membranes, and thus most of the Pd membrane literature includes data above 298ºC or at low pressures below 298ºC.

The inset of Figure 2-1 is a region of the isotherms where the square root of the hydrogen pressure is proportional to the molar H/Pd ratio. The proportionality constant is known as Sieverts' constant, shown in Equation 2.1. The linear dependence is only observed at low concentrations of hydrogen in Pd and when the surface interactions of hydrogen and Pd are at equilibrium.

$$P_{H_2}^{0.5} = K_s \cdot n_{H/Pd} \tag{2.1}$$

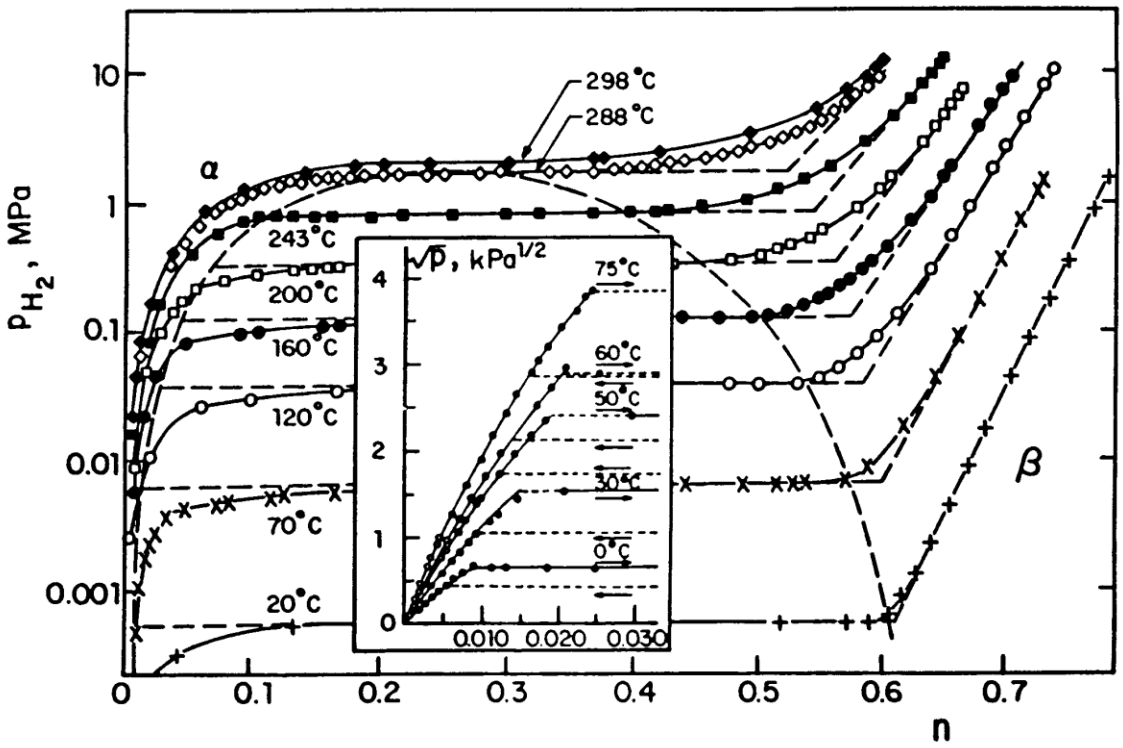

Figure 2-1 Pd – H diagram.[*]

[*] The figure was taken from Shu et al. (1991), which was adapted from Frieske and Wicke, 1973, and Wicke and Nernst, 1964. Values of the y – axis in the inset were mistakenly listed as 10, 20, 30, and 40 in Shu et al. (1991) and were corrected by Guazzone (2006) based on the original data from Wicke and Nernst, 1964.

2.2 Hydrogen Transport in Pd Membranes

2.2.1 Sieverts' Law

Hydrogen transport through Pd is governed by the solution diffusion mechanism whereby hydrogen adsorbs, dissociates and diffuses through the Pd lattice by "jumping" to and from the octahedral interstitial sites of the fcc Pd lattice (Alefeld and Volkl, 1978), schematically depicted in Figure 2-2. The hydrogen transport mechanism through Pd was summarized in seven steps (Shu et al., 1991) and shown schematically in Figure 2-3:

(1) diffusion of H_2 from the bulk feed to the Pd surface

(2) dissociative chemisorption of H_2 on the Pd surface

(3) dissolution of H from the Pd surface to the bulk metal

(4) diffusion of H through the Pd lattice

(5) transition of H from the Pd bulk metal to the surface

(6) recombination and desorption of H_2 from the Pd surface

(7) diffusion of H_2 from the Pd surface to the bulk gas

It is the dissociative chemisorption of hydrogen on Pd which enables only hydrogen to enter the Pd lattice and a potentially infinite selectivity for Pd membranes. The hydrogen flux is at a dynamic equilibrium and is expressed as the difference between adsorption and desorption rates, as seen in Equation 2.2.

$$J_{H_2} = -k_d \cdot (1-\theta)^2 + k_a \cdot P_{H_2} \theta^2 \tag{2.2}$$

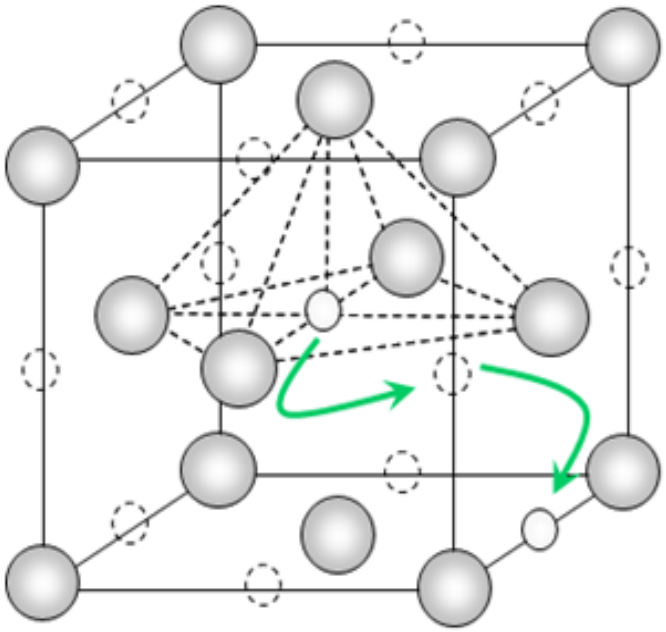

Figure 2-2 Pd unit cell with a hydrogen atom jumping to and from interstitial sites: Pd - grey, H - white, interstitial sites – dotted.

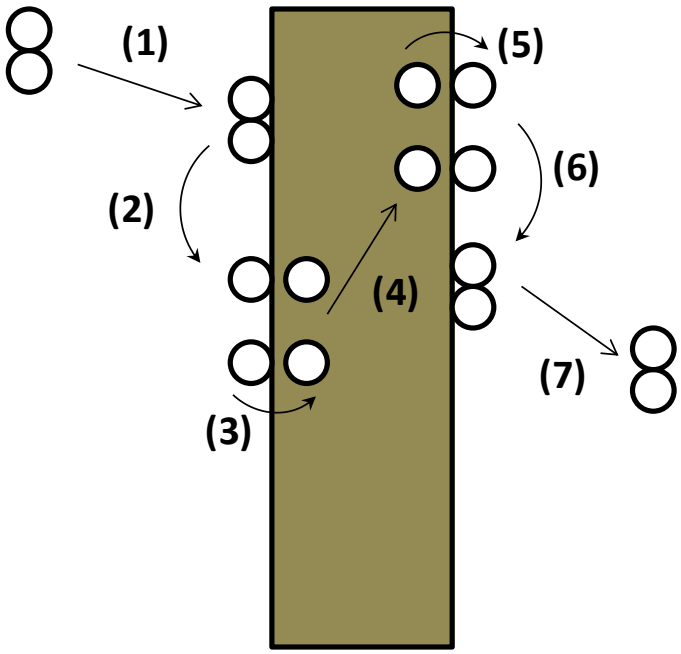

Figure 2-3 Schematic of hydrogen permeation through a Pd film.

During the dissolution of hydrogen into Pd, the adsorbed hydrogen atoms on the Pd surface enter the interstitial sites of the Pd lattice. The hydrogen dissolution into the bulk is at a dynamic equilibrium and the hydrogen flux is equal to the difference between the rates of the surface hydrogen entering and exiting the Pd lattice (Equation 2.3).

$$J_{H_2} = -k_o n_{H/Pd} \cdot (1-\theta) + k_i \cdot (1-n_{H/Pd}) \cdot \theta \tag{2.3}$$

The diffusion of hydrogen in the Pd bulk is expressed with Fick's Law of steady state diffusion (Equation 2.4). One dimensional diffusion is assumed for a tubular membrane if the membrane thickness is very small relative to the tube radius (l << r).

$$J_{H_2} = -D \cdot \frac{dC_H}{dz} \tag{2.4}$$

In Equation 2.5, the concentration of hydrogen in Pd is calculated from the product of the molar H/Pd ratio and the hydrogen solubility constant in Pd (κ) which has the same units as the concentration.

$$C_H = \kappa \cdot n_{H/Pd} \tag{2.5}$$

Substitution of Equation 2.5 into Equation 2.4 after integrating Equation 2.4 yields Equation 2.6:

$$J_{H_2} = -\frac{D \cdot \kappa}{l}\left(n_{H/Pd,1} - n_{H/Pd,2}\right) \tag{2.6}$$

At temperatures over 300°C and clean Pd foil thicknesses of 1 μm or greater, the rate of diffusion is far slower than the rates of the surface processes causing both adsorption and dissolution to be at a state of equilibrium (Ward and Dao, 1999). As a result, the overall rates of adsorption and dissolution (Equations 2.2 and 2.3) are equal to zero and the rate of diffusion is the rate determining step for the entire process.

If the system is in the α phase, the molar H/Pd ratio can be assumed to be very small and is neglected ($n_{H/Pd} << 1$) from the second term in Equation 2.3. Equation 2.7 shows the equating of Equations 2.2 and 2.3 to zero and the neglecting of $n_{H/Pd}$.

$$J_{H_2} = -k_a P_{H_2} \cdot (1-\theta)^2 + k_d \theta^2 = -k_o n_{H/Pd} \cdot (1-\theta) + k_i \cdot \theta = 0 \tag{2.7}$$

Combining terms in Equation 2.7 yields Equation 2.8.

$$\frac{\theta}{(1-\theta)} = \sqrt{\frac{k_a P_{H_2}}{k_d}} = \frac{k_o n_{H/Pd}}{k_i} \tag{2.8}$$

Solving for $n_{H/Pd}$ (Equation 2.9) in Equation 2.8 gives the mathematical relationship between the square root of the hydrogen pressure and the molar H/Pd ratio (Equation 2.1) shown graphically in Figure 2-1, and shows the physical meaning of Sieverts' constant (Equation 2.10) as defined by the rate constants in Equations 2.2 and 2.3. The rate constants are difficult to be measured individually, but Sieverts' constant can be calculated from the isotherm slopes in Figure 2-1.

$$n_{H/Pd} = \frac{k_i \cdot k_a^{0.5}}{k_o \cdot k_d^{0.5}} P_{H_2}^{0.5} \tag{2.9}$$

$$K_s = \frac{k_o \cdot k_d^{0.5}}{k_i \cdot k_a^{0.5}} \tag{2.10}$$

Upon substitution of Equation 2.1 into Equation 2.6, Sieverts' Law is derived (Equation 2.11). Sieverts' Law states that at a given temperature, the flux of hydrogen through Pd is linearly dependent on the difference of the square root of the transmembrane pressures. In accordance with the assumptions in the derivation of Equation 2.11, Sieverts' Law is only valid at low concentrations of hydrogen in the bulk Pd and when diffusion through Pd is the rate limiting step of hydrogen permeation.

$$J_{H_2} = \frac{D \cdot \kappa}{K_s \cdot l}\left(P_{H_2,2}^{0.5} - P_{H_2,1}^{0.5}\right) \tag{2.11}$$

When there is no α ↔ β phase transition, it is reasonable to assume that the diffusion coefficient is independent of the H_2 concentration in the Pd layer (Alefeld and Volkl, 1978). However, diffusion is a thermally activated process and is dependent on temperature (Equation 2.12).

$$D = D_o \cdot \exp\left(\frac{-E_D}{R \cdot T}\right) \tag{2.12}$$

Results collected by Alefeld and Volkl (1978) showed that for the α phase, D_0 = 0.0029 cm^2/s and E_D = 22.2 kJ/mol in a temperature range of 0 – 650°C. The hydrogen solubility constant divided by the Sieverts' constant (κ/Ks) yields the solubility of hydrogen in Pd (Equation 2.13).

$$S = S_o \cdot \exp\left(\frac{\Delta H_s}{R \cdot T}\right) \tag{2.13}$$

The product of the solubility and the diffusion coefficient gives the permeability (Q) of the membrane (Equation 2.14). In Equation 2.14, Q_0 is the product of D_0 and S_0 and the activation energy is equal to the sum of the activation energy of diffusion and the heat of solution.

$$Q = D \cdot S = Q_o \cdot \exp\left(\frac{-E_Q}{R \cdot T}\right) \tag{2.14}$$

Substituting Equation 2.14 into Equation 2.11 yields Equation 2.15. Equation 2.15 is also derived by using the solution-diffusion model which states that the material permeating through the membrane first dissolves into the membrane and then diffuses through the membrane (Wijmans and Baker, 1995).

$$J_{H_2} = \frac{Q_0 \exp\left(-E_Q \big/ R \cdot T\right)}{l}\left(P_{H_2,2}^{0.5} - P_{H_2,1}^{0.5}\right) \tag{2.15}$$

While the permeability is independent of the membrane thickness, the permeance (F) is inversely proportional to the thickness (Equation 2.16). Gravimetric calculation (by weight gain) of membrane thicknesses is generally inaccurate because of the non-uniformity of the support surfaces and membrane deposits. Therefore, the permeance is calculated instead of the permeability.

$$F = \frac{Q}{l} \tag{2.16}$$

2.2.2 Deviations from Sieverts' Law

There are situations in which Sieverts' Law does not apply and the exponent of the pressure (generally referred to as the n-value) deviates from 0.5 (Equation 2.17).

$$J_{H_2} = F\left(P_{H_2,2}^n - P_{H_2,1}^n\right) \tag{2.17}$$

The first cause for the n-value to deviate from 0.5 is if the membrane is in an area of the Pd – H phase diagram (Figure 2-1) where the molar H/Pd ratio is no longer proportional to the square root of the hydrogen pressure. If the hydrogen pressure is high, the concentration of hydrogen in Pd increases, the $(1 - n_{H/Pd})$ term of Equation 2.3 can not be neglected and Equation 2.15 is no longer valid.

The second cause for the n-value deviation is when diffusion ceases to be the rate limiting step. If diffusion is not the rate limiting step, the adsorption and dissolution steps will not be at equilibrium, Equations 2.2 and 2.3 will not necessarily be equal to zero, and Equation 2.15 will no longer valid.

From the integrated Fick's Law (Equation 2.6) the flux of hydrogen from diffusion is inversely proportional to the membrane thickness. When membranes become extremely thin, the diffusion nears and surpasses the rate of adsorption. The rate of mass transfer from adsorption is dependent on the hydrogen pressure (Equation 2.2), causing the n-value to increase from 0.5 to 1. Ward and Dao (1999) calculated that only Pd films of 1 μm or less resulted in n-values of 1. Wu et al. (2000) measured an n-value of 1 for a

Pd membrane of a thickness of 0.3 – 0.4 μm. The subsequent activation energy was 21.3 kJ/mol, which they explained as being characteristic of hydrogen adsorption being the rate determining process.

However, Ward and Dao's (1999) predictions are for ideal Pd foils. Deviating n-values have been observed for Pd films which were thicker than 1 μm and deposited on porous supports. Li et al. (2000) found an n-value of 0.65 for a 10 μm membrane. Tong and Matsumura (2004) measured an n-value of 1 for a 6 μm membrane and Tong et al. (2005) found an n-value of 1 for a 3 μm membrane. All attributed the high n-value to hydrogen adsorption being the rate limiting process.

Adsorption can also become the rate determining step if impurities such as CO or H_2S adsorb on Pd and significantly slow down the rate of hydrogen adsorption. As a result, the permeance decreases and the n-value increases to one. Guazzone et al. (2006a) found that the n-value decreased from 0.67 to 0.53 as a pure Pd membrane was heated from 300 to 500°C. The n-value increase was attributed to the removal of contaminants from the membrane surface upon heating and an increase in the region of linearity with increasing temperature, seen in Figure 2-1. Hurlbert and Konecny (1961) attributed deviations in permeance and n-values between their work and previous authors' (Silberg and Bachman, 1958, Jost and Widman, 1940, Barrer, 1940) to contaminants on the membrane surface and the accumulation of non-permeable gases on the feed side.

Cracks and pinholes in the membrane cause the n-value to deviate from 0.5. Hydrogen which permeates through defects does so as a diatomic molecule, and not interstitially as an atom. The mechanism for mass transport is the combination of Knudsen diffusion and viscous flow and is referred to as the dusty-gas model (Mason and

Malinauskas, 1983). The dependence of the flux on pressure does not yield an n-value of 0.5 (Equation 2.18).

$$J = \left(F_k + F_v \cdot P_{avg}\right) \cdot \Delta P = \left\{ \frac{2}{3}\sqrt{\frac{8}{\pi}} \frac{\varepsilon \mu_k r}{l\sqrt{RTM}} + \frac{1}{8} \cdot \frac{\varepsilon \mu_v r^2}{l \eta RT} \cdot P_{avg} \right\} \cdot \Delta P \tag{2.18}$$

Membranes through which hydrogen primarily permeates with Knudsen diffusion have a selectivity which is equal to the inverse ratio of the square root of molecular weights of the diffusing gases. Ceramic membranes which did not have a hydrogen selective layer exhibited Knudsen selectivity (Shu et al., 1991). Bryden and Ying (2002) observed Knudsen selectivity with palladium/iron alloy membranes. They reasoned that because increasing iron content shrunk the palladium lattice and possibly decreased the hydrogen solubility, interstitial diffusion slowed down drastically until the main mechanism of hydrogen transport was through cracks and pinholes in the metal. Guazzone et al. (2006a) found that at selectivities above 400, Knudsen and viscous diffusion of hydrogen did not affect the n-value. Dense Pd membranes that later formed sulfide scales exhibited Knudsen selectivity due to the lattice parameter change (Chen and Ma, 2010a).

A composite membrane is composed of several layers whose respective resistances to mass transfer are in series (Equation 2.19). The total resistance to mass transfer in the composite membrane is expressed as the sum of each layer thickness divided by its permeability (Henis and Tripodi, 1981).

$$R_{tot} = \frac{1}{F} = \frac{l}{Q} \approx \frac{l_1}{Q_1} + \frac{l_2}{Q_2} + \frac{l_3}{Q_3} + ...$$ (2.19)

From Equation 2.19, the resistance of an extremely thin layer, or the resistance of a layer which has an exceptionally large permeability in relation to the other layers, can be neglected when added to the other resistances. Even though the thickness of the Pd layer is much smaller than that of the porous support, the support permeability is often high enough to merit neglecting the support resistance (Guazzone, 2006).

Significant mass transfer resistance from supports increases the n-value. Collins and Way (1993) characterized an 11.4 μm thick Pd membrane deposited on an alumina support, calculated an n-value of 0.573 and attributed the deviation from 0.5 to support resistance. The activation energy of the permeance of 8.8 kJ/mol was a further indication of the support mass transfer resistance.

2.3 Pd composite membranes

2.3.1 Porous Supports

McKinley (1966) tested the hydrogen permeance of 1 mm thick Pd membrane foils and concluded that the low permeance of the membranes coupled with the high cost of Pd rendered the process impractical for scale-up. Depositing a thin layer of Pd on a porous support reduces the amount of Pd needed while maintaining the structural integrity of the membrane at high pressure both increasing the permeance of the membrane and decreasing the cost of hydrogen production.

If the support surface is smooth with small surface pore diameters, adhesion between the membrane and support will not be as strong, especially if the support is non-metallic. Theon et al. (2006) coated a 0.02 μm media grade alumina support with zirconia and fabricated a 1.3 μm $Pd_{95}Cu_5$ membrane which delaminated from the support after six days of testing at 350°C. The delamination was attributed to the membrane being too thin.

If the surface is too rough with large surface pore diameters, the membrane would need to be very thick in order to completely cover the surface pores. Mardilovich et al. (2002) calculated that the thickness of a dense Pd layer needed to be at least three times the diameter of the largest pore on the surface. However, pores which are too small may add resistance to the total mass transfer. The increase in the n-value due to mass transfer resistance observed by Collins and Way (1993) occurred with ceramic porous supports with a surface pore diameter of 10 nm.

The porosity of porous supports also affects the hydrogen mass transfer through the entire composite membrane. Mardilovich et al. (2002) calculated that a porosity less than 0.2 caused a significant mass transfer resistance contribution from the support.

Ceramics are popular asymmetric supports since there is more control over pore size and pore size distribution than with metallic supports. Ceramic supports were made with surface pore diameters as small as 5 nm (Shu et al., 1996). Also, the high melting point of ceramics enables them to be used at higher temperatures than metallic supports. Gryaznov et al. (1993) deposited a $Pd_{94}Ru_6$ alloy on a magnesia/yittria support. The membrane had a stable permeance of 82.5 $m^3/m^2*h*bar^{0.5}$ at 700ºC for 1000 hours.

Vycor glass has a greater thermal stability than metallic supports in addition to small surface pore diameters and narrow pore size distributions. Souleimanova et al. (2002) deposited Pd on Vycor glass with an average surface pore diameter of 3.6 nm. A disadvantage with ceramic and Vycor glass supports is their brittleness and fragility. If not handled carefully, the entire composite membrane could shatter. Also, the difference in the coefficients of thermal expansion between the Pd membrane and the ceramic and Vycor glass supports can cause cracks to form in the Pd layer during thermal cycling, damaging the selectivity.

Buxbaum and Kinney (1996) used niobium and tantalum as supports coated with a thin layer of Pd. The advantage of niobium and tantalum (as well as vanadium) is that they are also selective to hydrogen and have higher H_2 permeabilities than Pd by several orders of magnitude. However, Nb and Ta are much less resistant to surface contamination by water, CO and hydrocarbons than Pd and oxidize very easily, necessitating a protective Pd layer. The supports used were not porous and the selectivity

of the composite membranes was infinite. However, the operating temperatures were restricted due to the high critical temperatures of hydrogen embrittlement of the supports (350°C for Ta and 420°C for Nb). The hydrogen permeance of the Pd coated Ta support at 420°C was 7.8 $m^3/m^2*h*bar^{0.5}$ and declined linearly by 15% over a period of 31 days (Buxbaum and Kinney, 1996). The decline was attributed to weekly backflushing of the membrane with hydrogen to remove impurities from the membrane surface.

Metal supports do not crack and break as easily as ceramics and Vycor glass and the coefficient of thermal expansion of stainless steel is closer to that of Pd. In addition, stainless steel is much stronger than ceramic material and unlike ceramics, can easily be welded and attached to fittings. However, it is difficult to control the pore size and pore size distribution of porous metal. Efforts have been made to modify the surface of porous stainless steel (PSS) in order to decrease the surface pore diameter.

Jemaa et al. (1996) used shot peening to modify the surfaces of their PSS supports. The energy of bombarding pellets deformed the support in the radial direction from the points of contact, decreasing the average surface pore size. It was observed that Pd deposited on supports which had undergone the shot peening treatment with iron pellets of an average diameter of 125 μm and a pressure of 510 kPa for 5 minutes became dense at a thickness of 6 μm while identical supports which had not undergone the treatment had dense Pd layers at 20 μm. The hydrogen permeance of the membrane was 11 $m^3/m^2*h*bar^{0.5}$ at 400°C. The selectivity was not reported.

Filling the larger surface pores is another method of modifying the surface of PSS supports. Tong and Matsumura (2004) blocked the larger surface pores by vacuum suction and ultrasonic vibration of an $Al(OH)_3$ particulate solution. The solution

effectively narrowed the pore size distribution and a thin, dense membrane of 6 μm was deposited on PSS. When the membrane was heated, the water from the $Al(OH)_3$ evaporated, allowing the support pores to "open up," decreasing the mass transfer resistance from the support, and the hydrogen permeance increased. At 500°C the hydrogen permeance was 23 $m^3/m^2*h*bar$ and the selectivity was infinite. The activation energy of the permeance was 16.7 kJ/mol. The same group (Tong et al., 2005) prepared a 3 μm Pd membrane on PSS with a permeance of 36 $m^3/m^2*h*bar$ and an infinite selectivity at 500°C which was stable for 200 hours of testing. The activation energy of the membrane was calculated to be 38 kJ/mol.

Guazzone (2006) deposited alumina powder with successively smaller particle sizes to block larger pores. The resultant membrane was 6 μm thick and had a stable permeance of 39 $m^3/m^2*h*bar^{0.5}$ for 1000 hours at 500°C. The ideal H_2/He separation factor was 800. Wang et al. (2004) used ZrO_2 particles and fabricated a 10 μm thick membrane. At 500°C, the ideal H_2/Ar separation factor was 1500 and the permeance was 17.6 $m^3/m^2*h*bar^{0.5}$. The activation energy was 7.1 kJ/mol, signifying that the support added to the overall hydrogen mass transfer resistance. The stability of the membrane was not reported. Athayde et al. (1994) used a polymeric support (which can not be used at higher temperatures) onto which a sealant was deposited to block the larger pores and provide a smoother substrate.

Klette and Bredesen (2005) circumvented the need of thick deposits to block support pores by sputtering PdAg films (thickness ranged between 0.8 – 5 μm) on silicon wafers, peeling the films off and sealing them on PSS. The membranes were exposed to a

pressure difference of 15 bar and had a permeance of 27 m^3/m^2*h*bar at 300°C. The selectivity was not reported.

2.3.2 Intermetallic diffusion barrier

Another problem with depositing Pd on metallic supports is the intermetallic diffusion which occurs between the support metals and the Pd. The Tamman temperature is defined as half of the melting point in degrees Kelvin. Significant intermetallic diffusion occurs when one or two metals adjacent to each other are near their Tamman temperatures. At the Tamman temperature, the atoms of the metal become more mobile due to thermal vibration. Although the metal is still in the solid state, its molecules slowly diffuse into the adjacent metal. Intermetallic diffusion is accelerated in a hydrogen atmosphere (Edlund and McCarthy, 1995) and is marked by a decrease in hydrogen permeance. The iron (Bryden and Ying, 2002) and nickel (McKinley, 1966) in stainless steel decrease the H_2 permeability of Pd.

A decline in hydrogen flux was seen at 550°C, the Tamman temperature of stainless steel (Mardilovich et al., 1998). Therefore, it is advantageous to have a diffusion barrier between the metal support and the membrane to prevent permeance loss for high temperature operations. Edlund and McCarthy (1995) found that a thin layer of porous alumina pressed between the Pd layer and support (vanadium) prevented intermetallic diffusion. The permeance of the membrane was stable at 500°C for six months of operation, at 600°C for 60 days and at 700°C for two weeks. A similar membrane tested without the layer of alumina between the Pd and V exhibited a sharp permeance decline at 700°C.

A $Pd_{94}Ru_6$ alloy membrane had a permeance of 52 $m^3/m^2*h*bar^{0.5}$ at 800ºC which was halved after 1000 hours of testing due to metal from the porous support diffusing into the hydrogen selective layer (Gryaznov et al., 1993). Several intermetallic diffusion barriers were investigated by testing membranes at 800ºC for 1000 hours by Gryaznov et al. (1993). Of the barriers tested, those which did not decrease the initial permeace of the membrane were 0.8 μm tungsten, 0.1 μm tantalum oxide, 0.5 μm magnesia and 1.0 μm zirconia. A 1.2 μm layer of alumina caused an 8% decrease in permeance and a 0.08 μm layer of molybdenum caused a 30% decrease in permeance. Guazzone (2006) used alumina powder both for pore blocking and as an intermetallic diffusion barrier. The permeance of the membrane was 43 $m^3/m^2*h*bar^{0.5}$ at 500°C and remained stable for 1000 hours of testing. Ma et al. (2007) deposited a porous Pd/Ag barrier between the support and membrane to function as both an intermetallic diffusion barrier and a means for bridging the pores of the support. The permeance of the membrane reached 14 $m^3/m^2*h*bar^{0.5}$ at 500°C and remained stable for four days of operation.

A simpler method of forming an intermetallic diffusion barrier is the in-situ oxidation of the support itself. Ma et al. (2000) oxidized PSS supports at 900°C for four hours to produce an oxide layer rich in the thermodynamically stable Cr_2O_3 and found the hydrogen permeance of the deposited Pd membrane to be stable for 1000 hours at 350°C. However, high oxidation temperatures were found to reduce the support permeance (Akis et al., 2003).

2.3.3 Hydrogen selective layer

Alloying Pd with other metals can improve the performance of pure Pd membranes. Because of the relative ease of deposition, low cost (with the exception of

Au) and membrane enhancing properties, Cu, Ag, and Au alloys of Pd are the most studied. Figure 2-4 shows how the compositions of Cu, Ag and Au affect the permeability of Pd at 350 and 500ºC.

Alloying Pd with Ag increases the hydrogen permeability as much as 1.7 times (see Figure 2-4) between 10 and 30 wt% Ag. The wide range allows more room for error in alloy composition when producing high permeability Pd/Ag membranes. The enhanced permeability is due to the increased solubility of hydrogen in Pd/Ag alloys which peaks at 30 wt% Ag (Knapton, 1977). Another advantage of the Pd/Ag system is that the critical temperature of the $\alpha \leftrightarrow \beta$ phase transition is lowered. Hunter (1960) showed that 25 wt% Ag alloys did not have the deformation of shape that pure Pd had after 30 heating and cooling cycles in hydrogen.

Similar to Pd/Ag alloys, Pd/Cu alloys also prevent hydrogen embrittlement down to 150°C at a concentration of 40 wt% Cu (McKinley, 1969) and 50°C at concentrations lower than 10 wt% Cu (Uemiya et al., 1991). The disadvantage of alloying Cu with Pd is that most Pd/Cu alloys lower the permeability of the membrane rather than increasing the permeability as do Pd/Ag and Pd/Au alloys (McKinley, 1966). Figure 2-4 shows that Cu causes a decrease in permeability at small concentrations and then increases the permeability after 30 wt%. The curve peaks at 40 wt% where the permeability is 1.3 times higher than pure Pd, and then sharply decreases again towards zero. The increase is caused by the onset of the fcc-bcc phase transition and will be discussed more in depth in Chapter 5. The narrow range of the increased permeability makes high permeance Pd/Cu membranes more difficult to fabricate than high permeance Pd/Ag or Pd/Au membranes.

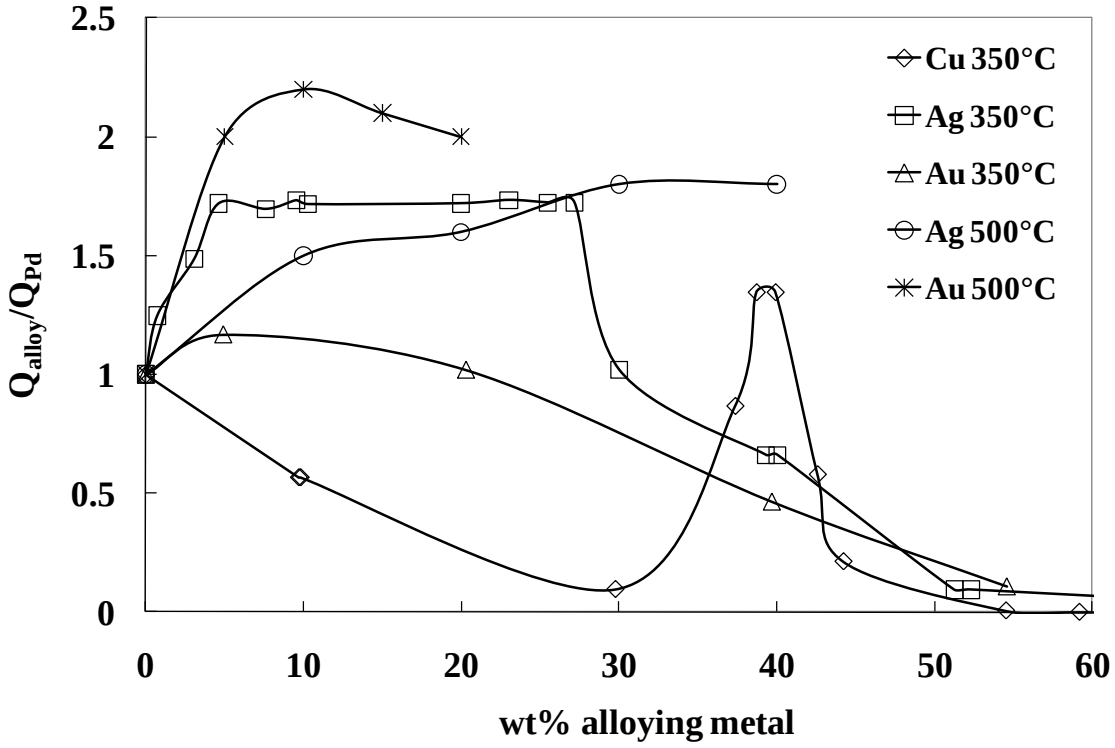

Figure 2-4 Relative permeability as a function of alloying metal content.[*]

[*] Data at 350ºC adapted from McKinley (1966, 1969), and Knapton, 1977, data at 500ºC taken from Gryaznov, 2000. The lines are for guiding the eye.

There is some disagreement as to the effect of Pd/Au on the hydrogen permeability. Some authors show a large increase at 500ºC (Gryaznov, 2000, shown in Figure 2-4) and a slight increase at 350ºC up to 20 wt% Au (McKinley, 1966, 1969, also shown in Figure 2-4). However, some authors have observed a decrease in hydrogen permeability. Grashoff et al. (1983) observed a 13% hydrogen permeability decrease with a 20 wt% Au alloy at 540ºC. Way et al (2008) also reported a decrease in permeability in 5 wt% Au membranes in comparison to pure Pd membranes at 400ºC. The decrease was attributed to Au segregating to the surface, thereby decreasing the catalytic activity of the membrane.

There are other alloys that have shown an increased permeability in relation to pure Pd such as 10 wt% Y and 7.7 wt% Ce which increase the permeability 3.8 and 1.6 times, respectively (Knapton, 1977), and 10 wt% Pt, 5 wt% Rh, and 4.5 wt% Ru that increase the permeability 1.2, 1.4 and 1.4 times, respectively, at 500°C (Gryaznov, 2000). Ternary alloys have also been shown to increase the hydrogen permeability. $Pd_{93.5}Ru_{0.5}In_{6.0}$ and $Pd_{80}Ag_{19}Rh_{1}$ increased the permeability 2.8 and 2.6 times, respectively, at 500°C (Gryaznov, 2000). However, producing homogeneous membranes with such specific concentrations would be quite difficult for composite membranes.

2.4 Pd Membrane Fabrication

Earlier studies used Pd and Pd alloy foils for permeation experiments (McKinley, 1966) but modern techniques, the most common of which are presented here, allow the deposition of thin Pd films on supports. Each method of membrane synthesis has advantages and disadvantages towards scale up feasibility, versatility, quality and deposit thickness.

2.4.1 Chemical Vapor Deposition and Spray Pyrolysis

In the chemical vapor deposition (CVD), Pd (or the desired metal for deposit) is complexed with a highly volatile medium that has a large difference between sublimation and decomposition temperatures. The complex is sublimated to vapor form and decomposed on the substrate (the porous support) thereby depositing the metal. The high temperature of the gas stream negates the possibility of using most metallic supports.

Uemiya et al. (1997) used CVD to synthesize Pd, Ru and Pt membranes on alumina supports. They observed that a Pd membrane produced by CVD with a gravimetric thickness of 3.2 μm had a hydrogen flux that was 1.6 times higher than a Pd membrane previously produced by electroless plating with a thickness of 4.5 μm (Uemiya et al., 1991). Uemiya et al. (1997) estimated that the effective thickness of the CVD membrane was 5 μm because Pd also deposited into the alumina support pores, not just on the surface. Therefore, they reasoned that the higher hydrogen permeance of the CVD membrane was not due to the difference in the gravimetrically calculated thickness, but due to a different permeation mechanism which consisted of both the solution-diffusion mechanism and surface diffusion of spillover hydrogen on the deposited Pd in the pores.

The hydrogen permeance and ideal H_2/N_2 separation factor of the Pd membrane produced by CVD were 11 $m^3/m^2*h*bar^{0.5}$ and 240 at 400°C, respectively.

Itoh et al. (2005) used TG-DTA (thermogravimetry and differential thermal analysis) to investigate the thermal properties of Pd diacetate, which they used in CVD. Decreasing the sublimation pressure increased the fraction of Pd depositing on the support and decreased the sublimation temperature. A linear dependence between the fraction of Pd diacetate which sublimated and the logarithm of the sublimation pressure was found. The dependence of the fraction sublimated on the heating rate was also investigated and a maximum was found at a heating rate of 4K/min. Based on the conclusions of their TG-DTA analysis, Itoh et al. (2005) used a pressure of 10 Pa and a heating rate of 4K/min to prepare a 2 – 4 μm Pd membrane on a tubular alumina support with forced flow CVD.

The rationale for the forced flow being that the pressure difference between the outside and inside of the tube would cause Pd to deposit preferentially on the walls of the support pores and plug the pinholes, making a thinner membrane. At 300ºC the ideal H_2/N_2 separation factor of the membrane was 5000 and the permeance was 102 $m^3/m^2*h*bar^{0.5}$.

In the spray pyrolysis, similarly to CVD, a metal-salt solution is evaporated and sprayed into an ignited gas stream (usually hydrogen and/or oxygen) where the salt solution is pyrolyzed. The gas stream flows around and then deposits on the substrate.

Li et al. (1993) was the first to use spray pyrolysis for producing Pd membranes. They fabricated a Pd/Ag alloy membrane less than 2 μm thick on alumina hollow fibers. Droplets of a $Pd(NO_3)_2$ and silver nitrate solution were produced by ultrasonic vibration

before entering the flame. A support temperature of 970ºC was sufficient to form a uniform Pd/Ag alloy. The membrane had a hydrogen permeance and ideal H_2/N_2 separation factor of 8 m^3/m^2*h*bar and 24 at 500ºC, respectively.

Spray pyrolysis facilitates alloy formation. The membrane anneals much faster at lower temperatures than with other deposition methods since more than one metal can be deposited at the same time and the high temperature of the system partially anneals the membrane during deposition. However, Li et al. (1993) found it difficult to control the alloy concentration because silver would evaporate after the simultaneous deposition of Pd and Ag and a second deposit of silver was needed.

2.4.2 Sputtering

In the magnetron sputtering, metallic atoms are sputtered at a high pressure towards argon atoms. The resulting loss of energy from the collisions cools the metal atoms which nucleate while in the gas phase. Lowering the pressure causes the airborne nanocrystals to deposit on the substrate. Although sputtering has the advantage of producing extremely thin membranes with negligible impurities and allowing greater control over the alloy concentration, grain size and structure than with other deposition methods, the cost of production renders the method impractical for industrial use.

Bryden and Ying (1995) deposited Pd on Vycor glass by sputtering. The resultant membranes had thicknesses ranging from 0.05 to 5 μm. Transmission electron microscopy (TEM) was used to determine the optimal sputtering pressure. Higher pressures of 7 Pa formed films which had a discontinuous morphology with large cracks. When lowering the pressure the film became more granular but still had defects. Only

when the sputtering pressure was reduced to 0.1 Pa was a uniform layer achieved. The membranes were not characterized.

Gryaznov et al. (1993) deposited uniform Pd alloys on PSS by sputtering. A 10 μm thick membrane with 6 wt% Ru had a permeance of 52 $m^3/m^2*h*bar^{0.5}$ at 800ºC and a 1.5 μm thick membrane with 6 wt% In and 0.5 wt% Ru had a permeance of 9.7 $m^3/m^2*h*bar^{0.5}$ at 372ºC. The respective permeances were stable for 1000 hours of testing. Both membranes were claimed to be crack and pinhole free for the duration of testing.

Athahyde et al. (1994) produced 24 wt% Ag membranes with thicknesses ranging between 250 – 1000 Å. The Pd/Ag alloys were deposited on porous supports covered with a simethylsiloxane sealant. The permeance of a 500 Å membrane at 25ºC was 0.5 $m^3/m^2*h*bar$. When tested for stability at room temperature, the permeance dropped slightly in the first 50 hours and then returned to the original value over the course of the 1400 hour testing period. A 50/50 mol% H_2/CO_2 mixture was used to test the selectivity. A permeate stream of 99% H_2 was obtained in the beginning of the testing period and after 1400 hours the stream was 98% pure. The low operating temperature was due to the polymeric support.

2.4.3 Electroless Plating

Electroless plating utilizes the negative potential inherent in Pd to reduce and deposit Pd on a substrate without an electric current. The plating bath has four components: a source of metal ions, a reducing agent, a complexing agent and a stabilizer.

The salts $Pd(NH_3)_4Cl_2$, $PdCl_2$, and Pd acetate are generally used as a source of Pd ions (Mallory and Hajdu, 1990). $Pd(NH_3)_4Cl_2$ acts as both a source of ions and a complexing agent when dissolved. The complexing agent is usually an organic acid or its salt, and is added to buffer the solution during deposition and prevent precipitation of the metal salt by complexing the metal ions, thereby reducing the effective metal ion concentration. In the case of $Pd(NH_3)_4Cl_2$, the ammonia molecules complex with the Pd^{2+} ion. EDTA and ethylenediamine are used both as complexing agents and stabilizers.

Typical reducing agents usually have two or more reactive hydrogen sites for the oxidation of the metal. Hydrazine, hypophosphate, amine borane or formaldehyde are used to reduce Pd. Hydrazine is preferred when plating membranes over hypophosphate and amine borane since the latter cause phosphorous and boron to deposit with Pd (Buxbaum and Kinney, 1996). However, hydrazine undergoes autocatalytic decomposition which necessitates replenishing the plating bath. Hypophosphate has a higher plating efficiency than hydrazine, but the hydrogen formed in the redox reaction caused delamination of the Pd coating (Cheng and Yeung, 2001). Formaldehyde reduces Pd^{2+} ions in acidic conditions, but the plating rate is slower than that of hydrazine baths.

The reaction between $Pd(NH_3)_4Cl_2$ and hydrazine is shown in Equation 2.20 (Mallory and Hajdu, 1990).

$$2Pd\left(NH_3\right)_4^{2+} + N_2H_4 + 4OH^- \rightarrow 2Pd + 8NH_3 + N_2 + H_2O \qquad (2.20)$$

Large concentrations of hydrazine result in high deposition rates, cause non-uniform layers and lead to bulk precipitation. Low concentrations of hydrazine slow the deposition rate and decrease the plating efficiency (Yeung et al., 1999).

Stabilizers prevent the solution from spontaneously decomposing and causing Pd to precipitate. However, high stabilizer concentrations can prevent the desired deposition from ever occurring. Na_2EDTA is commonly used as a stabilizer of Pd (Mallory and Hajdu, 1990). Ammonium hydroxide also acts as a stabilizer in addition to being a buffer. Small quantities of ammonium hydroxide increase the deposition rate but do not prevent bath decomposition. Larger quantities of ammonium hydroxide result in stable plating baths but slower deposition (Yeung et al., 1999).

Rhoda and Madison (1959) prepared a Pd plating bath consisting of $Pd(NH_3)_4Cl_2$, Na_2EDTA, hydrazine and ammonium hydroxide. Most plating has been done similarly since (Collins and Way, 1993, Buxbaum and Kinney, 1996, Mardilovich et al., 1998, 2002).

Yeung et al. (1999) examined the influence of each component on the plating rate and morphology and reported that high plating rates formed large grains and the resultant coating had pinholes. Deposits with smaller grain sizes were achieved with lower deposition rates, usually between 1 - 3 μm/h. Shu et al. (1994) reported that dilute Pd^{2+} solutions inhibited nucleation and produced loosely packed, large grained Pd crystals while more concentrated solutions produced tightly packed, small grained crystals.

Before plating, the substrate was sensitized and activated to avoid Pd deposition on surfaces other than the substrate (Feldstein and Weiner, 1972). Activating the surface of the substrate with Pd nuclei prior to plating caused the Pd to deposit only on the support since the presence of nuclei reduced the induction time, which could be between 20 - 45 minutes without nucleation (Yeung et al., 1999).

The widely used sensitizing/activating procedure (Shu et al., 1996, Yeung et al., 1999, Mardilovich et al., 1998, 2002) is used to coat the support with Sn^{2+} ions when immersed in an acidic $SnCl_2/SnCl_4$ bath and seeded with Pd nuclei after immersion in an acidic $PdCl_2$ bath through the reduction of the Pd^{2+} ions (Equation 2.21). Several cycles of immersion were required in order to produce a uniformly activated substrate. Too thick an activation layer lessened the adhesion of the plated layers (Mardilovich et al., 1998).

$$Sn^{2+} + Pd^{2+} \rightarrow Sn^{4+} + Pd^{0} \qquad (2.21)$$

Although the sensitizing/activating step was relatively easy to scale up, Zhao et al. (1998), Paglieri et al. (1999) and Wu et al. (2000) have found it time-consuming and possibly detrimental to the membrane because of the presence of undissolved tin compounds which have low melting points at the support/membrane interface. Also, it was possible that a non-uniform deposition of Pd resulting from the activation step caused Pd films to peel off of the supports. The disadvantages of the sensitization/activation procedure prompted investigation of different methods of activation.

Wu et al. (2000) used photocatalytic deposition (PCD) to activate the support instead of the standard sensitization/activation procedure. A semiconductor support (TiO_2) was immersed in a solution with Pd^{2+} ions and irradiated with UV light to form Pd nuclei. The membrane was deposited by electroless deposition with a resultant thickness of 0.3 – 0.4 μm. The permeance at 500ºC was 56.2 m^3/m^2*h*bar and the ideal H_2/N_2 separation factor was 1140. The activation energy was 21.3 kJ/mol. Testing the membrane for stability showed a decrease in permeance from 25.9 to 21.3 m^3/m^2*h*bar

at 400ºC over a 160 hour period. The considerable difference between the permeance of the membrane at 500 and 400°C gave an activation energy of 33 kJ/mol, which the authors did not report. The discrepancy could have been due to the properties of the membrane changing over time and temperature. The authors hypothesized that the decline in permeance at 400°C was due to the rearrangement of the Pd lattice, the same hypothesis given by Mardilovich et al. (1998) for a permeance decline seen at 350ºC. Activation by means of PCD could only be used with semiconductor supports with photocatalytic stability.

Zhao et al. (1998) activated supports with a boehmite sol-gel and plated the Pd under vacuum. The sol-gel also blocked the larger pores of the substrate while the vacuum deposition compressed the Pd deposit. However, the steps of synthesizing the sol-gel included drying at 5ºC for two days and calcining at 600ºC for 3 hours, making the sol-gel method very time consuming. The resultant membrane was 1 μm thick, with a permeance of 87 $m^3/m^2*h*bar$ at 450°C and an ideal H_2/N_2 separation factor of 23. The stability of this membrane was not reported.

Paglieri et al. (1999) immersed tubular alumina supports in a palladium acetate solution and after calcining the supports at 400ºC, reduced them at 500ºC in H_2. The results were compared with membranes fabricated with the unmodified $SnCl_2$ activation step and with the activation step modified by diluting the $SnCl_2$ solution by 1/100. Paglieri et al. (1999) observed that membranes prepared with the unmodified $SnCl_2$ solution developed leaks at 550ºC after several days of testing. Leak development also occurred in membranes prepared with the diluted sensitizing solution. SEM micrographs showed the appearance of pinholes in the Pd layer. A 10 μm membrane prepared with the

palladium acetate solution developed a leak at the same temperature, but a 21 μm membrane was stable for 50 days of testing at temperatures up to 550ºC. The thicker membrane developed a leak at 750ºC, showing more stability than the previous membranes. The ideal H_2/N_2 separation factor at 550ºC was 43 and the permeance was 6.4 $m^3/m^2*h*bar^{0.5}$. Membranes of the same thickness fabricated with the unmodified $SnCl_2$ activation step were not prepared and tested for comparison.

Yeung and Varma (1995) developed a variation of the electroless plating procedure utilizing osmosis. To obtain an osmotic pressure differential, a concentrated sucrose solution was placed on the permeate side of the membrane while the plating solution was on the feed side. The difference in osmotic pressure caused water from the plating solution to diffuse through the membrane and dilute the concentrated sucrose solution. Ideally, the water permeating through the membrane defects would cause the Pd ion concentration to increase in the defect, resulting in a faster deposition in the defect than in an area without any defects. Yeung and Varma (1995) plated Ag and Pd separately and co-deposited both metals with osmosis on alumina supports. They observed that the silver deposit plated without osmosis was porous and the silver deposit plated with osmosis was dense. The co-deposited films of Pd and Ag formed an alloy after two hours of annealing at 400°C in H_2.

Li et al. (1998) used a 3 M NaCl solution to provide an osmotic pressure differential to deposit a 10 μm membrane on a PSS support. A permeance of 17.4 $m^3/m^2*h*bar^{0.5}$ at 480°C and an ideal H_2/N_2 separation factor of 1000 were observed. No decrease in membrane performance was seen at temperatures of 400°C for 250 hours.

Li et al. (2000) applied electroless plating assisted by osmosis to repair already damaged membranes made by electoless plating on alumina supports without osmosis. In one example, the original membrane had a thickness of 7.6 μm and after two repairs the thickness increased to 10.3 μm. The ideal H_2/N_2 separation factor of the original damaged membrane was 10 and increased to 970 after the repair. The permeance decreased from 129 to 58.1 $m^3/m^2*h*bar^{0.5}$ at 467°C. The activation energy was 12.3 kJ/mol after the repair but the stability of the replated membrane was not investigated.

Souleimanova et al. (2002) compared the standard electroless plating procedure with electroless plating assisted by osmosis with a sucrose solution. Dense Pd membranes were deposited on Vycor glass supports with the thickness of the membrane fabricated with osmosis being less than half that of the membrane formed without osmosis (8 μm rather than 18 μm). The activation energy of the membrane plated with osmosis was less than the activation energy of the membrane plated without osmosis (18.8 kJ/mol as opposed to 21.6 kJ/mol). The difference in activation energies was attributed to the smaller grain size seen in the membrane produced with osmosis. The membranes were heated to 500°C in air and quenched to room temperature. After four cycles, the membrane fabricated without osmosis developed cracks and the membrane fabricated with osmosis remained "dense" even after 15 cycles. No ideal separation factor was reported. The permeance of the membrane plated with and without osmosis were 40 and 16 $m^3/m^2*h*bar^{0.5}$ at 500°C, respectively.

2.5 Sulfur Poisoning of Pd

2.5.1 S-Pd interactions

Sulfur poisoning poses a problem for both the fields of catalysis and membrane separation. Trace amounts of H_2S caused the deactivation of Pd catalysts (Gelin et al., 2003, Li-Dun and Quan, 1990, Feuerriegel and Klose, 1998) and the poisoning of Pd membranes (Musket, 1976, Gao et al., 2004). Much research has been devoted to the problem of sulfur poisoning (Oudar, 1980, Bartholomew et al., 1982, Biswas et al., 1988, Barbier, 1990) as it affects a wide range of industrial processes.

Bulk phase diagrams such as the Pd – S phase diagram shown in Figure 2-5 do not necessarily provide thermodynamic information on sulfur poisoning. Bulk nickel sulfides form at H_2S concentrations of 100 – 1000 ppm and higher in the temperature range of 450 – 550°C (Rosenqvist, 1954). However, Ni catalysts have been poisoned at H_2S concentrations of a few ppm, conditions at which bulk sulfides are not stable (Bartholomew et al., 1982). The same phenomena were seen with platinum catalysts (Biswas et al., 1988). Sulfur poisoning is highly dependent on the adsorption of H_2S onto the metal surface causing the formation of chemisorbed surface sulfides rather than bulk sulfides.

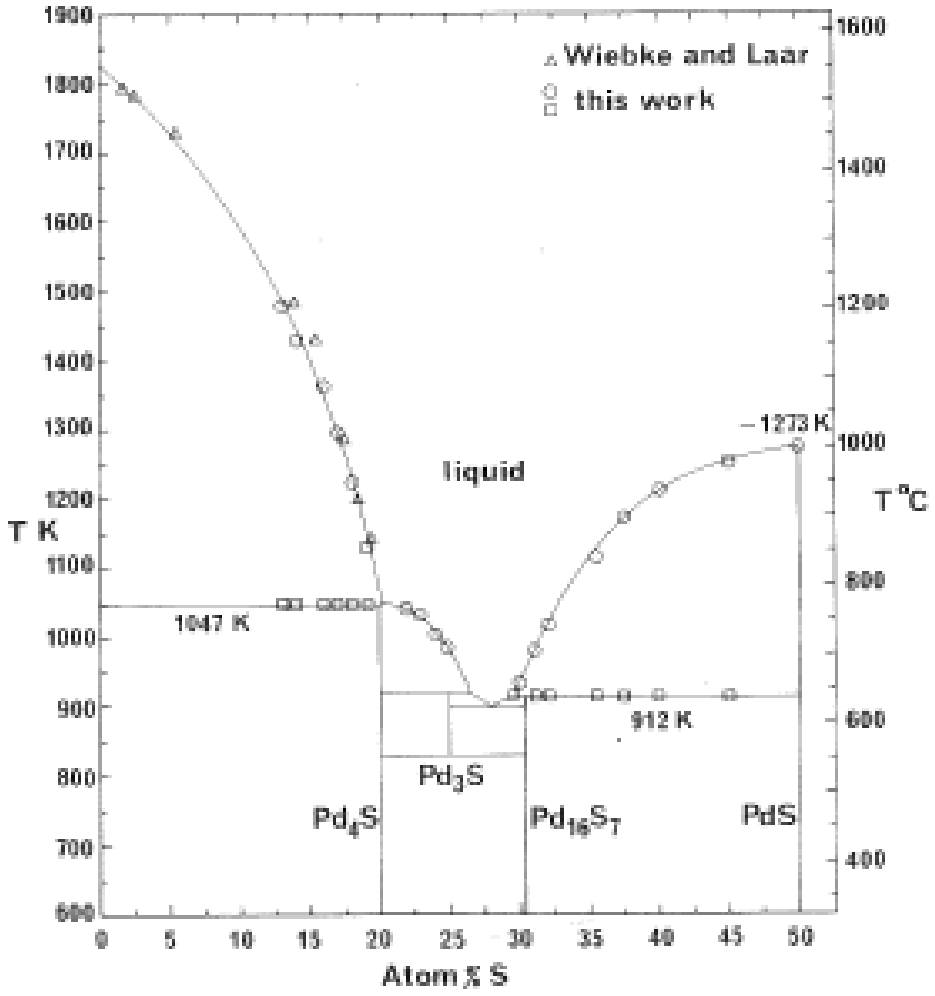

Figure 2-5 Pd-S phase diagram (Taylor, 1986).

Surface sulfides have been shown to be stable under conditions at which bulk sulfides are not stable. It was found that the Gibb's free energies of formation for surface sulfides were at least 40 kJ/mol more negative than their bulk sulfide counterparts (Bartholomew et al., 1982). Figure 2-6 shows a correlation between the Gibbs free energy of bulk sulfide formation and surface sulfide formation for several metallic sulfides. According to the regression of the experimental data $\Delta G^{o}_{surface}$ vs. ΔG^{o}_{bulk}, as shown in Figure 2-6, if the threshold for bulk sulfide formation was on the order of several thousand ppm of H_2S, the threshold for surface sulfide formation would be three orders of magnitude less. The higher stability of surface sulfides shows the susceptibility of transition metals to sulfur poisoning. In the case of Pd where several ppm are known to cause bulk sulfide formation, surface sulfide formation would still occur at a few ppb.

Under reducing atmospheres, H_2S undergoes dissociative chemisorption on most metals. The dissociative adsorption of H_2S on Pd was confirmed at temperatures as low as -80°C by Saleh (1970) when the presence of gaseous H_2 was observed following H_2S adsorption on Pd. The heat of adsorption as a function of the sulfur surface coverage, θ, is the difference between the activation energy of adsorption and desorption (Equation 2.22).

$$\Delta H_{\theta} = E_{a,\theta} - E_{d,\theta} \tag{2.22}$$

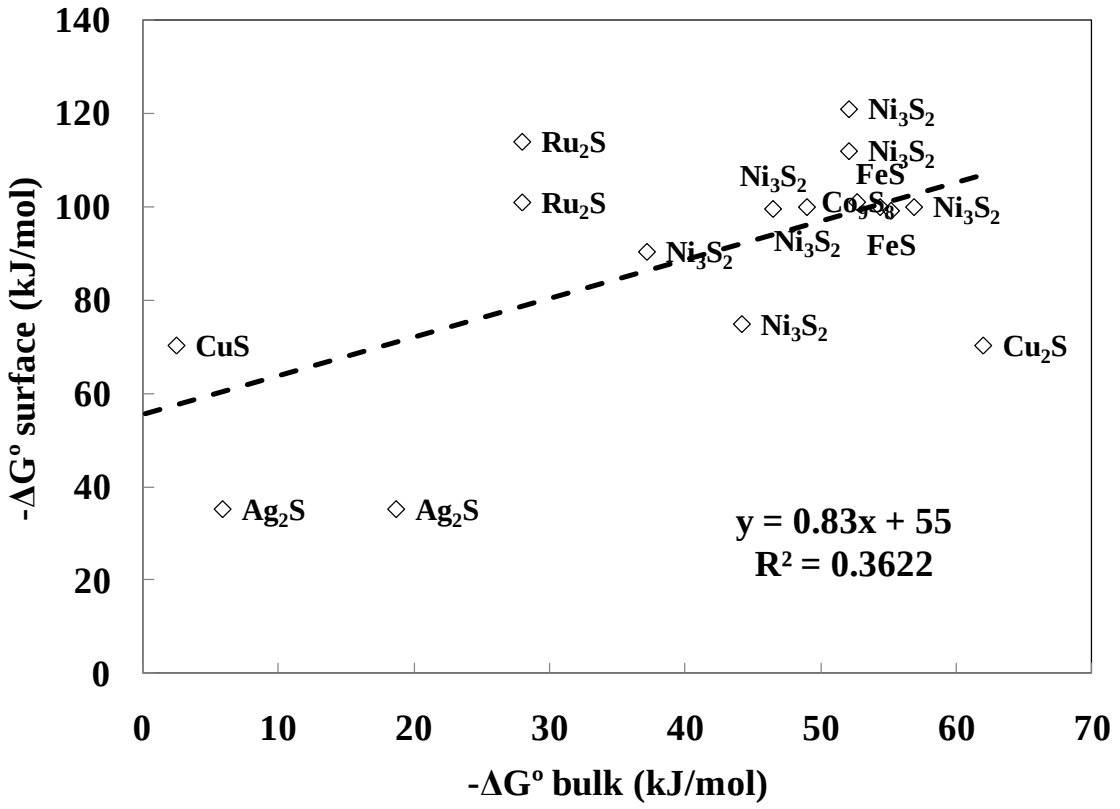

Figure 2-6 Correlation between the Gibbs free energy of formation of bulk sulfides and their surface sulfide counterparts (Bartholomew et al., 1982).

In the case of chemisorption on metals, the activation energy of adsorption was negligible relative to that of desorption and could be neglected, thus the absolute value of the heat of adsorption equaled the activation energy of desorption (Barbier et al., 1990). If the Van't Hoff equation was assumed, the heat of adsorption could be calculated from H_2S adsorption isotherms, as shown in Equation 2.23 (Oudar, 1980). However, adsorption isotherms for H_2S on Pd were not available in the literature.

$$\left.\frac{\partial \log\left(P_{H_2S} \big/ P_{H_2}\right)}{\partial T}\right|_{\theta} = \frac{-\Delta H_{\theta}}{RT^2} \tag{2.23}$$

Saleh (1970) investigated H_2S adsorption on Pd at temperatures ranging from -80ºC to 250ºC and found the activation energy for adsorption to be proportional to the inverse of X* (Equation 2.24).

$$E_{a,x} = 87.8 - \frac{160.247}{X} \pm 6.3 \tag{2.24}$$

Equation 2.23 supported the assumption that the activation energy of adsorption could be neglected, but only at small values of X. At values below X = 1.8, the activation energy for adsorption was equal to zero. A monolayer of sulfur was formed at X = 1.35, showing that for the chemisorption of H_2S on Pd the heat of adsorption was equal to the activation energy of desorption. As X increased, the activation energy for adsorption

* $X = V_s/V_m$ where V_s is the volume of H_2S adsorbed and V_m is the volume of a krypton monolayer on the Pd film. The film area was calculated from the physisorption of krypton at the temperature of liquid nitrogen (Saleh et al., 1961). When X = 1.35, θ_S = 1 ML (monolayer).

increased. The limiting value of $E_{a,x}$ was 87.8 kJ/mol. Assuming that the activation energy for desorption was constant with surface coverage, an increase in the activation energy for adsorption would cause the heat of adsorption to decrease (Equation 2.22). The increase in the activation energy of adsorption with X was explained by Saleh (1970) as bulk sulfide formation.

Similar results with nickel have shown that the heat of adsorption decreased from 165 kJ/mol to 75 kJ/mol when 1 ML was reached. The sudden decrease in the heat of adsorption was explained by the presence of HS^- and undissociated H_2S (Barbier et al., 1990). The affinity of H_2S to the sulfided surface was less than the affinity to the unsulfided surface. The same phenomena were seen with H_2S adsorption on Pt where the heat of adsorption decreased from 122 to 26 kJ/mol at 0.6 ML (Barbier et al., 1990).

The effect of H_2S adsorption was observed to be partially irreversible. After sulfiding Pt with a H_2S/H_2 mixture at 180ºC and then raising the temperature to 500ºC in a H_2 atmosphere, part of the sulfur desorbed immediately. The H_2S which did not desorb after 30 hours was deemed irreversible. The amount of irreversible sulfur was independent of the concentration of H_2S in the feed, but the total amount of sulfur deposited increased with increasing H_2S content. (Barbier et al., 1990), shown in Figure 2-7.

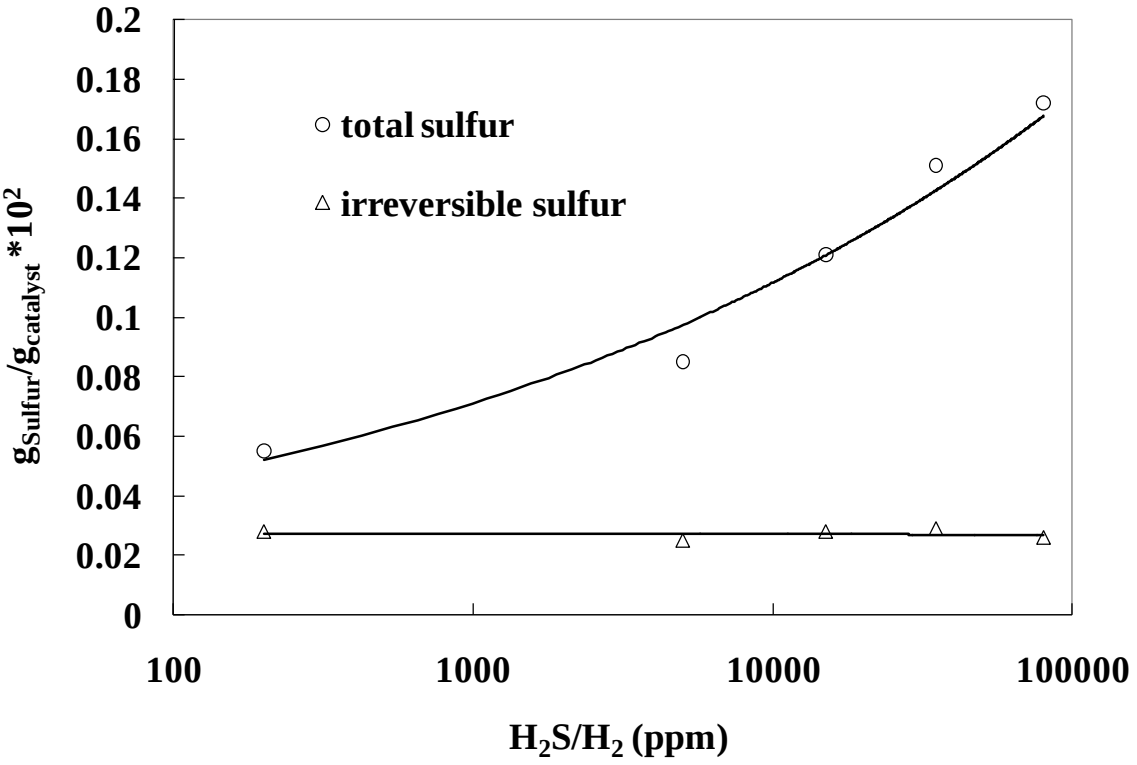

Figure 2-7 Sulfur adsorbed on Pt/Al_2O_3 catalysts at 180°C (Barbier et al., 1990).

There has been much research devoted to studying Pd-S interactions and how the presence of sulfur on the surface of Pd inhibits H_2 adsorption. Rodriguez et al. (1998) used both low energy electron diffraction (LEED) measurements and *ab-initio* calculations to analyze a Pd(1 1 1) surface. They concluded that the most energetically favorable bonding sites were the fcc hollows of palladium and that sulfur bonded with itself at surface coverages higher than 0.5 ML.

Speller et al., (1999) used LEED and scanning tunneling microscopy (STM) to investigate sulfur formations on Pd(1 1 1). They observed that the adsorption of H_2S on palladium produced different surface structures of sulfur than those produced by the segregation of impurity bulk sulfur towards the surface. While the segregation resulted in triangular "islands" of sulfur (Figure 2-8a, also observed by Bomermann et al., 1996), the adsorption resulted in "stripes" of sulfur (Figure 2-8b). The island formation was explained by a random walk model in which the sulfur atoms moved across the Pd surface while forming an increasing number of bonds with neighboring sulfur atoms until all sulfur atoms became immobile. There was no mathematical model to explain the formation of the stripes.

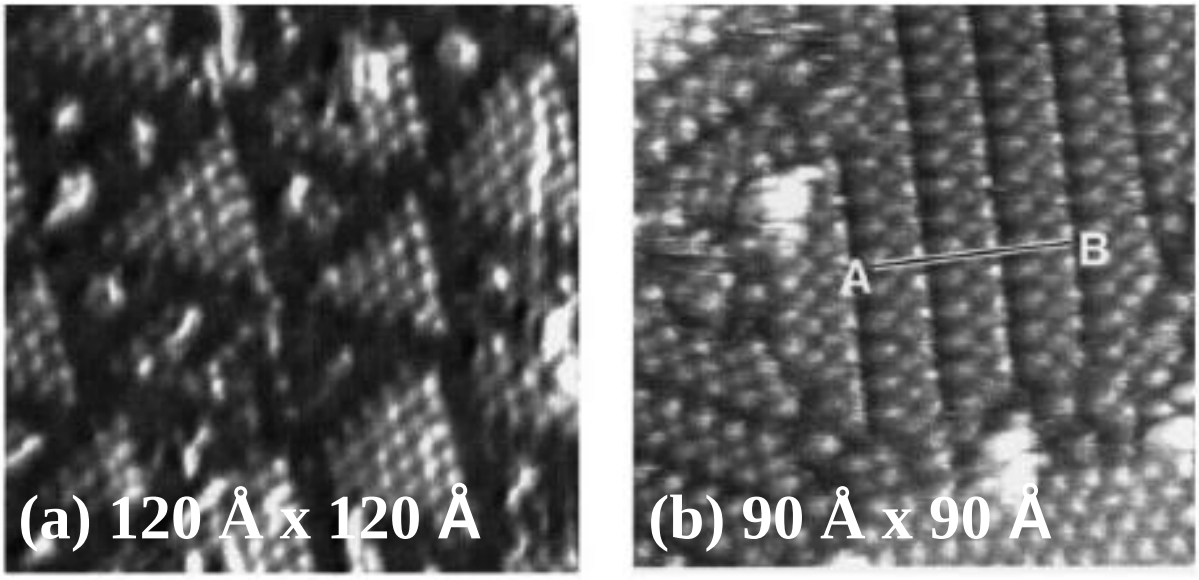

Figure 2-8 STM micrographs of (a) (2 x 2) triangular islands and (b) (2 x 2) stripes (Speller et al., 1999).

Alfonso et al. (2005) employed density functional theory (DFT) to model the adsorption and decomposition of hydrogen sulfide on Pd(1 1 1). The proposed mechanism included a series of elementary reactions shown in Equation 2.25:

$$H_2S_{(g)} \rightarrow H_2S_{(ad)} \rightarrow SH_{(ad)} + H_{(ad)} \rightarrow S_{(ad)} + H_{(ad)} \quad (2.25)$$

The adsorption of each of the species in Equation 2.25 was investigated on sulfur coverages of 0.06, 0.11, 0.22 and 0.33 ML. The absolute value of the binding energy of H_2S to Pd slightly decreased with the increase of the surface coverage, showing repulsive interactions between the H_2S molecules. The same trend was observed with adsorbed SH and S but the binding energies were successively more negative than those of H_2S, showing that Pd-S was more stable than Pd-SH which was more stable than Pd-H_2S.

When calculating the energetics of each elementary reaction in Equation 2.25, Alfonso et al. (2005) observed that the physisorption of H_2S had no activation barrier and was exothermic. The dissociation of H_2S to adsorbed SH and H and of SH to adsorbed S and H were also exothermic and had low activation barriers, leading Alfonso et al. (2005) to conclude that physisorbed H_2S was not stable on the Pd(1 1 1) surface and would undergo dissociative chemisorption within the range of surface coverages investigated.

Alfonso (2005) later performed DFT calculations on sulfur adsorbed on Pd(1 1 1) which showed that at coverages higher than 0.5 ML, the bond between S-Pd weakened and the interactions between adsorbed sulfur atoms became more significant. In addition, the subsurface sites became more energetically favorable for sulfur than the surface sites which Alfonso (2006) interpreted as being a precursor for bulk sulfide formation.

2.5.2 Effect of sulfur on hydrogen adsorption

The rate of the dissociative adsorption of hydrogen on palladium (given in Equation 2.26) was a product of the sticking probability (s) and the rate of hydrogen molecules colliding with the Pd surface (Γ) (Ward and Dao, 1999).

$$J_{H_2} = 2 \cdot s(\theta) \cdot \Gamma \frac{RT}{P} \tag{2.26}$$

The sticking probability was defined as the fraction of molecules adsorbing on the surface of all of the molecules colliding with the surface. Assuming that the concentration of H_2S in the feed is small enough not to affect the number of H_2 molecules colliding with the surface, it was only the sticking probability which was changed by the presence of sulfur on the membrane. A clean Pd surface had a hydrogen sticking probability of 1 (Ward and Dao, 1999). The sticking probability gradually decreased towards zero as sulfur occupied more adsorption sites, thus decreasing the area for adsorption. Peden et al. (1986) calculated that the sticking coefficient of hydrogen would need to be reduced to a value of 10^{-6} in order for adsorption to become the rate limiting step of hydrogen diffusion. However, such a large decrease in the order of magnitude indicated that hydrogen adsorption would seldom be rate limiting and did not account for thin membranes which have n-values of 1, where hydrogen adsorption was indeed the rate limiting process (Wu et al., 2000, Li et al., 2000, Tong and Matsumura, 2004, Tong et al., 2005).

Peden et al. (1986) studied the dissociative adsorption of hydrogen on both clean and sulfided Pd(1 1 0)[*] surfaces in an ultra high vacuum at 100°C. They observed that the rate of hydrogen adsorption decreased at sulfur coverages greater than 0.4 ML and that the rate of adsorption was proportional to the hydrogen pressure. Therefore, they reported that at surface coverages higher than 0.4 ML, the diffusion would cease to be the rate limiting step of the hydrogen transfer.

Burke and Madix (1990) performed temperature programmed desorption (TPD) experiments on both clean and varied levels of sulfided Pd(1 0 0) surfaces. They showed that the saturation coverage of hydrogen dropped linearly with the sulfur coverage. Upon extrapolation, they observed that a sulfur coverage of 0.28 ML reduced the hydrogen saturation coverage to zero, a monolayer value which was less than the Pd(1 1 0) surface examined by Peden et al., (1986). It appeared that the Pd(1 1 0) surface was more resistant to sulfur in that hydrogen still adsorbed at higher surface coverages (0.4 ML) than on the Pd(1 0 0) surface. Since one adsorbed sulfur atom blocked 3.7 adsorption sites for hydrogen on the Pd(1 0 0) surface, Burke and Madix (1990) concluded that sulfur blocked hydrogen by both geometric effects (physically blocking) and electronic effects (changing the nature of the valence band of Pd to which hydrogen would adsorb) in nearby Pd atoms.

The activation energy of hydrogen desorption was found to decrease from 80 kJ/mol on clean Pd(1 0 0) to 45 kJ/mol on 0.15 ML. They also found that the initial sticking probability of hydrogen decreased to 0.05 on Pd(1 0 0) at a sulfur coverage of

[*] Pd is known to have an fcc structure (Cullity, 1978) which does not have (1 0 0) or (1 1 0) planes. The authors are referring to surfaces, not planes of unit cells as with the DFT calculations of Alfonso et al. (2005).

0.25 ML. The presence of sulfur both decreased the probability of hydrogen remaining adsorbed to the Pd surface, and weakened the bond formed between H and Pd by dissociative chemisorption.

Similarly, Biswas et al. (1988) observed "electronic" blocking effects of H_2S. Geometric or steric blocking of hydrogen only happened when sulfur was adsorbed on a hydrogen ad-site (adsorption site). However, the presence of sulfur on the Pt surface blocking vacant ad-sites was attributed to an "effective blocking radius" caused by the S-Pt bond changing the nature of the electron density of neighboring Pt atoms which were not bonded with the sulfur ad-atom (adsorbed atom).

Wilke and Scheffler (1995) performed a theoretical study using DFT to compare the hydrogen adsorption on a clean and sulfided surface of Pd(1 0 0). They calculated the adsorption energies of hydrogen on Pd at different surface sites (hollow, bridge and subsurface) for 0, 0.25 and 0.5 ML of sulfur coverage. The hollow was found to be the most energetically favorable for hydrogen adsorption on clean Pd. At a coverage of 0.25 ML, a hollow site which had four sulfur atoms in the next nearest neighbor positions was found to be the most favorable. At 0.5 ML, subsurface sites were found to be more favorable because all hollow surface sites had four sulfur atoms as nearest neighbors, in agreement with the observation of Burke and Madix (1990) that H_2 did not adsorb at sulfur coverages higher than 0.28 ML.

Wilke and Scheffler (1995) concluded that at lower coverages of sulfur, hydrogen adsorption was more energetically favorable at further distances from the sulfur ad-atom. At higher coverages, a repulsive H-S interaction prevented hydrogen adsorption entirely. They explained the reduction in the initial hydrogen sticking probability observed by

Burke and Madix (1990) by the sulfur presence forming energy barriers which reduced possible reaction pathways for hydrogen adsorption.

2.5.3 Effect of sulfur on membrane performance

The effect of H_2S poisoning on the H_2 permeance of Pd membranes was first studied by McKinley (1967) who observed that in the presence of 4.5 ppm H_2S/H_2 at 350°C, pure Pd foils (1 mm thick) lost 70% of their permeance over a period of two days. Kajiwara et al. (1999) exposed a Pd membrane to 6200 ppm H_2S/H_2 at 400ºC which resulted in the membrane rupturing which was attributed to stress from the formation of PdS_x compounds. Mundschau et al. (2006) observed a drastic change in surface morphology due to Pd_4S formation after a Pd foil was exposed to 20 ppm H_2S (60% H_2, balance He) at 320ºC. After 5 days exposure, a 10 μm thick layer had formed on the surface. Pd_4S formation was also accompanied by a drastic reduction in the selectivity (Morreale et al., 2007, Chen and Ma, 2010a). Iyoha et al. (2007a) tested a pure Pd membrane in a water gas shift (WGS) catalytic membrane reactor (CMR) with 1000 ppm H_2S (53% CO, 35% H_2, 12% CO_2) at 900°C and also observed cracks in the membrane due to bulk sulfide formation.

Morreale et al. (2007) modeled the growth rate of the PdS_4 layer on a Pd foil in the presence of 1000 ppm H_2S (10% He, balance H_2) and the hydrogen permeance through the sulfide layer. Although the predicted activation energy agreed with the measured activation energy of 30.9 kJ/mol, the calculated permeabilities were an order of magnitude less than the experimental data, assuming that the n-value was equal to 0.5. The deviation was explained by the numerous cracks which had formed in the Pd_4S due to the structure change, allowing hydrogen to pass through. Miller et al. (2009) proposed

depositing a thin layer of the less permeable Pd_4S atop the Pd membrane to protect the Pd surface from poisoning. DFT was employed to calculate the surface reactivity of Pd_4S for hydrogen adsorption and dissociation. Miller et al. (2009) concluded that the hydrogen dissociation rates sufficed to function as a surface modification for a high permeance membrane. However, experimental data were not presented.

Not all sulfur compounds were detrimental to membrane performance. Kusakabe et al. (1996) exposed a pure Pd membrane to 2000 ppm CH_2SSCH_3/H_2 at 360°C and found that the hydrogen permeance did not decrease even after 200 hours of operation. However, the ideal H_2/N_2 separation factor decreased from 1000 to 100. When the experiment was repeated with a fresh membrane with 200 ppm CH_2SSCH_3/H_2, both permeance and selectivity remained constant. The size of CH_2SSCH_3 produced steric effects which blocked the sulfur from adsorbing on the Pd membrane.

Antoniazzi et al. (1989) observed that when Pd membrane foils became poisoned with sulfur and carbon, the hydrogen surface recombination step became rate limiting, rather than bulk diffusion. The permeance was measured as a function of temperature (82 – 357ºC) and impurity surface coverage. Sulfur surface coverage was varied by bulk sulfur segregating to the surface and surface coverage monitored with Auger electron spectroscopy (AES). The pressure of hydrogen was kept at a value that would not cause the $\alpha \leftrightarrow \beta$ phase transition. The activation energy for permeation varied between 21 – 27 kJ/mol with no trend in the surface coverages tested (which varied between 25 – 65 %). Antoniazzi et al. (1989) claimed that since the activation energy was independent of carbon and sulfur surface coverages, the impurities blocked ad-sites that were vacant,

indicating that the impurities had more than a physical blocking effect, in agreement with the findings of Burke and Madix (1990).

Many methods of modifying Pd membranes to make them resistant to sulfur poisoning have been investigated. Although the peak permeability of Pd/Cu alloys is at 40 wt% (Figure 2-4), McKinley (1967) demonstrated that this concentration was not sulfur resistant. At 350°C, 4.5 ppm H_2S/H_2 decreased the permeance of the membrane to less than 5% of the original value. The full permeance of the Pd/Cu membrane was recovered after two days of exposure to pure H_2.

Morreale et al. (2004) investigated Pd/Cu sulfur resistance and analyzed the results in conjunction with the Pd-Cu phase diagram (Figure 1-1). They found that sulfur resistance was due to the presence of the fcc phase. In a batch reactor, Pd/Cu alloy membranes in the fcc phase had little or no permeance decline at a concentration of 1000 ppm H_2S/H_2. The mixed fcc - bcc region gave partial sulfur resistance. A 40 wt% Cu alloy had a permeance decline of 99% at 340°C and 80% at 440°C. Increasing temperature increased the amount of the fcc phase present in the 40 wt% Cu alloy, which was part of the reason for the enhanced resistance as temperature increased. Morreale et al. (2004) concluded that H_2S concentration determined the amount of poisoning and not the time of exposure.

The reason for the lack of sulfur tolerance of the bcc phase could be due to the formation of a non-permeable sulfur compound formed near the surface. The work of O'Brien et al (2010) showed the possibility of a bulk Pd-Cu-S alloy which was 3 nm deep after poisoning a bcc phase Pd/Cu membrane for four hours with 1000 ppm H_2S/H_2 at 350°C.

A study by Kulprathipanja et al. (2005) concentrated on the effects of surface morphology of Pd/Cu membranes. They suggested that the sticking coefficient of hydrogen sulfide would be reduced and the sulfur resistance increased on a smoother membrane. Kulprathipanja et al. (2004) had previously shown via atomic force microscopy (AFM) that membranes produced by the electroless plating method were 3.5 times rougher than foils produced by casting and rolling and compared the sulfur resistance of both foils and electroless plated membranes (Kulprathipanja et al., 2005).

After Kulprathipanja et al. (2005) exposed the foils to 100 and 500 ppm H_2S/H_2, no change in the morphology was discerned. However, exposure to 1000 ppm caused pores to form. Membranes fabricated by electroless plating (8 μm thick) showed pores and particles of the same composition of Pd and Cu as the top layer of the membrane after exposure to 500 ppm. They found that copper segregated to the surface upon exposure to H_2S, also causing flux decline.

Similarly, Iyoha et al. (2007c) found that 20 wt% Cu foils formed morphology changing bulk sulfides when exposed to 1000 ppm H_2S/H_2 at 490°C, but no morphology change was observed after exposure to 100 ppm H_2S/H_2 at 560°C. At 400°C, the bulk sulfides were more stable after 100 ppm H_2S/H_2. The sulfidization of Pd and Pd/Cu membranes was compared to the thermodynamic stability of bulk Cu_2S and Pd_4S as a function of the H_2S/H_2 pressure ratio in order to predict membrane failure. However, bulk sulfide thermodynamics would not predict the surface sulfide formation causing the permeance decline.

While high concentrations of H_2S were detrimental to Pd/Cu alloy membranes, low concentrations did not affect the Pd/Cu alloys significantly. Mundschau et al. (2006)

reported a 20% decline in permeance for fcc Pd/Cu membranes upon exposure to 20 ppm H_2S (60% H_2, balance He) at 320ºC over a period of 100 hours.

Since platinum showed no deterioration in catalytic performance even in the presence of pure hydrogen sulfide at high temperatures, platinum membranes could be used in catalytic membrane reactors for converting hydrogen sulfide to hydrogen and sulfur. (Edlund and Pledger, 1993). Platinum membranes have also been shown to limit coke formation (Edlund and Pledger, 1994a). However, the hydrogen permeance through platinum was not as high as palladium (Buxbaum and Kinney, 1996) and platinum is an extremely expensive metal. Edlund and Pledger (1994a) tested platinum membranes with hydrogen permeances that were stable for eight hours in 100 psig of pure H_2S at 700°C.

Kajiwara et al. (1999) exposed a palladium membrane and a platinum membrane to 6200 ppmv H_2S/H_2 at 400°C. The flux of the platinum membrane decreased to 5.8% of the original value while that of the palladium increased remarkably due to the membrane cracking. It was observed that the platinum membrane was more structurally resistant even though the sulfidation decreased the flux. Since the lattice constant of palladium sulfide is double that of pure palladium (0.65 nm for the former and 0.39 nm for the latter), the membrane ruptured causing an increase in both hydrogen and nitrogen flux.

The difference between the experiments of Kajiwara et al. (1999) and Edlund and Pledger (1994a) was the operating temperature. While the study of Kajiwara et al. (1999) was performed at 400°C, that of Edlund and Pleder (1994a) was performed at 700°C. Edlund and Pledger (1994a) hypothesized that since platinum sulfide compounds were not stable above 225°C, platinum should be resistant to H_2S. However, the experiments of Kajiwara et al. (1999) were performed at 400°C and the H_2 permeance decreased. The

decrease in permeance was most likely due to the surface sulfide formation, which would occur at temperatures and H_2S concentrations that the bulk sulfides would not be stable.

Bryden and Ying (2002) hypothesized that a nanocrystalline membrane would be more resistant to sulfur because sulfur has an affinity to adsorb on high coordination number sites and not grain boundaries (Biswas et al., 1988). Bryden and Ying (2002) explained that hydrogen would still adsorb on sites which lay on the unsulfided grain boundaries and diffuse through the membrane even if the membrane was already sulfided.

Bryden and Ying (2002) performed their experiments at 200ºC to prevent the grains from growing and used Pd/Fe alloys to suppress hydrogen embrittlement. After exposing a 6 wt% Fe membrane to 51.9 ppm H_2S/H_2, the hydrogen permeance declined to 75% of the original value. Upon recovering the permeance in pure H_2, the membrane was annealed which caused the grain size to increase from 28 to 100 nm. Re-exposure to 51.9 ppm H_2S, resulted in almost a complete loss in H_2 permeance. Both exposure times lasted 2.5 hours. The permeance recovery time before the grain size growth was 30 minutes and the recovery time after the grain size growth was 400 minutes.

Ruthenium does not corrode from sulfur compounds, but is not employed because it has a lower permeance to hydrogen (Uemiya et al., 1997). Ryu et al. (1999) tested the H_2S resistance of bimetallic catalysts containing Rh and Ru alloys of palladium in the catalytic combustion of methane. The combustion took place with fresh catalysts and with catalysts which had been exposed to 100 ppm H_2S/air for five hours at 500ºC. The temperature required for a 90% conversion (T_{90}) was compared between the fresh and poisoned catalysts. $Ru/Pd/Al_2O_3$ had a T_{90} value of 356°C for the fresh catalyst and

404°C for the poisoned catalyst. Not only was the T_{90} value of the poisoned $Ru/Pd/Al_2O_3$ lower than the values of the other catalysts tested showing the greatest degree of catalytic activity after poisoning, but the difference between the fresh and poisoned T_{90} values was lower than that of the other catalysts tested, showing the greatest resistance to H_2S poisoning.

Pawelec et al. (2004) showed that Pd/Au catalysts were resistant to sulfur poisoning. Pd/Au catalysts supported on γ-alumina were tested for the hydrogenation of naphthalene and toluene and the hydrodesulfurization of dibenzothiophene (DBT). The concentration of DBT in the feed was 113 ppm (in 7% naphthalene, balance toluene) and the operating temperature ranged from 225 - 275°C. No decrease in catalytic activity was observed for any of the Pd/Au catalysts.

Similar interest in the sulfur tolerance of Pd/Au alloy membranes has engendered research. McKinley (1967) showed that a composition of 40 wt% gold had partial resistance, showing a flux decline of 56% at 350°C. No other gold compositions were tested and the maximum H_2S concentration in the feed was 20 ppm. Way et al (2008) observed a 38% drop in the hydrogen permeance of a 15 wt% Au membrane at 400ºC in the presence of 5 ppm H_2S/H_2. The greater H_2S resistance in comparison to pure Pd membranes was attributed to the segregation of Au to the membrane surface which lessened the binding energy of sulfur with increased Au content within the Pd/Au alloy.

Although Pd/Ag membranes are attractive due to the high hydrogen permeance, the Pd/Ag alloy has even less tolerance to sulfur than pure Pd membranes. McKinley (1967) observed that 3.5 ppm H_2S/H_2 decreased the permeance of a 27 wt% Ag membrane by roughly 99% at 350ºC and the permeance was not fully recovered after 5

days in pure H_2. Similarly, Mundschau et al. (2006) fed 10 ppm H_2S (80% H_2, balance He) to a 25 wt% Ag membrane at 320ºC and observed more than a 99% decrease in permeance. Furthermore, the size of the molecule attached to sulfur reduced the effect of the sulfur poisoning. Ali et al. (1994) exposed a 23 wt% Ag membrane to 1630 ppm of dimethyl disulphide (balance methylcyclohexane) and the permeance was reduced to 12% of the original value. As with Kusakabe et al. (1996) the size of the sulfur compound produced steric effects which prevented the sulfur from adsorbing as readily on the Pd/Ag surface.

Ceramic materials such as alumina and silica have been employed to separate hydrogen from gas containing sulfur compounds (Cicero and Jarr, 1990). Balachandran et al. (2005) dispersed Pd among a ceramic network composed of Y_2O_3-stabilized ZrO_2 (Pd/YSZ) forming a "cermet" membrane. A membrane with a thickness of 200 μm was exposed to a simulated syngas at 900°C (composition 61.3% H_2, 8.2% CH_4, 11.5% CO, 9.0% CO_2, and 10% He). After four hours, 100 ppm of H_2S was added to the feed. Within 1 hour the flux (1.3 m^3/m^2*h with the feed side pressure at 1 atm) decreased by 10% and remained stable for 90 hours. Similar results were seen at first with exposure to 400 ppm H_2S but after 270 hours of exposure, the flux increased and returned to the original value. The increase was attributed to a loss in some of the Pd metal as bulk sulfides formed. The phase transition caused pores to form within parts of the matrix which were not there previously, allowing more gas to permeate through.

However, when 3000 ppm H_2S was introduced to the same feed composition of syngas, the hydrogen flux decreased by 60% within the first hour and then continued to decrease. Large amounts of non-permeable gases (CH_4, CO, CO_2, He) appeared in the

sweep side, indicating that the membrane was no longer selective. The same test exposing a membrane to 3000 ppm H_2S at 600 instead of 900°C did not show an increase in non-permeable gases in the sweep side. The appearance of non-permeable gases in the sweep side was due to an increased porosity between the metal and the ceramic which formed at the higher temperature. EDX analysis showed Pd and S concentrations conducive to Pd_2S formation in the membrane.

2.6 Summary

The literature showed that Pd is subject to membrane failure or severe performance deterioration in the case where H_2S is in the feed. Alloying with Cu in the fcc phase increased the resistance of Pd membranes to H_2S significantly, but at the cost of a reduction in the hydrogen permeance. While these facts are well documented, there has been no thorough characterization of fcc Pd/Cu membranes within the operating temperatures of the water gas shift reaction in the literature, and no understanding of why Pd/Cu alloys are more sulfur resistant than pure Pd. This work presented full characterizations of the performance of Pd/Cu membranes in the fcc phase, attempted to explain the enhanced sulfur tolerance of Pd/Cu alloys through the analysis of poisoned surfaces, and fabricated high-permeance Pd/Cu membranes which are more sulfur tolerant than pure Pd.

3. Experimental*

3.1 Membrane synthesis

3.1.1 Porous metal supports

The metal substrates used in this study were provided by Mott Metallurgical, Inc. Sheets of 316L PSS (porous stainless steel) with a 0.1, 0.2 or 0.5 μm media grade were cut into coupons with dimensions of 1 cm x 1 cm x 0.1 cm. The coupons were largely used for plating, annealing, and surface studies. A hole was drilled into each coupon so the coupon could be hung by a hook in the plating solutions.

For permeation experiments, the porous supports consisted of porous Inconel. The chemical compositions for the metal supports used are found in Table 3-1. The membrane supports were tubular in shape (shown in Figure 3-1) with a length of 6 cm, an outer diameter of 1.25 cm, and a wall thickness of 0.16 cm. The porous Inconel tubes were welded to non-porous 316L SS at both ends with a blind cap on one end and a tube at the other end for ease of handling.

A 0.5 μm media grade indicates that the support rejectes 95% of particles with a diameter of 0.5 μm or greater. However, mercury porosymmetry analysis of a porous section of a 0.5 μm media grade cup resulted in a distribution of pores ranging in size up to a diameter of 12 μm and few isolated large pores of 20 μm diameter on the surface (Mardilovich et al, 2002).

* The experimental procedures outlined in this chapter were for the entirety of this body of work. Experimental procedures specific to certain chapters were presented in the chapters separately.

Table 3-1 Chemical composition (wt%) of porous metal supports. [*]

Element	316L SS	Inconel 625
Al		< 0.4
C	< 0.03	< 0.01
Cr	16 – 18.5	20 - 23
Co		< 1
Fe	balance	< 5
Ni	10 - 14	balance
Mo	2 - 3	8 - 10
Mn	< 2	< 0.5
Si	< 1	< 0.5
P	< 0.045	< 0.015
S	< 0.03	< 0.015
Ta		< 0.05
Ti		< 0.4

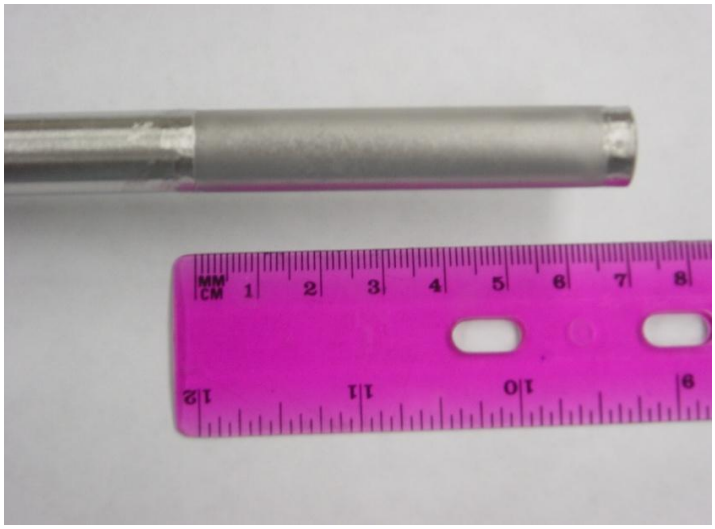

Figure 3-1 Tubular supports used for permeation experiments.

[*] www.azom.com

3.1.2 Pretreatment of porous metal supports

The procedure for cleaning (Mardilovich et al., 1998) consisted of immersing the supports in an alkaline solution in a heated ultrasonic bath at 60°C for half an hour to remove any dirt, particles and grease. The composition of the alkaline cleaning solution is shown in Table 3-2.

Table 3-2 Composition of the alkaline solution.

Component, purity	Amount	Merchant
$NaPO_4 \bullet 12H_2O$, 98 wt%	45 g/l	Alfa Aesar
Na_2CO_3, 99.5 wt%	65 g/l	Alfa Aesar
NaOH, 97 wt%	45 g/l	Alfa Aesar
Industrial detergent	5 ml/l	Alconox

Following the alkaline bath, the porous supports were immersed several times in a heated ultrasonic bath of deionized water (DI), also at 60ºC with each immersing lasting 10 minutes. A strip of a pH indicator was placed on the surface of the porous support after each rinsing. When the pH was equal to 7 the supports were immersed in either isopropanol or ethanol in an ultrasonic bath to facilitate the drying and dried at 120ºC for two hours.

After drying, the supports were oxidized to form an intermetallic diffusion barrier layer between the support metals and the H_2 selective Pd layer (Ma et al., 2000). The 316L PSS coupons were oxidized at 800°C for 10 hours to form a thick oxide layer and the Inconel tubes were oxidized at 700°C for 10 hours. A heating and cooling rate of 10ºC/min was used.

The lower oxidation temperature used for the tubes was to form an intermetallic diffusion barrier which would not greatly decrease the He flux of the tubular support. The mass of the bare supports was measured before and after oxidation and the He flux of the tubular supports was also measured before and after oxidation.

In the case of membrane N_02, 0.5 μm of Ru was deposited as an intermetallic diffusion barrier due to the high Tamman temperature (1030ºC) of Ru in order to prevent the diffusion between the metal support and the hydrogen selective layer. The Ru plating is discussed in more detail in Section 3.1.4.

3.1.3 Support activation

After oxidizing, the supports were activated according to the procedure outlined in Mardilovich et al. (1998). The solutions for the surface activation step are shown in Table 3-3. The $SnCl_2$ and $PdCl_2$ were added to acidic solutions with a concentration of 0.01 M HCl. While the $PdCl_2$ solution was stable for several months, the $SnCl_2$ solution was made fresh on the day of the activation due to possible changes in the properties of the solution with aging.

Table 3-3 Composition of activation solutions.

Component, purity	Amount	Merchant
$SnCl_2 \cdot 2H_2O$, 98 wt%	1 g/l	Aldrich
$PdCl_2$, 99.9 wt%	0.1 g/l	Alfa Aesar
HCl, 37 wt%	1 ml/l	Merck

Before activation, the supports were placed in DI water for several seconds, immersed in 1 M HCl for 30 seconds, and then immersed in DI water for 30 minutes. All DI water used for activating and plating was taken from the Thermo Scientific Barnstead E-pure water filtration system which produced DI water with a resistivity of 18.2 MΩ-cm. The activation sequence consisted of immersing the supports in the $SnCl_2$ solution for 5 minutes, DI water for two minutes, fresh DI water for 3 minutes, the $PdCl_2$ solution for 5 minutes, 0.01 M HCl for two minutes and then fresh DI water for 3 minutes. The sequence was repeated until a uniform brownish layer appeared, usually after 3 - 6 activation cycles.

Immersing the supports in DI water following the immersion in the $SnCl_2$ solution was to prevent the hydrolysis of the Sn^{2+} ions which could form $Sn(OH)_{1.5}Cl_{0.5}$ and other hydroxy-chlorides on the support. Similarly, the immersion in 0.01 M HCl prevented the hydrolysis of the Pd^{2+} ions. The resulting activation layer could either be plated immediately or dried at 120ºC for two hours to be plated at a later date.

3.1.4 Electroless plating

If the activation layer was previously dried, the supports were dipped in DI water for a few seconds, 1 M HCl for 30 seconds – 1 minute and then DI water for 5 minutes. If the plating was performed directly after the activation procedure, the activated supports were immersed in the plating solution without any treatment. The compositions and conditions of the plating solutions used in this work are listed in Table 3-4. It should be noted that Pd and Ag plating solutions were prepared at least 24 hours in advance to allow time for the metal ion complexes to form. The Ru solution, which was adapted from Torikai et al. (1984) and the Cu solution were used as soon as they were made.

Table 3-4 Plating bath compositions and conditions.

	Pd bath	Cu bath	Ag bath	Ru bath	Purpose	(Purity) Merchant
$Pd(NH_3)_4Cl_2 \cdot H_2O$ (g/l)	4				Pd^{2+} ion source	(99 wt%) Alfa Aesar
$CuSO_4 \cdot 5H_2O$ (g/l)		25			Cu^{2+} ion source	(99 wt%) Sigma
$AgNO_3$ (g/l)			0.519		Ag^{+} ion source	(99 wt%) Aldrich
$RuCl_3$ (g/l)				1.25	Ru^{3+} ion source	(99.9 wt%) Alfa Aesar
$Na_2EDTA \cdot 2H_2O$ (g/l)	40.1	47.5	40.1		complexant/stabilizer	(99 wt%) Aldrich
NH_4OH (28 %) (ml/l)	198		198	50	complexant/stabilizer/buffer	(28 wt%) Merck
$NaNO_2$ (g/l)				1.25	reducing agent	(97 wt%) Alfa Aesar
H_2NNH_2 (1 M) (ml/l)	5.6		5.6	50	reducing agent	(98.5 wt%) Alfa Aesar
H_2CO (37 %) (ml/l)		25			reducing agent	(36.7 wt%) Sigma
EDA (ppm)		112			grain refiner	(99 wt%) Alfa Aesar
$K_4Fe(CN)_6 \cdot 3H_2O$ (ppm)		35			accelerator	(99.9 wt%) Sigma
$(C_2H_5)_2NCS_2Na \cdot 3H_2O$ (ppm)		5			stabilizer	(99 wt%) Alfa Aesar
pH	10 - 11	12.0	10 - 11	13		
Temperature (°C)	60	20 - 25	60	55		

In the case of Pd plating, the support was placed in successive plating baths for 90 minute intervals with the hydrazine added just before the support was immersed. In between the successive platings, the support was immersed in DI water at 60ºC for 5 minutes before immersion in a fresh Pd plating solution. In the case of the coupons, no more than 5 rounds of Pd plating would take place at one time. In the case of the tubular supports, Pd was plated until no plating solution was found in the interior of the tube indicating that the membrane was "liquid dense," usually after 2 – 3 plating rounds. The membrane would then be rinsed with DI water and dried at 120ºC overnight. The He permeance would be measured and the membrane plated again.

After the membrane was liquid dense, the membrane was plated with a vacuum by attaching the tube side to an aspirator or vacuum pump. A slight vacuum was used at first (550 torr) and if the level of the plating solution did not decrease, indicating that the membrane was "liquid dense", the vacuum was increased to 380 torr. If the membrane was "liquid dense" at 380 torr then the vacuum was then increased to 75 torr to block the remaining pinholes. Between each round of plating, the membrane was dried and the He permeance measured. If the He leak of the membrane could not be detected at $\Delta P = 2.3$ bar at room temperature, the membrane was deemed dense.

If Cu was plated, a dense Pd membrane was immersed in the Cu plating bath (adapted from Ma et al., 2003, shown in Table 3-4) for 30 – 60 minutes, in accordance with the desired thickness. After electroless depositions of Cu, the supports were immediately immersed in 0.01 M HCl to neutralize any residual plating solution followed by rinsing with DI water and ethanol to facilitate drying in order to prevent oxidation of the Cu layer.

For plating a batch of eight coupons, an 80 ml beaker was filled with 70 ml of plating solution. For plating membranes, a 200 ml graduated cylinder was filled with 100 ml of plating solution. The volume of the plating bath was varied in accordance with the combined surface area of the supports to be plated in order to ensure a volume/surface area ratio of roughly 4 ml/cm^2.

The average thickness of the plated films was determined gravimetrically, where the weight gain of the plated support is divided by the product of the plated surface area and the density of the plated metal, shown in Equation 3.1

$$z = \frac{\Delta m}{A \cdot \rho} \cdot 10000 \tag{3.1}$$

where z is the film thickness in μm, Δm is the weight gain in g, A is the plated area in cm^2 and ρ is the density of the plated film in g/cm^3.

3.1.5 Support grading

For some of the tested membranes, the supports were modified further after the oxidation step. A slurry of Al_2O_3 particles of varying sizes in a 0.01 M HCl solution was prepared and stirred overnight before grading the support. The components of the slurry are shown in Table 3-5.

In order to block the larger pores of the support before plating the dense Pd layer, the support was attached to a vacuum of 550 torr and immersed in DI water for 5 minutes. The support was then immersed in 1 M HCl for 5 seconds and then in DI water for another 5 minutes. The immersion in the Al_2O_3 slurry lasted 10 seconds and the vacuum was increased to 75 torr after the support was taken out of the slurry. While still

at a high vacuum of 75 torr, the support was immersed in DI water for 5 minutes. The vacuum was disconnected and the support was dried at 140ºC for 12 hours and the He permeance measured.

Table 3-5 Components of Al_2O_3 slurry.

Component, particle size	Amount	Merchant
Al_2O_3, 1 µm	1 g/l	(99.95%) Alfa Aesar
Al_2O_3, 0.2 – 0.5 µm	0.5 g/l	(99.95%) Alfa Aesar
1 M HCl	0.5ml/l	Merck

To seal the slurry within the pores of the support, the support was activated once (one activation loop) under a vacuum of 550 torr and plated with Pd for 10 minutes. This step was referred to as "Pd glue." After the Pd glue was deposited, the He permeance was measured.

A porous Pd/Ag barrier was deposited which further bridged the larger pores of the support and also functioned as an additional intermetallic diffusion barrier between the support metals and the hydrogen selective layer (Ayturk et al., 2006a, 2006b). After three activation loops, Pd was plated for 30 minutes with 0.33 ml of hydrazine added per liter of plating solution, Ag for 60 minutes with 0.58 ml/l of hydrazine[*], Pd for 60 minutes with 0.38 ml/l of hydrazine, Ag for 60 minutes with 0.58 ml/l of hydrazine and finally Pd for 60 minutes with 0.58 ml/l of hydrazine. The resultant Pd/Ag barrier layer was lightly sanded with 2400 grit SiC paper and cleaned before plating the dense Pd

[*] Indicated ml of added hydrazine per liter of plating solution.

layer. Further details on the Pd/Ag barrier layer fabrication can be found in Ma et al. (2007).

3.1.6 Annealing and polishing

A method of annealing and polishing sequential layers of plated Pd was utilized for some of the membranes to inhibit leak growth. The annealing was performed in order to cause the Pd grains to reach an equilibrium configuration at a temperature higher than the temperature of testing (Saini, 2006, Ma et al., 2004b). After plating Pd, if the membrane was considered to be liquid dense, the membrane was placed in a furnace in which He was circulated on both the shell and tube sides of the membrane to prevent oxidation. The temperature was increased at a rate of 5ºC/min and held at 550ºC for 12 hours. The temperature was then decreased at the same rate.

After the annealing was completed, the Pd layer was mechanically treated with a lathe with 600 and then 1200 grit SiC sandpaper and cleaned with acetone and DI water to remove residual SiC. The polishing was performed both to smooth out the Pd surface and reduce the thickness of the layer, and to enable the next layer of Pd to block any pinholes that formed due to grain coarsening during annealing (Ma et al., 2004b) The membrane was then re-plated with Pd. The He leak was monitored in between all of the steps and the weight of the composite membrane measured. The sequence of annealing, polishing, and plating was repeated 3 – 4 times until the membrane was dense.

3.2 Membrane characterization

3.2.1 He leak measurement

As stated in Section 3.1, the He leak of the support and membrane was measured after every stage during fabrication. The He leaks were measured up to a pressure difference of 2.5 bar. After each synthesis step, the He leak would decrease, sometimes by 1 – 2 orders of magnitude requiring the use of three different flow meters able to measure different ranges of the He volumetric flow rate. The GCA Wet Test Flow Meter was used for high flow rates of 1.5 – 13 l/min. Usually the bare support, oxidized support, the support after grading with the Al_2O_3 slurry and after the Pd glue deposition step had He permeances which would fall in the high flow rate range.

For medium flow rates of 2 – 300 ml/min an Alltech 4068 digital flow meter was used. The composite membrane after the deposition of the porous Pd/Ag barrier and the first layer of dense Pd usually had a He permeance with a medium flow rate. For extremely small flow rates (< 2 ml/min), a bubble flow meter was used. The small flow rates were usually measured after the first dense layer of Pd and while continuing to make the Pd membrane gas tight.

3.2.2 Permeation apparatus

The shell and tube permeation set up shown in Figure 3-2 consisted of a 316L SS tubular casing with a 2.54 cm outer diameter and length of 41 cm. The casings were attached to the non-porous part of the composite membranes with reducing unions and a removable graphite ferrule. The reducing unions had holes drilled in them and were electrically welded to 0.32 cm tubing to allow the retentate gas to flow. The feed end of

the shell casing was a cap electrically welded to the 2.54 cm tube with a 0.64 cm tube welded to the cap for the feed to enter the shell casing. The permeation cell was mounted vertically into the furnace for ease of insertion and extraction, and the ends were wrapped with insulation strips to reduce the axial temperature drop.

The experimental setup for testing the performance of membranes is shown in Figure 3-3. Table 3-6 provides a key to the abbreviations. Hydrogen and helium were industrial grade (99.5% pure) and supplied by ABCO. The flow to the membrane was controlled with pressure regulator V1. A ballast volume of 500 ml was used to ease the transition between H_2 and He gases. When H_2S was used, the flow was regulated with the mass flow controller. The flow continued to the shell casing (see Figure 3-2). Permeable gases flowed through the membrane to the permeate line while non-permeable gases flowed out of the casing to the retentate line. The retentate was regulated with metering valve V3 and measured with a mass flow meter and then exiting to the vent. The He sweep was a low pressure line on the tube side regulated with metering valve V4 and was used to prevent the membrane from oxidizing during start up/shut down conditions and to ease the transition between H_2 to He atmospheres. The sweep flow was not used during permeation tests. All piping was of 316L SS. Any O-rings present in metering valves and on/off valves were made of Kelzar instead of the standard Viton for sulfur resistance.

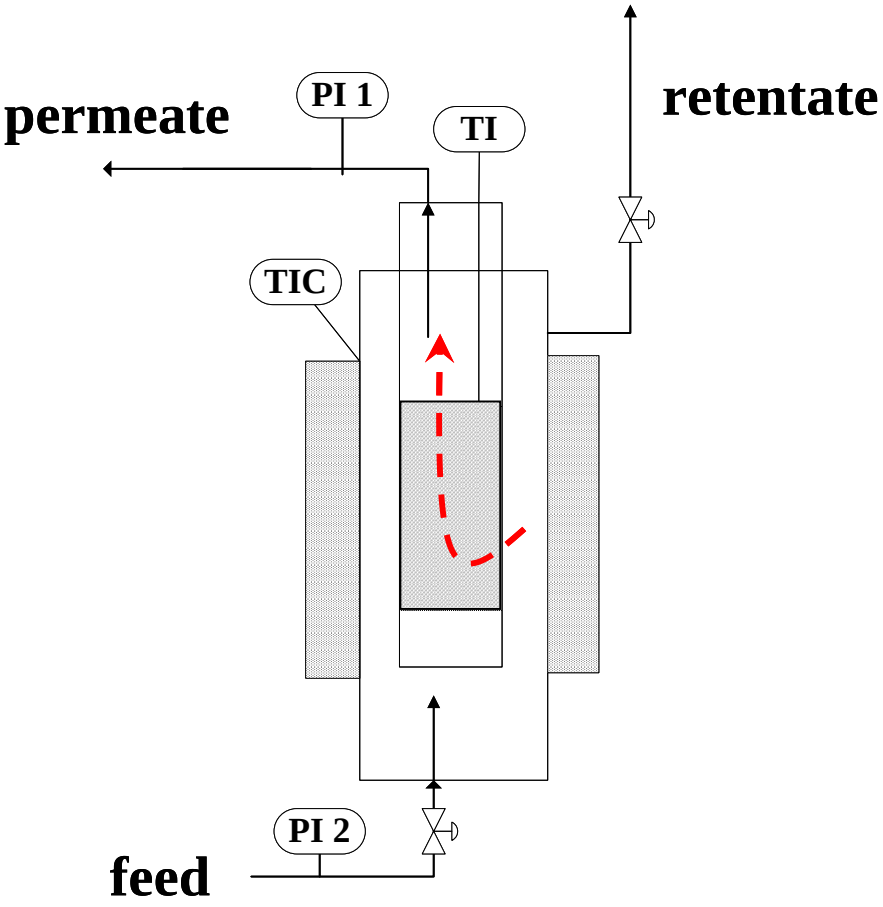

Figure 3-2 Detail of furnace in experimental apparatus.

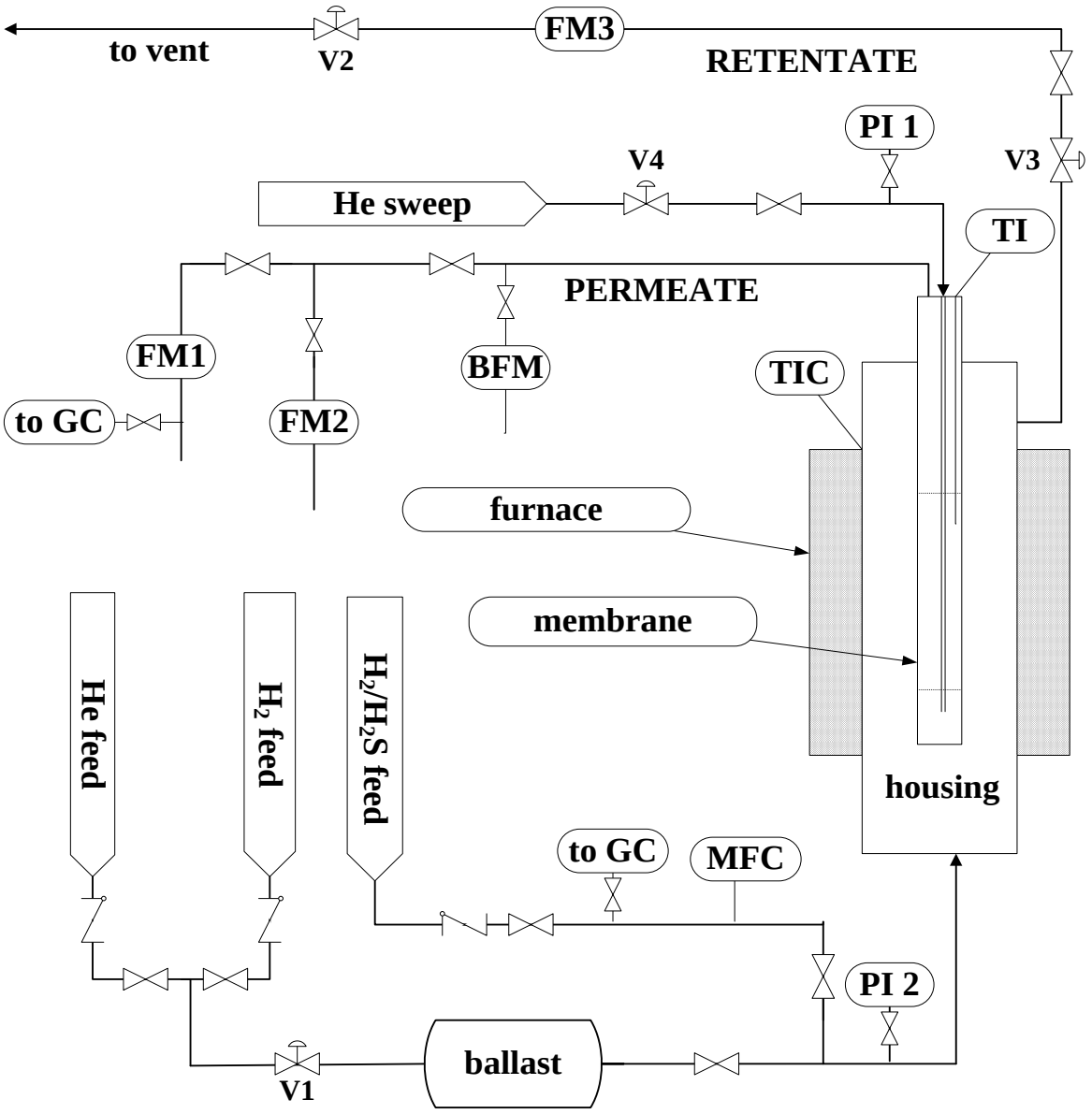

Figure 3-3 Experimental apparatus for testing permeance and sulfur tolerance.

Table 3-6 System key.

Symbol	Key	Merchant, range
BFM	bubble flow meter	
FM1	flow meter (permeate H_2)	MKS, 0 - 1000 sccm
FM2	flow meter (permeate He)	MKS, 0 - 20 sccm
FM3	flow meter (retentate)	MKS, 0 - 500 sccm
GC	gas chromatograph	SRI, TCD and FPD detectors
MFC	mass flow controller	MKS, 0 - 1000 sccm
PI 1	pressure indicator (permeate)	Transducers Direct, 0 - 30 psig
PI 2	pressure indicator (feed)	Transducers Direct, 0 - 100 psig
TI	temperature indicator	Omega Type K thermocouple
TIC	temperature indicator and controller	Eurotherm 2116 PID
V1	gas pressure regulator	
V2	back pressure regulator	
V3	metering valve	
V4	metering valve	

All parameters including temperature, pressure, and flow rates were continuously logged onto the computer. The data acquisition system included a shielded SCB – 68 data acquisition system box and LabView 6.1 software.

The permeance and selectivity of the membranes were measured by recording the permeate flow with mass flow meters. A bubble flow meter was used for very small He flow rates which did not fall in the range of the mass flow meter. Pressure was measured on the permeate and feed sides (P1 and P2, respectively) to calculate the transmembrane pressure difference. Type K thermocouples were used to monitor the temperature of the permeate flow inside the tube (TI) and the temperature between the shell casing and the Watlow furnace (TIC). The thermocouple between the shell casing and furnace was connected to the temperature PID controller (see Figure 3-2).

3.2.3 Characterization protocol

After inserting the tube into the shell casing, connecting the casing and sweep and properly insulating the casing, the system was flushed for roughly an hour with He with the shell side pressure being 2 bara and the tube side pressure being 1 bara. The tube side was flushed with the He sweep. After the system was thoroughly purged from any air and/or water vapor which could damage the membrane, the temperature was raised at a rate of 1ºC/min to 250ºC. The sweep was shut off so that any leak which developed in the membrane could be measured and hydrogen was flowed to the membrane at $\Delta P = 1$ bar (shell side pressure = 2 bara).

The same temperature and pressure conditions were kept for 1 – 5 days, depending on the length of time required for the permeance to stabilize, and the permeance calculated in accordance with Sieverts' Law (Equation 2.11). The pressure was increased and the permeance monitored in increments of 0.3 - 0.5 bar until a pressure difference of 3 bar was reached and a Sieverts' regression could be performed. The system was flushed again with He for roughly an hour, the sweep shut off and the leak measured. After the He leak stabilized, the temperature was increased to 300ºC.

The same procedure was repeated and the temperature was increased to 350, 400, 450 and 500ºC with the same procedure for determining permeance and the leak test repeated at each temperature. The permeance calculated at each temperature was used to determine the Arrhenius dependence on temperature and the activation energy of permeation of the membrane, as shown in Equation 2.15.

All membranes were characterized according to the above protocol, however the length of time spent at a given temperature varied if long-term stability was tested, and

not every temperature mentioned above was always tested with each membrane. In addition, it was later thought that introducing H_2 at 250ºC could be the cause of the beginning of leak formation and for some membranes H_2 was first introduced at 300 or 350ºC.

3.2.4 Testing in H_2S

When H_2S was used in the system, the composition of the feed and permeate was measured with a SRI 8610C gas chromatograph (GC) equipped with a flame photometric detector (FPD) with a measurement accuracy of H_2S down to 200 ppb. The calibration of the GC is described in detail in Appendix B.1. A photomultiplier tube (PMT) amplified the amount of photons reaching the detector. The column used for H_2S composition measurements was a 0.08 cm MXT stainless steel capillary tube.

The H_2S/H_2 mixtures were made by Airgas and had an analytical accuracy of ±2%. The conditions for H_2S detection were optimized for peak sharpness and height. The air and hydrogen gases used for fueling the FPD were flowed at pressures of 5 - 6 and 30 - 32 psia, respectively. The carrier gas was He and was flowed to the GC at a pressure of 19 - 20 psia. The oven temperature was set at 50ºC and the FPD temperature was set at 150ºC. A 10-way automatic actuator valve took samples from the flow to the GC by opening the valve to the loop at 0.1 minutes and closing the valve to the loop at 0.3 minutes. The residence time of the H_2S was roughly 1.7 - 1.8 minutes at the stated conditions.

To test the effect of more dilute concentrations of H_2S on membrane performance, a gas mixer was installed (shown in Figure 3-4) and connected to the membrane feed. The gas mixer itself was of the same dimensions of the shell casing used for permeation

experiments. A stream of H_2 controlled with an MKS mass flow controller entered the mixer from one side of the casing while the H_2S/H_2 mix entered from the opposite side of the casing, through 0.32 cm tubing punctured with holes to allow for cross current mixing where the two gas streams met. To cause further turbulence, the gas stream passed through stainless steel fillings before exiting to the system.

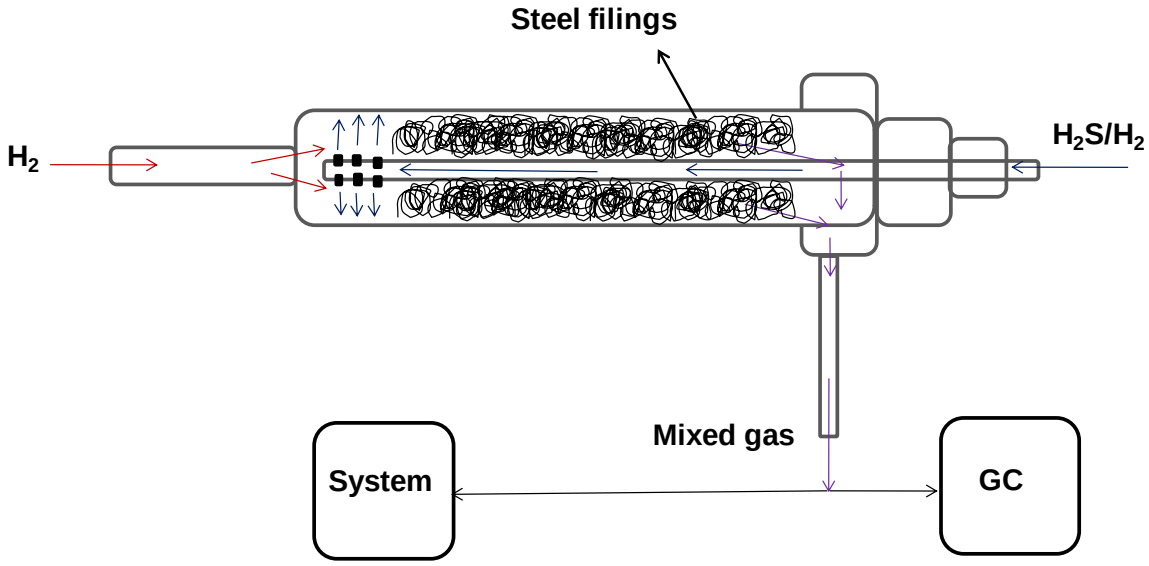

Figure 3-4 Mixer apparatus (from Chen and Ma, 2010b).

3.3 Instrumental analysis

3.3.1 SEM and EDX

The surface and cross-sectional characterizations were carried out with the Amray 1610 Turbo scanning electron microscope (SEM) equipped with a Princeton Gamma-Tech (PGT) Avalon energy dispersive X-ray (EDX) light element detector and a RBA-1610 5MC type Robinson retractable backscattered electron detector for qualitative and quantitative elemental analysis. Quantitative analysis for chemical compositions was carried out with the Spirit software (PGT Corporation). The spatial resolution for SEM-EDX lay between 0.8 – 1.2 μm for an accelerating voltage of 20 keV and the penetration depth was about 1 μm for the samples investigated (Goldstein et al., 2003).

To obtain cross sections, the samples were cut with a SiC saw blade and mounted in phenolic powder with a Smithells II mounting press. The samples were ground with SiC paper of increasing fineness from 60 to 2400 grit with the Metaserv 2000 grinder-polisher. The samples were further polished with α-Al_2O_3 slurries consisting of particles of increasing fineness from 1 μm, 0.3 μm to 0.05 μm. Prior to the cross-sectional analysis, samples were sputter coated using a gold/palladium target to avoid charging. All samples were stored in a desiccator prior to analysis.

The JEOL 840 SEM was also employed for surface and cross sectional characterization. The JEOL 840 was equipped with both secondary electron imaging (SEI) and backscattered electron imaging (BEI). Chemical analysis was carried out with the Kevex EDX Spectroscopy system.

3.3.2 XRD

General phase identification analysis of coupons was performed with a Rigaku Geigerflex X-Ray diffractometer (XRD) equipped with a CuKα radiation source (λ = 1.54 Å), and a curved crystal monochromator. Data analysis was performed with JADE 8.1 software.

The time resolved, *in-situ* HT-XRD experiments were performed at the High Temperature Materials Laboratories (HTML) at Oak Ridge National Laboratories (ORNL). The diffraction data were collected with the PANalytical X'Pert Pro θ/θ MPD/X-ray diffractometer (Cu Kα radiation source operated at 45 kV and 40 mA) equipped with an Anton Paar XRK-900 furnace which allowed the temperature to be varied between 25 and 900ºC. A Macor sample holder supported the sample in the furnace. The electrical heater of the furnace was designed to heat the volume of the sample with a minimal temperature gradient. A PANalytical X'celerator real-time multiple-strip detector was used to rapidly collect the data. A vacuum was applied while heating the samples to 250ºC at a rate of 50ºC/min. At 250ºC, a pure H_2 atmosphere was introduced at a pressure of 1 atm and the temperature was increased to the final annealing temperature at a rate of 50ºC/min. The scans ranged from 2Θ values of 37 - 45° and the total time of the scan varied from 30 seconds to 30 minutes, depending on the rate of phase change.

The quantitative analysis of the diffraction data was carried out with the software X'Pert Highscore Plus using a Le-Bail fit and a flat background. The weight fractions were calculated by the direct comparison method of the integrated peak intensities. (Cullity and Stock, 1978). At high temperatures, there was a significant overlap between

the bcc (1 1 0) and Cu (1 1 1) peaks. A standard of Cu plated on oxidized PSS was heated to each of the temperatures tested in this work and scanned to determine the peak position.

3.3.3 XPS

The near surface elemental analysis of the pure Pd samples was performed at the Center of Materials Science and Engineering (CMSE) at the Massachusetts Institute of Technology (MIT) with a Kratos AXIS Ultra X-ray Photoelectron Spectrometer (XPS) using a monochromatized aluminum source operated at 150 W, with an analysis area of approximately 300 x 700 μm and a maximum information depth of approximately 10 nm. The pass energy used for high energy resolution spectra was 20 eV. CasaXPS software (Fairbanks and Carrick, 2005) equipped with a Scofield-cross-section-based sensitivity factor library, was used for the peak-fitting and quantitative analysis. All spectra were calibrated using the adventitious carbon C 1s peak at 285.0 eV and a Shirley-type background was subtracted from the spectra.

The near surface elemental analysis of the Pd/Cu alloy samples was performed at the HTML at ORNL with a Thermo Scientific K-Alpha XPS using an Al K-α source operated at 200 W, with an analysis area of approximately 200 x 400 μm. The pass energy used for the survey spectra and high resolution spectra were 25 and 50 eV, respectively. Advantage 4.38 software (Thermo Scientific) was used for the peak-fitting and quantitative analysis. All spectra were calibrated using the adventitious carbon C 1s peak at 285.0 eV and a Smart-type background was subtracted from the spectra. Depth profiling was performed by sputtering the samples with He^+ ions. The depth scale from

ion sputtering was determined using a sputter rate calibrated with a standard SiO_2 film. A description of the peak deconvolution for quantitative analysis is found in Appendix D.

All coupon samples were cleaned in an ultrasonic bath with acetone and then ethanol before being dried at 120ºC. The samples were then wrapped in aluminum foil before being placed in plastic sample holder bags to reduce the amount of adventitious carbon which accumulated on the sample surface from contact with plastic sample bags.

3.3.4. Atomic Adsorption Spectroscopy (AAS)

The determination of the Pd and Cu concentration in the plating and displacement solutions was carried out with the Perkin Elmer AAnalyst 300 Spectrometer equipped with a six lamp turret for either hollow cathode lamps (HCL) or electrode discharge lamps (EDL), an HGA-850 Graphite Furnace System and AS800 Autosampler. An air/acetylene mixture was used as fuel for the flame. Instrument readouts were calibrated to display concentration directly. AA Winlabs Software was employed to run and calibrate the spectrometer. HCL lamps were used for both Cu and Pd detection. For Cu detection, a slit width of 0.7 nm, a wavelength of 324.8 nm and a lamp current of 15 V were used. For Pd detection, a slit width of 0.2 nm, a wavelength of 244.8 nm and a lamp current of 30 V were used.

Sample concentrations for calibration were prepared by diluting stock standards of 1000 ± 4 mg/l of Cu in 2% w/w HNO_3 and 1000 ± 4 mg/l of $Pd(NO_3)_2$ in 1 M HNO_3, in a solution of 1% v/v HNO_3 prepared from 80% w/w HNO_3 (EMD). Both stock standard solutions were purchased from Fluka Analytical.

The aliquot was taken from the plating and displacement solutions at different time intervals with a Finnpipette automatic pipette with a range of 0.100 – 1.000 ml. The

aliquots were diluted in 1% v/v HNO_3 in accordance with the desired dilution factor which would place the sample within the calibration curves (shown in Figure A-1 and Figure A-2) of the AAS. A summary of the volumes taken for dilutions and dilution factors for the plating and displacement solutions is shown in Table 3-7. A detailed description of the calibration process is found in Appendix A.

Table 3-7 Preparation of samples.

	Cu in Cu plating solution	Cu in Pd displacement solution	Pd in Pd displacement solution
aliquot (ml)	0.105	0.300	0.500
diluent (ml)	15	5	7.5
dilution factor	143	16.7	15

4. Solid-State Transformation Kinetics of Pd/Cu Alloy Bi-layers*

4.1 Introduction

As there is no Pd-Cu co-deposition bath known in the literature, the preparation of the Pd/Cu alloy membrane from the electroless deposition method requires the plating of sequential layers of Pd and Cu resulting in a bi-layer followed by the annealing of that bi-layer. While there has been research in the past which briefly investigated the formation of the bcc alloy from Pd/Cu bi-layers with *ex situ* methods (Ma et al., 2004a) and work which studied the kinetics of the fcc-bcc Pd/Cu phase transformation in a thin homogenous Pd/Cu layer (Guazzone, 2006), there has been no in depth *in-situ* investigation into the formation of the sulfur tolerant fcc Pd/Cu alloy from Pd/Cu bi-layers.

In the past, HT-XRD has been used in order to monitor the phase transformations *in-situ* which occurred as a result of a product film forming from a thin film of bi-layers. The time resolved measurements enabled kinetic constants to be obtained from the formation of $CuGaSe_2$ from GaSe/CuSe bi-layers (Kim et al., 2008), and $CuInSe_2$ from InSe/CuSe bi-layers (Kim et al., 2005) and provided a greater understanding of the mechanism of the phase transformations. Of particular relevance to this work is the HT-

* This chapter has been published in AIChE Journal.

Pomerantz, N., Payzant, E.A and Ma, Y.H. "Isothermal solid-state transformation kinetics applied to Pd/Cu alloy membrane fabrication." *AIChE Journal*, In press.

XRD investigation of the Pd/Ag alloy formation from Pd/Ag bilayers (Ayturk et al., 2008) which, through an investigation of the phase transformation, attained both qualitative and quantitative information with regards to Pd/Ag alloy membrane fabrication and permeance characteristics.

The main objective of this work was to employ the time resolved *in-situ* HT-XRD to investigate the annealing conditions required to form an fcc alloy from a deposited Pd/Cu bi-layer and to understand the mechanism of the annealing process. The knowledge was then applied to the fabrication of sulfur-tolerant Pd/Cu membranes and understanding the change in permeation at higher temperatures as a result of phase change.

4.2 Experimental

The coupon samples tested in this chapter are listed in Table 4-1. All coupons were oxidized at 800°C for 12 hours before the electroless deposition and plated with Pd followed by Cu as described in Section 3.1.4. The membrane tested in this chapter was oxidized at 700°C for 12 hours and plated with Pd until dense. A layer of Cu was deposited on the Pd. All samples had compositions which would place them in the fcc region of Pd/Cu phase diagram (see Figure 4-1) if they were uniform throughout the combined layer. The membrane characterizations were performed in the system described in Figure 3-3.

With regards to applying the coupon study to membrane fabrication, the thickness of the Pd alloy layers (10 – 20 μm) deposited on both the flat coupons and the tubular supports were smaller than the radius of the tube (0.625 cm) by over two orders of magnitude. Therefore, it was expected that the effect of the curvature of the tubular support could be neglected and a one dimensional flat plate geometry applied in both cases.

Table 4-1 Coupons tested in this chapter.

annealing temperature (ºC)	substrate	Pd layer (μm)	Cu layer (μm)	wt% Cu
as deposited	oxidized PSS	13.1	4.1	19
500	oxidized PSS	13.0	2.6	13
550	oxidized PSS	13.4	3.5	16
600	oxidized PSS	12.8	3.2	15

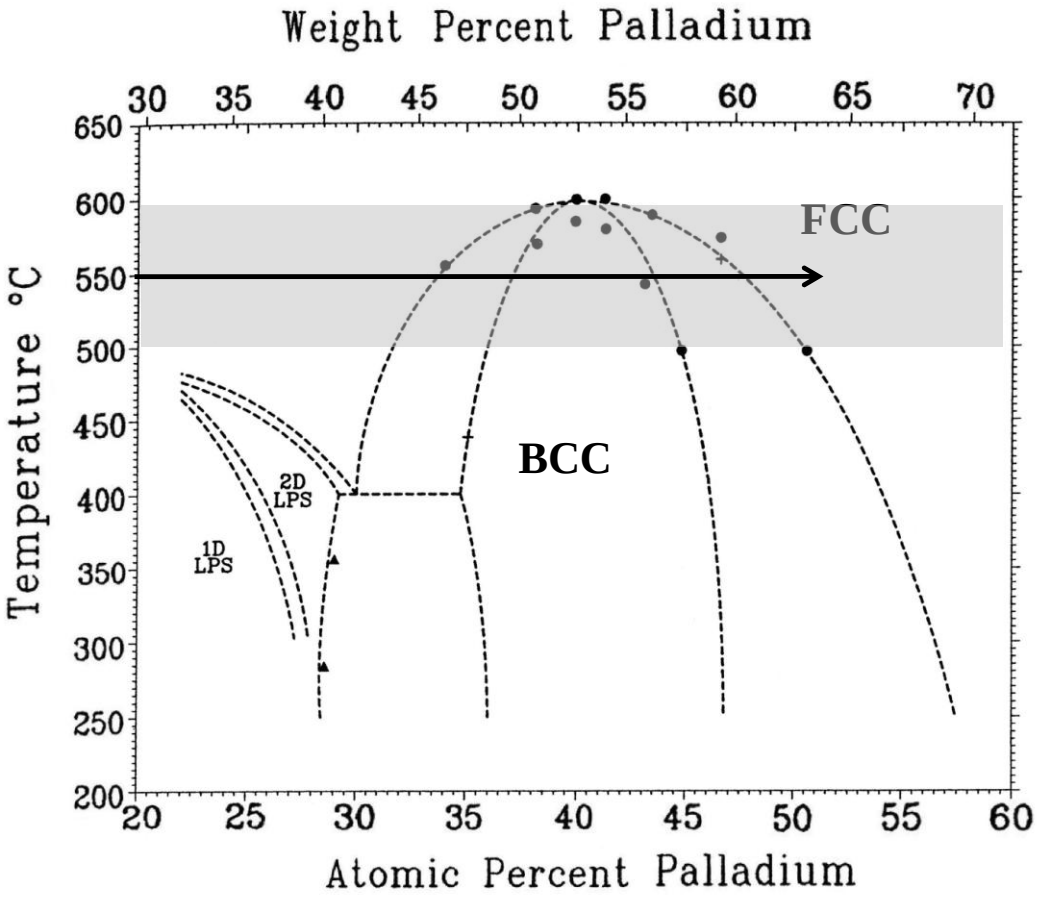

Figure 4-1 Pd-Cu phase diagram (Subramanian and Laughlin, 1990). The gray area indicates the temperature range tested in this work.

4.3 Results and Discussion

4.3.1 Cross sectional analysis

Figure 4-2a shows the cross section of an as-deposited Cu/Pd/PSS sample. The oxide intermetallic diffusion barrier layer appeared relatively uniform on the PSS. The Pd layer covered the surface of the substrate and entered some of the pores. The average thickness of the Pd layer was 10 μm and the average thickness of the Cu layer was 4.7 μm, which was close to the gravimetric estimate of Cu shown in Table 4-1. The Pd layer thickness was less than the gravimetric estimate shown in Table 4-1 due to the slight penetration of Pd inside the pores, which was not included in the visual approximation of the thickness from the micrograph.

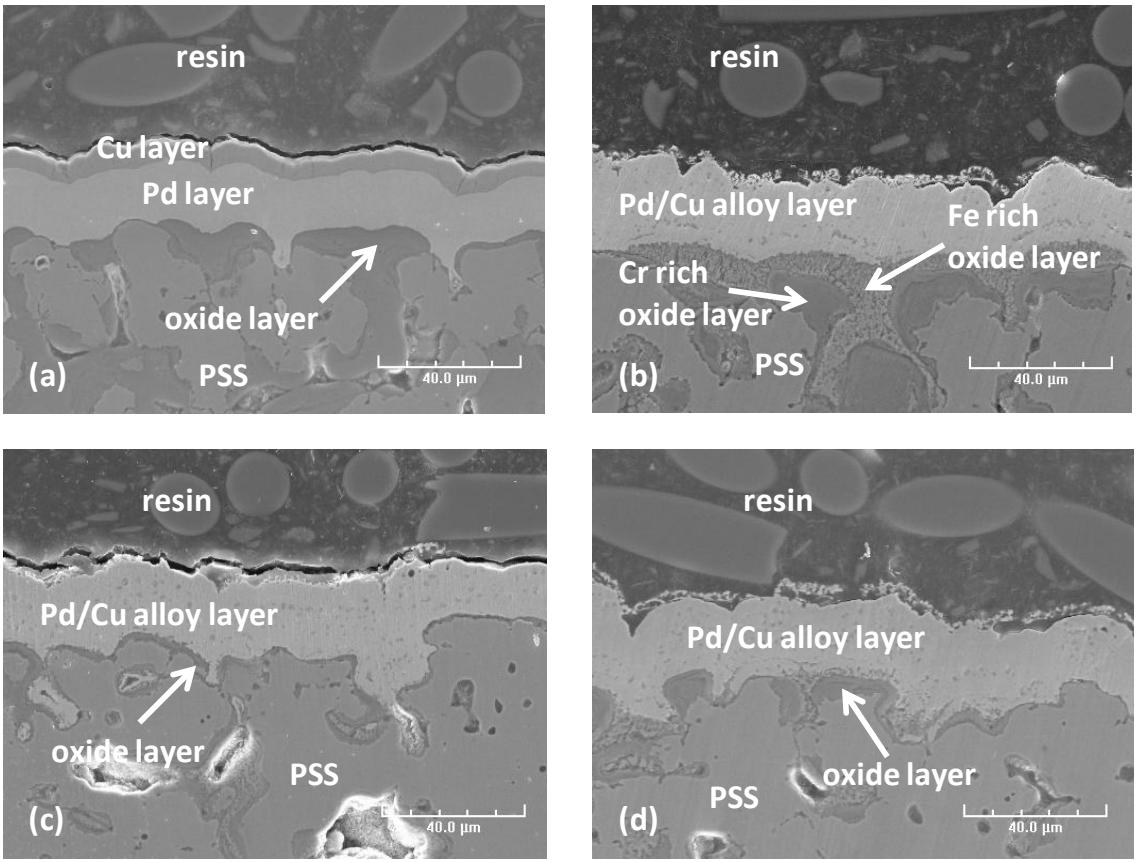

Figure 4-2 Cross-sectional micrographs at 1 kX for the PSS samples (a) as-deposited, annealed at (b) 500ºC, (c) 550ºC and (d) 600ºC.

It should be noted that the penetration depth of the XRD did not encompass the entire depth of the Pd/Cu bi-layer, and the phases detected were limited to those present within the penetration depth of the X-ray which ranged from 5.5 to 8.5 μm depending on the Cu concentration of the fcc or bcc alloy, shown in Figure 4-3. The penetration depth was calculated according to Equation 4.1 where G_x is the diffracted intensity at a distance, x, from the surface and μ is the linear absorption coefficient (Cullity and Stock, 1978).

$$G_x = 1 - \exp\left\{-\frac{2\mu x}{\sin\theta}\right\} \tag{4.1}$$

Figure 4-2b, c, and d show the cross sections of the Pd/Cu/PSS samples annealed in H_2 at 500, 550 and 600ºC for 50, 25 and 8 hours respectively. In all three Pd/Cu layers, the contrast between the Pd and Cu layers disappeared after the Pd/Cu alloy formed. In addition, a porous Pd/Cu alloy which was approximately half the thickness of the original Cu deposit had formed on top of a non-porous Pd/Cu alloy. The porous Pd/Cu alloy detached from the non-porous Pd/Cu alloy surface during the mounting and grinding process as described in Section 3.3.1. The porous Pd/Cu alloy is described further in Section 4.3.2.

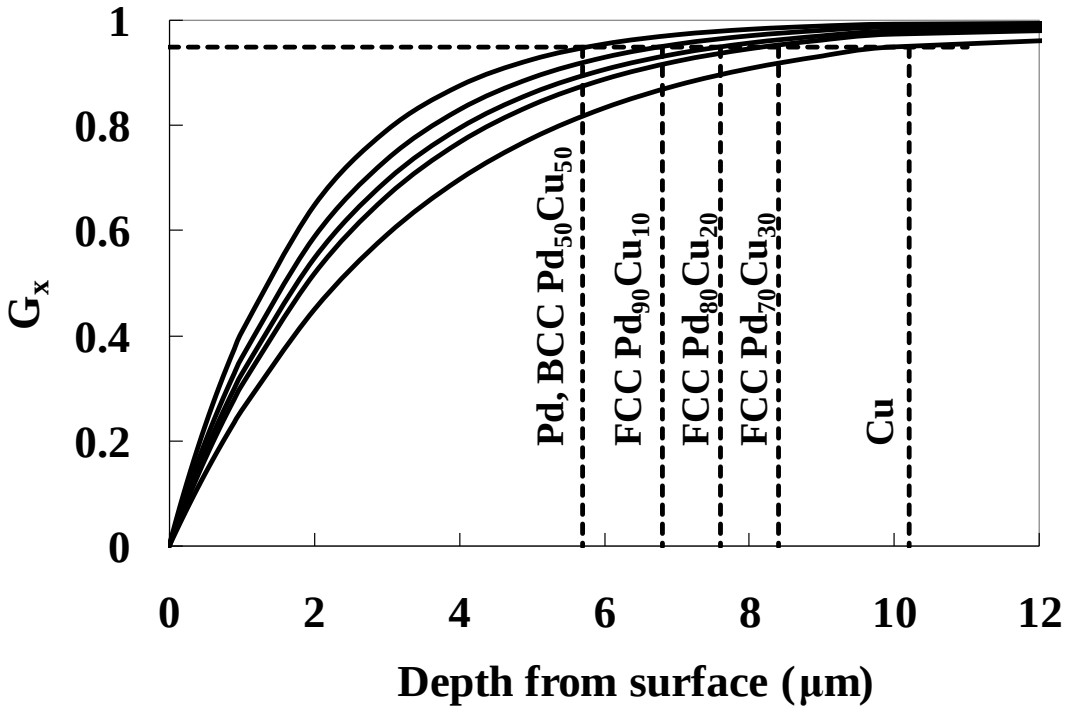

Figure 4-3 Fraction of the diffracted intensity (G_x) of a distance x from the surface for Pd, Cu and Pd/Cu alloys from the (1 1 1) plane of the fcc lattice structure and the (1 1 0) plane of the bcc lattice structure. The penetration depth is shown with dotted lines, taken from $G_x = 0.95$.

Figure 4-4 shows the cross section and corresponding elemental line scan at 3 kX of the as-deposited Cu/Pd/PSS sample. The boundary between the Cu and Pd layers was clearly seen at a distance of 16 μm. The increase in the oxygen content seen after 16 μm was most likely caused by the slight surface oxidation of the cross sectional surface of the pure Cu. Annealing Cu with Pd prevented copper oxides forming at room temperature and the surface of the cross section of the Pd/Cu layers in Figure 4-5a, b and c did not see an increase in oxygen content.

The oxide layer of the support in Figure 4-4a was rich in Fe towards the surface of the Pd layer possibly due to the enhancement of the Fe diffusion at higher oxidation temperatures (Samsonov, 1973). The Cr_2O_3, which was more stable in H_2 atmospheres (Samsonov, 1973) was more prevalent farther away from the Pd layer, also seen previously (Ma et al., 2004a). In Figure 4-5a, the decrease in oxygen with the oxide towards the interface of the Pd/Cu layer was accompanied by a decrease in Cr, showing that while part of the iron oxide was reduced during the annealing in H_2, the chromium oxide remained. The two distinct oxides are seen very clearly in Figure 4-2b, as determined by EDX.

Figure 4-5a, b and c show that the high temperature annealing in H_2 caused the Cu to diffuse to form fcc Pd/Cu alloys with a varying Cu content. The largest amount of Cu was found on the surface of the Pd/Cu layer. After eliminating the contributions of the support metals and oxygen to the line scans in Figure 4-5, the total weight percent of Cu on the surface of the Pd/Cu layers was 16, 17 and 12 wt% for the samples annealed at 500, 550 and 600ºC respectively.

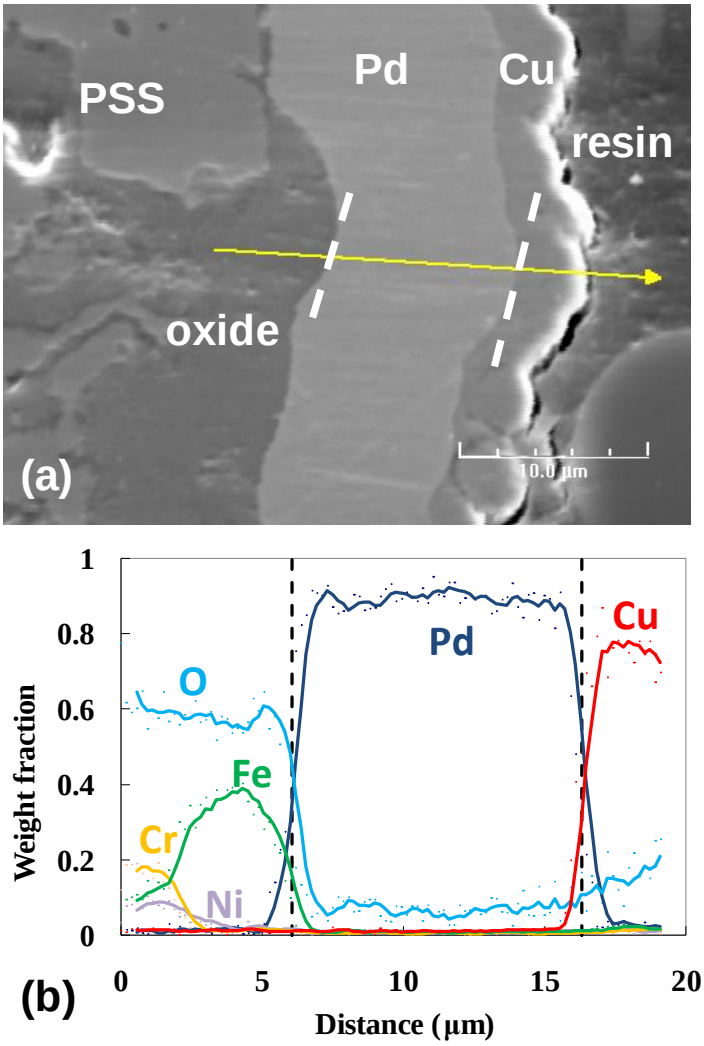

Figure 4-4 (a) Cross sectional micrograph at 3 kX and (b) corresponding elemental line scan for an as-deposited Pd/Cu sample. The dotted lines on the left and right mark the Pd/support and Pd/Cu interfaces, respectively.

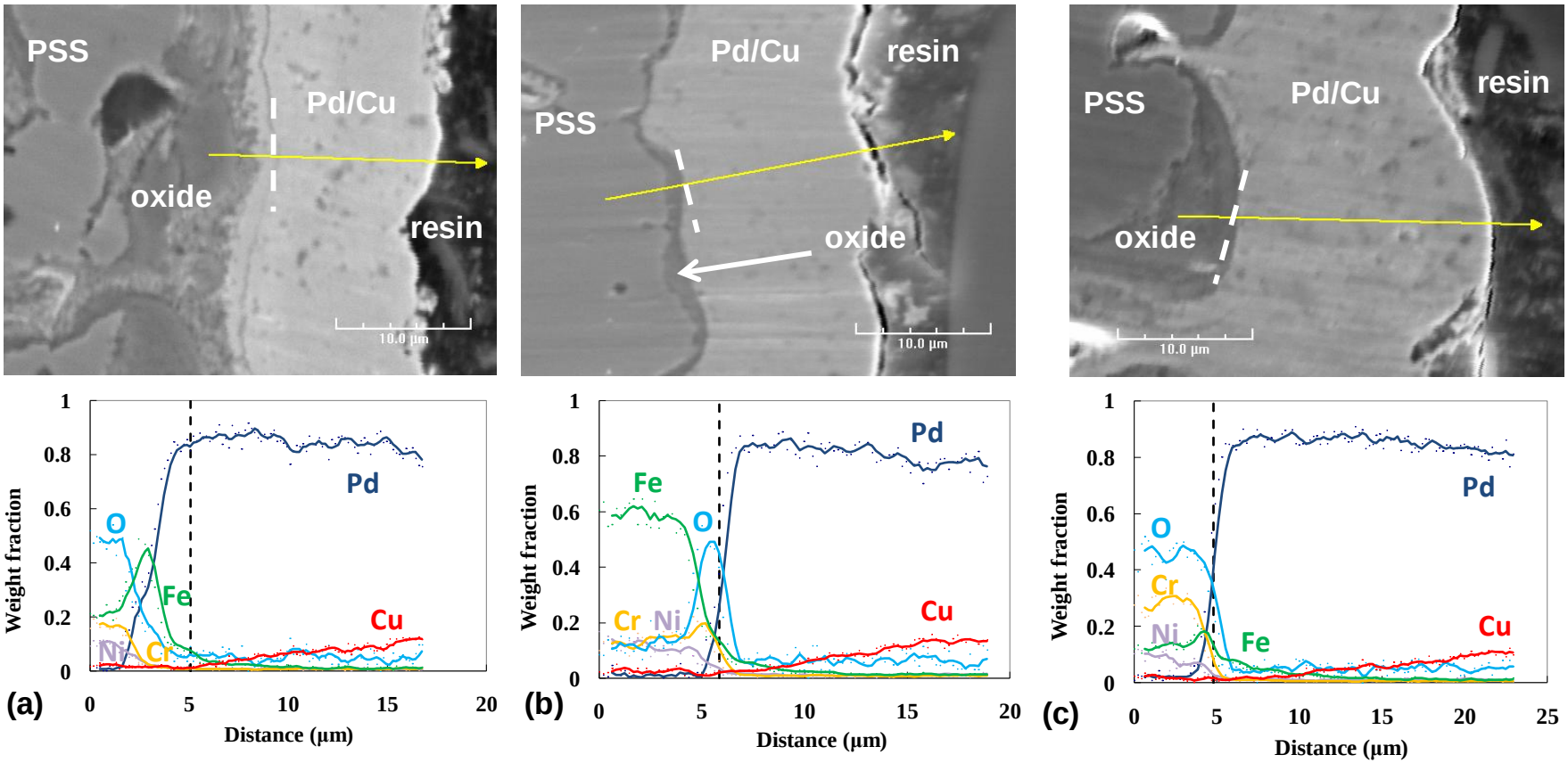

Figure 4-5 Cross sectional micrographs at 3 kX and corresponding elemental line scans for the samples annealed at (a) 500ºC, (b) 550ºC, and (c) 600ºC. The dotted lines on the left mark the Pd/support interface.

Several line scans were taken of each sample at various locations including where the Pd/Cu layer filled the pores of the PSS and where the layer covered the top surface of the PSS. The range of the Cu content seen near the surface varied from 8 – 15, 12 – 18 and 10 – 16 wt% for the samples annealed at 500, 550 and 600ºC respectively. The Cu gradient and range of the Cu content at the interface between the mounting resin and the surface of the Pd/Cu layer were similar for all of the samples, independent of the annealing temperature.

According to the Pd-Cu phase diagram in Figure 4-1, the miscibility gap for the fcc – bcc phase transition begins at 45 wt% Cu at 600ºC, 40 wt% Cu at 550ºC, and 38 wt% Cu at 500ºC. The gap widens with decreasing temperature, however for the temperatures tested the Cu concentrations of the annealed Pd/Cu layers as measured by EDX would correspond to the fcc region of the phase diagram.

4.3.2 Surface morphology

Figure 4-6a shows the surface morphology of the Pd/Cu bi-layer before the annealing. Some of the Cu clusters of the deposit appeared to be larger than others, however EDX analysis showed that the Cu covered the entirety of the Pd layer, and the cross sectional micrograph in Figure 4-4 confirmed that the Cu layer was uniform in thickness. After annealing, the morphology changed to a porous Pd/Cu alloy over a non-porous Pd/Cu alloy (see Figure 4-6b, c and d). The porous Pd/Cu alloy was caused by the Kirkendall effect (Porter and Easterling, 1981) which occurred when two metals underwent interdiffusion and the diffusion coefficients were unequal. In this case, the voids formed when Cu atoms diffused faster than the Pd atoms. Kirkendall porosity has been observed previously on the Cu side of Pd/Cu diffusion couples (Bitler et al., 1985).

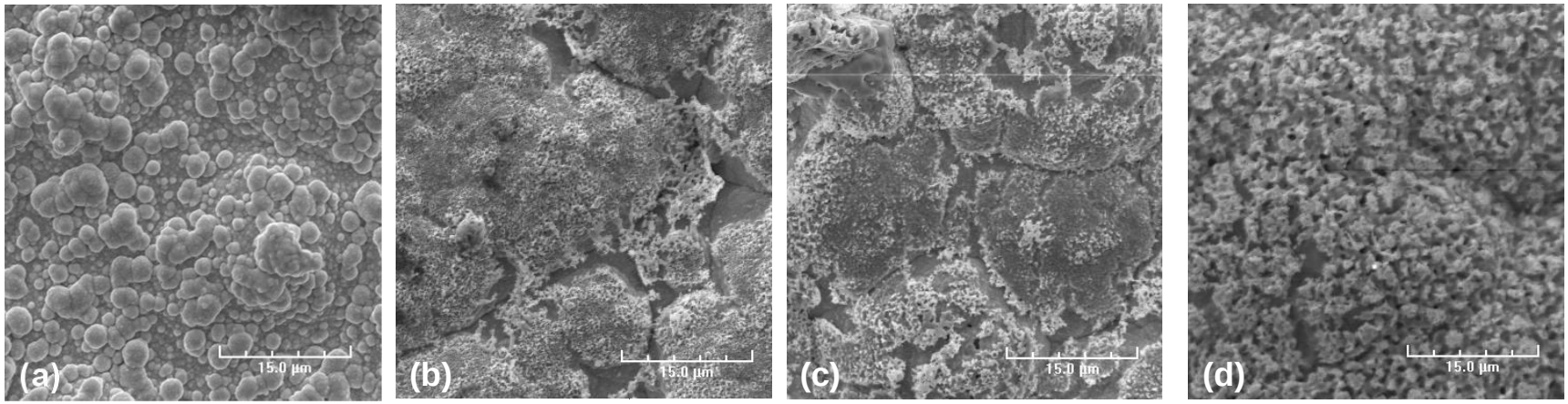

Figure 4-6 Surface micrographs at 2 kX for the samples (a) as – deposited, and annealed at (b) 500ºC, (c) 550ºC, and (d) 600ºC.

Another reason for the voids could be from the fcc – bcc transition. Indeed, the change in the lattice structure and the lattice parameter could cause irreversible structural changes. Yuan et al. (2008) observed H_2 permeation hysteresis in Pd/Cu membranes after temperature cycling to induce the fcc – bcc phase transformation. However, the hysteresis was attributed to a metastable hydrogenated PdCu(H) fcc phase.

Elemental analysis performed with EDX showed that the Cu concentration varied between 5 – 20 wt% on the surfaces of the annealed samples indicating a concentration within the fcc region of the phase diagram (Subramanian and Laughlin, 1990). As with the cross sectional analysis, the surface concentration had a similar range independent of temperature.

4.3.3 Time resolved in-situ HT-XRD

During the annealing process, between the temperatures of 500 - 600ºC, there can be a maximum of five phases present, shown in the grey area of Figure 4-1: the pure Pd and pure Cu phases, the Pd-rich and Cu-rich fcc phases, and the bcc phase. Figure 4-7 shows the X-ray diffraction data as time progressed for the coupon annealed at 550ºC in H_2. Before the annealing process began, the only phases present were from the bi-layers of Cu and Pd. The diffusion of Cu brought on by heating caused five phases to form with the phases the most rich in Cu towards the surface of the sample.

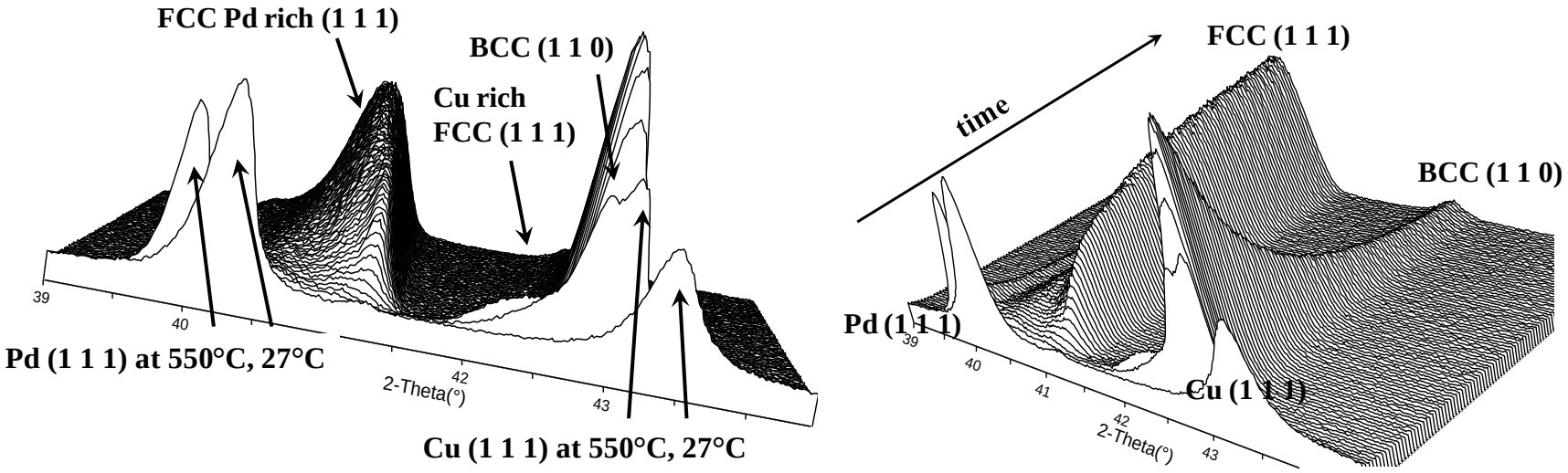

Figure 4-7 HT-XRD scans as a function of time at 550°C. The room temperature scans were taken before the annealing process began.

The first pattern in Figure 4-7 shows the peaks of the (1 1 1) plane for both Pd and Cu at room temperature. The second pattern was taken at 550ºC and showed the peak shift of both the Pd (1 1 1) and Cu (1 1 1) planes to a lower value of 2Θ due to the thermal expansion of the lattice. Also, the peak representing the (1 1 0) plane of the bcc phase of the Pd/Cu alloy appeared next to the Cu (1 1 1) peak, with significant overlap. The left tail of the bcc (1 1 0) peak showed the Cu-rich fcc phase (1 1 1) peak forming. The width of the peak attested to the concentration gradient within the Cu-rich fcc phase. As time progressed, the Cu (1 1 1) and Cu-rich fcc (1 1 1) peaks disappeared, the Pd (1 1 1) and bcc (1 1 0) peaks became smaller and the Pd-rich fcc (1 1 1) peak increased in size.

As Cu diffused into the Pd layer, the Cu-rich phases and pure Pd phase disappeared with only the Pd-rich fcc and bcc phases remaining. Further interdiffusion caused the interface between the bcc and Pd-rich fcc phases to move towards the surface of the Cu deposit. If enough time were to pass, the bcc phase would eventually disappear leaving the Pd/Cu layer a homogeneous alloy entirely in the Pd-rich fcc phase with a Cu concentration of 16 wt% (from Table 4-1).

Figure 4-8 shows the weight fraction for all of the phases as a function of time for the sample annealed at 500ºC. The pure Cu phase decreased sharply at the onset of the annealing while the pure Pd phase gradually decreased. Contrary to the continuously decreasing Cu and Pd or the continuously increasing Pd-rich fcc phase, the Cu-rich fcc and the bcc phases both had maxima.

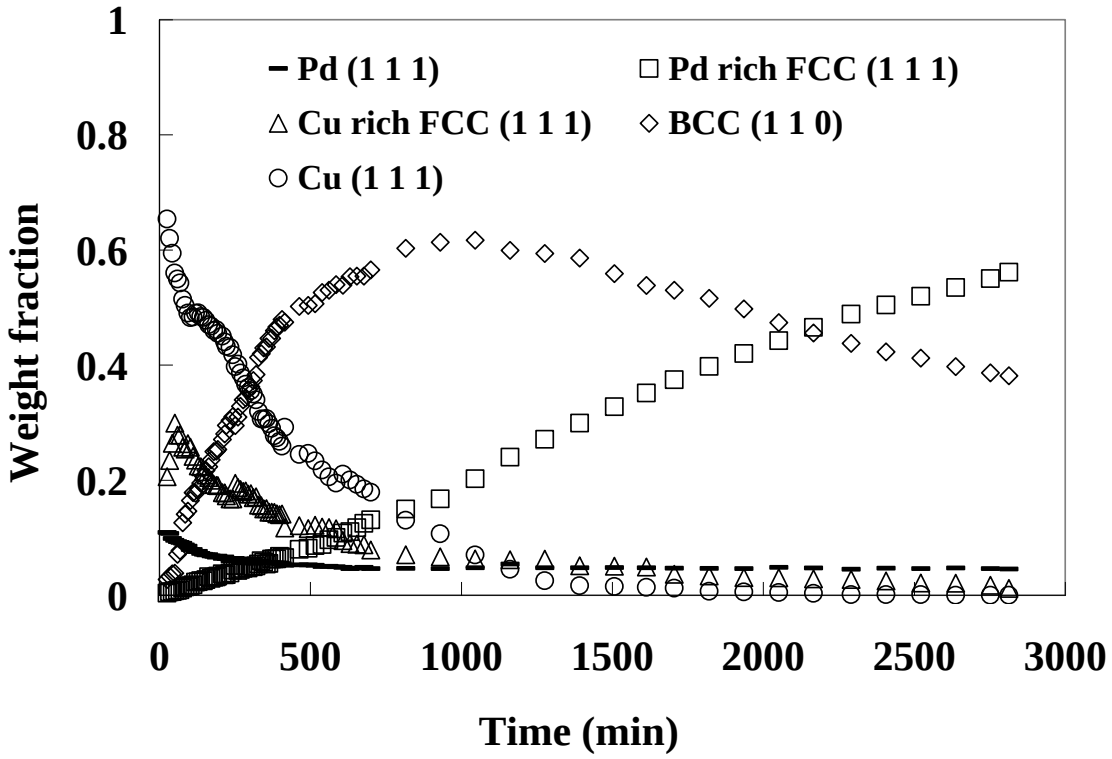

Figure 4-8 Weight fraction of the Pd-Cu phases as a function of time during annealing in H_2 at 500°C.

The Cu-rich fcc phase increased until 30 wt% at 50 minutes after which the wt% decreased until it could barely be detected. Similarly, the bcc phase increased until a maximum was reached at 61 wt% at ~1000 minutes. The maxima appeared because the Cu-rich fcc and bcc phases were interim alloy phases which formed prior to the Pd-rich fcc phase. The arrow in Figure 4-1 describes the annealing process of the bi-layer surface.

The diffusion and consequently the rate of phase transformation significantly slowed down with time and as expected, were strongly temperature dependent. In Figure 4-8, the pure Pd composition decreased from 11 wt% to 5 wt% within the first 400 minutes, and then decreased another 0.5 wt% over the next 2500 minutes. In Figure 4-9, the sample annealed at 550ºC showed that the pure Pd phase was undetectable after 1000 minutes, and in Figure 4-10, the sample annealed at 600ºC showed that the pure Pd phase was undetectable after only 400 minutes.

The decrease in the rate of the phase change was due in part to a lessening of the driving force as the concentration gradient of Cu in the sample became less steep and also due to the decreasing of the average diffusion coefficient as the sample alloyed. The Cu-Pd interdiffusion coefficient varied by two orders of magnitude depending on the alloy composition (Butrymowicz et al., 1976). The value was highest at Cu compositions of roughly 70 wt% and lowest at 0 wt%. Cu had a lower Tamman temperature than Pd (405ºC and 640ºC respectively) and therefore became mobile due to thermal vibrations at a lower temperature than Pd. The result was that Cu diffused into the Pd very quickly but as more Cu diffused into the Pd, more Pd would have to diffuse into the Cu from deeper within the bi-layer where the interdiffusion coefficient would be smaller and the driving force much less.

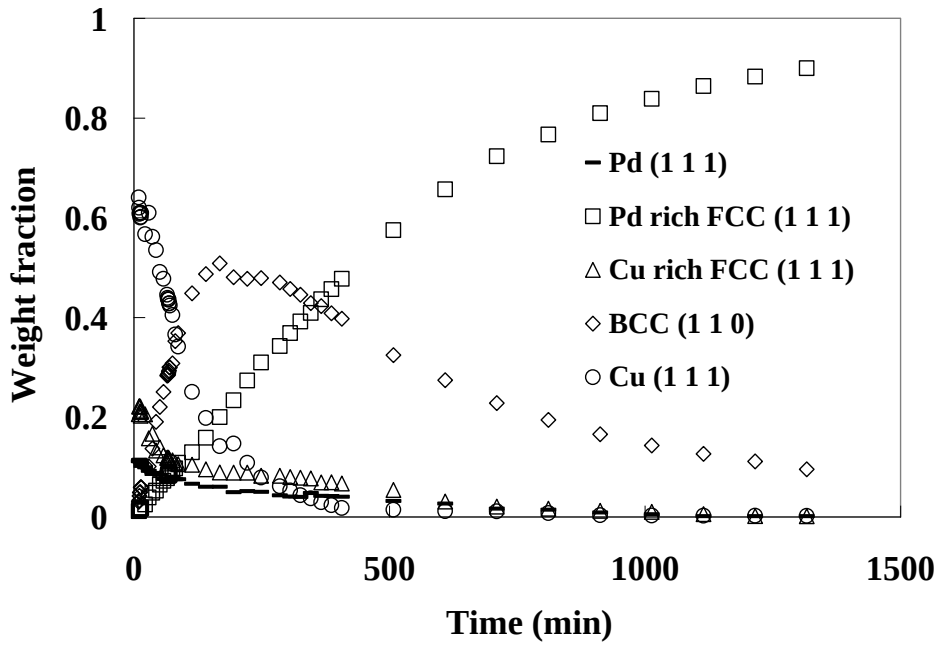

Figure 4-9 Weight fraction of the Pd-Cu phases as a function of time during annealing in H_2 at 550°C.

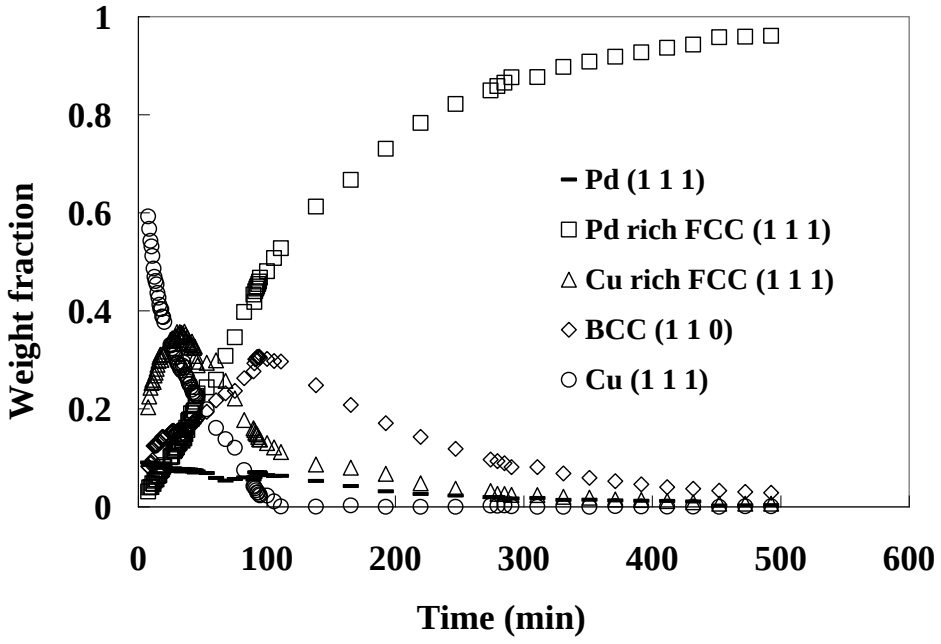

Figure 4-10 Weight fraction of the Pd-Cu phases as a function of time during annealing in H_2 at 600°C.

The pure Pd phase present within the penetration depth of the Pd/Cu layer (5.5 – 8.5 μm, see Figure 4-3) annealed at 550 and 600ºC disappeared while the amount of pure Pd phase present in the coupon annealed at 500ºC decreased very slowly after 400 minutes so that the amount appeared to not change at all. As the Cu diffused farther into the Pd layer, more heat and time were necessary for the transformation to progress. At 550 and 600ºC, there was enough thermal energy to increase the diffusivity to cause the Pd phase to disappear from the XRD penetration depth.

The slowing down of the diffusion process and consequently the phase transformation between the Pd-rich fcc phase and the bcc phase is shown in Figure 4-8, Figure 4-9, and Figure 4-10. At higher temperatures, less of the bcc phase and more of the Pd-rich fcc phase was present towards the end of the annealing. In addition, the maxima of the progression of the bcc phase weight fraction with time decreased with increasing temperature. The maxima were 61 wt%, 51% and 30 wt% at 500ºC, 550ºC and 600ºC respectively. The decrease was due to the shape of the phase diagram, shown in Figure 4-1. The miscibility gap where the bcc phase formed decreased in width with increasing temperature, resulting in less of the bcc phase forming at higher temperatures.

An important note with the coupon experiments was that the disappearance of the bcc phase never occurred even after the lengthy annealing time at 500ºC. Due to the one-dimensional direction of the Cu diffusion, the remaining bcc phase would be on the surface of the sample. The total concentration of the Pd/Cu bi-layers was roughly 15 wt% (see Table 4-1), which would place the total composition of the layer in the Pd-rich fcc phase portion of the Pd-Cu phase diagram (see Figure 4-1). However, at the end of the annealing at 500°C, 40 wt% of the bcc phase was still present, which contradicted the

results of the EDX analysis of both the surfaces and cross sections that showed that Cu concentrations were no higher than 20 wt%. It was likely that the bcc phase was present in certain areas of the porous Pd/Cu alloy seen in Figure 4-6b, c and d but that the roughness of the porous alloy made pinpointing where the bcc phase was more difficult due to the EDX resolution.

A H_2 atmosphere did cause a slight shift of the Pd/Cu miscibility gap to greater Pd compositions by 3 at% (Piper, 1966). Also, it is possible that the EDX was not as accurate in determining Cu composition since a composition of 34 wt% (taking into account the shift caused by the H_2 atmosphere) was needed at 500°C in order for the bcc phase to still be present. The coupons annealed at different temperatures all completed the annealing with different ratios of the fcc/bcc phases. However, there was little difference between them in the cross sectional line scans and the surface area scans, showing that EDX was not able to differentiate between them.

4.3.4 Kinetic analysis

A kinetic study of the phase growth was used to obtain qualitative information about the mechanism of the annealing process as well as quantitative information by estimating the rate constants. The Avrami model (Avrami, 1939, 1940, 1941) states that the new phase first appears in the form of nuclei dispersed throughout the previous phase. The nuclei grow three dimensionally into spherical grains. As the grains grow, they impinge upon each other, consequently slowing down the growth process as the transformation completes. The model is expressed in Equation 4.2 where f is the fraction of the new phase, n is the Avrami exponent which is dependent on the reaction mechanism, nucleation rate and nuclei geometry, and k is the kinetic rate constant which

is dependent on temperature, the size of the nuclei, the number of nucleation sites, and the nuclei growth rate.

$$f = 1 - \exp\left\{-(kt)^n\right\} \tag{4.2}$$

The Avrami equation is generally applied to systems with grain sizes on the order of several hundred micrometers, four to five orders of magnitude larger than the grain sizes of the electrolessly deposited Pd and Cu. The mechanical properties of systems with grain sizes of less than 1 μm change drastically since a significant portion of the atoms reside along the grain boundaries rather than within the bulk of the grain. However, a "quasi-nucleation and growth" mechanism can be applied to systems with nanosized grains, such as the system described in this work, by assuming that the nanosized grains act as nuclei themselves and grow at the expense of the surrounding grains (Chen et al., 1990, Lu et al., 1991, Averback et al., 1992, Wang et al., 1997). Such an assumption allows for the use of the Avrami nucleation and growth model.

The rate constants were calculated through the linearization of Equation 4.2, shown in Equation 4.3. The Avrami exponent and rate constant were calculated from the slope and intercept of the line, respectively.

$$\ln\left[-\ln(1-f)\right] = n\ln k + n\ln t \tag{4.3}$$

Figure 4-11 shows the linear regression of Equation 4.3 for the Cu/Pd/PSS samples annealed between 500 – 600ºC. The exponents for the Avrami model are listed in Table 4-2 and are all approximately 1.1. Hulbert (1969) has advocated the Avrami

model in the past and shown mathematically that Avrami exponents between the values of 0.5 – 1.5 indicated a diffusion-controlled, one-dimensional growth process with a decreasing nucleation rate and the exponents between the values of 1 – 2 indicated a phase-boundary controlled one-dimensional growth process with a decreasing nucleation rate. Avrami exponents equaling 1 indicated one-dimensional growth which was phase-boundary controlled with a zero nucleation rate, or saturation of the point sites. The one-dimensional growth was explained as the thickening of needles or rods which had undergone complete edge impingement; in this case forming the layer of the new phase as it thickened (Christian, 1978).

Previous studies involving product layers forming from bi-layers of Pd/Ag (Ayturk et al., 2008), GaSe/CuSe (Kim et al., 2008), and InSe/CuSe (Kim et al., 2005) have resulted in low Avrami exponents ($0.3 < n < 0.8$) showing a one-dimensional diffusion controlled process and indicating a zero nucleation rate (Hulbert, 1969). Table 4-2 shows that the Avrami exponents did not differ in the temperature range tested, indicating that the nucleation mechanism did not change with temperature. Of the works cited, the $CuGaSe_2$ formation had an athermal nucleation process (Kim et al., 2008) while the Pd/Ag alloy (Ayturk et al., 2008) and $CuInSe_2$ formations (Kim et al., 2005) had Avrami exponents which increased with temperature indicating that higher temperatures had overcome the nucleation barrier.

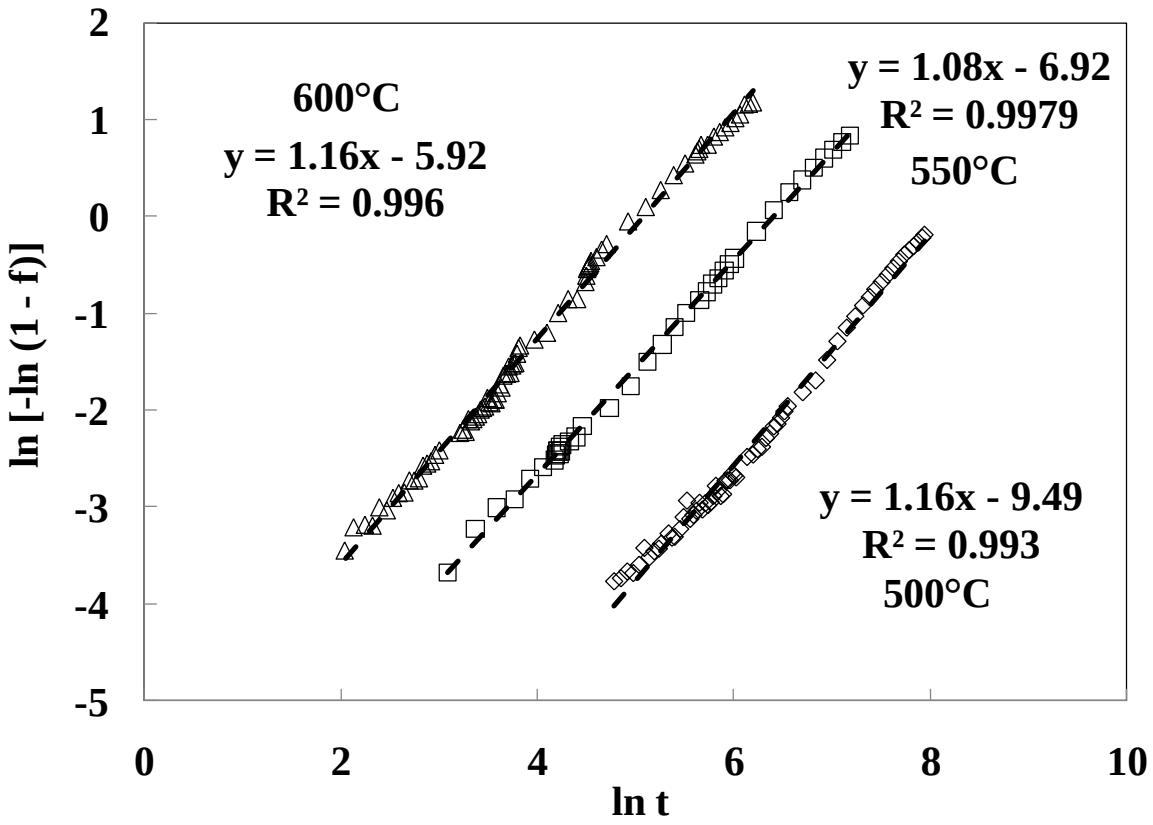

Figure 4-11 Avrami model plots for the isothermal annealing at different temperatures. Values less than f = 0.02 were not used due to the difficulty in determining peak area.

Table 4-2 Kinetic parameters for the Pd/Cu alloy formation from a bi-layer.

temperature (ºC)	k (1/min)	n	t_{99} (h)*
500	$2.73*10^{-4}$	1.16	225
550	$1.62*10^{-3}$	1.08	42
600	$6.22*10^{-3}$	1.16	10

* t_{99} refers to the amount of time estimated by Equation 4.2 for 99% of the Pd-rich fcc alloy to form.

From the estimated Avrami rate constants shown in Table 4-2, the amount of time needed for 99% of the Pd-rich fcc alloy to form was calculated and listed in Table 4-2. While a lengthy annealing time was required at 500ºC, a relatively short annealing time was required at 600ºC. It should be noted that these annealing times would only be sufficient to form a Pd/Cu layer with an fcc alloy on the surface and not a homogeneous layer, which would require higher temperatures and/or longer annealing times.

Figure 4-12 shows the fit of the experimental data to the Avrami model that has shown to be capable of describing the annealing of the Pd/Cu layer from the original bi-layers. The model predicted the process quite well for the temperature range tested in this work.

Equation 4.4 shows the Arrhenius temperature dependence of the Avrami rate constant and Figure 4-13 shows the regression used to estimate the activation energy, yielding a value of 175 kJ/mol which corresponded with the range of the activation energies for the interdiffusion of Pd/Cu alloys which ranged from 165 kJ/mol for a 10 wt% Cu alloy to 224 kJ/mol for a 80 wt% Cu alloy (Borovskii et al., 1966, Badia, 1969) rather than the activation energy for the fcc – bcc Bain transformation of 40 kJ/mol (Guazzone, 2006). It would appear that the activation energy calculated from the Avrami rate constants corresponded to that of the diffusion of a low Cu content Pd/Cu alloy. However, the temperature range for the studies mentioned previously (Borovskii et al., 1966, Badia, 1969) was 800 - 1050ºC.

$$k = A \exp\left[-\frac{Ea}{RT} \right] \tag{4.4}$$

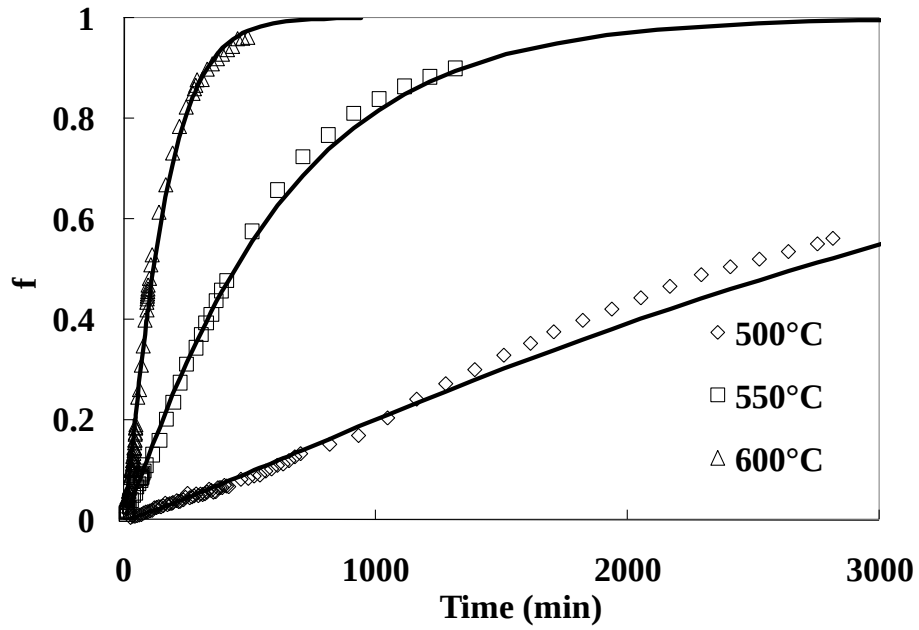

Figure 4-12 Weight fraction of the Pd-rich fcc phase as a function of time. The solid lines correspond to the Avrami model.

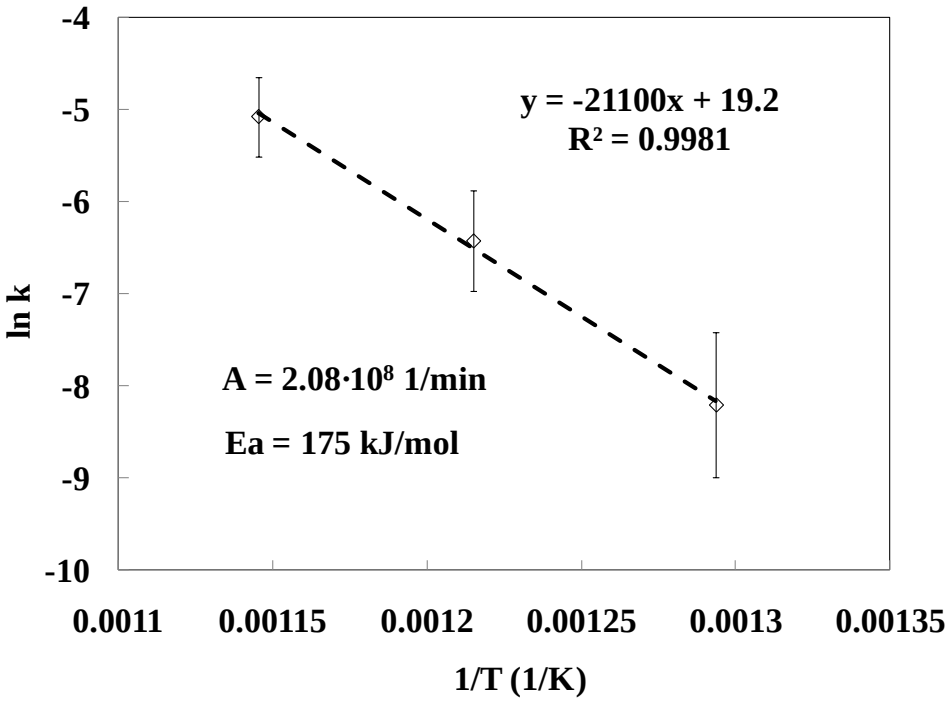

Figure 4-13 Arrhenius plot for the rate constants and the resultant activation energy based on the Avrami model.

At low temperatures, diffusion occurs primarily between the grain boundaries of metal while at high temperatures, diffusion mostly occurs within the lattice of the grains. Lattice or bulk diffusion requires more thermal energy than grain boundary diffusion and therefore, the activation energy for the bulk diffusion is higher than that of the grain boundary diffusion (Porter and Easterling, 1981). The transition temperature between the grain boundary and the bulk diffusion for Pd/Cu alloys was found by Bitler et al. (1985) who studied the interdiffusion kinetics of wrought Pd/Cu diffusion couples and electroplated Pd on Cu in the temperature range of 550 - 900ºC. For the wrought diffusion couples, at high temperatures the activation energies varied between 203 - 273 kJ/mol for Cu compositions of 13 - 71 wt%, while at lower temperatures, activation energies varied between 90.2 - 123 kJ/mol for the same Cu compositions.

The transition temperature for grain boundary to bulk diffusion was found by extrapolating the Arrhenius regressions of the diffusivities according to the calculated activation energies of the two diffusion regimes. The temperature at which the two lines met was deemed the transition temperature between the grain boundary and bulk diffusion regimes, and varied between 745 - 772ºC, depending on the alloy composition (Bitler et al., 1985). Transition temperatures tend to be roughly 2/3 of the melting point in degrees Kelvin. The melting point of a 20 wt% Cu alloy is roughly 1620K while the transition temperature varied between 1020 - 1050K, roughly 2/3 of the melting point.

Contrary to a single weld interface such as with wrought diffusion couples, the presence of many small grains in plated diffusion couples can significantly increase the overall area for diffusion. Whereas with the wrought couples the area for diffusion would be equal to the area of the weld, with the plated Pd/Cu, the area would not only include

the interface between the two metals, but also the grain boundaries themselves. Decreasing the size of the grains would result in a higher area for diffusion. The diffusing atoms enter the grain boundaries and penetrate much more deeply into the opposing layer than with the wrought couple and enter the lattice of the grains from the grain boundaries. As a result, plated diffusion couples would have grain boundary diffusion even at higher temperatures.

Similarly, Bitler et al. (1985) found activation energies for plated Pd/Cu couples which were much lower than those of the bulk diffusion and varied less over the Cu concentration range tested. They found activation energies of 106 – 121 kJ/mol for compositions between 13 - 71 wt% Cu for the entire temperature range from 550 - 900ºC. The grain size of the plated deposits was very small (10 – 20 nm) which allowed for grain boundary diffusion to occur at much higher temperatures than with the wrought Pd/Cu. No transition temperatures were observed, showing that the grain size of the metal from the fabrication method of the diffusion couples affected the mechanism of the diffusion.

In addition, the diffusivities measured for the plated Pd/Cu were an order of magnitude higher than the diffusivities measured for the wrought Pd/Cu. Higher diffusivities are usually accompanied by lower activation energies, as was the case with the plated Pd/Cu. Similarly, Chow et al. (1998) investigated the diffusion of electrodeposited Pd on Cu substrates between the temperatures of 300 - 700ºC and also found that the activation energies did not differ greatly with Cu composition, varying between 102 – 116 kJ/mol for compositions ranging between 20 – 80 wt% Cu. The activation energies were also significantly lower than activation energies for wrought Pd/Cu and for the bulk diffusion regime.

Al-Kassab et al. (1995) measured diffusion coefficients for a composition of 37 wt% Cu at 300 and 350ºC and extrapolated their results to those of previous studies performed at high temperatures (Borovskii et al., 1966, Badia, 1969) to show that the activation energy was similar. Philofsky and Hilliard (1969) found activation energies of 204 and 277 kJ/mol for Cu compositions of 20 and 5 wt% respectively, between the temperatures of 355 - 440ºC.

The samples by Al-Kassab et al. (1995) consisted of sputter deposited layers of Pd and Cu of a total thickness of 20 nm. The reason that the low temperature data (Al-Kassab et al., 1995) yielded an activation energy corresponding to bulk diffusion at low temperatures was due to the very few grain boundaries present in the sample because of the method of deposition, thus producing bulk diffusion at a low temperature. The submicron films of Philofsky and Hilliard (1969) contained short wavelength composition modulations produced by evaporation, upon which the interdiffusion coefficients were dependent. They theorized that extrapolating the wavelengths to infinity yielded true bulk diffusion coefficients at low temperatures.

The studies of Bitler et al. (1985), Chow et al. (1998), Al-Kassab et al. (1995) and Philofsky and Hilliard (1969) showed that the fabrication method of Pd/Cu diffusion couples not only influenced the value of the interdiffusion coefficients measured, but also the mechanism of the diffusion, as seen by measuring the activation energy. Although Bitler et al. (1985) was the only group that measured the actual grain size, they together with Chow et al. (1998) and Al-Kassab et al. (1995) all attributed the deviation from the expected diffusion regime to the grain size.

The Avrami activation energy calculated in this work was significantly higher than the activation energies reported for electodeposited Pd/Cu samples which were slightly larger than the activation energies of grain boundary diffusion. The difference could be due to the grain size. The measured grain sizes of electrolessly deposited Pd were previously estimated by XRD and TEM (transmission electron microscopy) to be roughly 50 nm (Saini, 2006) which were larger than the grain sizes measured by Bitler et al. (1985) most likely due to the method of deposition, the former utilizing electroless plating and the latter using electroplating.

In addition, the grain growth of the Pd was found to be significantly larger in a H_2 atmosphere than in an inert He atmosphere. After 48 hours in He at 500°C, Pd grains had grown to a size of 70 – 100 nm, while after 48 hours in H_2, the grains had grown to 100 – 200 nm (as measured by TEM, Saini, 2006). In contrast to the hydrogen atmosphere used in this work, the diffusion experiments mentioned previously (Bitler et al., 1985, Chow et al., 1998) were performed in evacuated quartz tubes.

The activation energies measured for the electrodeposited couples were higher than those of grain boundary diffusion for wrought diffusion couples which had grain sizes several orders of magnitude larger on the order of ~100 μm. Since it has been shown that grain size did affect the diffusion mechanism (Bitler et al., 1985, Chow et al., 1998, Al-Kassab et al., 1995), it is possible that even though the temperatures tested in this work were below the transition temperature for the grain boundary/bulk diffusion mechanism, the larger grain size in this work than those mentioned previously (Bitler et al., 1985) caused by the different deposition conditions and the subsequent annealing in

H_2 increased the activation energy of diffusion to a value closer to that of bulk diffusion than grain boundary diffusion.

Furthermore, the H_2 atmosphere used in this work would enhance the diffusion process by increasing the lattice constant of the alloy, as hydrogen does with pure Pd, although to a lesser extent as H_2 is less soluble in Pd/Cu alloys (Lewis, 1967). The H_2 enhanced diffusion could also enable bulk diffusion to take place at a lower temperature than without the presence of H_2. Thus, the rate determining process for the solid-state transformation was the bulk diffusion of Cu into Pd. Ayturk et al. (2008) had also observed an activation energy which corresponded to bulk diffusion for the Pd/Ag bi-layers annealed in H_2, rather than grain boundary diffusion, however no discussion was given by Ayturk et al. (2008) with regards to the two diffusion regimes.

4.3.5 Membrane permeation

The total bi-layer thickness of membrane N_03 was 12.5 µm Pd and 1.5 µm Cu resulting in a total composition of 8 wt% Cu. Figure 4-14 shows the characterization of N_03 between the temperatures of 250 - 450°C. Before characterization, the membrane was pre-annealed for five hours at 500°C in H_2 to cause the Pd/Cu layers to alloy. While the H_2 permeance stabilized fairly quickly (< 24 h) upon reaching the testing temperatures at 250, 300 and 350°C, the permeance required approximately 100 and 150 hours to stabilize at 400 and 450°C respectively, indicating that the Pd/Cu layer was continuing to anneal. The He leak of N_03 was undetectable for this temperature range.

After the permeance stabilized at each temperature, the permeance was calculated in accordance with Sieverts' Law (Equation 2.15), shown in Figure 4-15. The linear dependence of the H_2 flux on the difference of the square root of the trans-membrane

pressure indicated that the H_2 permeation was one dimensional and limited by the diffusion of H_2 through the Pd/Cu layer.

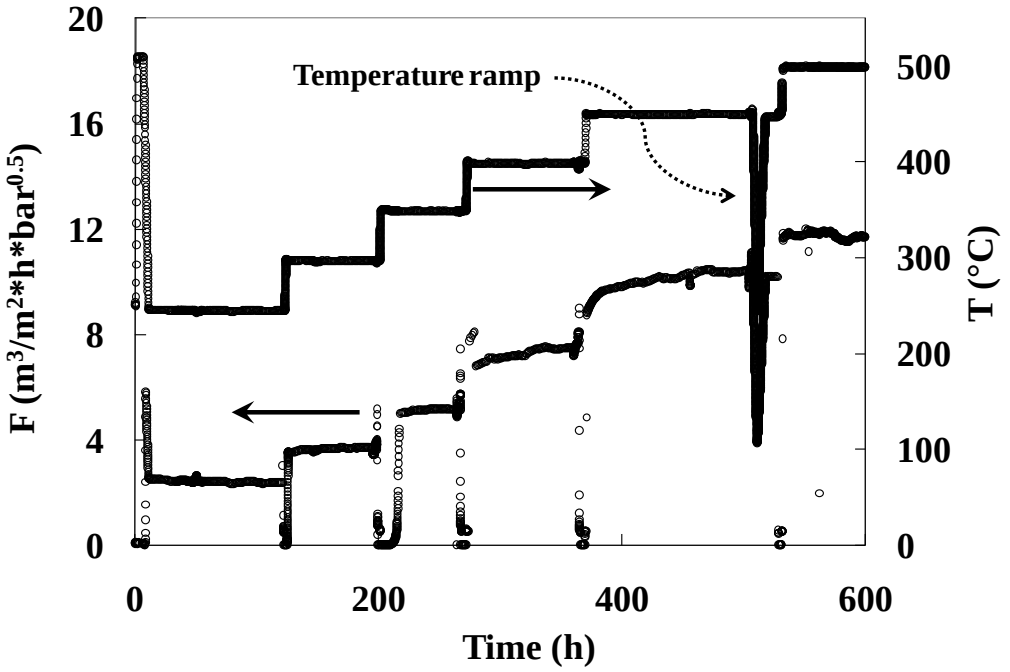

Figure 4-14 Permeance of N_03 as a function of time.

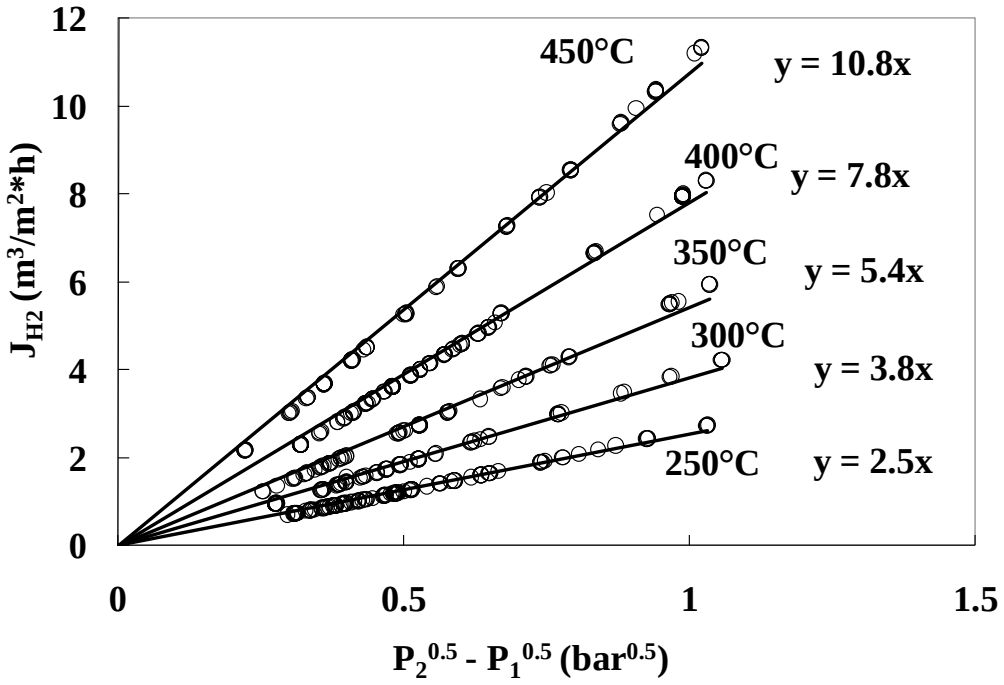

Figure 4-15 Sieverts' Law regressions for N_03. The R^2 values from the linear regressions were close to 1.

The permeance calculated from the Sieverts' Law regression at various temperatures was plotted in Arrhenius fashion to calculate the activation energy, shown in Figure 4-16. The activation energy calculated before the annealing at 450ºC was taken from a regression of the Sieverts' Law calculations shown in Figure 4-15. In order to determine the activation energy after the annealing at 450ºC, the permeance was calculated according to the linear regression for Sieverts' Law (as shown in Figure 4-15) at 450ºC. The temperature was ramped in hydrogen at a rate of 0.5ºC/min to 250ºC (shown in Figure 4-14 at 525 h) with the permeance calculated upon the assumption of Sieverts' Law, instead of the linear regression, from each measurement of flux and pressure (ΔP = 1 bar, P_{feed} = 2 bara, $P_{permeate}$ = 1 bara). When 250ºC was reached, the permeance was calculated in accordance with the Sieverts' Law regression to verify that the measurements throughout the ramping were at a pseudo-steady state thus ensuring the accuracy of the permeance calculations during the temperature ramping. The activation energy was calculated from the regression of the permeance measurements taken during the temperature ramping. The same procedure was used to determine the activation energy after the dwell time at 500ºC.

As shown in Figure 4-16, the activation energy from the characterization between 250 - 450°C was 21.0 kJ/mol. However, after the period of annealing at 450ºC, the permeance had increased at lower temperatures, resulting in a lower activation energy of 14.6 kJ/mol, showing that both the structure and the composition of the membrane had changed at 450°C.

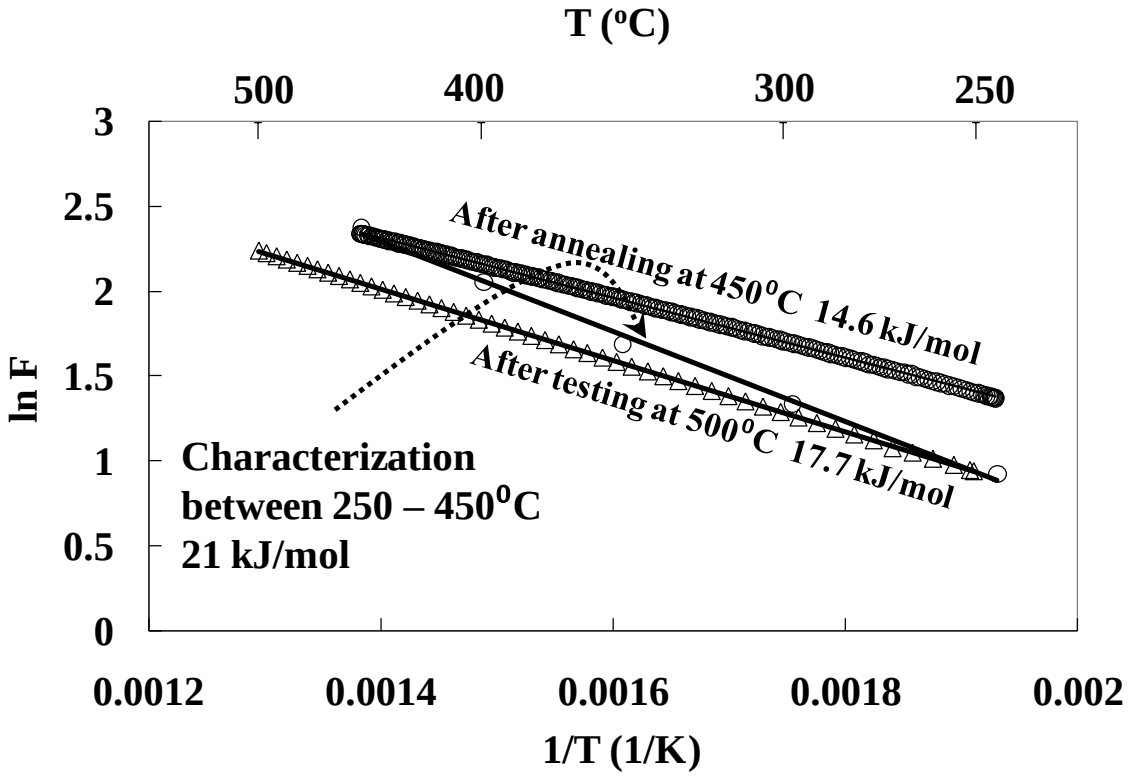

Figure 4-16 Activation energy of N_03 before and after different stages of annealing.

According to Figure 4-8, the pre-annealing at 500°C would have resulted in approximately 30% of the bcc phase forming within the XRD penetration depth of the layer if not more, since the heating/cooling rate of the membrane during the pre-annealing was 1°C/min which was much slower than the heating/cooling rate of the furnace used with the HT-XRD analysis. While the characterization of the membrane between the temperatures of 250 - 350°C did not provide enough thermal energy to cause further diffusion of the Cu into the Pd layer, heating at 400 and 450°C did cause additional annealing of the layer, increasing the amount of the bcc phase since the bcc phase had not yet reached the maximum seen in Figure 4-8. As a result, the permeance increased due to the higher permeability of the bcc phase (McKinley, 1966).

The high activation energy of 21.0 kJ/mol before the structure change was due to the steep gradient of Cu within the Pd/Cu layer increasing the mass transfer resistance of the layer to H_2 transport. The increased Cu content in a Pd/Cu fcc alloy decreased the lattice constant and would affect both the diffusion and the solubility of hydrogen atoms in the lattice (Subramanian and Laughlin, 1991). The increase in the permeance seen with the formation of more of the bcc phase was accompanied by a decrease in mass transfer resistance within the Pd/Cu layer and the activation energy decreased.

Figure 4-17 shows the continued testing of N_03 at 500°C. The permeance decreased within the first 200 hours by 26% (from 12 $m^3/m^2*h*bar^{0.5}$ to 8.9 $m^3/m^2*h*bar^{0.5}$) and then remained stable for the duration of the high temperature testing. The ideal H_2/He separation factor decreased from 3980 to 350 during the long-term testing at 500ºC due to the grain growth (Guazzone and Ma, 2008). According to the

predictions of the Avrami model, the time required for the bcc phase to disappear (t_{99} in Table 4-2) at 500°C was 225 hours, which was close to the time duration of the decrease in permeance. In addition, the activation energy of permeation measured after 1300 hours at 500ºC slightly increased to 17.7 kJ/mol. The transformation of the bcc phase to the fcc phase would be accompanied by a decrease in the H_2 permeance and increase in activation energy of permeation.

The decrease in the permeance seen in Figure 4-17 was again explained by the findings of the Avrami model, showing that the Avrami model could be used not only to describe the annealing mechanism of the Pd/Cu bi-layers, but also to describe the increase in permeance seen at 450°C and the accompanying decrease in the activation energy and the decrease in the permeance at 500°C and the accompanying increase in activation energy caused by the phase change.

As for the fabrication of Pd/Cu membranes for catalytic membrane reactors, when mass produced on an industrial scale, many steps can be shortened or removed completely. With 24 hour automated production, the total fabrication time of a batch of dense Pd membranes could be cut down to several days, reducing the production cost considerably. With regards to adding Cu for sulfur resistance, the preferred annealing time would depend on the required level of hydrogen purity in the permeate stream. While annealing at 600°C would be less expensive and result in a quickly formed fcc alloy, it is likely that a membrane annealed in this manner would form leaks due to grain coarsening, likewise with annealing at 550°C. (Guazzone and Ma, 2008) If the hydrogen purity needed is less than 99.5%, then the high temperature annealing would be less time consuming, more cost effective and therefore preferable. Higher purity hydrogen in the

permeate stream would require a lower annealing temperature even though the membrane preparation would take longer to complete, and the fabrication process would be more expensive.

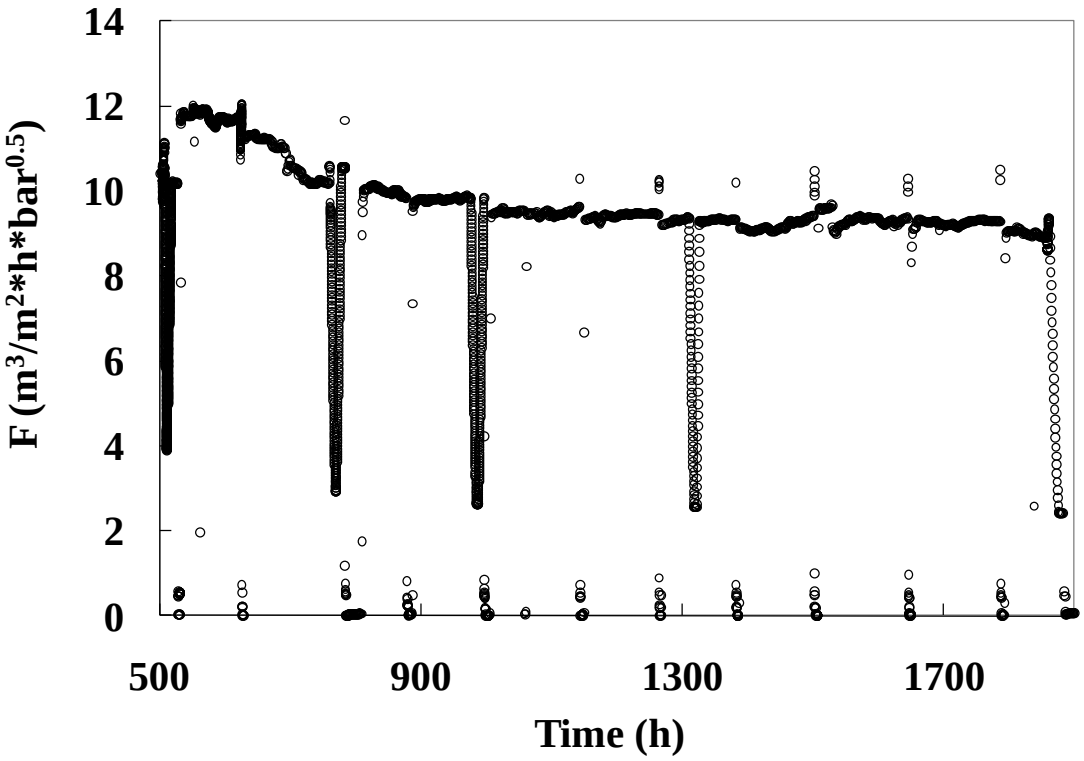

Figure 4-17 Permeance of N_03 at 500ºC.

4.4 Conclusions

By implementing HT-XRD and calculating the weight fractions of the phases, this work has successfully applied the Avrami model to investigate the annealing process of Pd/Cu bi-layers to form the sulfur resistant fcc Pd/Cu alloy. The Avrami exponent of 1.1 indicated that the nucleation and growth of the fcc phase was one-dimensional in nature and that the nucleation itself was athermal due to a lack of dependence of the Avrami exponent on temperature. The activation energy calculated from the Avrami rate constants was 175 kJ/mol and indicated that the rate limiting process of the solid-state transformation was the bulk diffusion of Cu into Pd. The experimental data fit well to the Avrami model which showed that 225 hours would be needed to completely form the surface fcc phase from Pd/Cu bi-layers at 500°C. The shorter annealing times achieved at higher temperatures would be detrimental to the selectivity of a membrane due to grain coarsening and pinhole formation.

Finally, the Pd/Cu membrane was characterized between the temperatures of 250 - 500°C and changes occurred both in permeance and activation energy following phase transformations at higher temperatures. The Avrami model explained the change in the permeation and activation energy over time both qualitatively and quantitatively as the amount of the more permeable bcc phase increased and then decreased in favor of the less permeable fcc phase.

5. H_2 transport in fcc Pd/Cu membranes

5.1 Introduction

The dilemma with Pd/Cu alloy membranes stems from the fact that the fcc phase which gives the enhanced sulfur resistance is the phase in which adding Cu decreases the permeance of the membrane. The addition of only 10 and 30 wt% Cu decreased the permeance of Pd membranes, respectively by 35% and 85% (McKinley, 1969). At 540ºC the permeance decreased by 20 and 40% at concentrations of merely 5 and 10 wt% Cu respectively (Grashoff et al., 1983).

The significant hydrogen permeance decrease seen in fcc Pd/Cu alloy membranes requires ultra-thin membranes to be fabricated in order to achieve permeances which are comparable to pure Pd membranes (Knapton, 1977) in which case the selectivity and structural integrity of the membrane becomes questionable (Thoen et al., 2006). In addition, the relatively wide pore size distribution of porous metal supports makes reducing the membrane thickness more difficult than with ceramic supports whose pore size distribution is more easily controlled (Shu et al., 1996, Mardilovich et al., 1998).

However, since H_2S poisoning happens on and near the surface of the membrane, an fcc alloy on the top layer of the Pd membrane would protect the surface of the membrane without greatly reducing the permeance. Rather than targeting a homogeneous alloy of 20 wt% Cu, a non-homogeneous membrane could be fabricated with the near surface having a composition of 20 wt% Cu and the concentration of Cu decreasing towards the support, forming a Cu gradient within the Pd/Cu layer.

In addition, a Pd/Cu membrane with a thin top fcc layer would preclude the need to form a homogeneous alloy. As yet there is no known co-deposition Pd-Cu bath, the application of which could drastically decrease annealing times and temperatures. Depositing Pd/Cu bi-layers and annealing them with the purpose of forming a homogeneous alloy required temperatures as high as 600°C (Ma et al., 2004a) for the Pd and Cu layers to completely diffuse into each other. In this chapter, permeance data collected from Pd/Cu foils was examined in order to mathematically prove the advantages of a non-homogeneous Pd/Cu layer in the fcc phase as opposed to a homogeneous Pd/Cu layer with the same surface concentration.

5.2 Experimental

The coupon samples presented in this chapter were prepared on 0.5 micron grade 316L PSS and oxidized at 800°C for 12 hours, as described in Section 3.1.2. The coupons were plated with a bi-layer of Pd and Cu as described in Chapter 4 and annealed in H_2 for 75 h at 500°C. The Pd and Cu thicknesses and compositions are listed in Table 5-1.

Table 5-1 Coupons tested in this chapter.

Pd layer (μm)	Cu layer (μm)	wt% Cu
13.2	1.4	7
12.5	2.3	13
12.8	3.1	16
13.5	4.5	20

The membranes tested in this chapter are listed in Table 5-2. Membrane N_02 was plated with 0.5 μm Ru for an intermetallic diffusion barrier while membranes N_03, N_08 and N_08a were all oxidized at 700ºC for 12 hours. N_08 and N_08a were graded with the Al_2O_3 slurry which was sealed with the "Pd glue" as described in Section 3.1.5. A Pd/Ag barrier was deposited as further grading and an additional intermetallic diffusion barrier as described in Section 3.1.2. A dense Pd layer was plated on all membranes. On N_02, N_03 and N_08a, Cu was plated on the Pd. The thicknesses of all of the layers are listed in Table 5-2. All membranes with Cu had compositions which would place them in the fcc region of the Pd/Cu phase diagram (see Figure 1-1). Membranes N_02 and N_03

were pre-annealed in H_2 for 5 hours at 500ºC before the characterization in H_2 and He to begin the annealing between Pd and Cu. The membrane characterizations were performed in the system described in Figure 3-3. The characterization of N_03 was described fully in Secton 4.3.5.

Table 5-2 Membranes tested in this chapter.

Membrane	Intermetallic diffusion barrier	grading	Pd glue (μm)	Pd/Ag barrier (μm)	Pd layer (μm)	Cu layer (μm)	wt% Cu
N_02	0.5 μm Ru	none	none	none	10.8	3.4	19
N_03	air/700ºC/12 h	none	none	none	12.5	1.5	8
N_08	air/700ºC/12 h	Al_2O_3 slurry	0.2	5.1	7.0	none	none
N_08a[*]	air/700ºC/12 h	Al_2O_3 slurry	0.2	5.1	7.6	3.8	18

[*] After the characterization, N_08 was replated with 0.6 μm of Pd and plated with 3.8 μm of Cu. The replated Pd/Cu alloy membrane was referred to as N_08a.

5.3 H_2 transport through a Pd/Cu film

Figure 5-1 shows a compilation of hydrogen permeance data taken from Pd/Cu alloy foils between the temperatures of 350 and 540°C which were normalized to hydrogen permeance data for pure Pd foils. The decrease in permeability accompanying the increase in Cu content stems from the decrease in lattice parameter in the fcc phase due to the smaller size of Cu relative to Pd.[*] The lattice parameter change in the Pd/Cu system can be described in accordance with Vegard's Law which states that the lattice parameter is linearly dependent on the alloy composition (Cullity and Stock, 1978).

The decreased lattice parameter in the Pd/Cu alloy caused a decrease of the hydrogen diffusion since the interstitial space that hydrogen occupies becomes smaller. Also, the increased Cu content causes a decrease in hydrogen solubility (Kamakoti et al., 2005). The increase in hydrogen permeability seen at concentrations higher than 30 wt% Cu in Figure 5-1 was caused by the fcc-bcc phase transformation (Figure 1-1). The phase change enlarged the interstitial space through which hydrogen diffused, thus increasing the hydrogen diffusivity. However, the solubility of hydrogen within the lattice continued to decrease with the addition of Cu, causing the decrease following the peak in permeability (Kamakoti et al., 2005). The permeability reached a maximum at 40 wt% Cu at 350°C before decreasing to near-zero values.[*] However, further increase in the Cu content resulted in a decrease of the bcc lattice parameter and the hydrogen permeability sharply decreased with increasing Cu content.

[*] The atomic radii of Pd and Cu are 137 and 128 pm, respectively (www.wikipedia.com).

[*] The peak in permeability would shift to higher Cu concentrations with increasing temperature due to the narrowing of the miscibility gap of the Pd-Cu phase diagram with increasing temperature.

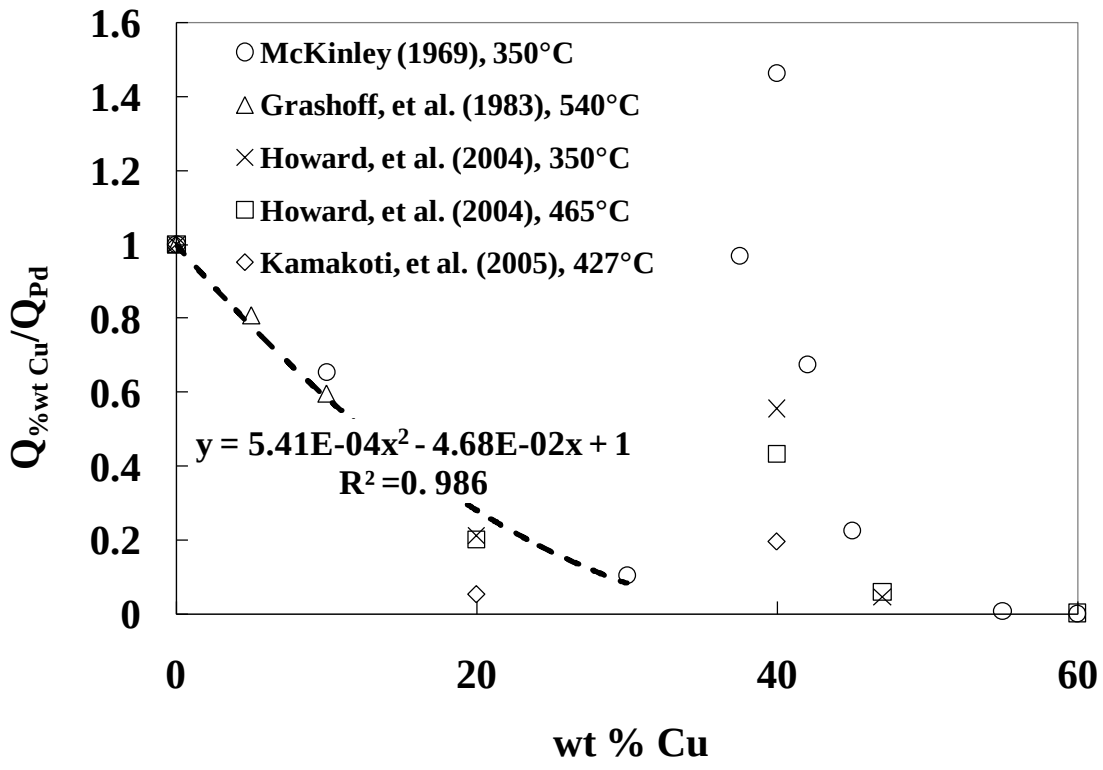

Figure 5-1 Permeability as a function of Cu content for Pd/Cu foils.

In order to calculate the dependence of the hydrogen permeance on Cu content, a polynomial regression was performed on the normalized permeance data measured for the fcc Pd/Cu foils at 350°C shown in Figure 5-1, excluding the data taken at other temperatures and the data taken in the fcc-bcc miscibility gap after 30 wt% Cu. The empirical regression is shown in Equation 5.1 and is only valid between Cu concentrations of 0 and 30 wt% and at 350ºC.

$$\frac{Q_{\%wt\,Cu}}{Q_{Pd}} = 0.000541 \cdot \left(wt\%\ Cu\right)^2 - 0.0468 \cdot \left(wt\%\ Cu\right) + 1 \qquad (5.1)$$

Kamakoti et al. (2005) modeled the permeability of hydrogen through Pd/Cu membranes at Cu compositions varying between 0 – 53 wt% and in the range of the fcc – bcc phase transition. The model correctly predicted trends with concentration and temperature and was able to qualitatively explain the unusual peak seen in the permeability of Pd/Cu alloy membranes. However, the calculated permeabilities deviated from experimental data within the literature.

As with the hydrogen permeability a regression showing the dependence of the activation energy of permeation on Cu content can also be calculated from existing data within the literature. Figure 5-2 shows the activation energy of Pd/Cu foils as a function of Cu content, omitting conditions at which the membranes were in the bcc and mixed fcc-bcc phase regions of the phase diagram.

The empirical regression is shown in Equation 5.2. As can be seen, increasing Cu content increases the activation energy of permeation quite drastically at high concentrations reaching 70 kJ/mol at 60 wt% Cu. The decreased diffusion and solubility

of hydrogen in Pd/Cu alloys resulted in an increase in the mass transfer resistance within the Pd/Cu layer, which in turn caused the increase in the activation energy of permeation. Clearly, the addition of Cu caused hydrogen transfer within Pd membranes to be a much more highly activated process, requiring more thermal energy to produce high permeabilities than with pure Pd.

$$E_{Q,\%wtCu} = 0.0132 \cdot (wt\%\ Cu)^2 + 0.0884 \cdot (wt\%\ Cu) + 14.9 \qquad (5.2)$$

The higher activation energy would be expected because hydrogen transport through Pd/Cu layers is governed by the solution-diffusion mechanism. According to Equations 2.12, 2.13 and 2.14, a higher activation energy would require a higher heat of solution and/or a higher activation energy of hydrogen diffusion. Increasing Cu content in the fcc phase does indeed increase the activation energy for diffusion (Butrymowicz et al., 1976) and the decreased solubility of hydrogen with the addition in Cu would indeed result in an increase in the heat of solution (Kamakoti et all, 2005).

Figure 5-1 and Figure 5-2 both show the deleterious effect of Cu on the membrane performance when in the fcc phase. Pd/Cu alloy membranes fabricated in the fcc phase for sulfur tolerance have a lower performance than Pd or other Pd alloy membranes when not exposed to gas mixtures with H_2S. The most commonly studied composition of Pd/Cu membranes with regards to sulfur tolerance is 20 wt% Cu (Morreale et al., 2004, Mundschau et al., 2006, Iyoha et al., 2007a, Kamakoti et al., 2005). According to Equations 4.1 and 4.2, the 20 wt% Cu membranes would have a permeability which was 26% of pure Pd and an increase in activation energy to 21.9 kJ/mol.

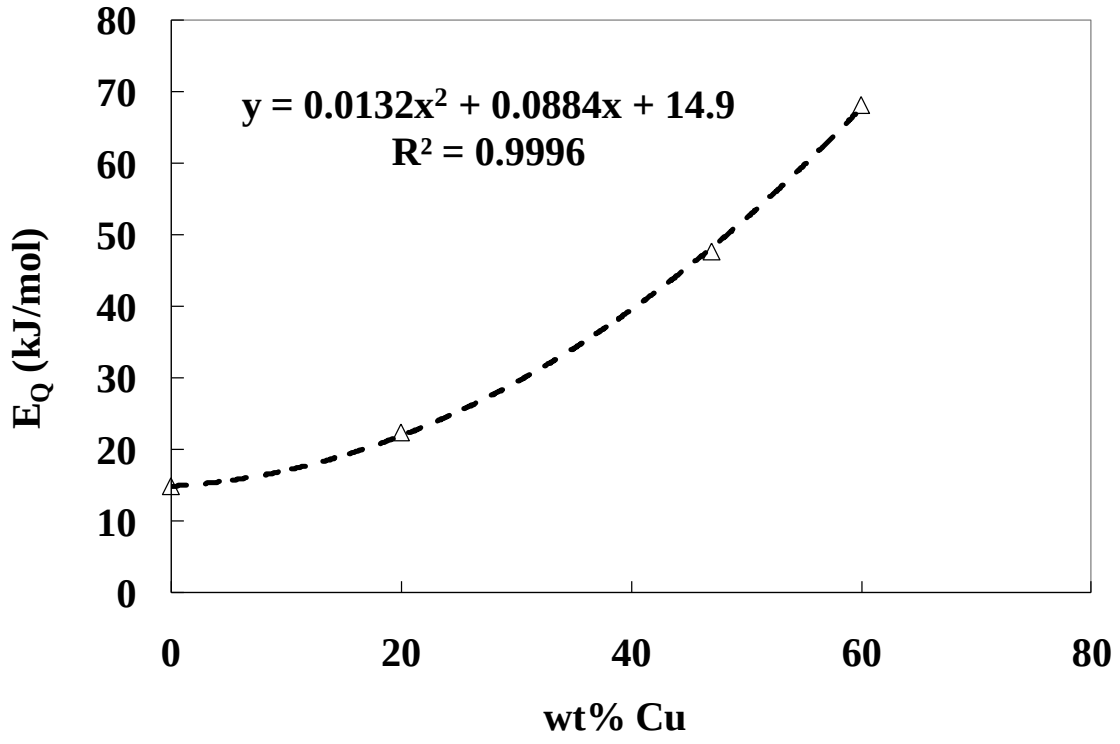

Figure 5-2 Activation energy as a function of Cu content. The activation energy for pure Pd was taken from Guazzone (2006) and the activation energies for Pd/Cu* were calculated from data reported by Howard et al. (2004).**

* The Pd/Cu data were only taken from membranes in the fcc phase.

** The data for the activation energy calculations taken from Howard, et al (2004) was limited to data at 908 K and below due to the intermetallic diffusion between the Pd/Cu foils and the metallic porous support at higher temperatures.

5.4 Non-homogeneous Pd/Cu alloys

A non-homogeneous alloy with the fcc phase on the surface of the Pd membrane and a Cu gradient within the layer would protect the surface from sulfur poisoning without decreasing the permeance of the membrane as much as a homogeneous fcc alloy. Figure 5-3 shows the cross sectional micrograph of an annealed Pd/Cu bi-layer with the gravimetric Cu composition of 20 wt%, described in Table 5-1.

Figure 5-4 shows the line scan of the same coupon which resulted in a concentration of 20 wt% Cu near the surface. The origin marks the interface of the Pd/Cu layer and the PSS support, shown with the dotted line on the left side of Figure 5-3, and the x-axis in Figure 5-4 follows the distance along the arrow in Figure 5-3 to the surface of the deposit. The Cu content is shown as well as the corresponding hydrogen permeability relative to pure Pd at each point in the scan, as calculated from Equation 5.1. Near the surface of the Pd/Cu layer where the Cu concentration was the highest at 20 wt% Cu (balance Pd), the permeability was the lowest at 25% of the permeability of a pure Pd foil. However, the decrease in Cu further into the layer caused the permeability to sharply increase. Finally, the Cu reached a concentration of roughly 5 wt% for the remainder of the Pd/Cu layer and the permeability was at 80% of a pure Pd foil. It should be noted that the permeabilities calculated are from regressions of data measured at 350ºC.

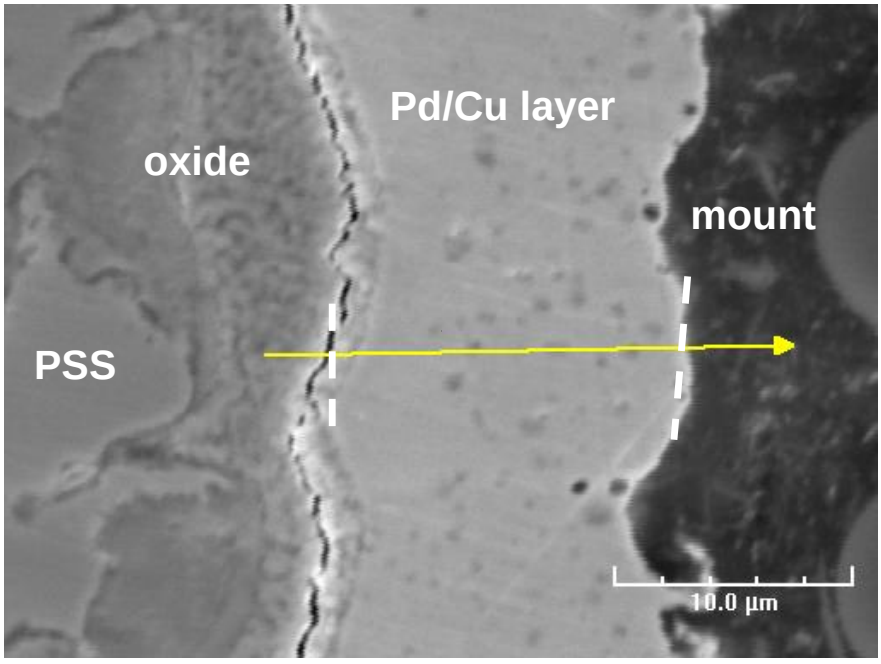

Figure 5-3 Cross sectional micrograph of a non-homogeneous Pd/Cu alloyed layer with 20 wt% Cu on the surface.

The dotted line in Figure 5-4 shows the permeability of a homogeneous Pd/Cu foil with the same surface concentration of 20 wt% Cu. In contrast to the non-homogeneous Pd/Cu layer, the entirety of the homogeneous Pd/Cu layer would perform at 25% of the permeability of a pure Pd foil.

Figure 5-5 shows the Cu concentration profile (balance Pd) for a line scan which resulted in 15 wt% Cu on the surface from the 16 wt% Cu coupon shown in Table 5-1. The scan with 15 wt% Cu on the surface was similar to the scan with 20 wt% Cu on the surface in that the Cu gradient near the surface was relatively steep for 3 – 4 μm until the Cu concentration tapered off at 5 wt% for the remainder of the layer. In accordance with the Cu concentration profile, the hydrogen permeability was very low at the surface reaching 35% of the permeability of a Pd foil before increasing with distance from the surface. As with the 20 wt% scan, the performance at 80% of a Pd foil for the majority of the layer was an improvement over the yield of a 15 wt% Cu homogeneous alloy with a permeability at 40% of a Pd foil.

The line scans with 10 and 5 wt% Cu on the surface are shown in Figure 5-6 and Figure 5-7, respectively and are taken from the 13 and 7 wt% Cu coupons described in Table 5-1. The Cu gradients in Figure 5-6 and Figure 5-7 were not nearly as steep as with the Pd/Cu layers with 15 and 20 wt% Cu on the surface. The Cu content gradually lessened from the surface of the Pd/Cu layer towards the support. Likewise, the hydrogen permeability decreased gradually from the interface of the support to the surface of the sample.

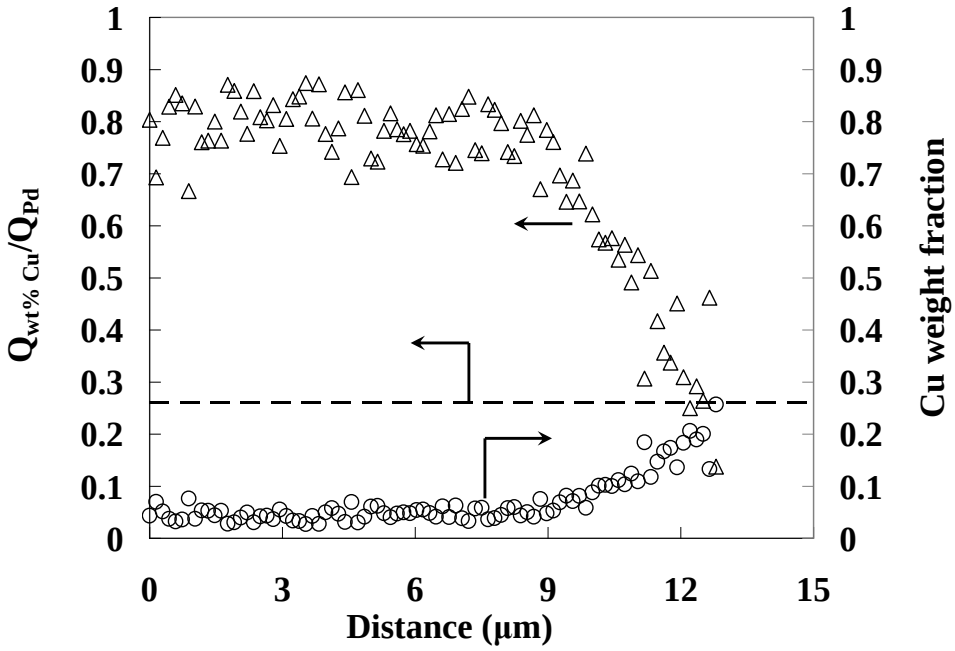

Figure 5-4 Cu content and permeability as a function of distance for a coupon with 20 wt% Cu on the surface and a 20 wt% Cu homogeneous alloy.

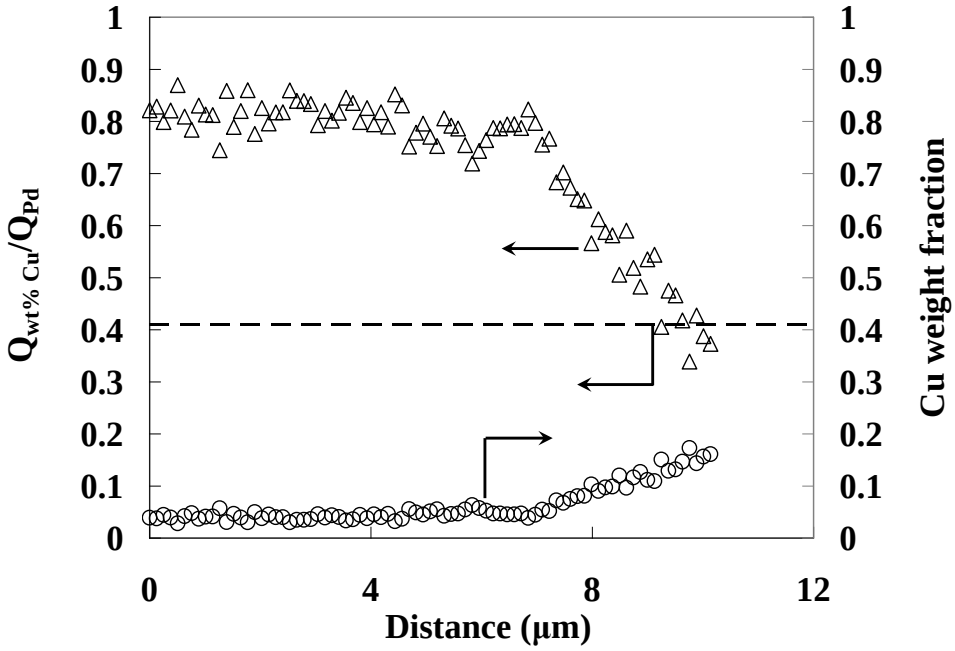

Figure 5-5 Cu content and permeability as a function of distance for a coupon with 15 wt% Cu on the surface and a 15 wt% Cu homogeneous alloy.

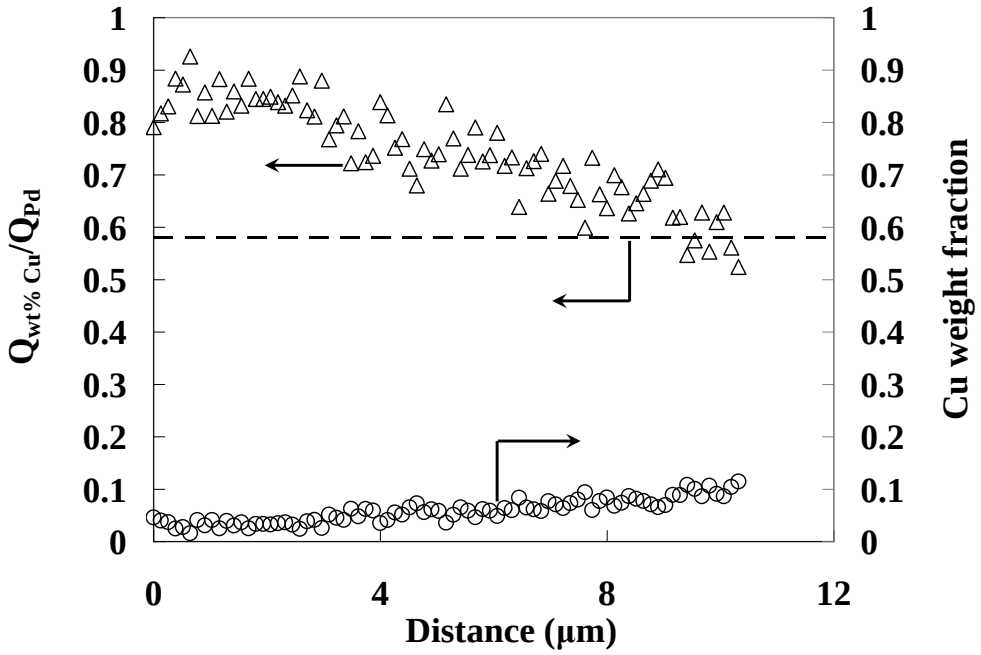

Figure 5-6 Cu content and permeability as a function of distance for a coupon with 10 wt% Cu on the surface and a 10 wt% Cu homogeneous alloy.

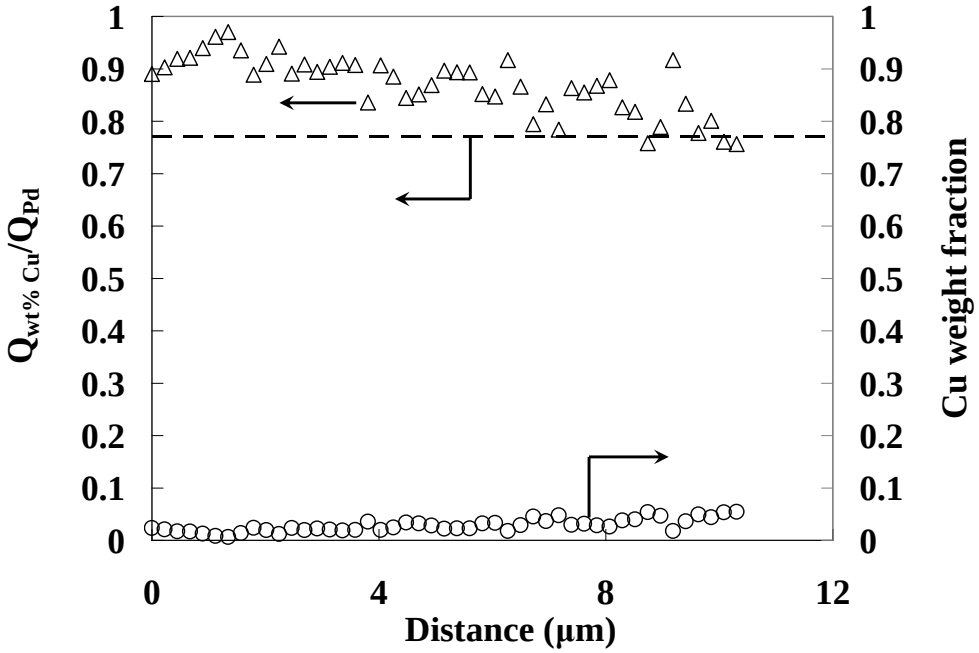

Figure 5-7 Cu content and permeability as a function of distance for a coupon with 5 wt% Cu on the surface and a 5 wt% Cu homogeneous alloy.

The steadily increasing value of the permeability from the surface of the support interface shows an improvement over the permeability of the homogeneous counterparts which were 58 and 77% of pure Pd foils for the 10 and 5 wt% Cu alloys, respectively. The increased performance of the non-homogeneous Pd/Cu layers with surface concentrations of 5 and 10 wt% Cu was not as drastic as with the surface concentrations of 15 and 20 wt% Cu.

In order to calculate the effective hydrogen permeability of the non-homogeneous Pd/Cu alloys, the overall resistance of the non-homogeneous Pd/Cu alloy was calculated by treating the data points as a series of layers with different mass transfer resistances (shown in Equation 2.19) in which the resistance is the inverse of the permeability (Henis and Tripodi, 1981). The effective permeability of a series of layers with different resistances would then be expressed as in Equation 5.3, where x_n and Q_n are the thickness and permeability of each layer respectively, and X is the total thickness of the layer.

$$Q_{eff} = \frac{X}{\frac{x_1}{Q_1} + \frac{x_2}{Q_2} + ... + \frac{x_n}{Q_n}} \tag{5.3}$$

The effective permeability over the entire layer can be calculated from the integral of the sums of the inverse of the permeability as a function of the Cu content of each sub-layer as expressed in Equation 5.4.

$$Q = \frac{x}{\int_x \frac{dx}{Q(wt\%\ Cu(x))}} \tag{5.4}$$

Figure 5-8 shows the inverse of the permeability and the Cu content of an annealed Pd/Cu coupon with 20 wt% Cu on the surface as a function of distance. The grey area under the top curve shows the denominator in Equation 5.4, graphically. The integral was calculated numerically with Polymath software. Similar calculations were performed from the data from the samples with 5, 10 and 15 wt% Cu on the surface.

Figure 5-9 compares the effective hydrogen permeability of both homogeneous and non-homogeneous fcc Pd/Cu alloys of the same surface concentration based on the data presented in Figure 5-4, Figure 5-5, Figure 5-6 and Figure 5-7. As can be seen, the effective permeability of the non-homogeneous Pd/Cu alloys was much larger than the homogeneous Pd/Cu alloys at every fcc composition calculated. Seeing as the majority of the non-homogeneous Pd/Cu layers had Cu concentrations far below that of their respective surfaces, the higher resistance to hydrogen transport caused by the high Cu content within the Pd/Cu layer was minimized. The gap between the respective permeabilities increased with increasing Cu content due to the sharp decrease in permeability with Cu content seen in Figure 5-1.

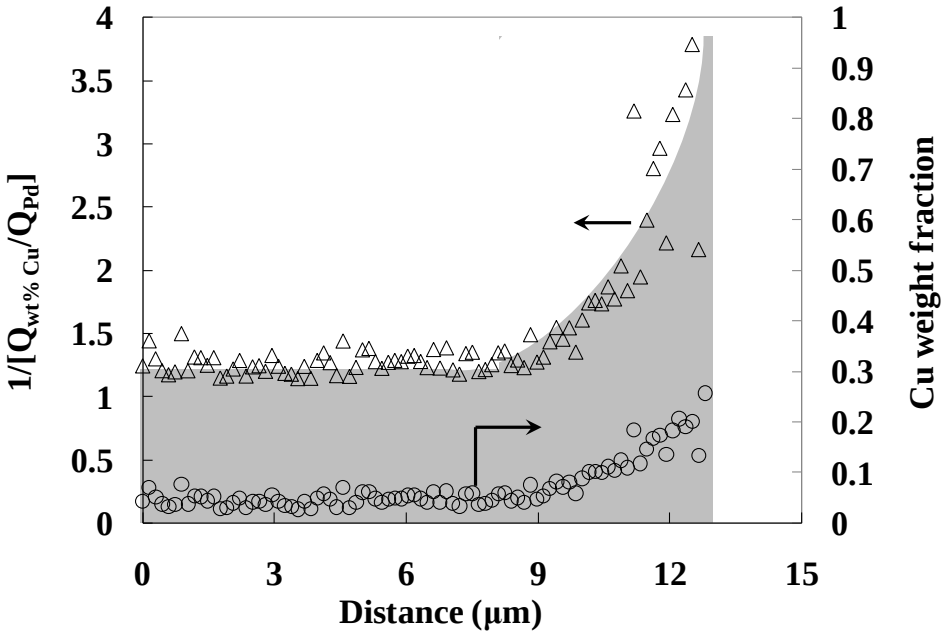

Figure 5-8 Cu content and the inverse permeability as a function of distance for a coupon with 20 wt% Cu on the surface.

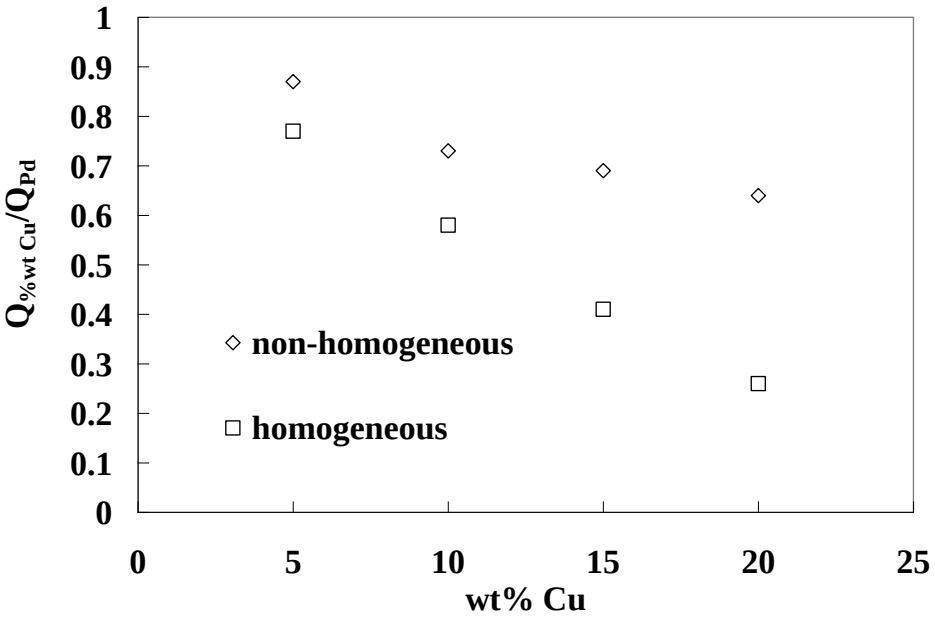

Figure 5-9 Permeability of homogeneous and effective permeatbility of non-homogeneous fcc Pd/Cu membranes with the same surface concentration.

5.5 H_2 permeance of non-homogeneous Pd/Cu alloy membranes

5.5.1 H_2 permeance

Membranes N_02 and N_03 were characterized for over 1700 and 2300 hours respectively between the temperatures of 250 - 500°C, a temperature range suitable for the water-gas shift reaction. N_08 and N_08a were characterized for 700 and 1200 hours respectively between the temperatures of 250 - 450°C.

Figure 5-10 shows that all four membranes followed the Sieverts' Law in the temperature ranges tested, indicating that one dimensional diffusion through the Pd or Pd/Cu hydrogen selective layer was the rate determining step of hydrogen permeation through the composite membrane. The hydrogen permeance of the composite Pd membrane N_08 was equal to the hydrogen permeance of a free-standing Pd film of a thickness of 16 μm (Guazzone, 2006, Ayturk, 2007). Plating an additional 4.4 μm of Pd should have resulted in N_08a having a permeance of 23 $m^3/m^2*h*bar^{0.5}$ which is equal to a free-standing film of 20.4 μm (Guazzone, 2006, Ayturk, 2007). However, since increasing the Cu concentration lowered the permeance of Pd membranes (McKinley, 1969), plating 0.6 μm of Pd with 3.8 μm of Cu decreased the permeance even further, resulting in a permeance of 18.0 $m^3/m^2*h*bar^{0.5}$ for N_08a.

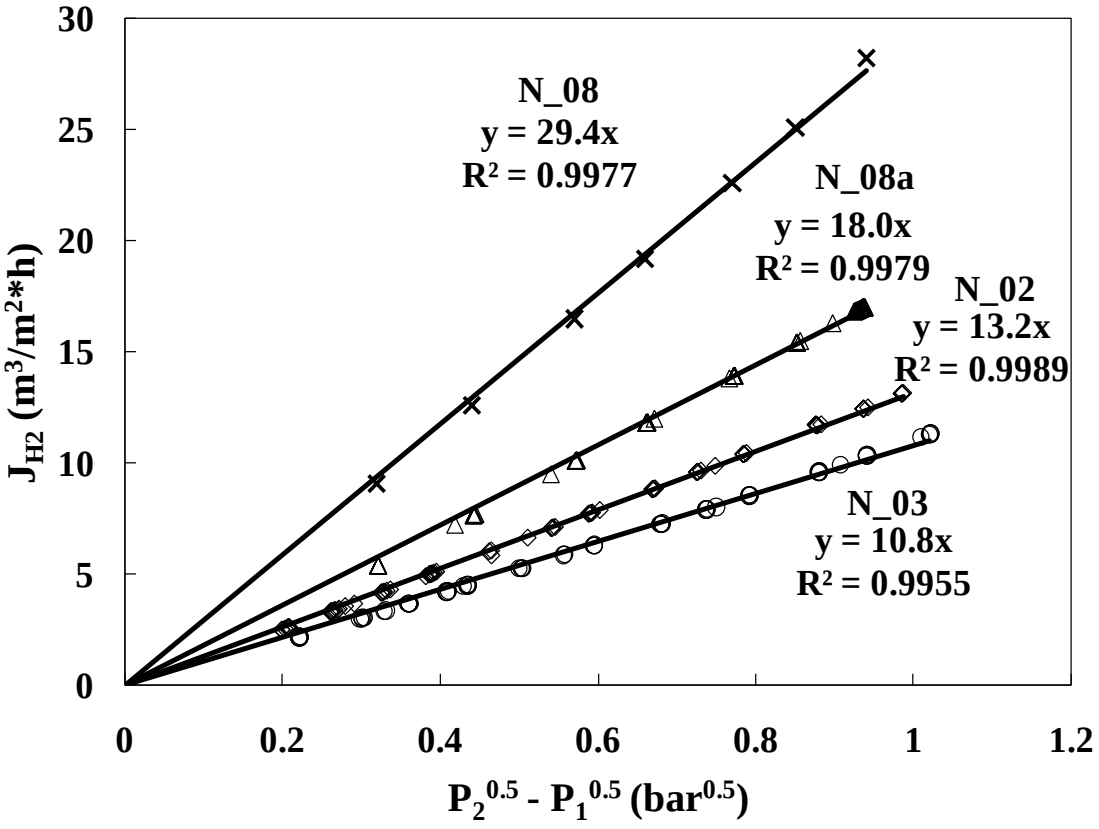

Figure 5-10 Sieverts' Law regression at 450ºC for the Pd/Cu membranes before the long-term testing of N_02 and N_03 in H_2 at 500ºC. P_1 = 1 bara.

One would expect that a membrane of higher Cu content and similar thickness would have a smaller permeance due to the negative effect that Cu has on the permeance of fcc Pd/Cu alloys. The Cu composition of N_02 was more than double that of N_03, and the membranes had similar thicknesses. Although neither membrane was homogeneous, N_02 should have had a permeance less than that of N_03. However, the permeance of N_02 was higher than that of N_03. The reason for the discrepancy could be due to the inaccuracy in determining the thickness and Cu concentration of the membrane layers with the gravimetric method. The Cu composition of N_08a was similar to that of N_02. Even so, the H_2 permeance of N_08a was higher than that of either N_02 or N_03 because of the Al_2O_3 grading layer and Pd/Ag barrier, which prevented Pd from deeply penetrating into the pores of the support (see section 7.3.1 for further discussion).

For the duration of the H_2 testing, N_08 and N_08a had stable permeances at 450ºC for 600 and 500 hours respectively and N_03 had a stable permeance for over 1150 hours of testing at 500ºC after an initial decrease of permeance of 26% (from 12 to 8.9 $m^3/m^2*h*bar^{0.5}$) due to the fcc-bcc phase transition, as explained in Section 4.3.5. However, N_02 exhibited steady intermetallic diffusion of the support metals into the hydrogen selective layer at 500°C and the permeance decreased from 15.0 to 3.3 $m^3/m^2*h*bar^{0.5}$, showing that the 0.5 μm Ru was not an effective barrier.

Figure 5-11 shows the Arrhenius plot of the permeance as a function of temperature for all of the membranes tested in this work, following the long-term testing in H_2 and He. In order to determine the activation energy of permeation, the permeance was calculated according to the linear regression for Sieverts' Law (as shown in Figure 5-10) at 500ºC for N_02 and N_03 and at 450ºC for N_08 and N_08a.

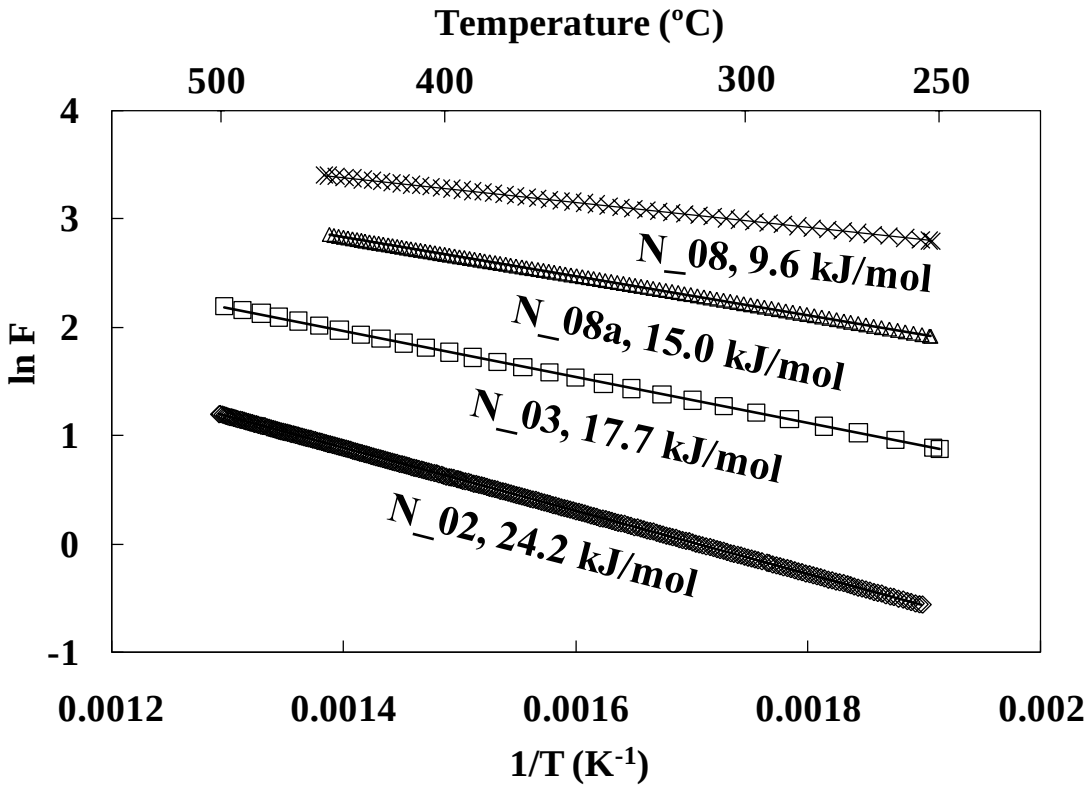

Figure 5-11 Hydrogen permeance as a function of temperature after the long-term testing of N_02 and N_03 in H_2 at 500ºC. The respective activation energies are listed alongside the membrane name.

The temperature was ramped in hydrogen at a rate of 0.5ºC/min to 250ºC with the permeance calculated upon the assumption of Sieverts' Law, instead of the linear regression, from each measurement of flux and pressure (ΔP = 1 bar, P_{feed} = 2 bara, $P_{permeate}$ = 1 bara). When 250ºC was reached, the respective permeances of N_02, N_03, N_08 and N_08a were calculated in accordance with the Sieverts' Law regression to verify that the measurements throughout the ramping were at a pseudo-steady state thus ensuring the accuracy of the permeance calculations during the temperature ramping. The activation energy was calculated from the regression of the permeance measurements taken during the temperature ramping.

While activation energies of composite pure Pd membranes ranged between 8 – 12 kJ/mol (Guazzone, 2006), the activation energy of a composite Pd membrane with 8 wt% Cu was 16.4 kJ/mol (Guazzone, 2006), which was similar to the activation energies of N_03 and N_08a. The lower activation energy of N_08 was within the range of activation energies measured for pure Pd membranes produced by Guazzone (2006). The unusually high activation energy for N_02 of 24.2 kJ/mol was caused by intermetallic diffusion because the presence of the support metals in the hydrogen selective layer both decreased the H_2 permeance and increased the mass transfer resistance of the H_2 selective layer.

It should be noted that the support and support modification can lower the activation energy by increasing the mass transfer resistance of the support. An activation energy of 16.4 kJ/mol was measured for a ~20 μm pure Pd membrane deposited on a 316L PSS support (Mardilovich et al., 1998) which was closer to the activation energies of the Pd/Cu membranes measured in this work. However, the grade of the support used

by Mardilovich et al. (1998) was 0.5 micron which was much larger than the 0.1 micron grade of the supports used in this work and by Guazzone (2006). Furthermore, the supports used by Guazzone (2006) were graded with Al_2O_3 particles, as were N_08 and N_08a. Therefore, while the activation energy of the Pd membrane made by Mardilovich et al (1998) was closer to the activation energy of a Pd foil (Guazzone, 2006, Ayturk, 2007), the composite Pd membranes presented here and in Guazzone (2006) were lower than that of a Pd foil due to the mass transfer resistance from the support.

5.5.2 Cross sectional analysis

Figure 5-12, Figure 5-13 and Figure 5-14 show the cross sectional micrographs and corresponding line scans of N_02, N_03 and N_08a respectively. A Cu gradient can clearly be seen in all three membranes indicating that a homogeneous alloy had not formed even after the long-term testing at 450 and 500ºC. The Cu as detected by EDX extended 6 μm into the Pd layer of N_02, 5 μm into the Pd layer of N_03 and 4 μm into the Pd layer of N_08a. The Cu gradient of N_02 was sharper than that of N_03 and N_08 due to the higher Cu content of the membrane (see Table 5-2). However, the Cu penetration into the Pd layers had similar lengths and the Cu gradient enabled only part of the Pd/Cu membranes to have a high Cu content in the fcc region. The result of which would be a membrane with a higher permeance than a homogeneous Pd/Cu membrane of the same surface composition in the fcc phase.

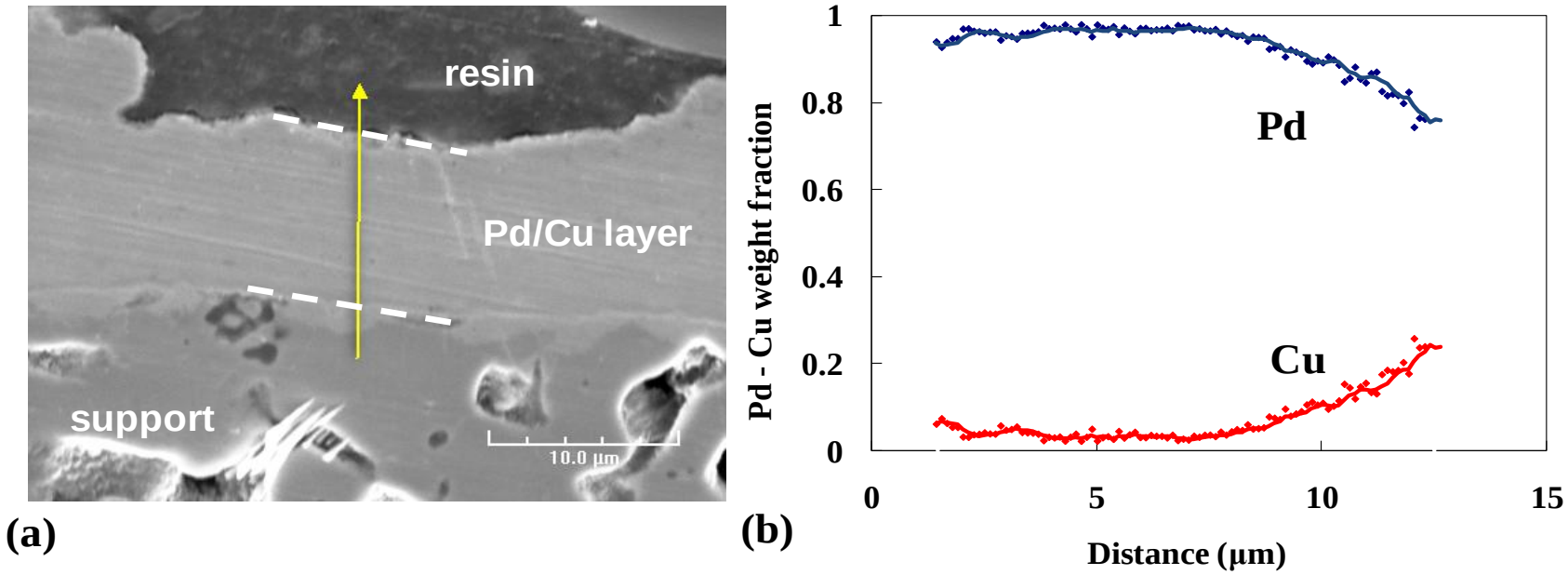

Figure 5-12 The (a) SEI cross sectional micrographs and (b) corresponding EDX line scan of membrane N_02.

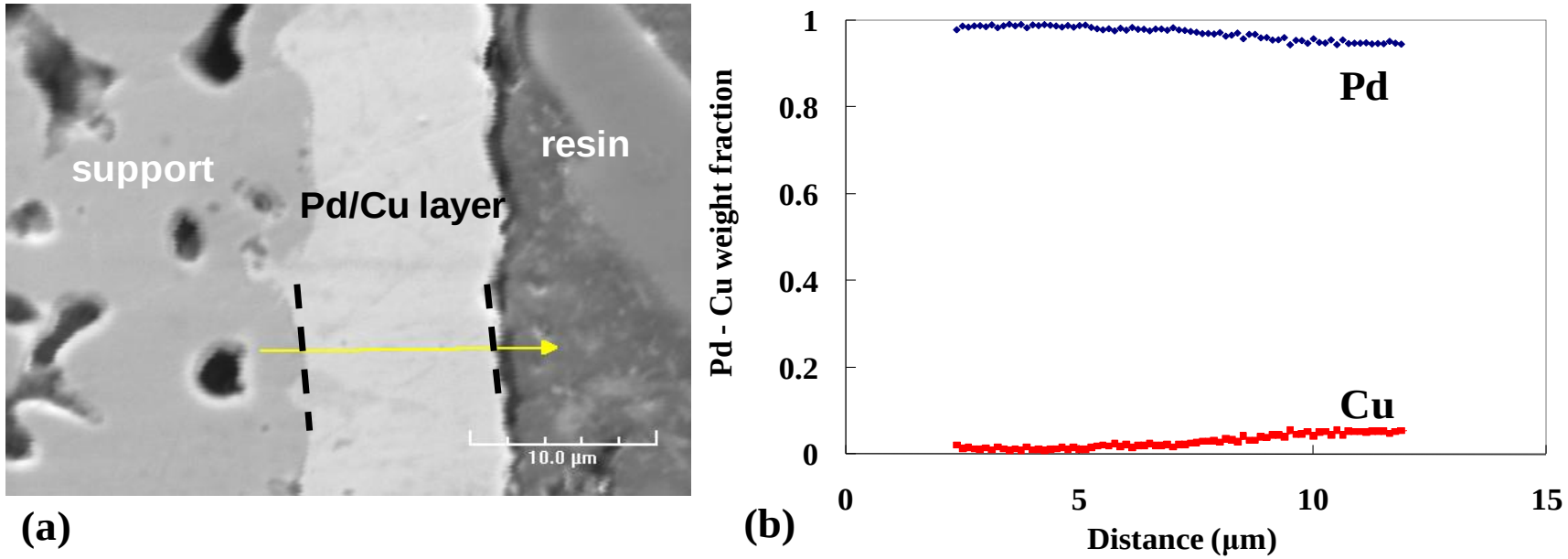

Figure 5-13 The (a) SEI cross sectional micrographs and (b) corresponding EDX line scan of membrane N_03.

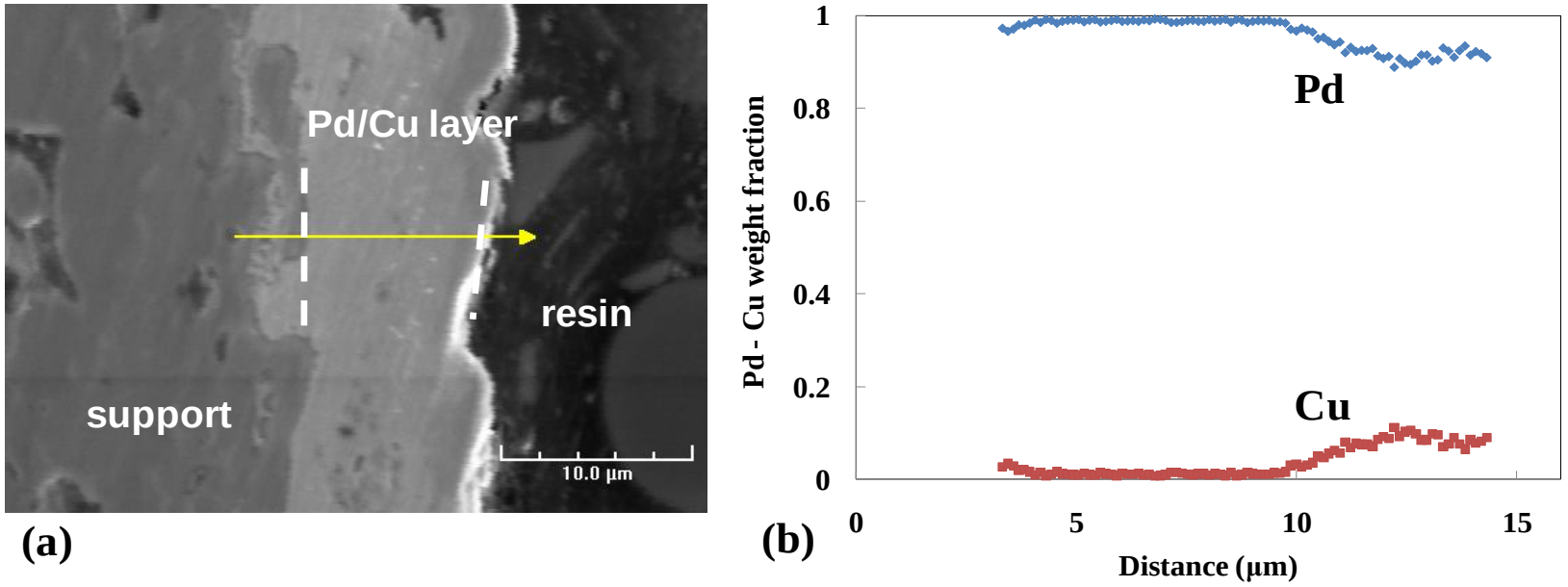

Figure 5-14 The (a) SEI cross sectional micrographs and (b) corresponding EDX line scan of membrane N_08a.

In the same fashion as with the coupon samples in Section 5.4, the effective permeabilities of membranes N_02, N_03 and N_08a were calculated based on the Cu content of their respective cross sections scans in Figure 5-12b, Figure 5-13b and Figure 5-14b. The effective permeabilities are shown in Figure 5-15 as well as the corresponding permeabilities of homogeneous membranes of the same surface composition. As with the results of the coupon samples presented in Figure 5-9, the calculated effective permeability of the membranes was higher than the homogeneous counterparts with the difference increasing with increasing surface Cu content.

Furthermore, the actual permeability of the membranes was calculated from the Sieverts' Law regressions in Figure 5-10 and the gravimetric membrane thicknesses listed in Table 5-2, and plotted with the theoretical effective permeabilities in Figure 5-15. The theoretical effective permeabilities of the membranes were all much higher than the measured permeabilities. The discrepancy could be due to several reasons.

Firstly, the theoretical calculation of the effective permeability was based on the EDX measurement of Cu content. EDX is a semi-quantitative method of analysis and a difference between the measured Cu content and the actual Cu content would impact the actual effective permeability. One would expect that the Cu concentration near the surface would be higher than the overall Cu composition as calculated gravimetrically. However, in the case of N_02 and N_08a, the gravimetric composition was higher than the composition measured near the surface. The discrepancy would be due both to the inaccuracy of the EDX and the gravimetric thickness estimate.

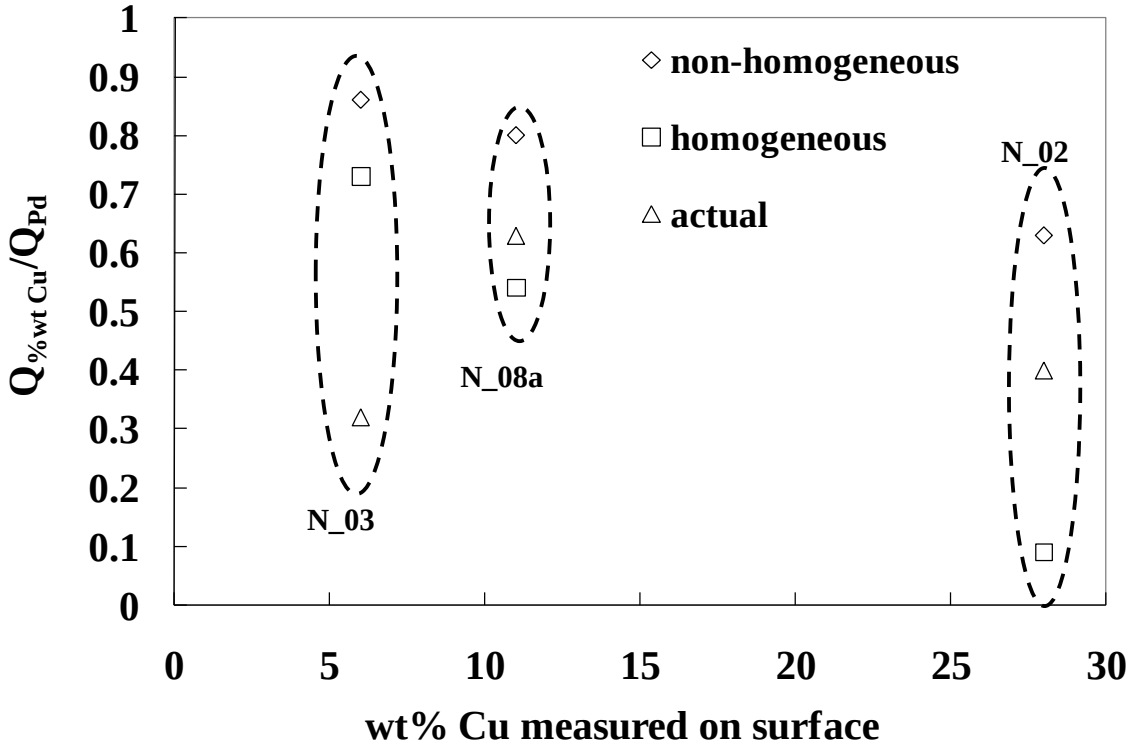

Figure 5-15 Effective permeability as a function of surface Cu content*, theoretical and actual.

* Note, the surface Cu content is not equal to the gravimetric Cu composition listed in Table 5-2.

Also, the permeability of the composite membranes was affected not just by the amount of Cu present in the Pd/Cu layer, but the method of support modification and grading, as was already seen. Thirdly, the regression correlating between permeability and Cu content in Figure 5-1 was taken from data collected at 350°C while the membrane permeabilities in Figure 5-15 were taken from data collected at 450°C. The dependence of permeability on Cu content would be slightly different at the higher temperatures, as seen in Figure 5-2 with the activation energy increase. Lastly, EDX has a resolution of 1 μm and within the near surface it is quite probable that there is a higher Cu concentration than what is able to be detected by the line scan. The higher Cu concentration in the near surface area would decrease the actual permeability of the membrane but would not affect the theoretical calculations accordingly.

Nevertheless, with N_08a and N_02, the actual permeability fell in between the theoretical calculations of the effective permeability of the non-homogeneous layer and the homogeneous layer, showing that the permeability of the homogeneous layer was below the actual permeability. With N_03, the actual permeability fell far below the permeability of the homogeneous layer of the same surface concentration, which was not expected. The effect of a higher Cu concentration in the near surface would be much more apparent in the case of N_03 because the surface concentration measured in the EDX line scan was very low at roughly 6 wt%. The low resolution (0.5 – 1 μm) of the EDX could be the reason that the actual permeability fell far below the permeability of a homogeneous layer of the same surface concentration.

Figure 5-16 shows the measured activation energies of membranes N_02, N_03 and N_08a as a function of the surface Cu content with the activation energy measured

for Pd/Cu foils in the fcc phase, shown in Figure 5-2. Since the Pd/Cu membranes were not homogeneous, there was less mass transfer resistance to hydrogen transport within the Pd/Cu layer and the activation energy of N_02 fell below the curve. It is important to note that one would not expect a composite Pd/Cu membrane to have the same activation energy as a Pd/Cu foil because support modifications and grading are liable to lower the measured activation energy. N_03 and N_08a had activation energies which were closer to the curve, but as explained previously, the inaccuracy in determining the surface Cu content by EDX could make the error in placing the data points on the x-axis rather large, and it is difficult to determine exactly where the membrane activation energies would lie on the plot in Figure 5-16. However, the agreement between the computed curve and the experimental data appears to be reasonable.

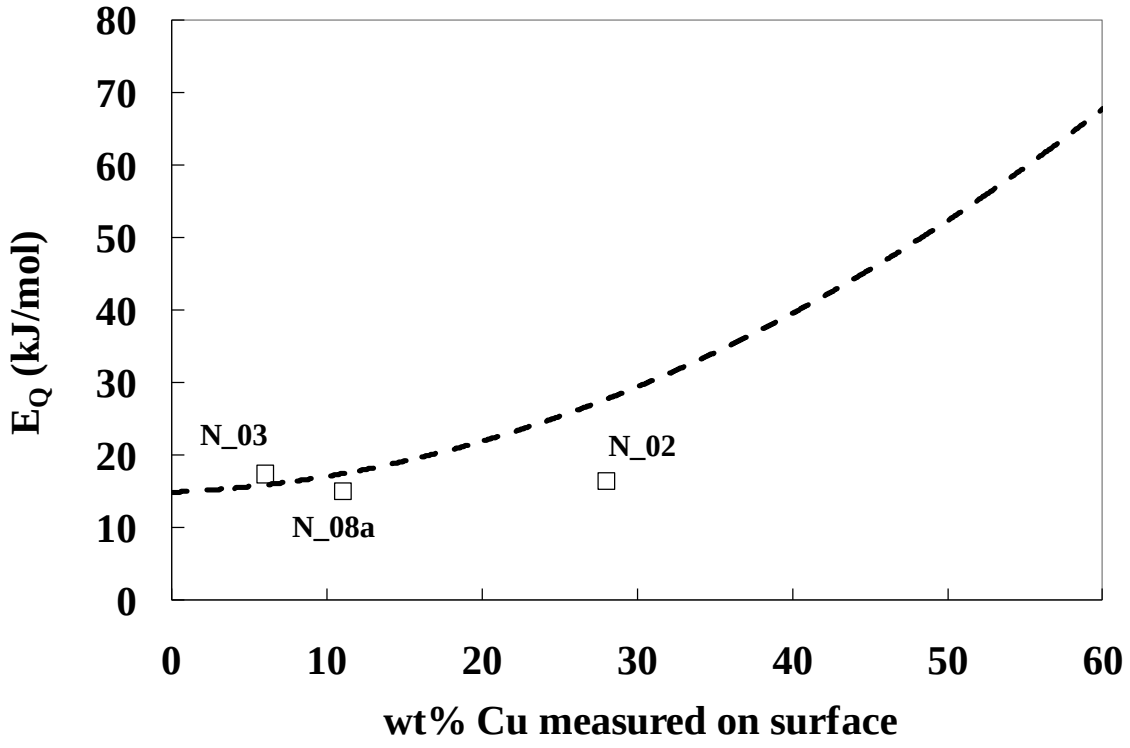

Figure 5-16 Activation energy as a function of surface Cu content, theoretical and actual.

5.6 Conclusions

Fabricating non-homogeneous Pd/Cu alloy membranes in the fcc phase rather than homogeneous fcc Pd/Cu membranes would be cost effective not only due to the fact that non-homogeneous alloys would not require the high temperatures and lengthy annealing times needed to homogenize Pd/Cu bi-layers, but also because the non-homogeneous membrane would have a higher effective permeability to hydrogen. The advantage of the higher effective permeability increased with increasing surface Cu concentration while still in the fcc alloy phase for sulfur resistance. Furthermore, the performance of the non-homogeneous Pd/Cu membranes would exceed that of the homogeneous Pd/Cu membranes of the same surface composition, without sacrificing sulfur tolerance for permeance.

6. Sub-micron Cu and Pd layers for a top surface fcc alloy*

6.1 Introduction

Homogeneous Pd/Cu membranes in the fcc phase all perform at a fraction of the potential permeance of their pure Pd counterparts (Thoen et al., 2006, Zhang et al., 2008, Roa et al., 2001, Guazone, 2006). In order to lessen the impact of alloying Pd with Cu on the hydrogen permeance while still retaining the sulfur resistance, Pd/Cu membranes with an fcc alloy only on the top layer have been fabricated and characterized by plating and annealing the bi-layers of Pd and Cu, as seen in Chapter 5. It is anticipated that further reducing the Cu content in the top layer would result in an even higher hydrogen permeance.

In addition, the HT-XRD studies shown in Chapter 4 yielded that very long annealing times in H_2 were necessary to produce the fcc alloy on the surface and for the less resistant bcc phase to disappear from the Pd/Cu bi-layers. Less lengthy annealing times were achieved at temperatures as high as 600ºC but the exposure to such high temperatures would be damaging to the membrane selectivity, even for short time periods (Guazzone and Ma, 2008).

The main objective of this chapter was to study the effect of stirring on the electroless deposition of Cu and the galvanic displacement of Cu by Pd with the purpose

* This chapter has been submitted to the Journal of Membrane Science.

Pomerantz, N. and Ma, Y.H. "Novel method for producing high H_2 permeance Pd membranes with a thin layer of the sulfur tolerant Pd/Cu fcc phase." *Journal of Membrane Science*, Submitted.

of depositing uniform sub-micron layers on the surface of dense Pd membranes for enhanced sulfur tolerance. Furthermore, the resulting Pd/Cu/Pd tri-layer would require lower annealing times and temperatures than Pd/Cu bi-layers to form the fcc phase. The result of the uniform sub-micron layer deposition would be a surface fcc Pd/Cu alloy on a Pd membrane that would not sustain the loss in permeance observed with Pd/Cu membranes in the fcc phase.

6.2 Experimental

The coupons used in this study were cut to retain a plating bath volume/plated area ratio of 3.9 – 4.3 cm. The coupons for Cu plating had dimensions of 1 cm x 1 cm x 0.1 cm and the coupons for the Pd displacement had dimensions of 5 cm x 1 cm x 0.1 cm. The Pd displacement bath was of the same composition as the $PdCl_2$ activation solution and is described in Table 3-3. The components of the standard and dilute Cu baths are listed in Table 6-1. The compositions of the plating and displacement solutions were determined by atomic absorption spectroscopy, as described in Section 3.3.4.

Table 6-1 Cu plating bath compositions and conditions.

	standard Cu bath	dilute Cu bath
$CuSO_4 \cdot 5H_2O$ (g/l)	25	2.5
$Na_2EDTA \cdot 2H_2O$ (g/l)	47.5	4.75
H_2CO (37 %) (ml/l)	25	2.5
EDA (ppm)	112	11.2
$K_4Fe(CN)_6 \cdot 3H_2O$ (ppm)	35	3.5
$(C_2H_5)_2NCS_2Na \cdot 3H_2O$ (ppm)	5	0.5
pH	12.0	12.7
Temperature (°C)	20 - 25	20 - 25

6.3 Results and Discussion

6.3.1 Effect of bath agitation on Cu plating

The standard plating bath used to plate Cu is listed in Table 6-1 and was adapted from Ma et al. (2003). While the standard Cu plating bath had a high plating rate and yielded a relatively uniform deposition morphology, the bath had a high Cu concentration and the deposition rate was unpredictable. For the purpose of plating thin Cu layers on Pd membranes, a more dilute solution was used with one tenth the concentration of the components and an increase in the pH from 12.0 to 12.7 as shown in Table 6-1. In addition, a more dilute solution would reduce the cost of the plating bath and the price of disposing unused chemicals.

Figure 6-1 shows the deposition morphology of oxidized coupons plated with both the standard and dilute Cu baths, neither with bath agitation. The gravimetric thickness estimates of the Cu layers were 1.2 μm for Figure 6-1a and c and 0.9 μm for Figure 6-1b and d. The thicknesses of both layers were similar and as the micrographs show, there was little difference between the morphologies of the two depositions, indeed they appeared nearly identical. As Figure 6-1a and b show, both the standard and dilute Cu plating baths completely covered the oxidized support, both on the surface and inside the pores. The higher magnification in Figure 6-1c and d shows that the cluster size of both Cu deposits were roughly the same, varying between 0.5 – 1 μm in diameter.

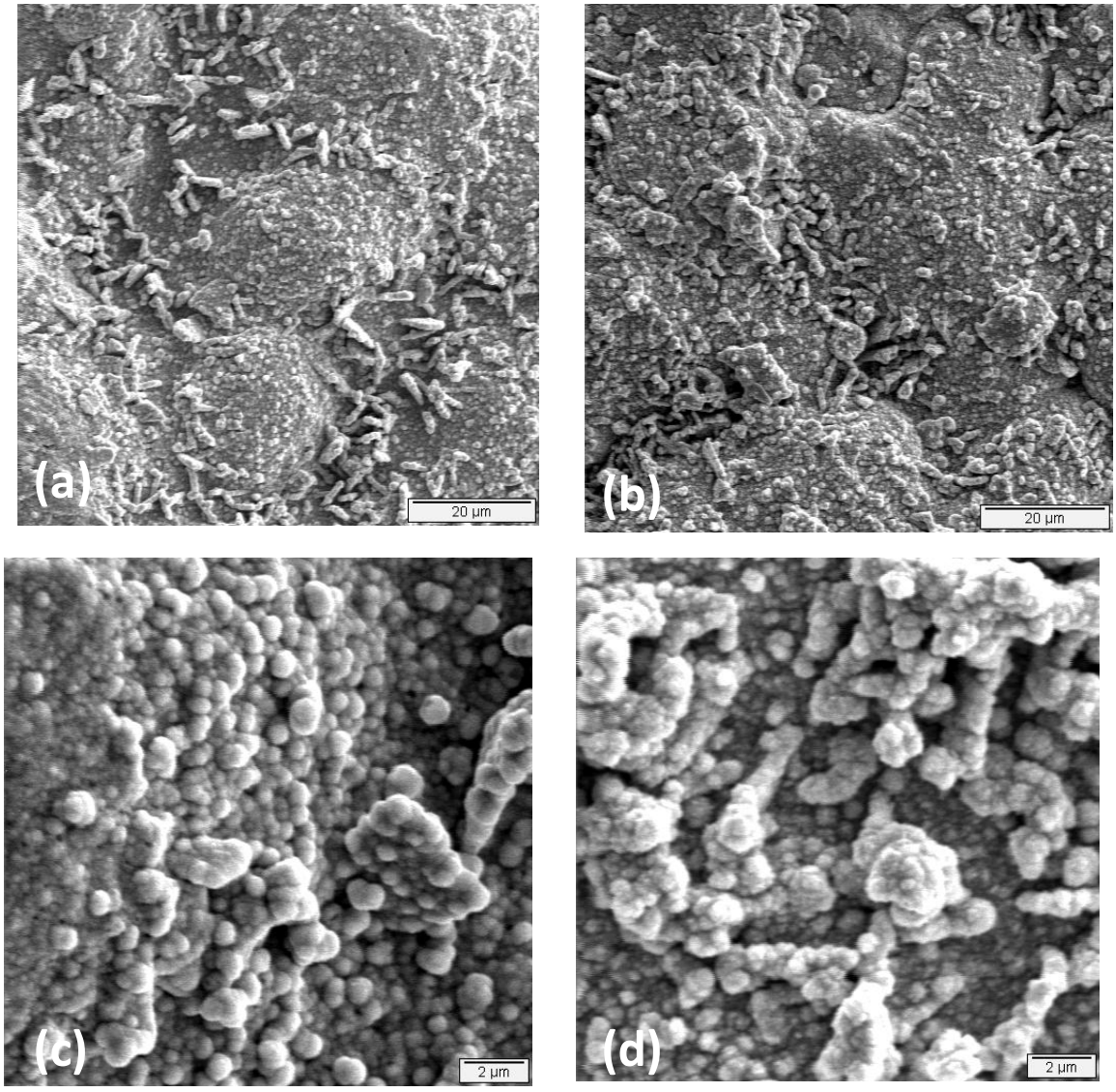

Figure 6-1 SEI surface micrographs at 1 kX of the samples plated with plating bath compositions of (a) 100 mM Cu^{2+} and (b) 10 mM Cu^{2+} and at 5 kX of the samples plated at (c) 100 mM Cu^{2+} and (d) 10 mM Cu^{2+}.

However, the plating rate (estimated by the average gravimetric weight gain of the plated samples) was much higher for the standard Cu bath. The plating rate for the standard Cu bath was roughly 3 μm/h while the plating rate for the dilute Cu bath was roughly 0.5 μm/h.

Figure 6-2a and b show the surface morphology of the Cu deposit from the dilute Cu plating bath at agitation speeds of 200 and 400 rpm respectively. The thickness of each deposit was 1.2 and 1.7 μm respectively. In comparison to the Cu deposit which was plated without bath agitation in Figure 6-1, the thin layers resulting from agitated plating baths were much more uniform consisting of very fine, evenly dispersed clusters. Plating without agitation resulted in clusters which were both large and small, yielding a less uniform surface. The Cu layer thickness of the sample plated with the unagitated bath would vary much more than with the agitated bath.

Figure 6-2c and d show that the cluster size was reduced to the order of hundreds of nanometers with the agitation speed at 200 rpm, and further agitation at 400 rpm reduced the cluster size even further. Stirring the plating bath reduced the mass transfer resistance caused by the diffusion of the Cu ions to the plated surface, allowing more Cu nuclei to attach to the oxidized PSS and finer grains to form. Similar results were seen with agitated plating baths of Pd and Ag (Ayturk and Ma, 2009). Increasing the agitation speed to higher than 400 rpm yielded no change in the cluster size or deposit morphology.

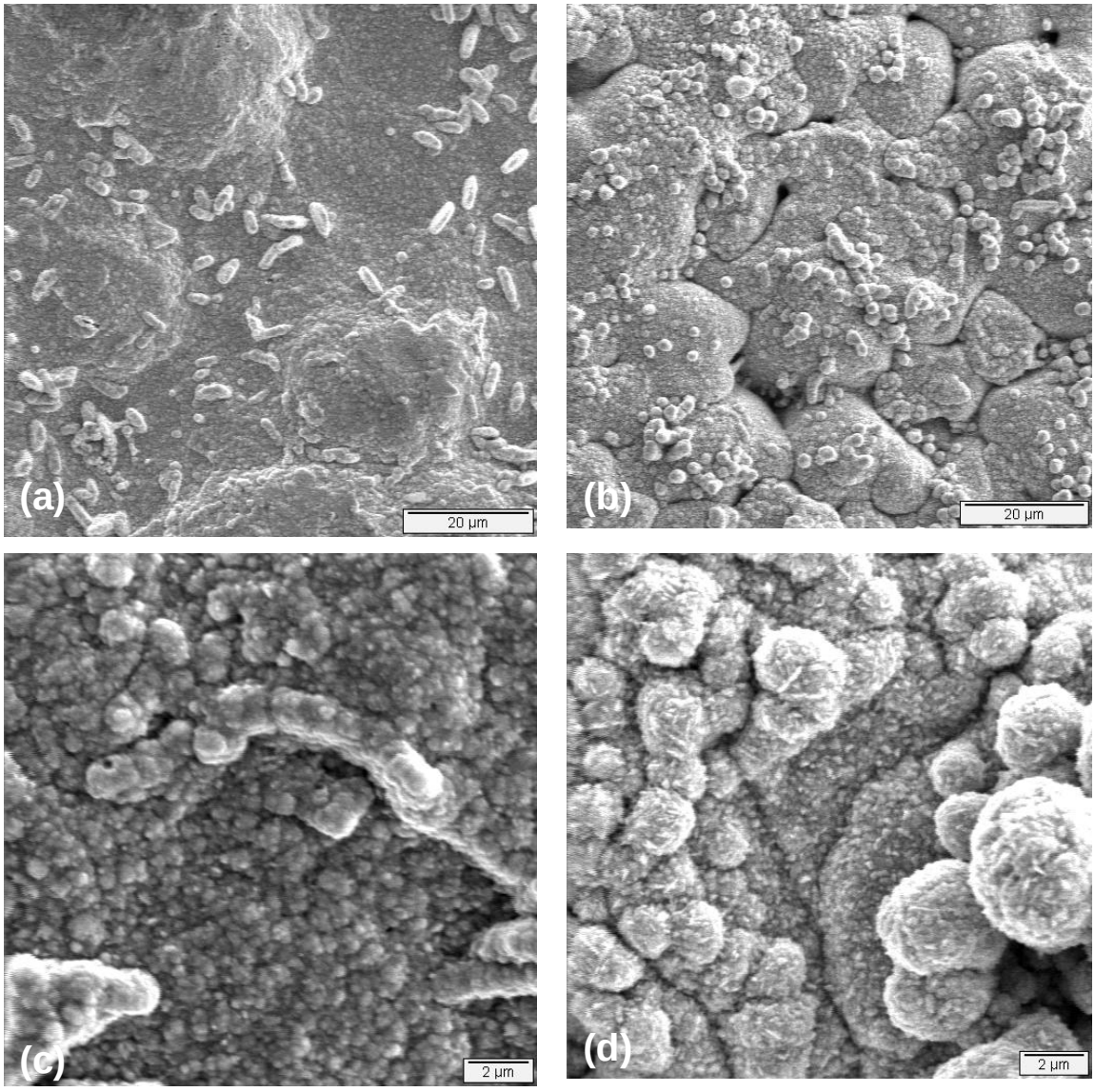

Figure 6-2 SEI surface micrographs at 1 kX of the samples plated with the 10 mM Cu^{2+} plating bath with an agitation speed of (a) 200 rpm and (b) 400 rpm and at 5 kX at (c) 200 rpm and (d) 400 rpm.

It should be noted that at agitation speeds of 400 rpm and above, the activation layer was dried for two hours at 120°C prior to plating. While it was possible to plate directly after activation at agitation speeds below 400 rpm, the higher agitation speeds appeared to have removed the activation layer from the coupons preventing the plating reaction from initiating, even after 60 minutes. Furthermore, the samples plated with stirring rates of 400 rpm or higher were first plated without stirring for 30 seconds before increasing the stirring rate to 200 rpm for 30 seconds and then continuing at speeds of 400 rpm or higher.

Using a Cu plating bath diluted to one tenth (10 mM) of the standard concentration (100 mM) yielded a better utilization of the plating bath. No reduction in Cu^{2+} ion concentration was observed in the 100 mM Cu plating bath after two hours of plating and subsequently no increase in conversion, due to the small amount of Cu being depleted relative to the overall concentration of Cu in the bath.

Figure 6-3 and Figure 6-4 show the Cu^{2+} ion concentration (C) and conversion (x, defined in Equation 6.1 where C_0 is the initial Cu^{2+} ion concentration), respectively, of the 10 mM plating bath as a function of time and agitation speed.

$$x = \frac{C_0 - C}{C_0} \tag{6.1}$$

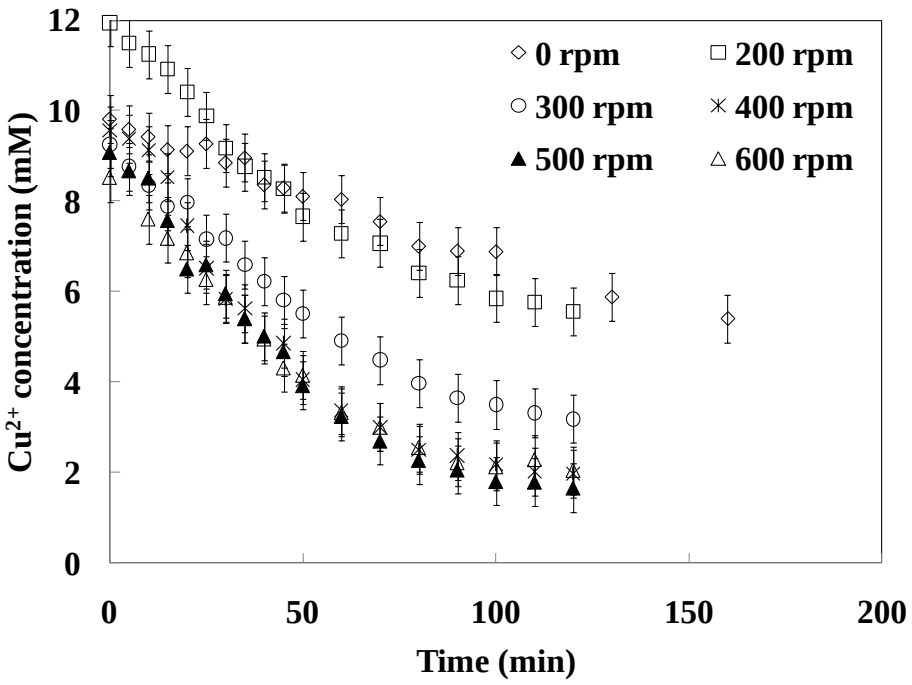

Figure 6-3 The Cu^{2+} ion concentration in the plating bath as a function of time at different agitation speeds.

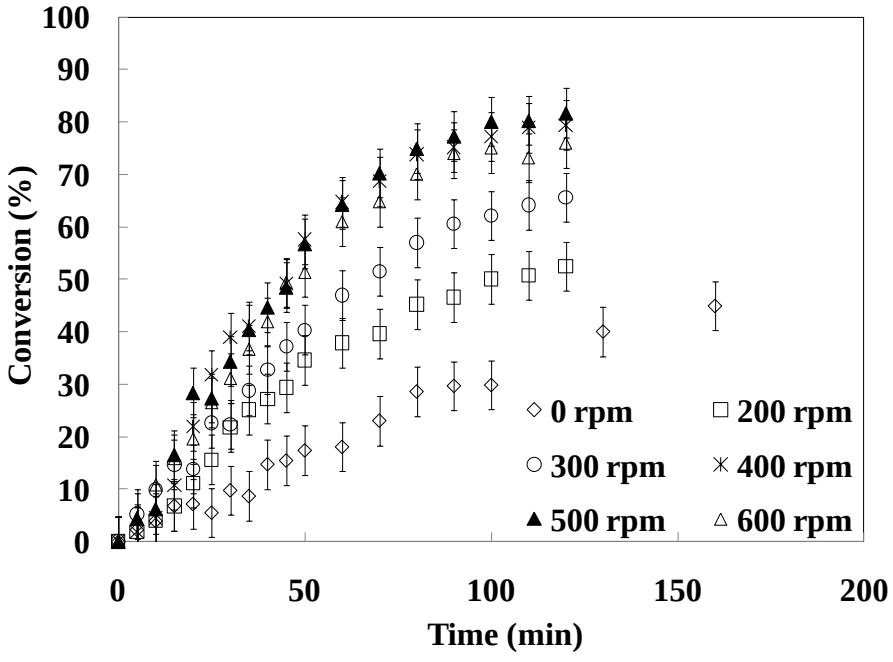

Figure 6-4 Conversion as a function of time at different Cu plating bath agitation speeds.

As the Cu deposited on the samples, the Cu^{2+} ion concentration in the bath was depleted. For the first hour of plating, the decrease in Cu^{2+} ion concentration and the increase in conversion were linear for all agitation speeds. During the second hour, the rate of decrease in Cu^{2+} ion concentration and increase in conversion slowed down in the unagitated bath, but the Cu continued to deposit on the sample. For the agitated baths, both rates decreased significantly during the second hour until little change could be seen after 100 minutes.

Figure 6-3 showed that the depletion of Cu^{2+} ions in the plating bath increased with increasing agitation speed. The exception was with the speed of 200 rpm which resulted in a final Cu^{2+} ion concentration of 6 mM after two hours. The final concentration of the 200 rpm bath was higher than that of the unagitated bath due to the fact that the initial Cu^{2+} ion concentration of the 200 rpm bath was higher than that of the unagitated bath. When expressed in terms of conversion, which took the initial Cu^{2+} ion concentration into account, the conversion of the bath stirred at 200 rpm was higher than that of the unagitated bath after two hours, at 50% and 40% respectively. The conversion after two hours increased to 60% at 300 rpm and to roughly 80% at 400, 500 and 600 rpm, showing a more efficient use of the plating bath.

Figure 6-5 shows the linear regressions for the first 60 minutes of the Cu plating. The slope of the regressions was used as the linear plating rate, shown in Figure 6-6. The unagitated bath yielded a plating rate of roughly 0.5 μm/h. The plating rate increased with agitation speed until 400 rpm at roughly 1.75 μm/h. No appreciable change was seen in the plating rate upon further increase of the bath agitation speed. The increase in the plating rate seen at lower agitation speeds was due to the bath agitation lessening the

effects of the diffusional mass transfer resistance within the plating solution. At 400 rpm the effect of diffusion was minimized by stirring and the plating rates observed at 400, 500 and 600 rpm approached the actual rate of reaction of the Cu deposition. The uniform deposition observed coupled with the high plating rate make a bath agitation rate of 400 rpm the optimum condition for plating Cu on dense Pd membranes.

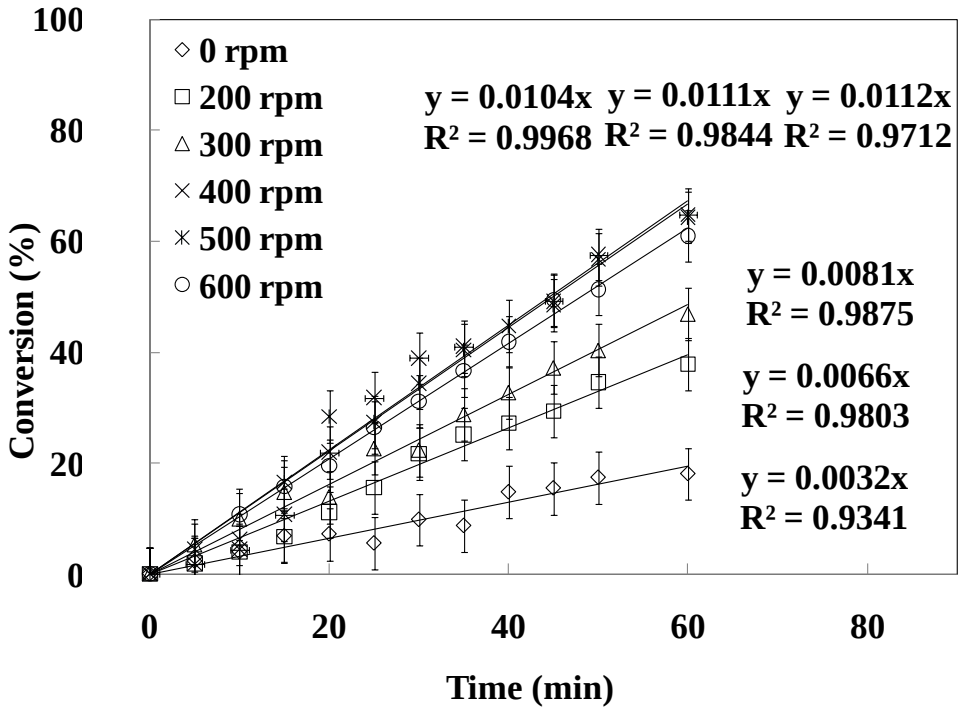

Figure 6-5 Linear regressions for the first 60 minutes of Cu plating.

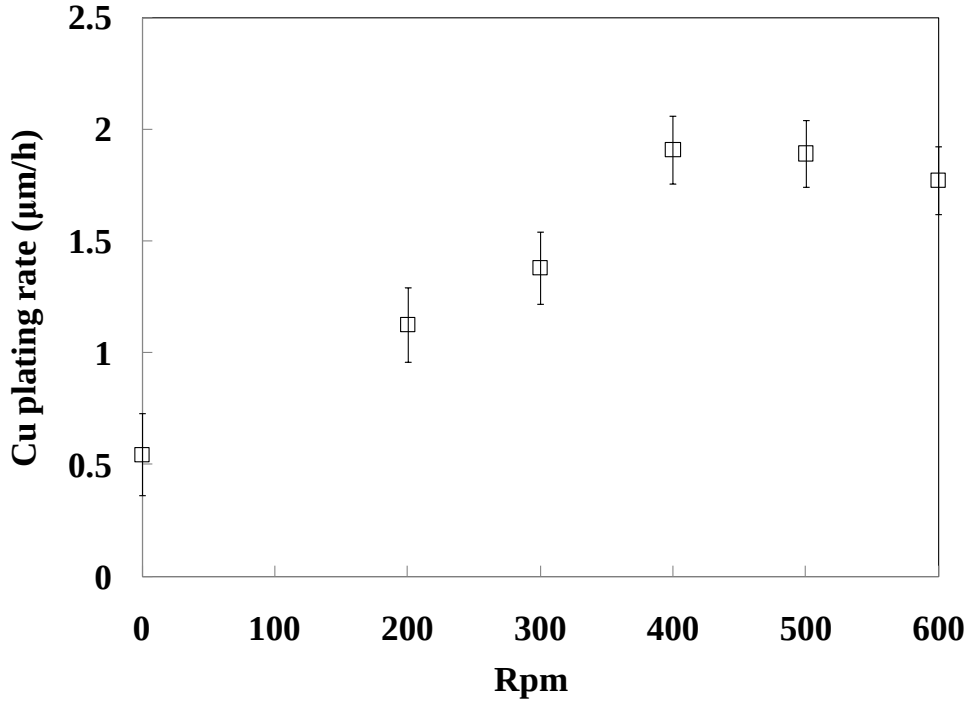

Figure 6-6 Cu plating rate as a function of the plating bath agitation speed.

6.3.2 Effect of bath agitation on the Pd displacement of Cu

Figure 6-7 shows the surface morphology of samples which were plated with roughly 1.5 μm of Cu and then deposited with Pd through the galvanic displacement of Cu at varying bath agitation speeds for 1.5 hours. The morphology of the surface resulting from the unagitated bath yielded cluster sizes of roughly 1 – 3 μm in diameter. Increasing the agitation speed to 200 rpm resulted in no change in cluster size, but increasing the speed to 400 and 600 rpm showed cluster sizes which were much smaller at less than 1 μm in diameter.

In addition, the Pd deposit was much more uniform at 400 and 600 rpm, covering most of the surface with the same amount of Pd whereas the growth of the deposit in Figure 6-7a and b was largely in the vertical direction from the plating surface with clusters forming on top of one another making for a less uniform surface coverage. As with the results from Section 6.3.1, the bath agitation speeds of 400 rpm and above minimized the effect of diffusional mass transfer resistance within the solution, allowing many more sites for Pd displacement to occur, yielding an evenly dispersed layer of clusters smaller in size than the clusters resulting from the unagitated bath and the bath agitated at a rate of 200 rpm.

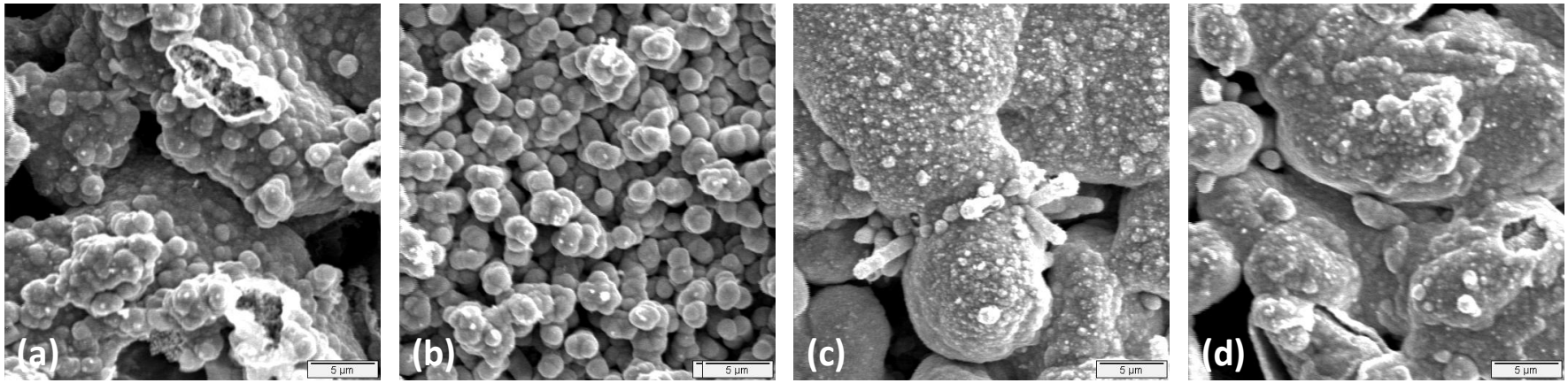

Figure 6-7 SEI surface micrographs at 3 kX of Cu samples displaced by Pd with (a) an unagitated bath and agitation speeds of (b) 200 rpm, (c) 400 rpm and (d) 600 rpm.

Figure 6-8 shows the concentration of the Pd^{2+} ions in the displacement bath as a function of time. The Pd^{2+} ion concentration of the unagitated bath decreased linearly, but even after two hours the reaction showed no signs of slowing down as only a small portion of the Pd^{2+} ions were depleted. However, when the bath was agitated at 200, 400 and 600 rpm the Pd^{2+} ion concentration decreased much more rapidly. The decrease was linear for the first 30 minutes and proceeded to slow down until after two hours when the reaction had completed. More Pd had deposited on the samples immersed in the agitated bath, as observed with the EDX scans performed on the sample surfaces seen in Figure 6-7. Between 45 – 50 wt% Pd was observed on the surface of the samples with bath agitation speeds of 200, 400 and 600 rpm. Only 20 wt% Pd was detected on the sample from the unagitated bath.

Figure 6-9 shows the conversion (defined in Equation 6.1) as a function of time for the displacement baths. Again, the first 30 minutes of the reaction had a linear rate for the agitated baths but the unagitated bath proceeded linearly almost for the entire duration of the experiment. While the unagitated bath reached a conversion of only 25% after two hours, the agitated baths all reached conversions of roughly 80% after one hour due to the minimization of the diffusional mass transfer resistance within the solution resulting in an increased deposition rate.

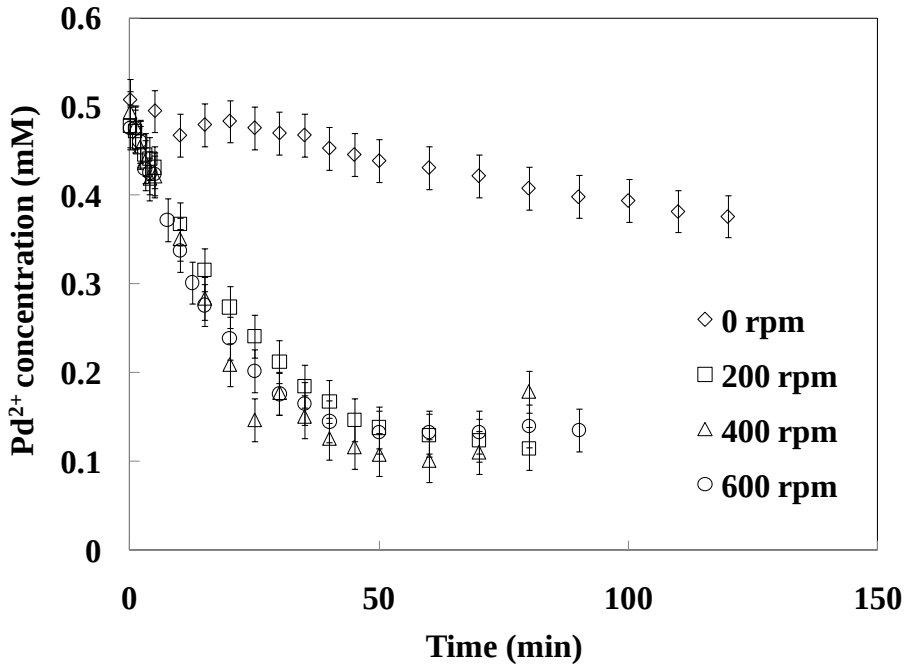

Figure 6-8 The Pd^{2+} ion concentration in the displacement bath as a function of time at different agitation speeds.

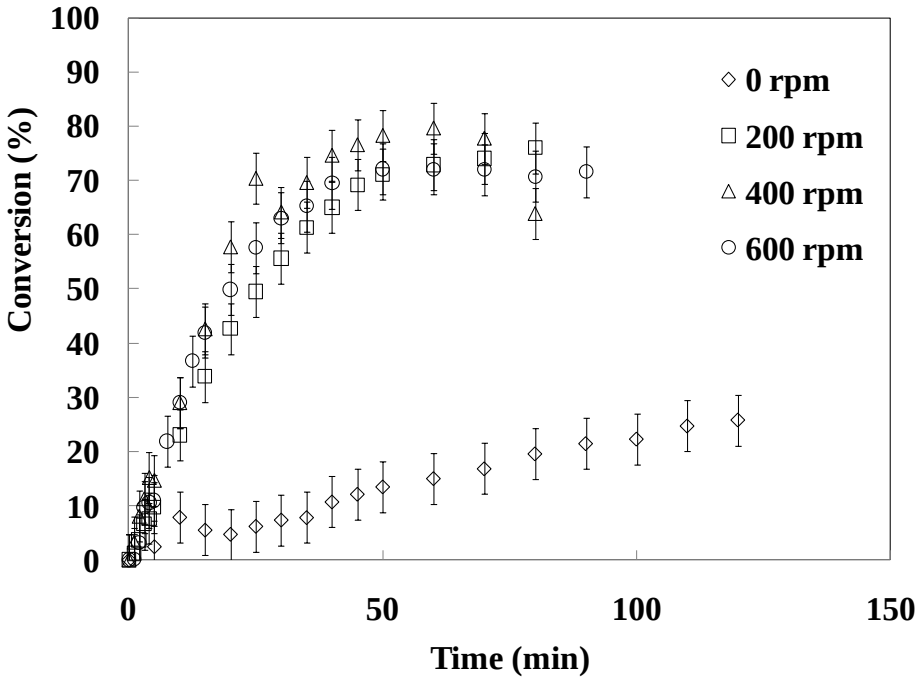

Figure 6-9 Conversion as a function of time at different displacement bath agitation speeds.

Figure 6-10 shows the regressions from the linear portions of the reaction shown in Figure 6-9. Figure 6-11 shows the linear deposition rate calculated from Figure 6-10 as a function of agitation speed. While the deposition rate of the Pd was very slow with the unagitated bath, stirring increased the rate dramatically at 200 rpm. Increasing the agitation rate to 400 rpm resulted in a slight increase in deposition rate but no further increase in the deposition rate was observed at 600 rpm showing that the deposition rate observed at 400 and 600 rpm were essentially equal to the reaction rate.

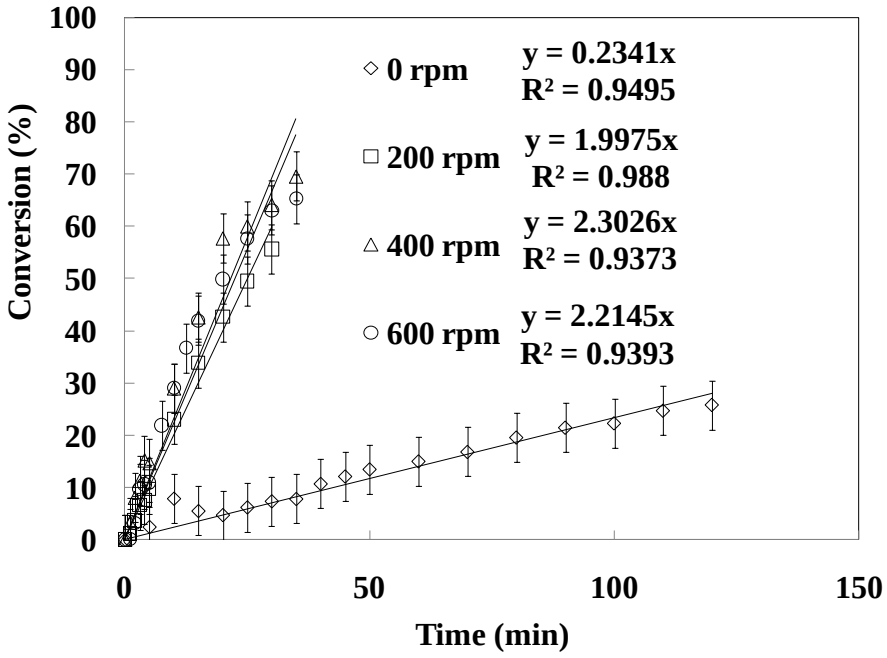

Figure 6-10 Linear regressions for the linear portions of the reactions for the Pd displacement of Cu.

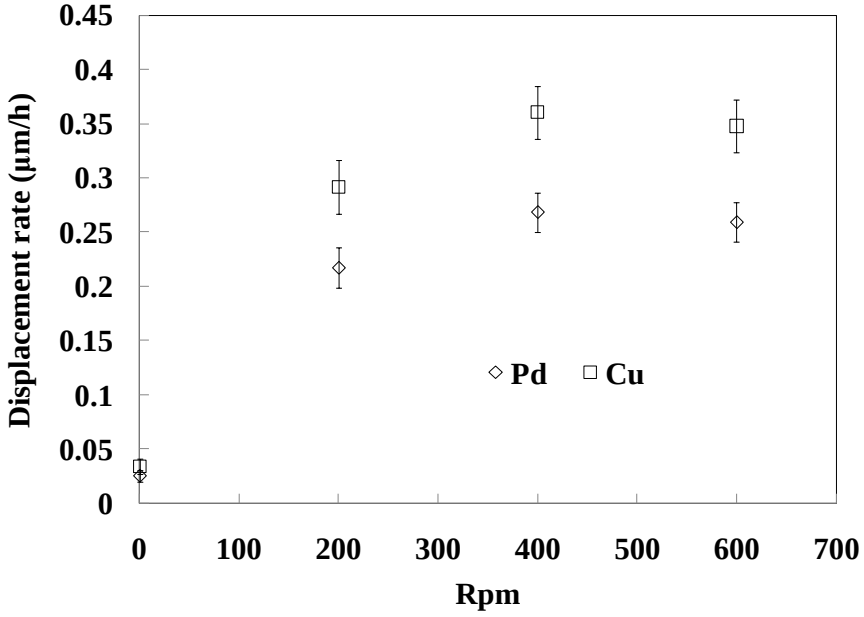

Figure 6-11 The displacement rate of Cu and the rate of Pd deposition as a function of the agitation speed, taken from the linear portion of the reaction.

6.3.3 Kinetics

In accordance with the results of Section 6.3.1, the kinetics of the dilute Cu plating bath were calculated from the data measured at 400, 500 and 600 rpm after the effects of the diffusional mass transfer resistance within the solution were minimized through bath agitation. The reaction for the reduction of the Cu^{2+} ions by formaldehyde is shown in Equation 6.2 and the corresponding empirical rate equation is shown in Equation 6.3 where r is the reaction rate, k is the rate constant and α, β, γ and δ are the reaction orders for the respective species.

$$Cu^{2+} + 2H_2CO + 4OH^- \rightarrow Cu^0 + H_2 + 2H_2O + 2HCOO^- \quad (6.2)$$

$$r = -\frac{d\left[Cu^{2+}\right]}{dt} = k\left[Cu^{2+}\right]^{\alpha}\left[H_2CO\right]^{\beta}\left[OH^-\right]^{\gamma}\left[EDTA^{4-}\right]^{\delta} \quad (6.3)$$

To ease the estimation of the reaction parameters, the concentration of OH^- ions in the solution was assumed to be constant. The presence of Na_2EDTA buffered the plating bath enabling the pH of the solution to remain essentially constant as the OH^- ions reacted, and so the OH^- concentration was assumed to be constant. Furthermore, while the ligand of the complexing agent is generally included in Cu plating reaction rate equations, some studies found the reaction order for the $EDTA^{4-}$ ions to be less than 0.02 (Molenaar et al., 1974), or equal to -0.04 (Donahue et al., 1980), while others found rate equations independent of $EDTA^{4-}$ concentration (Dumesic et al., 1974, Donahue and Shippey, 1973). Therefore, δ was assumed to be zero.

To further reduce the number of parameters to be estimated, an excess of formaldehyde was used in one of the experiments, with three times the amount used in the dilute Cu plating solution in Table 6-1. Assuming that the concentration of formaldehyde remains relatively constant, Equation 6.4 can be used to calculate the reaction order of the Cu^{2+} ions while the rate constant included both the concentration of OH^- and H_2CO, shown in Equation 6.5.

$$r = -\frac{d\left[Cu^{2+}\right]}{dt} = k''\left[Cu^{2+}\right]^{\alpha} \tag{6.4}$$

$$k'' = k \cdot \left[H_2CO\right]^{\beta}\left[OH^-\right]^{\gamma} \tag{6.5}$$

Integrating Equation 6.4 results in the following where both the new rate constant and reaction order can be calculated through a non-linear regression where x is the conversion as defined in Equation 6.1, for $\alpha \neq 1$:

$$x = 1 - \left[(\alpha - 1)\left[Cu^{2+}\right]_0^{\alpha-1} k'' \cdot t + 1\right]^{\frac{1}{1-\alpha}} \tag{6.6}$$

The value of α as calculated from the non-linear regression of Equation 6.6 from the experiment performed with an excess of H_2CO is shown in Table 6-2. The value of k" was calculated to be 0.01 $1/(mM^{0.6}*min)$. The fit of the regression with the experimental data is shown in Figure 6-12. As seen in Figure 6-12, the regression was a satisfactory fit to the experimental data.

Table 6-2 Summary of the reaction rate parameters for Cu plating.

Parameter	Value
$k'_{Cu,T=25°C}$ ($1/mM^{0.9}*min$)	1.15
α	1.6
β	-0.3

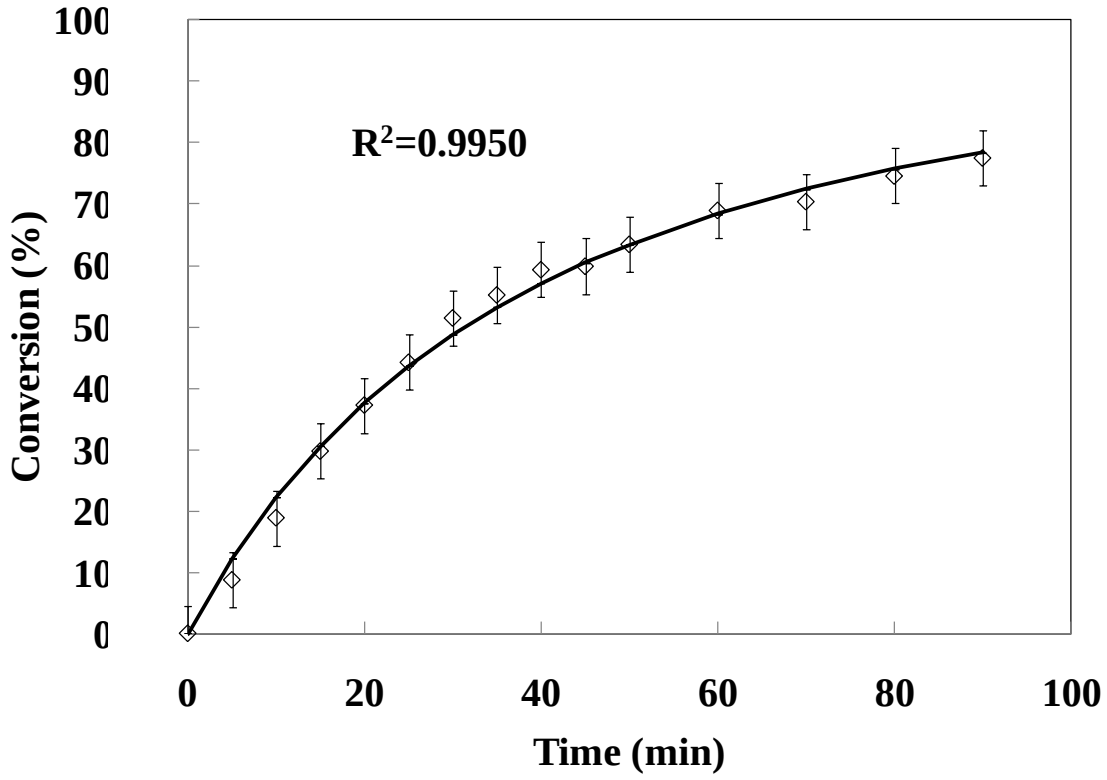

Figure 6-12 Non-linear regression for the Cu plating bath with 100 mM of H_2CO.

For Cu plating conditions without an excess of H_2CO, the initial linear reaction rates from the first 60 minutes were used to determine β and the rate constant, k', as shown in Equation 6.7 which was then linearized, as shown in Equation 6.8.

$$r = -\left.\frac{d\left[Cu^{2+}\right]}{dt}\right|_0 = k'\left[Cu^{2+}\right]^{\alpha}\left[H_2CO\right]^{\beta} \tag{6.7}$$

$$-\alpha \ln\left[Cu^{2+}\right] = \ln k' - \ln r\big|_0 + \beta \ln\left[H_2CO\right] \tag{6.8}$$

Figure 6-13 shows the regression performed for the reaction order of the H_2CO and rate constant from Equation 6.8. Again, the linear regression showed a satisfactory fit to the experimental data the values of β and the rate constant are listed in Table 6-2.

Donahue and Shippey (1973) observed a reaction order for the Cu^{2+} ions of 1.7, which was similar to the value of the reaction order calculated in this work. However, previous research found that the Cu^{2+} ion reaction order was 0.78 (Molenaar et al., 1974) and 0.43 (Donahue et al., 1980). The reaction order for H_2CO given from the work of Donahue and Shippey (1973) was most similar to the value of β calculated here at -0.23, but others observed values of 0.13 (Molenaar et al., 1974) and 0.16 (Donahue et al., 1980). While there has been work which studied the effect of bath agitation on Cu plating kinetics (Dumesic et al., 1974, Donahue, 1980, Donahue, 1981), Dumesic et al. (1974) determined the reaction orders of Cu^{2+} and H_2CO to be 0.37 and 1, respectively, after minimizing mass transfer effects.

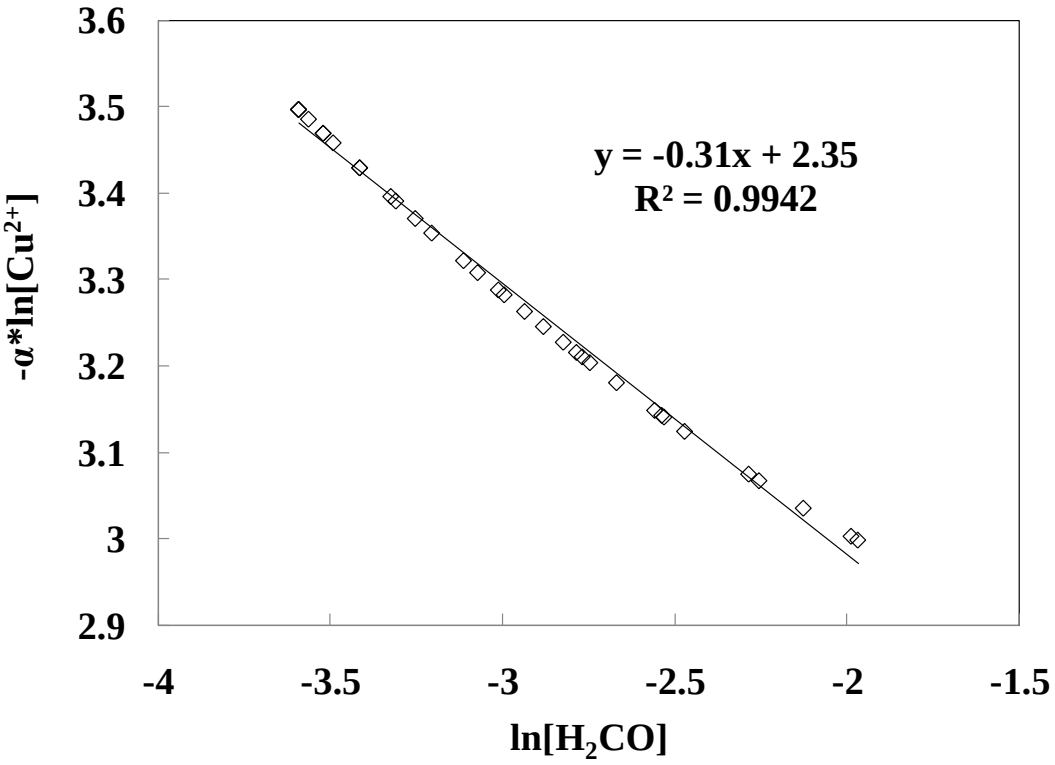

Figure 6-13 Regression for the initial rate of the Cu plating bath at 400, 500 and 600 rpm.

Even though the reaction orders calculated by Donahue and Shippey (1973) were most similar to those observed here, the reaction orders found by Donahue and Shippey were of the cathodic reaction, while the work of Molenaar et al. (1974), Donahue et al. (1980), and Dumesic et al. (1974) calculated the constants according to the same empirical rate law used in this work Equation 6.2.

There did not appear to be a consensus in the literature with regards to the reaction orders of the rate equation. Therefore, an explanation for the similar orders obtained with the empirical cathodic reaction parameters rather than the overall empirical rate equation cannot be adequately given. Most authors ascribed the differences in reaction parameters to mass transport effects within the solution, catalytic activity of the surface, the time frame of the measurements and the method of obtaining reaction rate parameters.

Furthermore, in the previous work mentioned, only the reactants represented in Equation 6.3 were used in the plating solutions. In this work, the plating solutions had additional components used as stabilizers and grain refiners (EDA, $K_4Fe(CN)_6 \cdot 3H_2O$, $(C_2H_5)_2NCS_2Na \cdot 3H_2O$) shown in Table 6-1. Consequently, while the reaction rate parameters calculated in this work fell into the range seen in the literature, the parameters should only be applied to systems with similar substrates and plating bath additives, and where the effects of the diffusional mass transfer have been minimized.

Figure 6-14 shows the Cu thickness as a function of time taken experimentally and as predicted from the calculated reaction rate parameters. Since the calculation of β assumed that the initial rate was constant, the model did not adequately describe the

reaction after 60 minutes, however the model was accurate during the initial linear period.

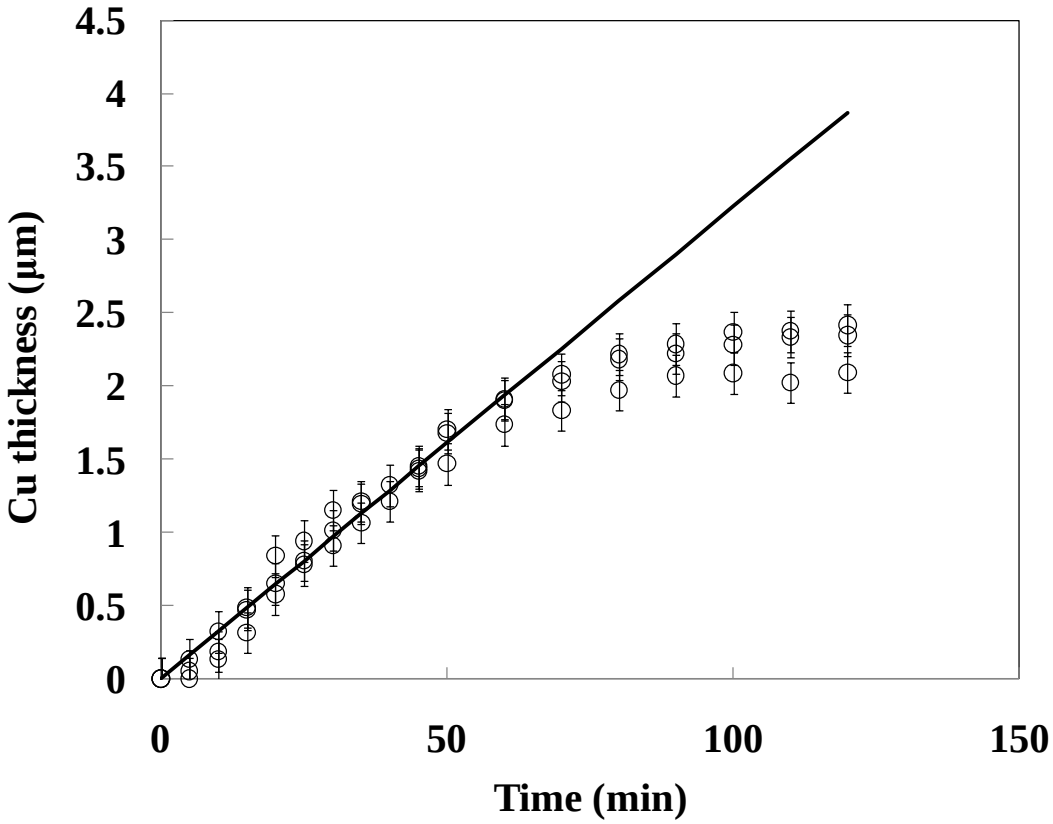

Figure 6-14 Cu thickness as a function of time for the dilute Cu plating bath. The line represents the data predicted from the model.

In accordance with the results of Section 6.3.2, the kinetics of the Pd galvanic displacement reaction were calculated from the data measured at 400 and 600 rpm after the effects of the diffusional mass transfer resistance within the solution were minimized through bath agitation. The complete reaction for the galvanic displacement of Cu by Pd^{2+} is shown in Equation 6.9.

$$\begin{aligned} Pd^{2+} + 2e^- &\rightarrow Pd^0 \quad E^0 = 0.951\,V \\ +\,Cu^{2+} + 2e^- &\rightarrow Cu^0 \quad E^0 = 0.3419\,V \\ \hline Pd^{2+} + Cu^0 &\rightarrow Pd^0 + Cu^{2+} \quad E^0 = 0.6091\,V \end{aligned} \tag{6.9}$$

The empirical rate equation for the Pd displacement of Cu is described as follows:

$$r = -\frac{d\left[Pd^{2+}\right]}{dt} = k\left[Pd^{2+}\right]^{\alpha} \tag{6.10}$$

Assuming that the displacement is a first order reaction and that α is equal to one yields Equation 6.11 where x is the conversion as defined by Equation 6.1.

$$x = 1 - \exp(-k \cdot t) \tag{6.11}$$

Figure 6-15 shows the linear regression to find the rate constant for the Pd displacement reaction, assuming a first order reaction. The value for the rate constant at room temperature is listed in Table 6-3. The linear regression appeared to be consistent with the assumption of a first order reaction. Figure 6-16 shows that the fit of the conversion data as a function of time with the first order reaction model was satisfactory

in describing the Pd galvanic displacement of Cu. A better fit could be achieved by allowing both the reaction order and the rate constant to be calculated as with the Cu plating solution in Equation 6.6. Calculating both parameters resulted in a reaction order of 1.3 and a rate constant 0.05 $1/(min*mM^{0.3})$ with an R^2 value of 0.9901. However, since the R^2 value of the regression in Figure 6-15 was close enough to one, there was no justification for the use of a second parameter in the regression and a first order model could be assumed.

Table 6-3 Summary of the reaction rate parameters for the Pd galvanic displacement of Cu.

Parameter	Value
$k_{Pd,T=25°C}$ (1/min)	0.031
α	1

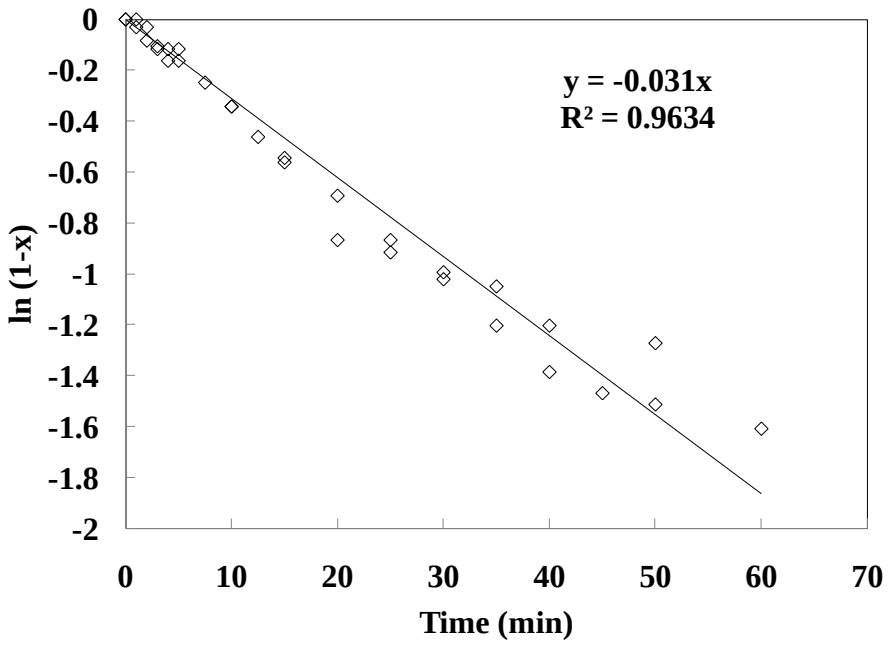

Figure 6-15 Linear regression of the Pd displacement of Cu for a first order reaction.

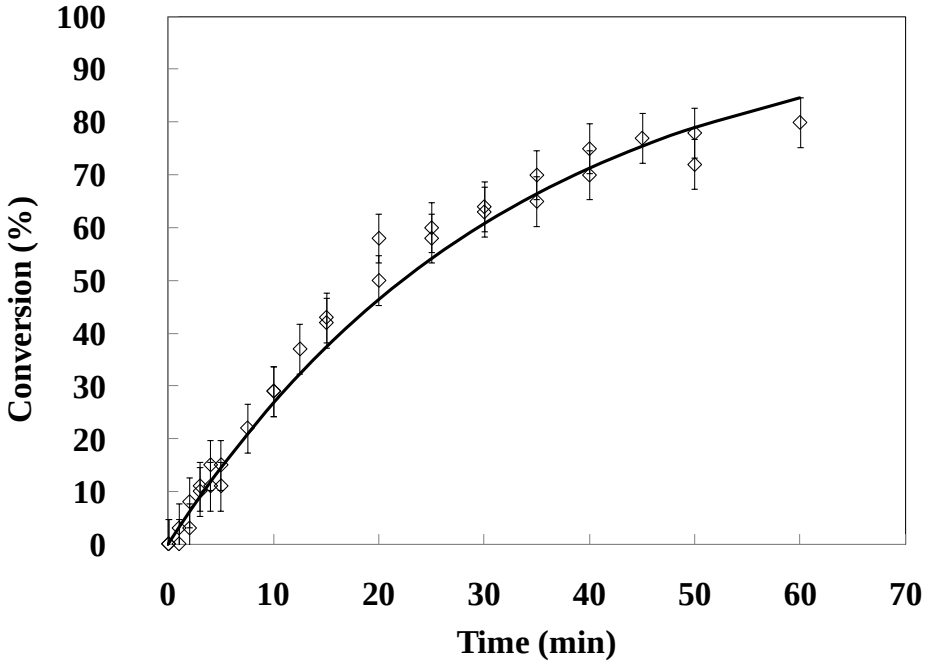

Figure 6-16 Experimental data taken at agitation speeds of 400 and 600 rpm. The solid line represents the calculated values from the first order reaction model.

Figure 6-17 shows the thickness of the Pd and Cu deposits as a function of time in comparison to the thicknesses predicted from the first order reaction model. It should be noted that while it was possible to estimate how much Cu was plated through weight gain, it was very difficult to estimate the amount of Pd deposited through the galvanic displacement on such small samples by the gravimetric method, and consequently, the amount of Cu displaced. The use of AAS to monitor Pd^{2+} ion concentration enabled both the deposition rate of Pd and the displacement rate of Cu to be estimated in order to determine the respective thicknesses as a function of time. As with the conversion data in Figure 6-16, the first order reaction model predicted the thickness of the Pd deposit and displaced Cu reasonably well.

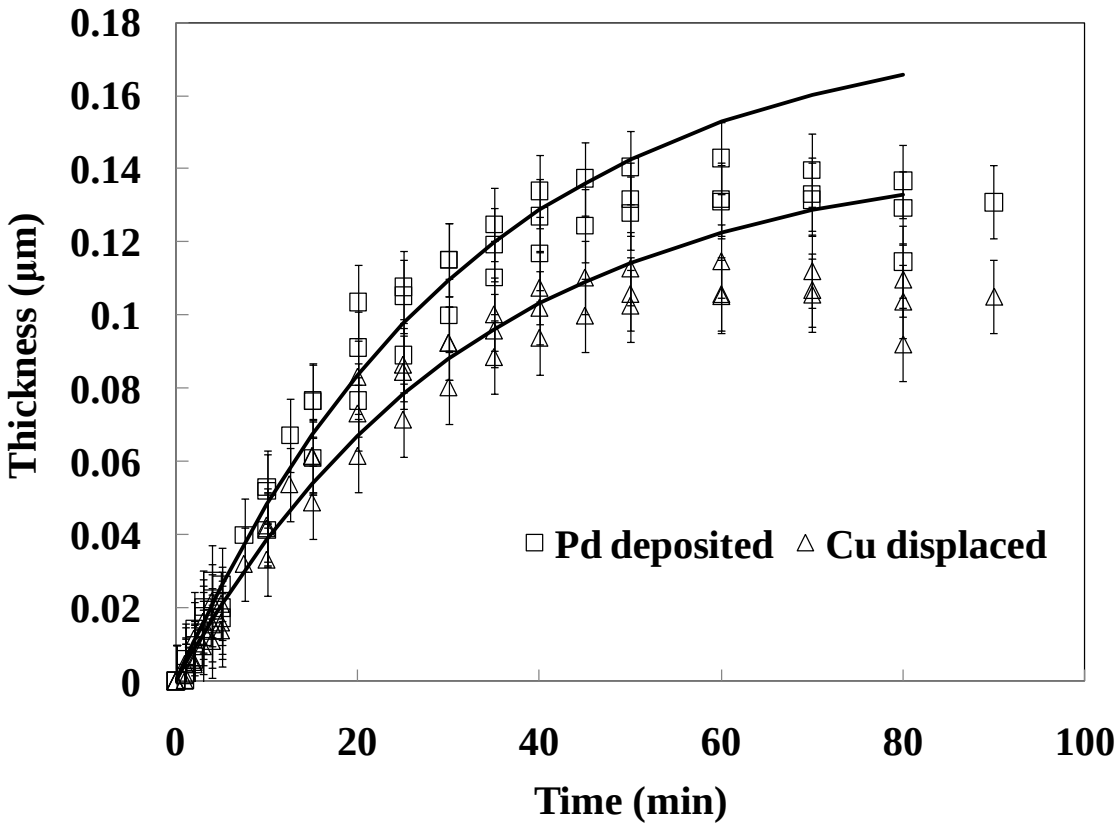

Figure 6-17 Pd and Cu thicknesses from the displacement bath as a function of time. The solid lines represent the data predicted from the first order reaction model.

6.3.4 XRD analysis of annealed samples

A coupon with a Pd/Cu/Pd tri-layer was fabricated based on the results of Sections 6.3.1 and 6.3.2. In order to obtain both a high deposition rate and uniform surface coverage with small cluster sizes, bath agitation rates of 400 rpm for both the Cu plating and the Pd displacement baths were used. The first layer of Pd was 8.0 μm and a 0.5 μm layer of Cu was deposited within 15 minutes of plating, determined gravimetrically. The sample was then immersed in the displacement bath for 60 minutes yielding a deposition of 0.15 μm of Pd and 0.12 μm of Cu displaced according to Figure 6-17.

Figure 6-18a shows the XRD data for the tri-layer before annealing. The only peaks observed were for the aluminum sample holder and for Pd. The Cu peak would normally appear slightly to the left of the aluminum peak at 43.30º but the peak was not observed in the scan because the resultant Cu layer following the galvanic displacement was too thin to be detected by XRD. After annealing in H_2 at 450ºC for 24 hours (Figure 6-18b), the Pd peak still remained and both the fcc and bcc Pd/Cu alloys were present at concentrations of 45 wt% and 2 wt% respectively with Pd as the balance.

As seen in Figure 4-7, annealing a bi-layer of Pd/Cu yielded 2 wt% of the bcc phase after 7.5 hours of annealing at 600ºC in H_2, and only reached 10 wt% at 550ºC (see Figure 4-9) and 38 wt% at 500ºC (see Figure 4-8) after 25 and 50 hours of annealing in H_2, respectively, showing that a thin tri-layer of Pd/Cu/Pd formed the sulfur tolerant fcc phase much more quickly than with the bi-layer, and at a lower temperature.

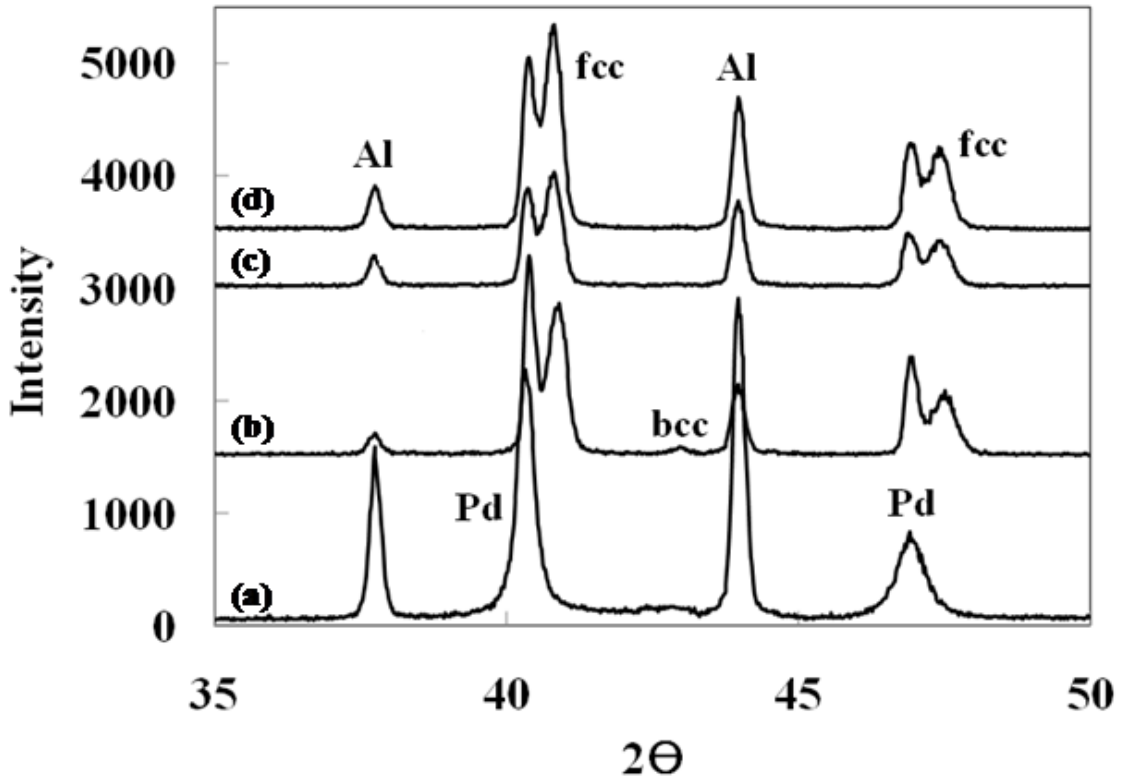

Figure 6-18 XRD scans of the Pd/Cu/Pd tri-layer coupon (a) as-deposited and after annealing in H_2 at 450°C for (b) 24 h (c) 36 h and (d) 144 h.

In addition, it was possible that no further annealing would be required in order for the fcc phase to be present on the surface. In contrast to an annealed Pd/Cu bi-layer which would have the highest concentration of Cu on the surface, a tri-layer would have the highest concentration of Cu just below the surface of the sample. In the case of a tri-layer, a membrane could have the fcc phase on the surface even though the bcc phase would still be present within the layer. In the case of a bi-layer, the presence of the bcc phase would be on the surface of the membrane, resulting in a top layer which was not sulfur resistant.

Further annealing of the sample in H_2 at 450ºC for another 12 hours (Figure 6-18c) resulted in the disappearance of the bcc phase. The composition of the XRD scan after a total annealing time of 36 hours was 43 and 57 wt% for the Pd and fcc phases respectively. Further annealing in H_2 at 450ºC for a total of 144 hours (Figure 6-18d) showed no change in the composition showing that the fcc alloy remained near the surface. Continued diffusion of Cu into the Pd layer would require more thermal energy due to the decrease in the diffusion coefficient with increased Pd content and corresponding increase in Tamman temperature (Butrymowicz et al., 1976). For bi-layers of Pd/Cu, the complete disappearance of the bcc phase would take place after 225 hours in H_2 at 500ºC, 42 hours at 550ºC and 10 hours at 600ºC, as seen in Table 4-2. Again, the Pd/Cu/Pd tri-layer yielded the same sulfur resistant phase on the surface after just 36 hours of annealing at 450ºC in H_2.

Figure 6-19 shows the surface of the Pd/Cu/Pd tri-layer after annealing at 450ºC in H_2 for 144 hours. The numerous holes and bumps (circled in Figure 6-19b) seen after the alloying of Pd and Cu were caused by the Kirkendall effect, explained in Section

4.3.2. Similar morphologies of Pd/Cu annealed layers were seen previously (see Figure 4-6 and Guazzone, 2006) and the Kirkendall effect in Pd/Cu diffusion couples has also been reported (Bitler et al., 1985).

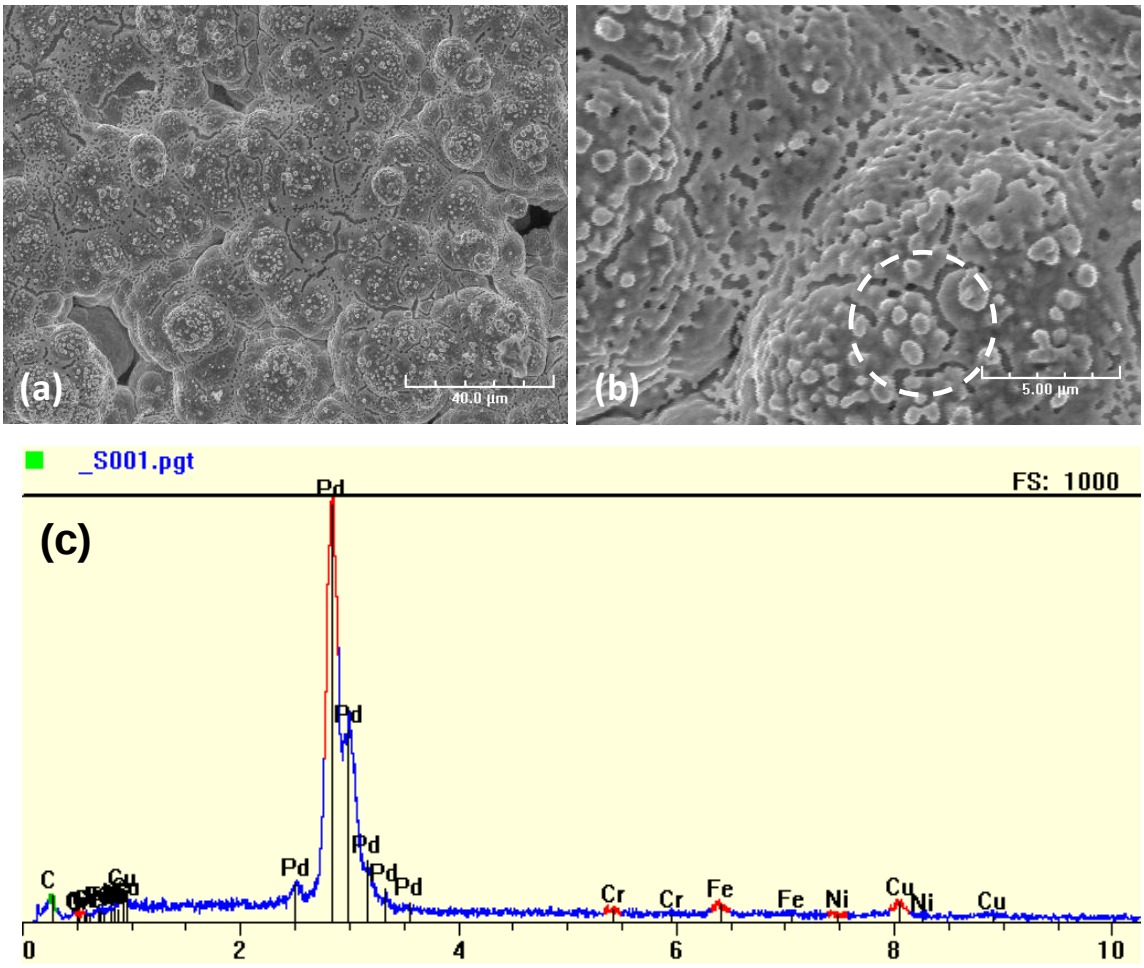

Figure 6-19 SEI micrographs of the surface of the annealed coupon at (a) 1 kX and (b) 5 kX and (c) the corresponding EDX area scan.

Figure 6-20 shows the cross sectional micrograph and corresponding elemental line scan of the annealed Pd/Cu/Pd tri-layer. Even though the presence of Cu was confirmed with the detection of the fcc alloy in Figure 6-18, no Cu could be detected in the line scan in Figure 6-20b. The lack of detection of Cu was due to the Cu layer thickness after the Pd galvanic displacement, which was less than the resolution of the line scan (roughly 0.8 μm at 15 kV). Even though the annealing at 450ºC thickened the layer with a presence of Cu as the Cu diffused into the Pd, there was not a large enough amount of Cu to distinguish the signal from the background of the EDX spectrum. However, the Cu could clearly be detected on the surface of the sample shown in Figure 6-19c. EDX area scans yielded Cu concentrations which varied between 5 – 10 wt%.

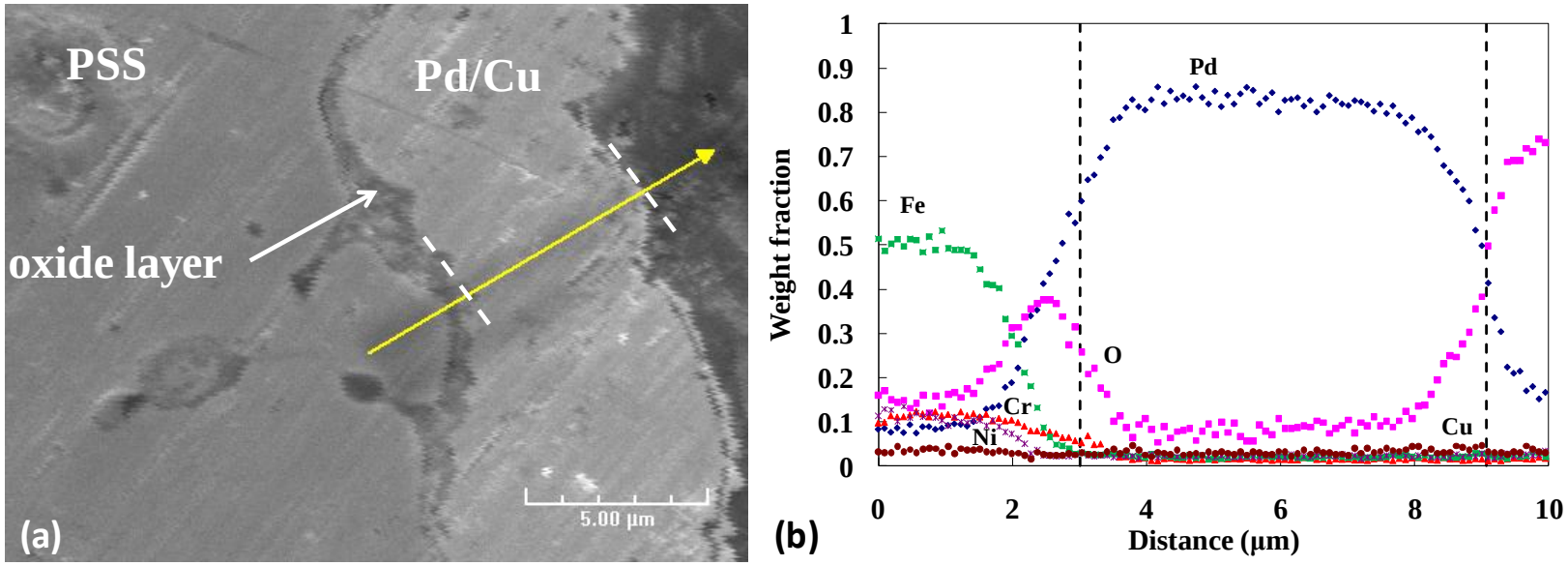

Figure 6-20 (a) Cross sectional micrograph at 5 kX and (b) corresponding elemental line scan of the annealed tri-layer coupon.

6.4 Conclusions

An optimum stirring rate of 400 rpm for both the Cu plating bath and the Pd galvanic displacement bath was sufficient to minimize the diffusional mass transfer resistance within the solutions and yielded a higher plating rate. The resultant layers of Cu and Pd were both of a more uniform thickness and morphology of evenly dispersed clusters than those with lower bath agitation rates. The Cu plating reaction rate had empirical reaction orders of 1.6 and -0.3 for the Cu^{2+} ion and H_2CO species respectively, and the Pd displacement of Cu was observed to be a first order reaction. The agitated baths enabled an extremely thin Pd/Cu surface alloy to be formed on a dense Pd layer.

Annealing a tri-layer of Pd/Cu/Pd to which sub-micron layers of Cu and Pd were deposited on a thicker layer of Pd resulted in the formation of the sulfur tolerant fcc phase after 36 hours of annealing at 450°C in H_2. The Cu had not penetrated deeply into the Pd layer and the composition of the surface alloy remained stable even after continued annealing in H_2 at 450°C due to the increase in Tamman temperature with increased Pd content.

7. High permeance fcc Pd/Cu membranes

7.1 Introduction

The significant hydrogen permeance decrease seen in fcc Pd/Cu alloy membranes forces ultra-thin membranes to be fabricated in order to achieve permeances which are comparable to pure Pd membranes or the more highly permeable Pd/Ag membranes (Knapton, 1977). The relatively wide pore size distribution of porous metal supports makes reducing the Pd/Cu membrane thickness more difficult than with ceramic supports whose pore size distribution is more easily controlled. In addition, the selectivity and structural integrity of such ultra-thin Pd/Cu membranes is then more likely to deteriorate quickly.

Table 7-1 shows a summary of various fcc Pd/Cu alloy membranes tested in the literature. The membranes varied in thickness, alloy content, support type and support modification, however the commonality of the membranes was that their permeances were far below the theoretical permeance of pure Pd foils of the same gravimetric thickness, all exhibiting the detrimental effect of Cu on the hydrogen permeance. While the thinner membranes of just a few microns in thickness did have high permeances, they too performed at just a fraction of the permeance of pure Pd membranes of the same thickness.

Table 7-1 Comparison of fcc Pd/Cu membrane permeances in the literature.

wt% Cu	Thickness (μm)	F_T ($m^3/m^2*h*bar^{0.5}$)*	T (ºC)	$F_{foil,T}$ ($m^3/m^2*h*bar^{0.5}$)	%F of Pd foil	reference
5	1.3	116	365	256	45	Thoen et al., 2006
5	3	60.1	480	173.6	35	Zhang et al., 2008
6	7	44.6	480	74.4	60	Zhang et al., 2008
6.2	18.9	6.1	450	24.8	24	Uemiya et al., 1991
7	5	52.3	480	104.2	50	Zhang et al., 2008
9	11	3.2	350	28.1	11	Roa and Way, 2003
9	12	24.6	450	39.1	63	Roa et al., 2001
9	12	55.9	500	46.3	121	Roa et al., 2003
10	25.4	6.7	350	12.2	55	McKinley, 1969
10	1	19.1	350	309.4	6	Roa and Way, 2003
10	3.5	10.9	350	88.4	12	Roa and Way, 2003
10	1	33.0	350	309.4	11	Roa et al., 2001
16	5	53.7	440	90.6	59	Gao et al., 2005
17	10	29.9	450	47.0	64	Guazzone, 2006
19	11.6	14.4	450	40.5	36	Roa et al., 2001

* In the case where the pressure exponent was not 0.5, the flux was calculated according to the exponent as given by the author and permeance recalculated according to a pressure exponent of 0.5.

wt% Cu	Thickness (μm)	F_T ($m^3/m^2*h*bar^{0.5}$)*	T (ºC)	$F_{foil,T}$ ($m^3/m^2*h*bar^{0.5}$)	%F of Pd foil	reference
19	11.6	36.3	500	47.9	76	Roa et al., 2003
20	11	24.4	500	50.5	48	Roa et al., 2003
20	100	0.03	450	4.7	1	Howard et al., 2004
22	12.5	12.6	450	37.6	33	Roa et al., 2003
22	12.5	10.2	450	37.6	27	Roa et al., 2001
25	4	10.8	450	117.4	9	Pan et al., 2005
26	35.2	1.3	350	8.8	15	Ma et al., 2003
28	27.6	2.1	500	20.1	10	Roa et al., 2003
28	1	31.4	350	309.4	10	Roa and Way, 2003
30	25.4	1.1	350	12.2	9	McKinley, 1969
30	1.5	43.3	350	206.3	21	Roa and Way, 2003
30	1.5	46.1	350	206.3	22	Roa et al., 2003
37	2	164.7	450	234.8	70	Nam and Lee, 2001

* In the case where the pressure exponent was not 0.5, the flux was calculated according to the exponent as given by the author and permeance recalculated according to a pressure exponent of 0.5.

The exception in Table 7-1 was with the 12 μm, 9 wt% Cu membrane which had a permeance which was 121% of the theoretical permeance of a Pd foil of the same thickness (Roa et al., 2003). However, the permeance of this particular membrane was not stable for the duration of the testing, decreasing by 25% over the course of two days before increasing again, doubling in value and decreasing again at lower temperatures. It was unclear if the permeance had reached a steady state value and no explanation was given to the large increases and decreases seen at the testing temperatures.

The best performing membrane was an 11.6 μm, 19 wt% Cu membrane which had a permeance which was 76% of the permeance of a pure Pd foil. Only 4 membranes of those surveyed had permeances which ranged from 61 – 76% of that of pure Pd foils, three membranes had permeances which ranged from 51 – 60%, 6 membranes had permeances which ranged from 31 – 50% and 14 membranes had permeances which were equal to or less than 30%. Clearly, there is ample room to improve the potential for obtaining high permeance Pd/Cu membranes. The objectives of this chapter were to present and characterize Pd membranes, Pd/Cu membranes made with the bi-layer method presented in Chapter 4 and Pd/Cu membranes made with the tri-layer method presented in Chapter 6, and to compare all three types of membranes in an effort to show that high permeance Pd/Cu membranes can indeed be fabricated.

7.2 Experimental

The membranes presented in this chapter are summarized in Table 7-2. The preparation of N_02, N_03, N_08 and N_08a was described in Section 5.2. Membranes N_09a and N_12 were prepared in the same fashion as N_08a by oxidizing the support, applying the grading/intermetallic diffusion barrier of the Pd glue and Al_2O_3 slurry (Section 3.1.5) and then by forming a dense Pd/Cu bi-layer, as explained in Section 3.1.4. Additionally, N_09a was fabricated with the annealing/polishing procedure described in Section 3.1.6. The Pd membranes N_13 and N_16 were fabricated in the same manner of fabrication as N_08 with the exception in that they were also treated with the annealing/polishing procedure as with N_09a.

Membranes N_20 and N_21 were fabricated with a Pd/Cu/Pd tri-layer, as described in Section 6.3.4. The dilute Cu plating bath shown in Table 6-1 was used with an agitation speed of 400 rpm for 15 and 25 minutes to deposit the Cu layer on N_20 and N_21, respectively. The Pd activation solution shown in Table 3-3 was used with an agitation speed of 400 rpm to deposit Pd by the displacement of Cu. The total dense Pd layer shown in Table 7-2 includes the Pd deposited by displacement.

Table 7-2 Membranes presented in this chapter.

membrane	F_{He} bare support (m^3/m^2*bar*h)	intermetallic diffusion barrier	grading	Pd glue (μm)	Pd/Ag barrier (μm)	Pd layer (μm)	Cu layer (μm)	total thickness (μm)	wt% Cu
N_02	159	0.5 μm Ru	none	none	none	10.8	3.4	14.2	19
N_03	180	air/700ºC/12 h	none	none	none	12.5	1.5	14.0	8
N_08	258	air/700ºC/12 h	Al_2O_3 slurry	0.2	5.1	7.0	none	12.3	none
N_08a*	258	air/700ºC/12 h	Al_2O_3 slurry	0.2	5.1	7.6	3.8	16.7	18
N_09a*	450	air/700ºC/12 h	Al_2O_3 slurry	3.3	4.3	7.9	1.6	17.1	7
N_10	341	air/700ºC/12 h	Al_2O_3 slurry	2.1	5.9	10.9	none	18.9	none
N_12	418	air/700ºC/12 h	Al_2O_3 slurry	1.4	2.8	4.7	4.7	13.6	28
N_13	422	air/700ºC/12 h	Al_2O_3 slurry	1.1	2.9	7.7	none	11.7	none
N_16	437	air/700ºC/12 h	Al_2O_3 slurry	1.6	5.9	5.2	none	12.7	none
N_20	421	air/700ºC/12 h	Al_2O_3 slurry	1.6	6.1	11	0.3	19.0	2
N_21**	516	air/700ºC/12 h	Al_2O_3 slurry	3.7	2.1	3.2	0.6	9.6	5

* After the characterization, N_08 was replated with 0.6 μm of Pd and plated with 3.8 μm of Cu. The replated Pd/Cu alloy membrane was referred to as N_08a. Similarly, N_09a was a Pd membrane that developed a leak of 80 sccm shortly after the characterization. The membrane was replated with Pd and Cu and characterized. Due to the large leak of N_09 before the replating, the hydrogen permeance results were not presented..

** After annealing N_21 for 12 hours in He during fabrication, a mass loss equal to 4.9 μm of Pd was observed. While a small mass loss was observed after the first annealing step with N_13, N_16 and N_09a, typical values ranged in a mass equivalent from 0.5 – 1.5 μm of Pd and were assumed to be negligible. It is possible that the thickness of N_21 was slightly more than what was recorded here.

7.3 Results

7.3.1 Fabrication of the Pd and Pd/Cu membranes

With the exception of membranes N_02 and N_03, all of the membranes in this chapter were made with the same method of support modification. Figure 7-1 shows the cross sectional micrographs of N_10, which was never characterized due to support defects preventing the making of a dense Pd layer. The Al_2O_3 slurry and Pd glue stages (Section 3.1.5) of the fabrication were intended to grade the porous support by blocking the larger pores. However, the effectiveness of the grading layer varied, depending on the support.

The circled areas in Figure 7-1b indeed showed pores which had been blocked off by the presence of the slurry and the Pd glue, thereby preventing the Pd from entering the pores and enabling a dense layer to be formed with less Pd in that immediate vicinity. The line scans in Figure 7-2a and c show the presence of both Al and O in the pore which has been blocked to Pd. In some areas, the slurry was less effective. The circled areas in Figure 7-1c and d show pores that have been partially blocked as seen by the 5 – 7 μm holes in the Pd layer. Closer inspection yields that the Pd surrounded the Al_2O_3 particles and deposited on the walls of the pores.

Even in Figure 7-2a and c, the presence of Pd could still be detected by EDX where the Al and O has seemingly blocked the pore, albeit in a much smaller quantity than the dense layer atop the support. The rest of the interface between the Pd layer and the porous support in Figure 7-1c and d shows a deep penetration of Pd into the pores which have not been blocked off, although the Pd in the pores was porous in nature since it surrounded the finer particles of Al_2O_3 during plating.

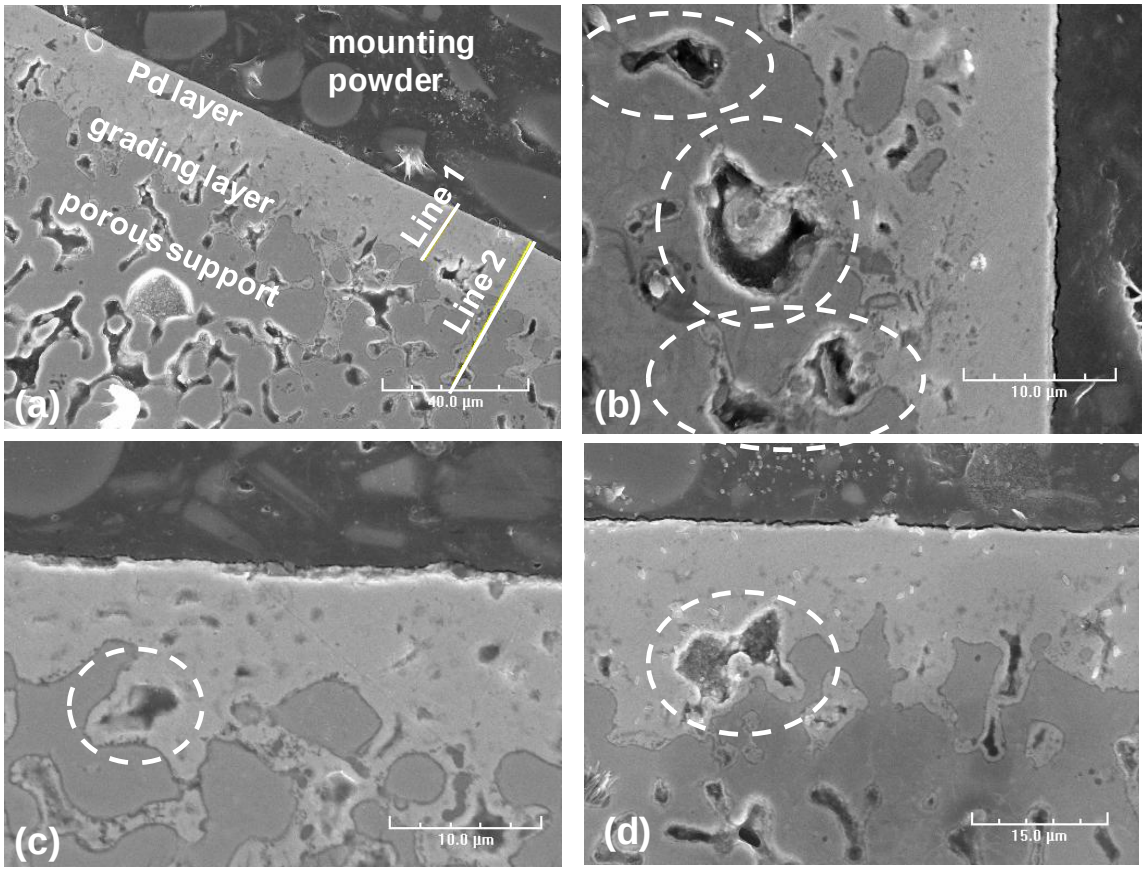

Figure 7-1 Cross sectional micrographs of membrane N_10 at (a) 1 kX, (b) 3 kX, (c) 3 kX and (d) 2 kX.

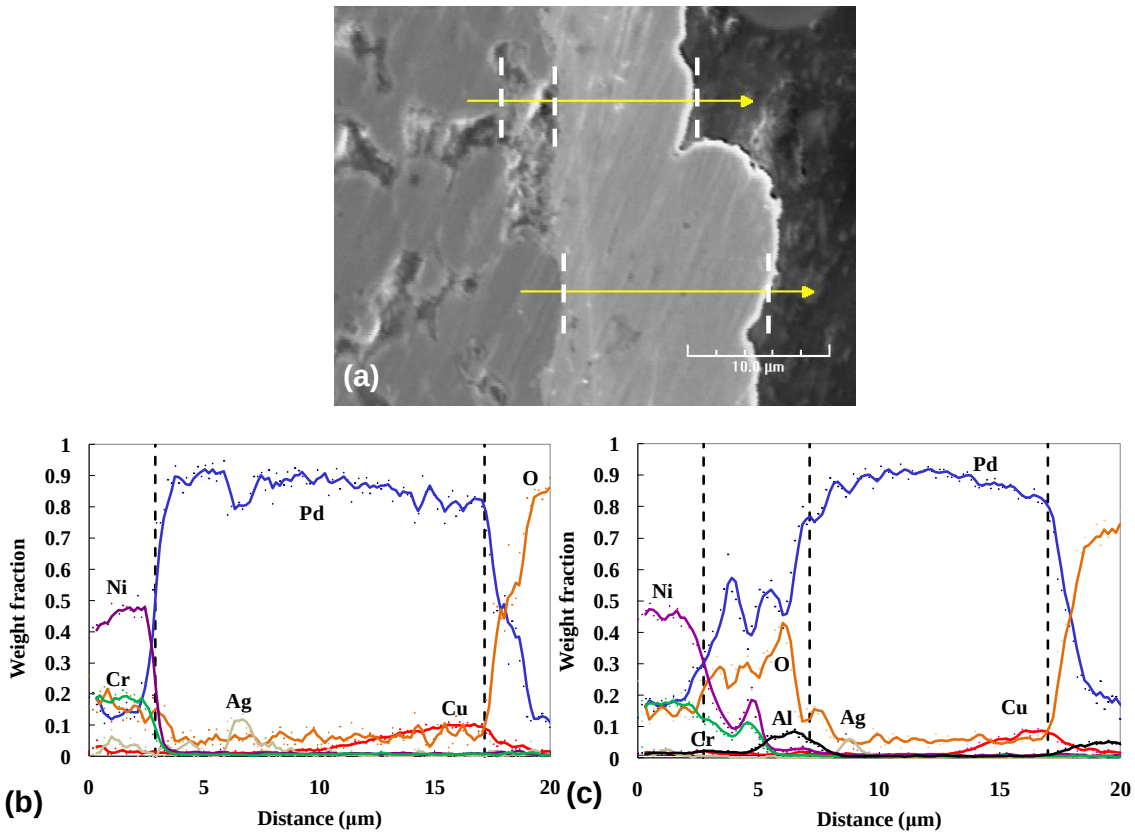

Figure 7-2 (a) Cross sectional micrograph of N_08 and the corresponding line scans of (b) the lower arrow in (a) and (c) the upper arrow in (a).

The disadvantage of the grading layer was that the Pd extended inward a distance 2 times that of the total thickness of the layer (the gravimetric thickness was 18.9 μm, see Table 7-2). Line number two in Figure 7-1a showed that the Pd penetrated as much as 44 μm into the support. On the other hand, the porosity of the Pd layer inside the pores would have enabled the 44 μm layer to have a hydrogen permeance much higher than that of the 16 μm non-porous Pd layer starting from the support interface and continuing to the membrane surface (line number one in Figure 7-1a). In the case that the Pd penetrating into the pores was porous in nature, the relatively thick Pd deposit would not be as detrimental as expected.

The Pd/Ag intermetallic diffusion barrier was deposited relatively uniformly over the surface of the support, and has already been proven to be effective in preventing intermetallic diffusion between the support metals and the Pd layer at temperatures where the oxide layer failed to do so (Ayturk et al., 2006b). Figure 7-2a and b show that the thickness of the Pd/Ag alloy was roughly 2 – 3 μm atop the support, thus forming an effective barrier between the dense Pd layer and the support. Also, Figure 7-2a and c show that the Pd/Ag alloy was deposited over the blocked pore with an alloy thickness of 1 – 2 μm, showing that the Pd/Ag barrier did indeed contribute to grading the support. However, as with the Al_2O_3 slurry, the effectiveness of the Pd/Ag barrier as a grading layer varied, depending on the support.

7.3.2 Characterization of Pd membranes

The characterization and selectivity change of N_08 was described in Section 5.5. N_13 was characterized for 800 hours between the temperatures of 250 - 450°C during which the membrane remained at 450°C for 530 hours, shown in Figure 7-3. The ideal

H_2/He separation factor decreased during the period of time at 450°C from 32,000 to 83. However, there was no increase in H_2 permeance resulting from the decrease in selectivity. Both the permeance and activation energy of N_13 remained the same before and after the selectivity drop, as seen by the dotted lines connecting the permeance at 350 and 400°C. Even though the decrease in selectivity was accompanied by the growth of the He leak to a value of 7 sccm, the H_2 flow was large enough (550 sccm) that the contribution of the H_2 flow through cracks and defects in the membrane did not affect the permeance. N_16 was characterized for 600 hours between 250 - 450°C during which the membrane remained at 450°C for 100 hours. The ideal H_2/He separation factor decreased from 650 to 550 during the time period tested at 450°C.

Figure 7-4 shows the Sieverts' Law regressions at 450°C for the Pd membranes tested in this chapter. As seen in Table 7-2, the total thicknesses of all three Pd membranes were very similar and should have resulted in nearly identical permeance values. Although the permeance values of N_13 and N_16 were very close, the permeance of N_08 was smaller. Even after taking the differing thicknesses into account and comparing the permeance at 450°C to the permeance of pure Pd foils of similar thicknesses, as seen in Table 7-3, N_08 still had a lower percentage of permeance than N_13 and N_16.

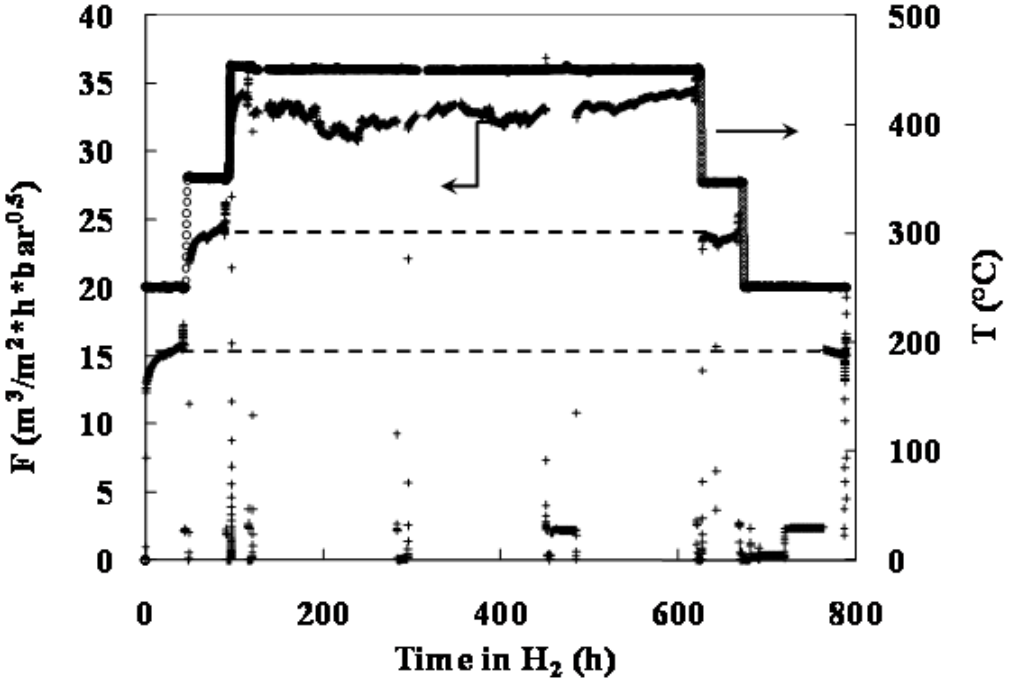

Figure 7-3 Permeance as a function of time and temperature for N_13.

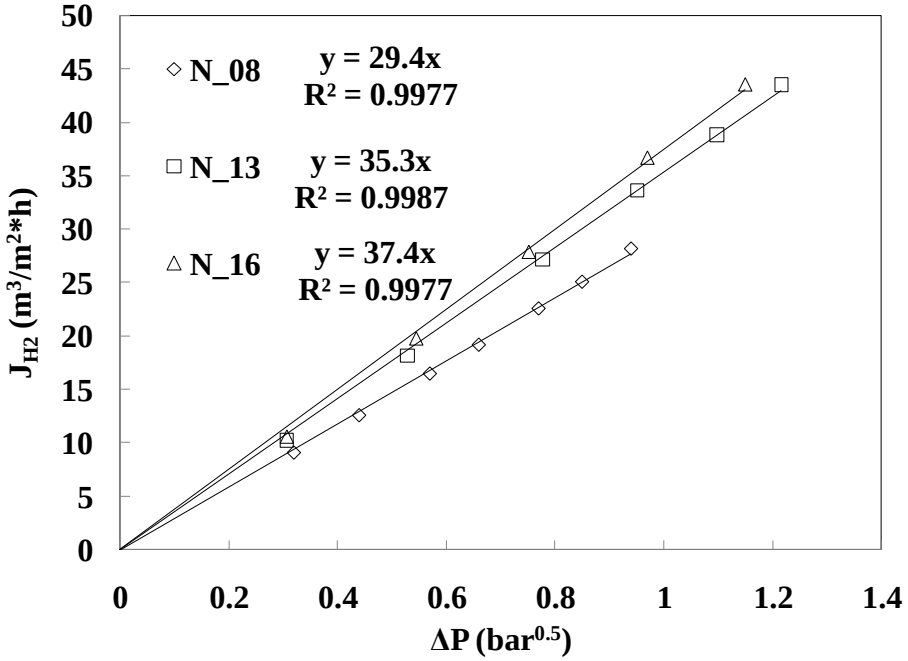

Figure 7-4 Sieverts' Law regressions for the Pd membranes at 450°C.

Figure 7-5 shows the regressions for the activation energy of permeation for the Pd membranes. The dependence of the permeance of a 12.2 μm Pd foil (the average thickness of the Pd membranes) on temperature overlaid for comparison. Table 7-3 summarizes the activation energy values. The activation energies of the Pd membranes fell in the range of 9.5 – 14.1 kJ/mol. The activation energy of Pd foils was 14.9 kJ/mol (Guazzone, 2006, Ayturk, 2007). Due to the fact that the composite Pd membranes were composed of several layers to modify the support and block off pores, the smaller activation energy in comparison to an unsupported foil could be due to the mass transfer resistance from the support and the grading layers.

Nevertheless, the permeances of all three membranes were very similar to that of the 12.2 μm foil throughout the temperature range tested. Due to the smaller activation energy, the permeance of N_08 was closer to the permeance of the foil of similar thickness between 250 - 350°C while the permeance of N_13 was closer to the foil permeance between 350 - 450°C due to the difference in the membrane activation energies from a free standing Pd film. The permeance of N_16 followed the permeance of the foil almost exactly throughout the temperature range tested, and due to the similar activation energies, the membrane permeance continued to follow closely to the foil permeance at 250°C (see the dotted line extending from the regression of N_16 in Figure 7-5).

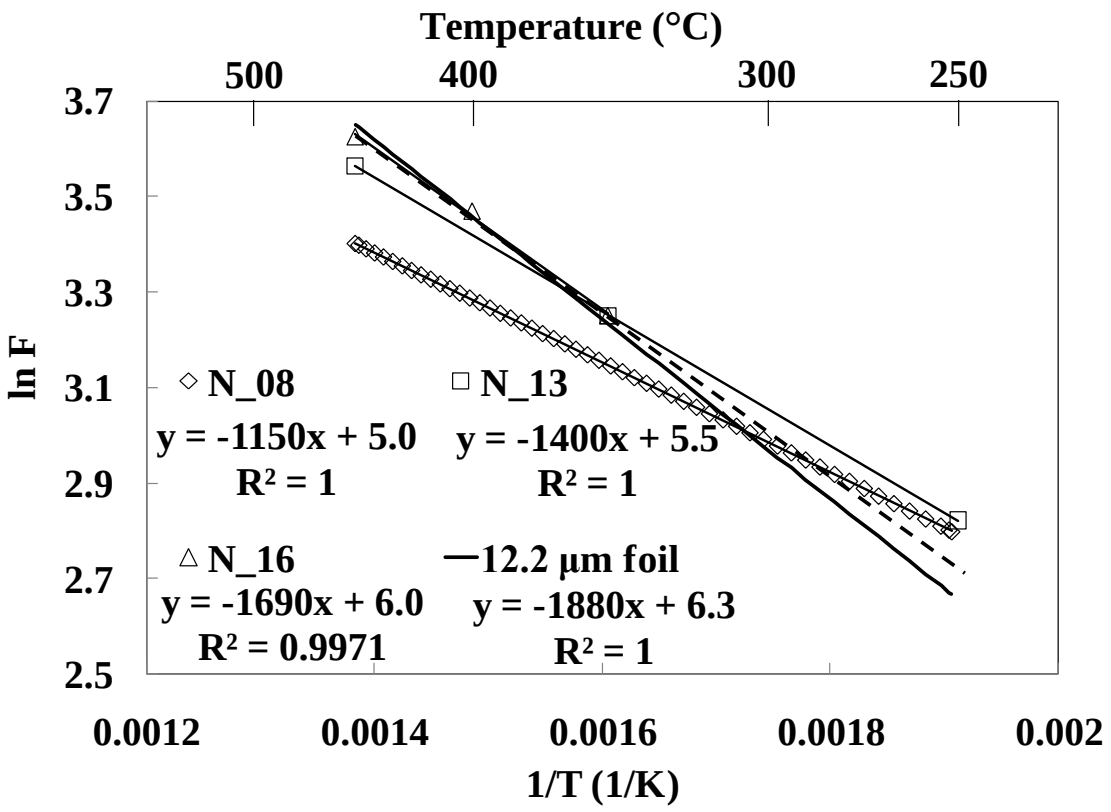

Figure 7-5 Activation energy of permeation for the Pd membranes.

Table 7-3 Performance summary for the Pd membranes.

membrane	$F_{450°C}$ ($m^3/m^2*h*bar^{0.5}$)	$F_{450°C, foil}$ ($m^3/m^2*h*bar^{0.5}$)	%F foil	Ea (kJ/mol)
N_08	29.4	38.2	77	9.5
N_13	35.3	40.1	88	11.6
N_16	37.4	37.5	100	14.1

The smaller permeance of N_08 was most likely due to the lower He permeance of the bare support. While the He permeance of the bare support of N_08 was 258 $m^3/m^2*h*bar$ (see Table 7-2), the He permeances of the bare supports of N_13 and N_16 were 422 and 437 $m^3/m^2*h*bar$, respectively. The bare support permeance of N_08 was roughly 60% of the bare support permeances of N_13 and N_16. The mass transfer resistance from the support could have resulted in the smaller support permeance and lessened the hydrogen permeance of N_08 relative to N_13 and N_16. Indeed the smaller activation energy of N_08 seen in Table 7-3 could be a result of the additional mass transfer resistance of the support.

Overall, the composite Pd membranes yielded similar permeances to pure Pd foils in comparison with the total membrane thicknesses. Also, the activation energies of the composite Pd membranes were similar. It was not known why the permeances of the composite Pd membranes were so similar to the permeances of Pd foils of the same thickness since the study of the microstructure of the membranes in Section 7.3.1 showed that not all portions of the membrane would have equal permeabilities. Some portions of the membranes were porous, some were dense, and some were alloyed with Ag, which would increase the permeability in the area of the alloy. Furthermore, the micrographs shown in Figure 7-1 were from only a small portion of one membrane. Choosing a different section would have yielded different thicknesses of the dense Pd and porous Pd extending into the support. However, due to the consistency of the comparison with Pd foils, the combination of all the layers in the composite Pd membrane provided a valid source of comparison to judge the performance of the Pd/Cu bi-layer and tri-layer membranes in Section 7.3.3 which were made in the same way.

7.3.3 Characterization of Pd/Cu membranes

The characterizations and selectivities of the bi-layer Pd/Cu membranes N_02, N_03 and N_08a were reported in Section 5.5. Membrane N_09a was characterized for over 1400 hours over the temperature range of 250 - 500°C. The time tested at 500°C was 1100 hours during which the ideal H_2/He separation factor decreased from 16,300 to 622. The permeance did not change significantly during the characterization due to the fact that N_09a had been previously characterized and replated as a Pd/Cu membrane and the alloying had nearly completed during which a large leak had developed. The Sieverts' Law and activation energy data were taken after the long term annealing period at 500°C. Membrane N_12 was characterized for 500 hours between the temperatures of 250 - 500°C. Over 300 hours were spent at 500°C during which the ideal H_2/He separation factor decreased from 330 to 220. As with N_09a, the Sieverts' Law and activation energy data were taken after the annealing period at 500°C.

The tri-layer Pd/Cu membrane N_20 was characterized between the temperature range of 350 - 450°C for 250 hours with 170 hours of the characterization tested at 450°C. The ideal H_2/He separation factor of the membrane decreased from infinity (the He leak was undetectable even at a pressure difference of ΔP = 3 bar) to 535 over the course of the 170 hours where the permeance increased slightly due to the membrane stabilizing (see Figure 7-6). It was reasonable to assume that the slight increase in permeance seen by some of the membranes was not due to the increase in leak since the permeance eventually reached a steady state value whereas the leak continued to increase over time.

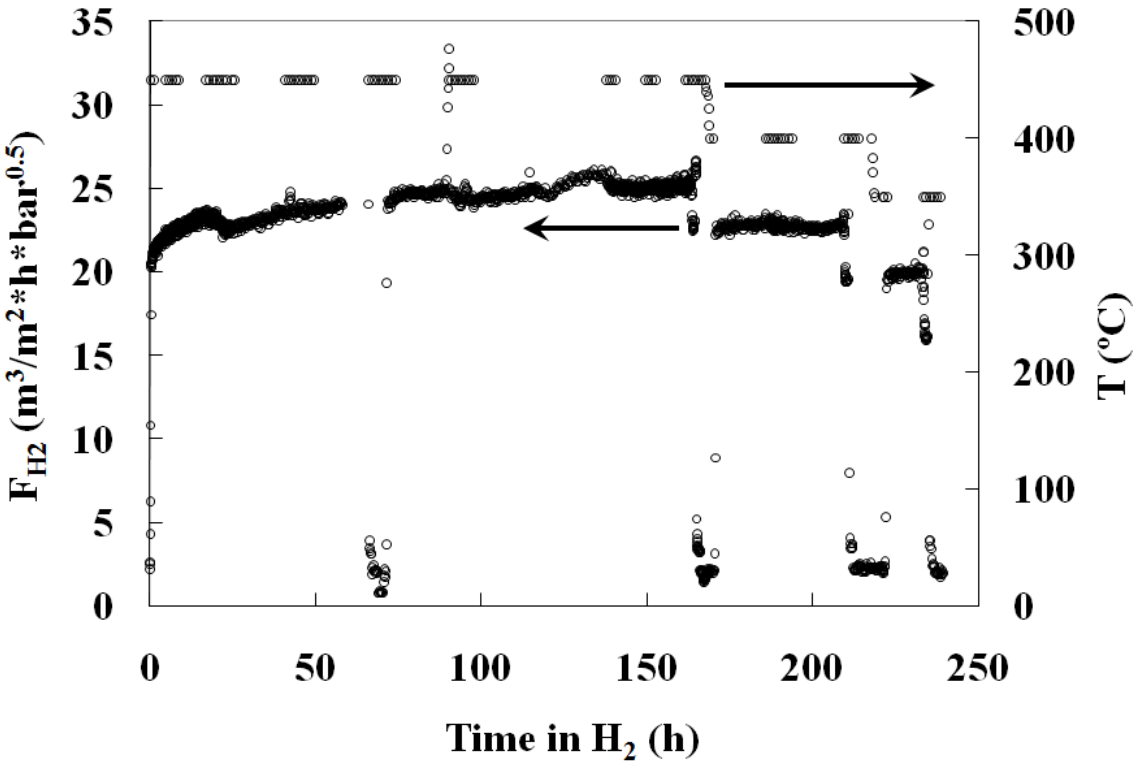

Figure 7-6 Characterization of the Pd/Cu tri-layer membrane N_20.

Contrary to the tri-layer membrane N_20, the permeance of the tri-layer membrane N_21 decreased slightly over the annealing time period at 450°C (see Figure 7-7), most likely due to the Pd/Cu alloying since more Cu was deposited than was originally intended and there was twice as much Cu near the surface. As with N_20, the ideal H_2/He separation factor of N_21 decreased to 560 during the course of the annealing at 450°C.

Figure 7-8 shows the Sieverts' Law regressions for all of the bi-layer and tri-layer Pd/Cu membranes at 450°C and Figure 7-9 shows the activation energy of permeation regressions for each membrane with the values of the bi-layer and tri-layer membranes listed in Table 7-4 and Table 7-5 respectively. Membranes N_02 and N_03 had significantly lower hydrogen permeances than the other Pd/Cu membranes, however this was to be expected because the supports were not modified in the same manner as the other bi-layer Pd/Cu membranes and the tri-layer Pd/Cu membranes.

Grading the supports with the Pd glue, Al_2O_3 slurry and Pd/Ag barrier improved the hydrogen permeance considerably, especially when compared to the permeance of pure Pd foils of the same thickness (Table 7-4). While N_02 and N_03 had permeances of 40 and 32% of a Pd foil respectively, the bi-layer Pd/Cu membranes with the support grading had permeances which ranged between 45 – 63% of pure Pd foils, thus improving the permeance of the Pd/Cu membranes. The grading caused part of the Pd layer to be porous which lessened the mass transfer resistance to hydrogen within the layer and increased the overall permeance.

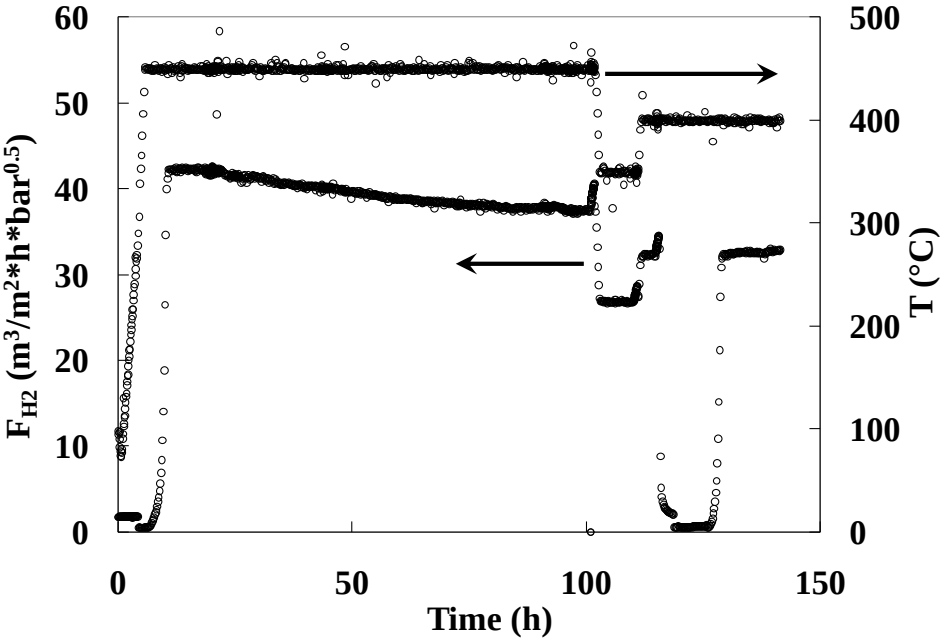

Figure 7-7 Characterization of membrane N_21.

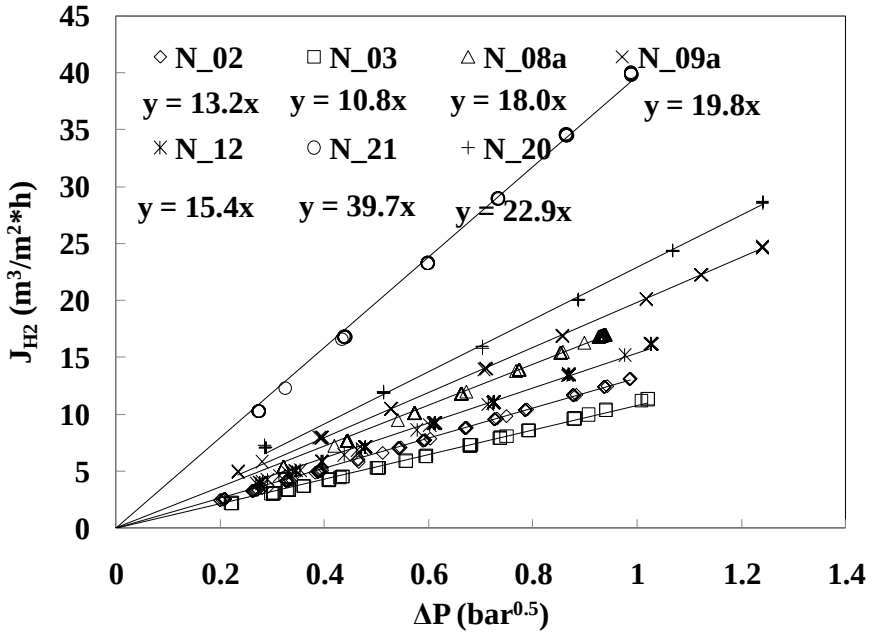

Figure 7-8 Sieverts' Law regressions for the Pd/Cu membranes at 450ºC.*

* The permeance for N_09a was measured at 500°C.

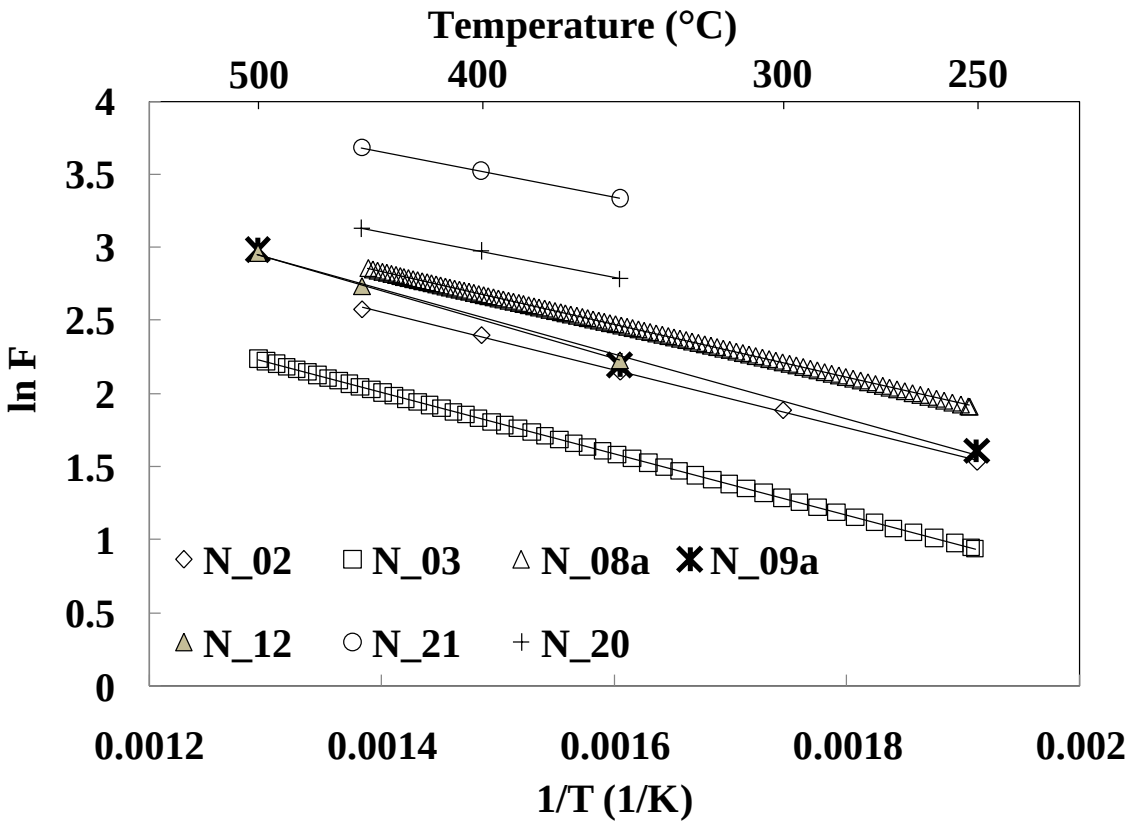

Figure 7-9 Activation energy of permeation regressions for the Pd/Cu membranes.

Table 7-4 Performance summary for the bi-layer Pd/Cu membranes.

membrane	$F_{450°C}$ ($m^3/m^2*h*bar^{0.5}$)	$F_{450°C, foil}$ ($m^3/m^2*h*bar^{0.5}$)	%F foil	Ea (kJ/mol)	grading
N_02	13.2	33.1	40	16.4	no
N_03	10.8	33.5	32	17.4	no
N_08a	18.0	28.5	63	15.0	yes
N_09a*	19.8	32.5	61	18.5	yes
N_12	15.4	41.6	45	19.4	yes

* The permeance for N_09a was measured at 500°C and the foil permeance was calculated at 500°C.

Table 7-5 Performance summary for the tri-layer Pd/Cu membranes.

membrane	$F_{450°C}$ ($m^3/m^2*h*bar^{0.5}$)	$F_{450°C, foil}$ ($m^3/m^2*h*bar^{0.5}$)	%F foil	Ea (kJ/mol)
N_20	22.9	24.7	93	13.0
N_21	39.7	48.9	81	12.9

The bi-layer Pd/Cu membranes deposited on graded supports had permeances which landed in the top tier of permeances of fcc Pd/Cu membranes in the literature when compared to Pd foils (Table 7-1). The exception was N_12 which had a permeance only slightly higher that of the bi-layer membranes deposited on ungraded supports. The smaller permeance was most likely due to the high Cu content (Table 7-2), which would have reduced the permeance accordingly.

The activation energies of all of the bi-layer Pd/Cu membranes fell in the range of 15.0 – 19.4 kJ/mol (Table 7-4), a higher range than the activation energies of the Pd membranes presented in Section 7.3.2. Due to the fact that the activation energies of the bi-layer membranes deposited on ungraded supports were not especially low in comparison to the activation energies of those deposited on graded supports, it can be assumed that there was not a significant contribution from the mass transfer resistance of the ungraded supports even though the bare support He permeances were relatively low (see Table 7-2).

The tri-layer membranes had the highest permeances of all even though the total thickness of the tri-layer Pd/Cu membrane N_20 was a few microns larger than the thicknesses of the rest of the bi-layer Pd/Cu membranes. Of even more importance, when comparing the measured membrane permeances to the theoretical permeances of pure Pd

foils of the same thickness as the Pd/Cu membranes in Table 7-4 and Table 7-5, the tri-layer Pd/Cu membranes performed similarly to the Pd membranes in Table 7-3. Since it was possible that the gravimetric thickness of the tri-layer membrane N_21 was slightly larger than what was recorded due to the mass loss during annealing, as explained in the footnote of Table 7-2, the performance of N_21 could be even better when compared to a Pd foil since the permeance of a thicker foil would be less. Even with the uncertainty of the thickness, N_21 still performed within the range of Pd membranes recorded in Table 7-3.

The measured permeances of the Pd membranes ranged between 77 – 100% of the theoretical permeance of pure Pd foils of the same thickness. The tri-layer Pd/Cu membranes had permeances which were 93 and 81% of the theoretical permeance of pure Pd foils which was in the range of the performance of the pure Pd membranes made with the same method of support modification. Bi-layer Pd/Cu membranes made with the same method of support modification had permeances which ranged between 45 – 65% of the permeance of Pd foils of the same thickness. Furthermore, none of the fcc Pd/Cu membranes recorded in the literature surpassed a hydrogen permeance of 76% of the pure Pd foil, regardless of the Cu composition.

Even more so, while the activation energy of permeation for the bi-layer Pd/Cu membranes ranged between 15 – 19.4 kJ/mol, as seen in Table 7-4, the activation energy of the Pd membranes fabricated with the same support modification ranged between 9.5 – 14.1 kJ/mol, seen in Table 7-3. The activation energy of the tri-layer membranes were roughly 13 kJ/mol, shown in Table 7-5, which fell in the range of Pd membranes presented in Table 7-3. Consequently, the Pd/Cu tri-layer membranes showed permeation

properties that were characteristic of the Pd membranes rather than the Pd/Cu membranes. The reduced Cu content of the tri-layer membranes clearly mitigated the permeance reduction caused by alloying Cu with Pd in the fcc phase.

Figure 7-10 and Figure 7-11 show the depth profile XPS scans of an annealed Pd/Cu bi-layer and tri-layer, respectively. Both samples had large amounts of adventitious carbon on the surface which nearly disappeared after the sputtering leaving just the Pd and Cu underneath. The profiles of both samples were flat, due to the scale of the depth profile. A gradient in Cu could clearly be seen in the bi-layer samples in Figure 4-5. However the scale of the concentration profiles in Figure 4-5 were 10 μm while the scale of the depth profile in Figure 7-10 was two orders of magnitude less at 0.1 μm, likewise with Figure 7-11. Due to the extremely small scale in the XPS concentration profile, Cu gradients were not observed.

As can be seen from Figure 7-10 and Figure 7-11, about half the Cu was present in the near surface region of the tri-layer as with the bi-layer due to the smaller amount of Cu in the tri-layer membranes. However, both near surface regions had concentrations which were conducive to the fcc region of the Pd-Cu phase diagram (Figure 4-1). The difference between the bi-layer and tri-layer was not just with the amount of Cu in the near surface region, but also the amount that diffused into the Pd layer. Unlike with the bi-layers in Figure 4-5, no Cu could be detected in the cross section of the tri-layer in Figure 6-20 showing that the Cu gradient following the depth profile in Figure 7-11 must not have extended past 0.5 – 1 μm, which was the resolution of the EDX line scan in Figure 6-20. And so, while the small Cu content near the surface of the tri-layer membranes was enough to form the fcc phase as shown in Section 6.3.4, the permeation

of the membrane was not affected, nor the activation energy, thus showing that Pd/Cu membranes could be fabricated with the sulfur tolerant fcc phase without reducing the hydrogen permeance.

Although the thicknesses of the tri-layer Pd/Cu membranes N_20 and N_21 were 19.0 and 9.6 μm respectively, the combined thickness of the top layers of the Cu and Pd were roughly 0.4 and 0.8 μm, respectively. Gas-tight Pd membranes thinner than the Pd/Cu tri-layer membranes presented in this work could also have the sub-micron layers deposited on the surface without reducing the overall hydrogen permeance. However, if the hydrogen selective layer was very thin the top alloy layer would consist of a larger fraction of the total membrane thickness and consequently, a larger fraction of the total mass transfer resistance to hydrogen transport within the Pd layer. The result would be that the overall permeance would be more significantly reduced in an extremely thin membrane than a thicker membrane by the presence of the surface alloy, but not as drastically as with the homogeneous fcc Pd/Cu alloy membranes presented in the literature.

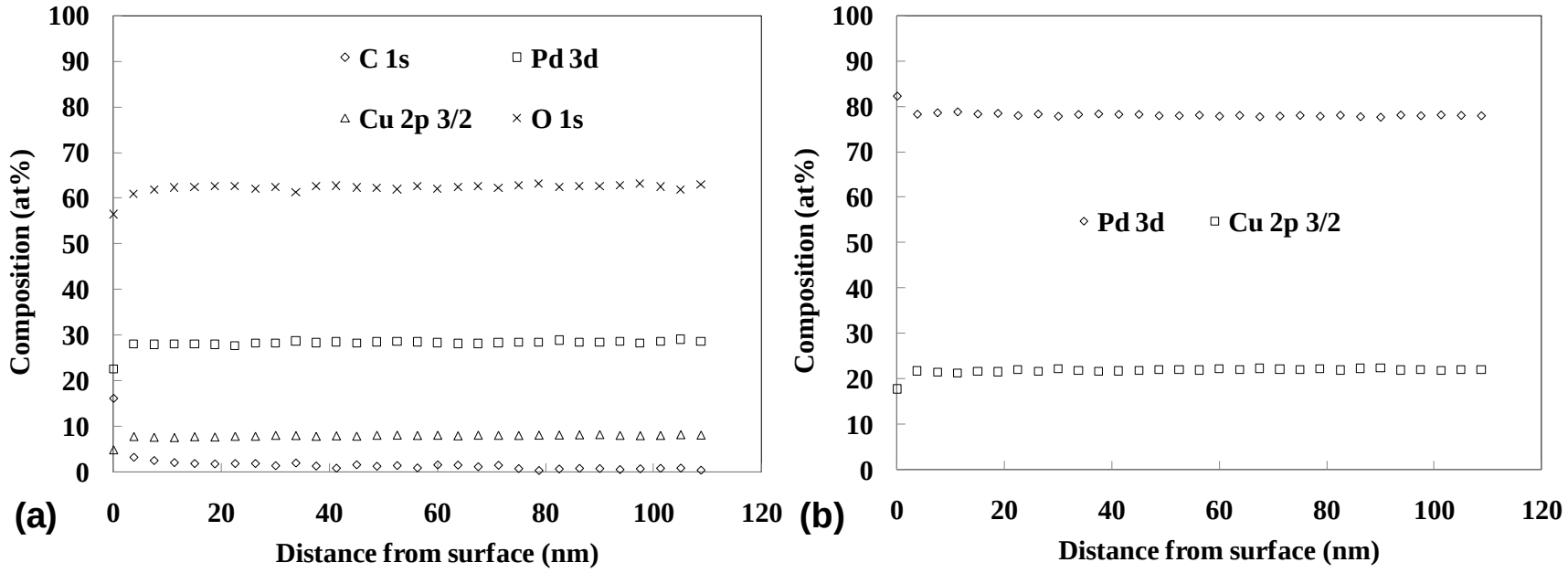

Figure 7-10 Depth profile XPS data for a bi-layer coupon annealed at 600ºC for 12 hours in H_2 including (a) all major elements detected and (b) only Pd and Cu.*

* While there was oxygen present on the surface of the coupon, the unusually high oxygen content throughout the depth profiling was due to calculation errors caused by the overlap between the O 1s and Pd $3p_{1/2}$ orbital peaks.

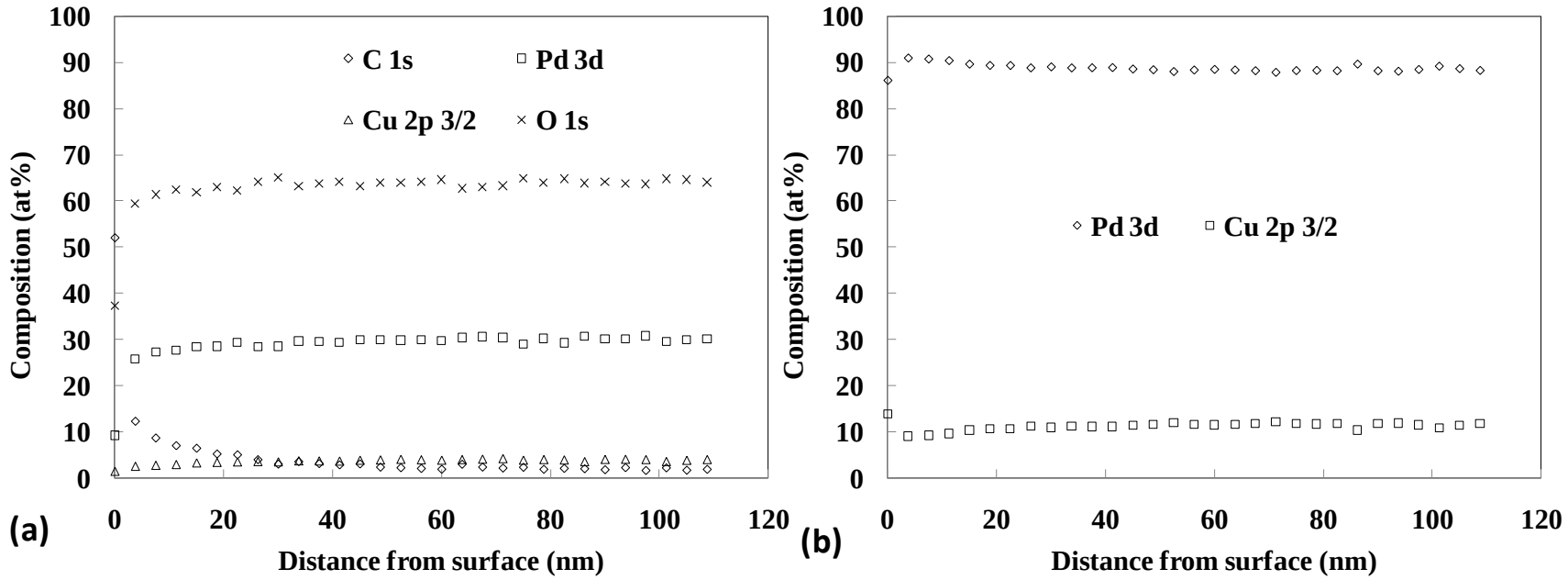

Figure 7-11 Depth profile XPS data for a tri-layer coupon annealed at 450ºC for 144 hours in H_2 including (a) all major elements detected and (b) only Pd and Cu.*

* While there was oxygen present on the surface of the coupon, the unusually high oxygen content throughout the depth profiling was due to calculation errors caused by the overlap between the O 1s and Pd $3p_{1/2}$ orbital peaks.

7.4 Conclusions

The tri-layer Pd/Cu/Pd alloy membranes were fabricated based on the findings of the coupon study in Chapter 6 and characterized between 350 - 450°C for 150 and 250 hours. While the bi-layer Pd/Cu fcc alloy membranes made with the same method of support modification resulted in permeances at roughly 45 – 65% of the permeance of pure Pd foils of the same thicknesses, the tri-layer membranes had permeances which were 93 and 81% of the permeance of pure Pd foils of the same thicknesses and activation energies conducive to Pd membranes rather than Pd/Cu membranes due to the smaller amount of Cu. Additionally, when compared to pure Pd foils of the same permeance, the tri-layer Pd/Cu membranes out-performed all of the fcc membranes reported in the literature. Consequently, the disadvantage of the decreased hydrogen permeance which accompanied the sulfur-tolerant fcc phase in Pd/Cu membranes was eliminated.

8. Effect of H_2S on the Performance and Stability of Pd/Cu Membranes*

8.1 Introduction

Although there has been research which has examined the sulfur poisoning and tolerance of Pd/Cu membranes, as was described in Section 2.5.3, none have fully characterized Pd/Cu membranes in H_2, He and H_2S atmospheres over the temperature range expected for steam reforming and water gas shift reactions. Nor have the regenerative characteristics of the membranes been investigated after poisoning. Furthermore, no testing of non-homogeneous fcc Pd/Cu membranes has been tested.

The main objective of this chapter was to fabricate composite Pd membranes with a thin top Pd/Cu layer with the electroless deposition method, to characterize the performance of the Pd/Cu membranes in atmospheres of approximately 45 - 55 ppm H_2S/H_2 and to study the regenerative properties of the membranes. The effects of the temperature of exposure to the H_2S/H_2 mixture on the permeance and the recovery in pure H_2 were investigated to determine the influence on the sulfur tolerance and the irreversibility of the poisoning. The effect of the time of exposure on the membrane performance was also investigated and lastly, the effect of the H_2S/H_2 mixture on the

* This chapter has been published in Industrial and Engineering Chemical Research.

Pomerantz, N. and Ma, Y.H. "Effect of H_2S on the performance and long-term stability of Pd/Cu membranes." *Industrial and Engineering Chemical Research*, **48**(8) (2009) 4030 - 4039.

selectivity characteristics of the membranes was investigated to provide information on the long-term membrane leak stability.

8.2 Experimental

The membranes tested in this chapter are listed in Table 8-1. Membrane N_02 was plated with 0.5 μm Ru for an intermetallic diffusion barrier while membranes N_03, N_08 and N_08a were all oxidized at 700ºC for 12 hours. N_08 and N_08a were graded with the Al_2O_3 slurry which was sealed with the "Pd glue" as described in Section 3.1.5. A Pd/Ag barrier was deposited as further grading and an additional intermetallic diffusion barrier as described in Section 3.1.2. A dense Pd layer was plated on all membranes. On N_02, N_03 and N_08a, Cu was plated on the Pd. The thicknesses of all of the layers are listed in Table 8-1. All membranes with Cu had compositions which would place them in the fcc region of the Pd/Cu phase diagram (see Figure 1-1). The membrane characterizations were performed in the system described in Figure 3-3. The characterization of N_03 is described fully in Section 4.3.5 and the characterizations of N_02, N_08 and N_08a are described in Section 5.5.1.

Table 8-1 Membranes tested in this chapter.

Membrane	Intermetallic diffusion barrier	grading	Pd glue (μm)	Pd/Ag barrier (μm)	Pd layer (μm)	Cu layer (μm)	wt% Cu
N_02	0.5 μm Ru	none	none	none	10.8	3.4	19
N_03	air/700ºC/12 h	none	none	none	12.5	1.5	8
N_08	air/700ºC/12 h	Al_2O_3 slurry	0.2	5.1	7.0	none	none
N_08a[*]	air/700ºC/12 h	Al_2O_3 slurry	0.2	5.1	7.6	3.8	18

[*] After the characterization, N_08 was replated with 0.6 μm of Pd and plated with 3.8 μm of Cu. The replated Pd/Cu alloy membrane was referred to as N_08a.

8.3 Results and Discussion

8.3.1 Effect of H_2S exposure on membrane performance

Prior to the poisoning study, membranes N_02, N_03 and N_08a were characterized in pure H_2. The permeance and selectivity data are found in Section 5.5.1. Figure 8-1 shows the percent of permeance decline and recovery as a function of time at 450ºC during testing with 42.7 ppm H_2S/H_2 and the subsequent recovery in pure H_2. The y-axis shows the relative permeance where F is the permeance and F_0 is the permeance before the H_2S exposure at that temperature. Membrane N_03 was exposed to 42.7 ppm H_2S/H_2 for two hours, and then pure H_2 was reintroduced to recover the hydrogen permeance until a stable value was reached. The feed concentration of H_2S was chosen in accordance with a DOE suggested guideline (Hydrogen from Coal Program, 2009). The effect of H_2S poisoning on the He leak was examined by monitoring the He leak flux before each poisoning experiment and after each recovery in pure H_2.

As seen in Figure 8-1, the permeance of N_03 dropped sharply by approximately 80% within the first few minutes of the exposure to the H_2S/H_2 mixture. The permeance decline occurred instantaneously and for the duration of two hours of poisoning, the permeance did not change. The permeance decline was caused by surface sulfide formation where adsorbed sulfur atoms blocked H_2 adsorption sites with the surface sulfide. According to the results in Section 9.3.2, the sulfides formed would have been both Pd and Cu sulfides, in accordance with the alloy composition.

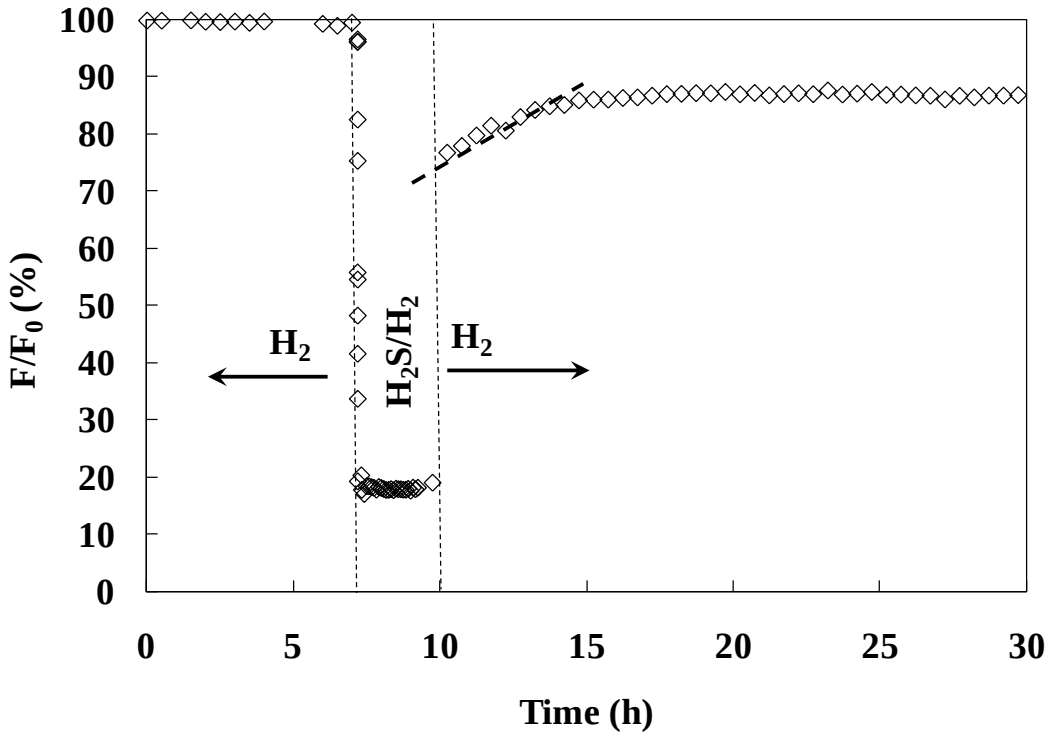

Figure 8-1 The poisoning of N_03 at 450ºC in 42.7 ppm H_2S/H_2 and the recovery in pure H_2.

Assuming that the poisoning was purely a surface phenomenon, the magnitude of the decline would have indicated that 80% of the H_2 adsorption sites were blocked, reducing the effective area for H_2 adsorption and dissociation. The bulk sulfide formation either caused the hydrogen permeance to have a continuous decline during poisoning as the sulfide layer formed and thickened (Morreale et al, 2007) or caused the hydrogen permeance to increase while accompanied by an increase in the flux of non-permeable gases as the sulfide ruptures the membrane (Kajiwara et al, 1999). Since the permeance and the ideal H_2/He separation factor for N_03 remained relatively constant during poisoning the permeance decline appeared to be the result of the surface sulfide formation.

N_02 and N_03 were exposed to 42.7 ppm H_2S/H_2 for two hours at several temperatures. N_02 was tested twice at 450 and 400°C (in that order) and N_03 was tested twice at 500, 450, 400 and 350°C (in that order). The permeance decline of N_02 at 450ºC was similar in both magnitude and manner to that of N_03 at 450ºC, but was difficult to measure accurately because the flow of the permeate was small relative to the range of the mass flow meter after the prior permeance loss caused by the intermetallic diffusion.

The permeance recovery of the membranes occurred in three stages as shown in Figure 8-1. The first stage was marked by an instantaneous permeance increase starting from F/F_0 = 20% upon the introduction of pure H_2, indicating that the adsorbed sulfur combined with H_2 and desorbed from the surface. The second stage was linear (marked by the dashed line in Figure 8-1) which was at a slower rate than the first stage and lasted

between 3 – 10 hours. The third stage was characterized by a very slow increase lasting between 50 - 200 hours.

The first stage involved the greatest amount of hydrogen permeance recovered with the percent recovery varying between 50% (at 350ºC) and 85% (at 500ºC). The linear stage recovered roughly an additional 10% of the permeance, and the third stage recovered the least amount of permeance which varied between 5 – 10%. As explained in more detail in Section 9.3.3, the different stages of recovery corresponded to the rates of flushing the H_2S out of the system with H_2.

Furthermore, the desorption of sulfur from the Pd/Cu surface would change the binding energy of the remaining sulfur ad-atoms (adsorbed atoms). The more sulfur that desorbed from the membrane, the harder it would be to desorb the remaining sulfur. According to the previous theoretical work (Alfonso, 2005), the binding energy of sulfur to the fcc sites of the Pd(1 1 1) surface decreased from 5.07 to 3.29 eV/atom at 0.11 and 1.0 ML (monolayers) respectively, meaning that the strength of the bond decreased as the surface coverage increased. A similar trend was seen with the hcp (hexagonal close packed) surface adsorption sites and with the tetragonal and octahedral subsurface adsorption sites as the sulfur coverage increased (Alfonso, 2005, Alfonso, 2006). This phenomenon was also seen with sulfur adsorption on Ni and Pt where the heat of adsorption increased with increasing sulfur coverage. The difficulty in completely regaining the hydrogen permeance would correspond to the increasing binding energy (heat of adsorption becoming less negative) of sulfur to Pd as the surface coverage decreased due to sulfur desorption (Barbier et al, 1996).

In addition, the binding energy of sulfur to an adsorption site changes depending on the location of the site and alloy composition. Alfonso et al. (2003) calculated the binding energies for the adsorption sites on the Pd(1 1 1), Cu(1 1 1), $PdCu_3$(1 1 1), Pd_3Cu(1 1 1) and PdCu(1 1 0) surfaces and found that the greatest difference in the binding energy between the most energetically favorable sites of the surfaces was 0.42 eV, showing a differing bond strength of sulfur to alloyed surfaces of different compositions. In addition, the PdCu(1 1 0) surface had a difference of 0.22 eV between the sulfur adsorption sites, showing differing bond strengths for different adsorption sites on the same surface. The sharp increase in permeance upon the reintroduction of H_2 would be from sulfur desorbing from the least energetically favorable sites (lowest binding energy). The linear stage of recovery would be from sites which were more energetically favorable and the last stage of recovery from sites which were the most energetically favorable.

Even though the last stage of recovery was lengthy in time, not all of the permeance could be recovered. At 450ºC, 95% of the hydrogen permeance of N_03 was recovered after poisoning, showing that at these conditions, part of the sulfur could not be desorbed at the given temperature. It was unlikely that bulk sulfide formation was the cause of the permeance that was not recovered since bulk sulfides had previously caused a continuous permeance decline during poisoning (Morreale et al, 2007), contrary to the unchanged permeance of N_03 during exposure.

Since the process of sulfur desorbing from the membrane surface would increase the binding energy of the remaining adsorbed sulfur atoms and increase the heat of adsorption for the remaining adsorbed sulfur due to a lessening in repulsive forces

between the adsorbed sulfur atoms during desorption (Alfonso, 2005), the permeance which was not recovered could have been caused by adsorbed sulfur atoms which had very high binding energies. Also, it was found that the sub-surface sulfur adsorption became energetically favorable after 0.5 ML of sulfur was adsorbed on the Pd(1 1 1) surface (Alfonso, 2006). Once sulfur was present in the subsurface of Pd, desorption would take longer and higher temperatures would be needed for desorption. The results of Section 9.3.2 showed that the majority of the permeance that was not recovered was due to sulfur binding with Cu, forming surface Cu sulfides.

Irreversible and reversible H_2S poisoning has been seen with many catalysts (Barbier et al, 1996). Previous work with Pt/Al_2O_3 (Barbier et al, 1985) showed that the amount of irreversibly adsorbed sulfur remained constant at 500ºC while the amount of reversibly adsorbed sulfur increased with increasing H_2S concentration in H_2 (shown in Figure 2-7). Horanyi and Ritzmayer (1986) have identified irreversible sulfur poisoning within a monolayer of sulfur coverage on Pt as PtS, while reversible sulfur poisoning was identified as PtS_2. It was possible that the formation of more than one surface sulfide resulted in part of the permeance of the Pd/Cu membranes not being recovered. Furthermore, the XPS results of Section 9.3.2 showed that although Cu sulfides caused the majority of the permeance that was not recovered, Pd sulfides were still present.

8.3.2 Effect of the temperature of H_2S exposure on membrane performance

The sudden drop in permeance upon the introduction of the H_2S/H_2 mixture with no further decrease during the two hours of exposure was observed at each of the temperatures tested. The only difference between each temperature was the magnitude of the permeance loss. As seen in Figure 8-2 (y-axis on the left), there was a slight increase

in the amount of permeance lost during exposure to the H_2S mixture with decreasing temperature.

Similar to the recovery at 450ºC, the permeance recovery at 350, 400 and 500ºC occurred in three stages. The fact that the only differences among the recovery curves at each temperature were the rate and magnitude of each stage indicated that the poisoning and recovery mechanisms were the same for the range of temperatures tested in this work. Figure 8-2 shows the values of the final percent recovery (y-axis on the right) as a function of temperature. The remaining percent permeance of N_03 during poisoning and after the recovery in pure H_2 slightly increased with temperature, showing that the amount of recoverable permeance increased with increasing temperature.

Figure 8-3 shows the amount of time required for the hydrogen permeance to stabilize during recovery in pure H_2 as a function of temperature. While recovery times were short (roughly 20 h) at 500ºC, the total time needed for the permeance to stabilize in pure H_2 greatly increased at lower temperatures. In addition, the rate of recovery of the linear stage increased with increasing temperature. Indeed, membrane regeneration at higher temperatures would be more reasonable in an industrial setting should a membrane become exposed to larger quantities of H_2S.

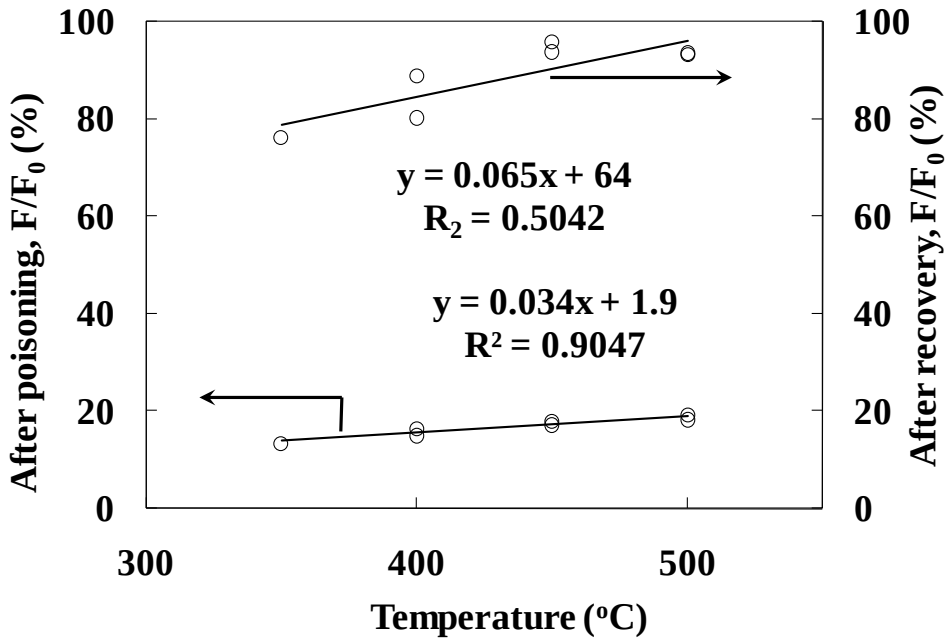

Figure 8-2 Percent of hydrogen permeance during exposure to 42.7 ppm H_2S/H_2 for two hours (y-axis on left) and percent of hydrogen permeance recovery after reintroducing pure H_2 (y-axis on right) as a function of temperature for N_03.

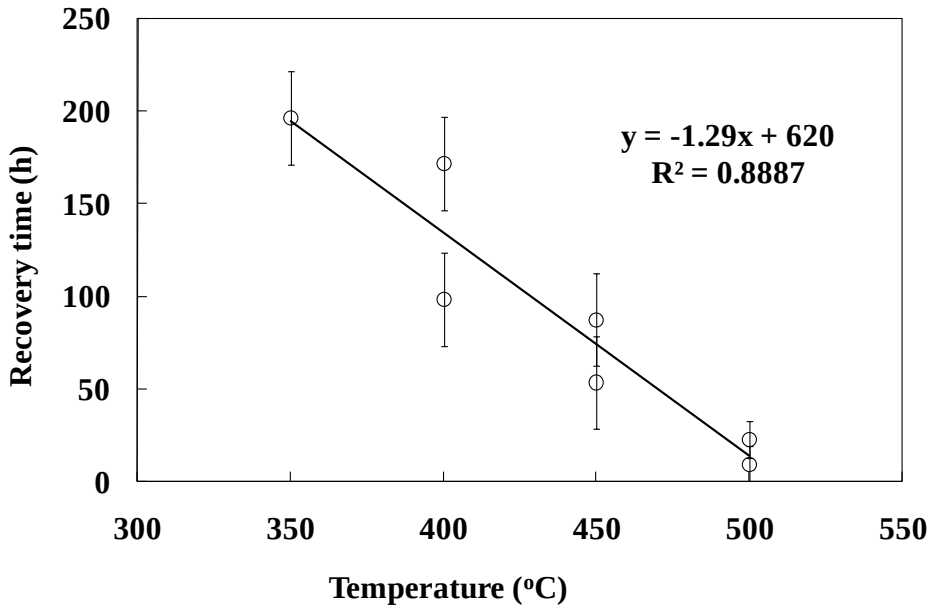

Figure 8-3 Time required for the hydrogen permeance to be recovered in pure H_2 as a function of temperature for N_03.

The dissociative chemisorption of H_2S on metals is an exothermic reaction:

$$H_2S + M \leftrightarrow S - M + H_2 \quad \Delta H_{ads} < 0 \tag{8.1}$$

and increasing the temperature of the system would shift the equilibrium of the reaction towards the reactants, resulting both in less H_2S chemisorption during poisoning and more H_2S desorption during recovery. Assuming that the poisoning is due primarily to sulfur adsorption on the membrane surface, higher temperatures would result in more overall tolerance. The increased rate of the permeance recovery with temperature seen in Figure 8-3 would be the result of the increased H_2S desorption rate but the increasing amount of recoverable permeance with increasing temperature would be due to the exothermic nature of the H_2S adsorption.

8.3.3 Effect of the length of H_2S exposure on membrane performance

Figure 8-4 shows the permeance decline and recovery for membrane N_08a which was exposed to 54.2 ppm H_2S/H_2 for 125 hours at 450ºC. The permeance dropped instantaneously and did not change throughout the lengthy exposure to the H_2S/H_2 mixture. The magnitude of the drop was ~80% of the original permeance at 450ºC, which was similar to the permeance drop that N_03 experienced at 450ºC. However, the period of recovery lasted over 500 hours, which was much longer than the 95 hours needed after the two hour exposure of N_03 at 450ºC seen in Figure 8-3. Moreover, only 65% of the permeance of N_08a was recovered in comparison to the 95% that was recovered with N_03 at 450ºC

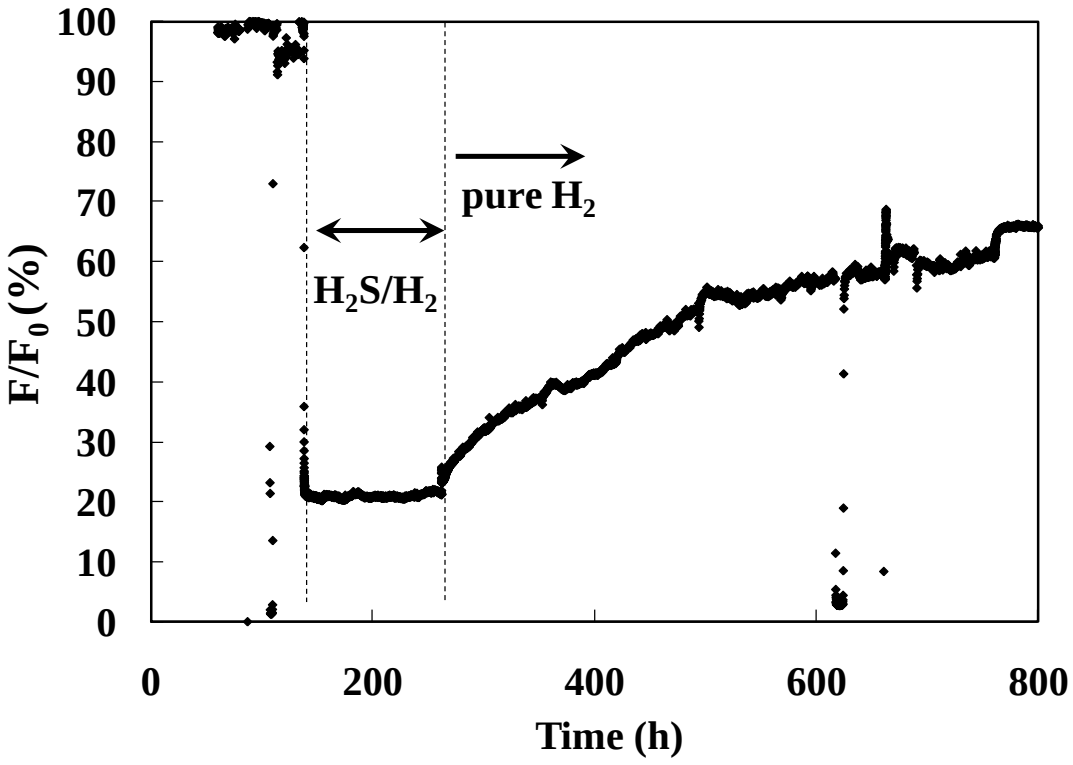

Figure 8-4 Permeance as a function of time for N_08a during the exposure to 54.2 ppm H_2S/H_2 at 450ºC and the recovery in pure H_2.

The decreasing amount of recovered permeance showed that the irreversibility of the membrane poisoning increased with the H_2S exposure time. The longer period of recovery was due to the system becoming saturated with H_2S, as explained in Section 9.3.3. If the irrecoverable permeance was caused by adsorbed sulfur, either at binding sites with very high binding energies or in subsurface adsorption sites, the amount of sulfur at these sites would gradually increase with increased exposure time. Since increasing the amount of sulfur on the surface decreased the bond strength of the adsorbed sulfur (Alfonso, 2005), it would appear that it was the amount of subsurface adsorbed sulfur which increased with exposure time, thereby increasing the irreversibility of the membrane poisoning.

The activation energy of hydrogen permeation of N_08a after the permeance recovery was 13.8 kJ/mol shown in Figure 8-5. The fact that the activation energy did not significantly change before (15.0 kJ/mol, shown in Figure 5-11) and after the H_2S testing indicated that the sulfur which remained adsorbed on the membrane did not significantly change the hydrogen transport mechanism, even though the permeance was not recovered at that given temperature. In addition, the negligible change in the activation energy indicated that the remaining adsorbed sulfur caused a decrease in the effective membrane area for the H_2 adsorption and did not cause the formation of bulk sulfides.

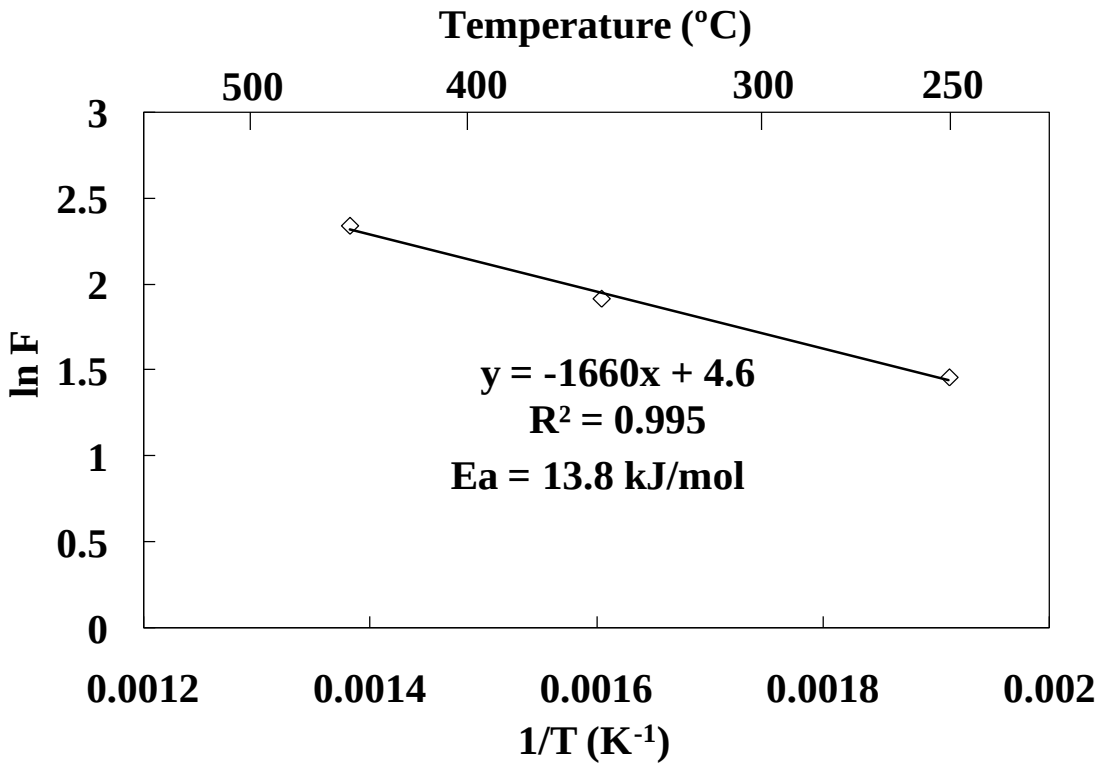

Figure 8-5 Activation energy of N_08a after the H_2S testing and recovery.

Following the experiments described in Section 8.3.2, N_03 was tested in 54.8 ppm H_2S/H_2 for 2, 8, 29, 50, 94 and 59 hours (in that order) at 450ºC with the permeance recovery in pure H_2 monitored in between each poisoning experiment. The effect of H_2S poisoning on the selectivity was examined by measuring the He leak before and after each exposure to the H_2S/H_2 mixture.

Figure 8-6 shows the poisoning for eight hours and subsequent recovery of membrane N_03. As with the two hour poisoning shown in Figure 8-1, the introduction of 54.8 ppm H_2S caused an instantaneous drop in permeance to roughly 20% of the original value at 450ºC, after which the permeance remained stable. However, there were a few differences between the eight hour poisoning shown in Figure 8-6 and the two hour poisoning shown in Figure 8-1. The first was that the permeance of the membrane started off at roughly 85% of the original permeance before the eight hour poisoning due to the remaining sulfur on the membrane from the set of experiments presented in Sections 8.3.1 and 8.3.2. The second difference was that the jump seen upon the reintroduction of pure H_2 for the eight hour poisoning was not as large as with the two hour poisoning due to the accumulation of H_2S on the walls of the system during the longer poisoning time. Indeed, no jump at all is seen with the 125 hour poisoning of N_08a seen in Figure 8-4. The third difference was that the linear and final stages of recovery lasted longer in the case of the eight hour poisoning due to the difficulty in flushing out the greater quantity of H_2S as it desorbed from the system, as was also seen in Figure 8-4.

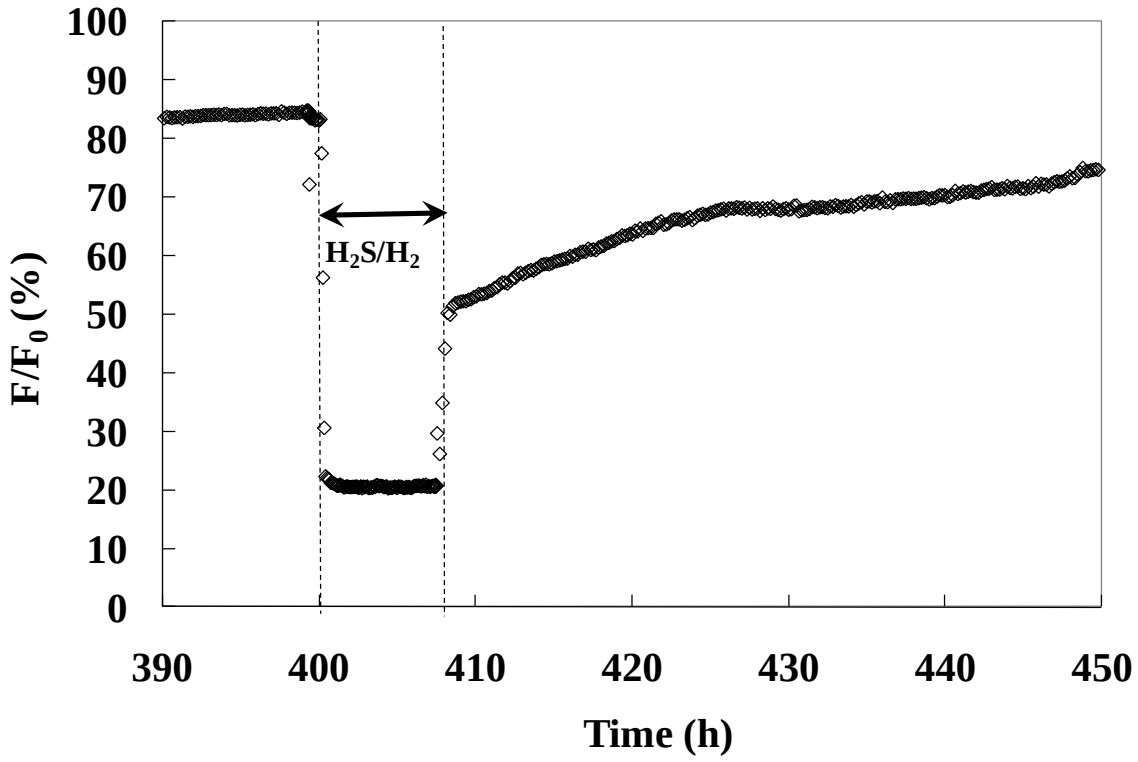

Figure 8-6 The poisoning of N_03 at 450ºC in 54.8 ppm H_2S/H_2 for 8 hours and the recovery in pure H_2.

Figure 8-7 shows the final value of the permeance recovery as a function of cumulative exposure time to the H_2S/H_2 mixture (not including the recovery time in pure H_2). After exposure to the H_2S/H_2 mixture for two and eight hours, the percent recovery was 85%, only slightly lower than the percent recovery which was measured at 450ºC during the previous experiments shown in Figure 8-2. However, after a cumulative exposure time of 250 hours, the recovery appeared to have reached a limiting value at 60%. The decline in the total permeance recovery with time proved that not only was the H_2S poisoning mechanism irreversible at a given temperature, but also that the extent of the irreversible poisoning increased with time. Previous studies have concluded that the extent of H_2S poisoning of Pd and Pd alloy membranes was dependent upon the H_2S concentration and temperature (Kulprathipanja et al, 2005, Morreale et al, 2004) but not upon the time of exposure. However, permeance recovery experiments were not performed in these studies.

The results of the permeance recovery of N_08a were superimposed on the results from N_03 in Figure 8-7. The percent recovery of N_08a after one lengthy exposure to the H_2S/H_2 mixture fell only slightly below the curve for N_03 which had several recovery periods in between each exposure to the H_2S/H_2 mixture. Therefore, the recoverable permeance was solely dependent on the total amount of poisoning time, regardless of whether or not the membrane was recovered intermittently by flushing the system in hydrogen.

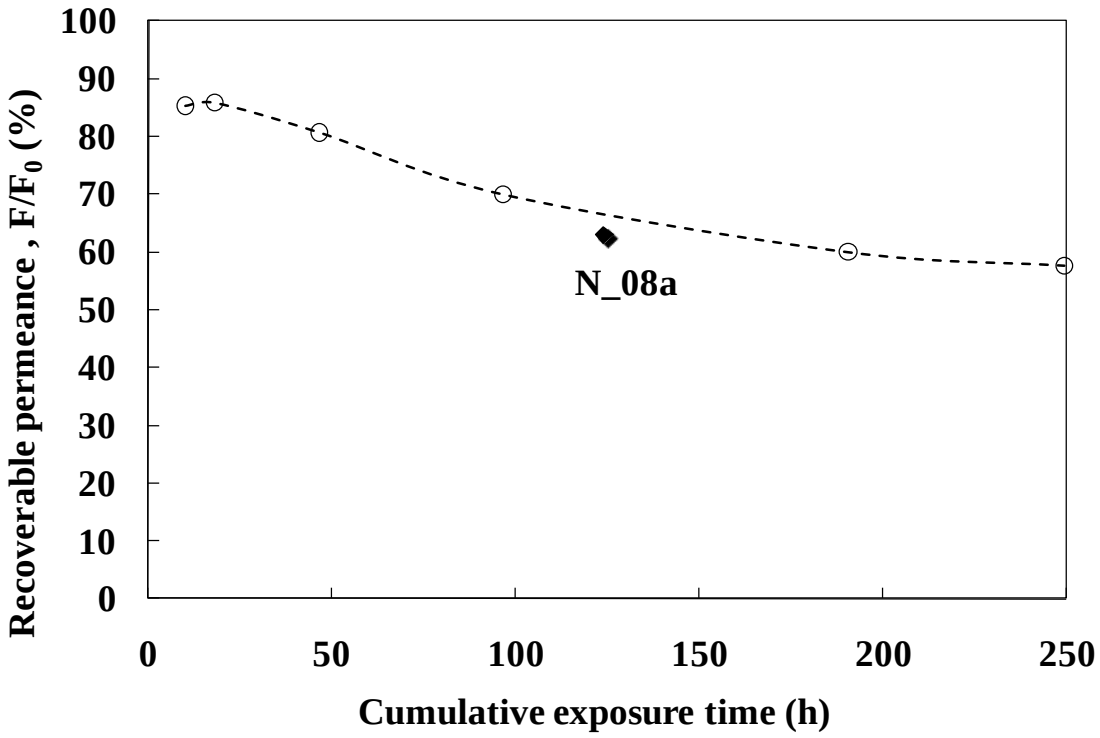

Figure 8-7 The total permeance recovery as a function of cumulative exposure time to the H_2S/H_2 mixture for membrane N_03 at 450ºC. The results for the poisoning of membrane N_08a at 450ºC were superimposed on the graph for comparison. The line is for guiding the eye.

8.3.4 Effect of H_2S exposure on leak stability

Figure 8-8 shows the He leak as a function of time for membrane N_03 while N_03 was being characterized in pure H_2 and during the series of H_2S testing and permeance recoveries. The ideal H_2/He separation factors are shown in parentheses. At the beginning of the characterization, the He leak could not be detected. The progression of the He leak over time during the long-term testing of N_03 shown in Figure 8-8 shows a contrast in the trend before and after the H_2S testing. During the long-term characterization in pure H_2, the He leak of N_03 increased and the ideal H_2/He separation factor decreased.

After the poisoning and recovery experiments began, the He leak remained relatively stable for 1500 hours, oscillating between 0.8 – 1 sccm, and then decreased drastically to 0.13 sccm after an additional 500 hours. The leak oscillated between 0.13 – 0.3 sccm for the next 2000 hours of testing at 450ºC, and did not show a steady increase. Not only did the leak stop increasing with the onset of the H_2S experiments, but the leak decreased to values towards the beginning of the characterization. However, the ideal H_2/He separation factor decreased at times even though the He leak lessened because the permeance of N_03 did not recover to the original value after the H_2S poisoning. Even so, the ideal H_2/He separation factor at 450°C at the beginning of the H_2S testing was 83 and increased to 540 as the H_2S testing progressed over a period of 1800 hours, despite the fact that the permeance decreased.

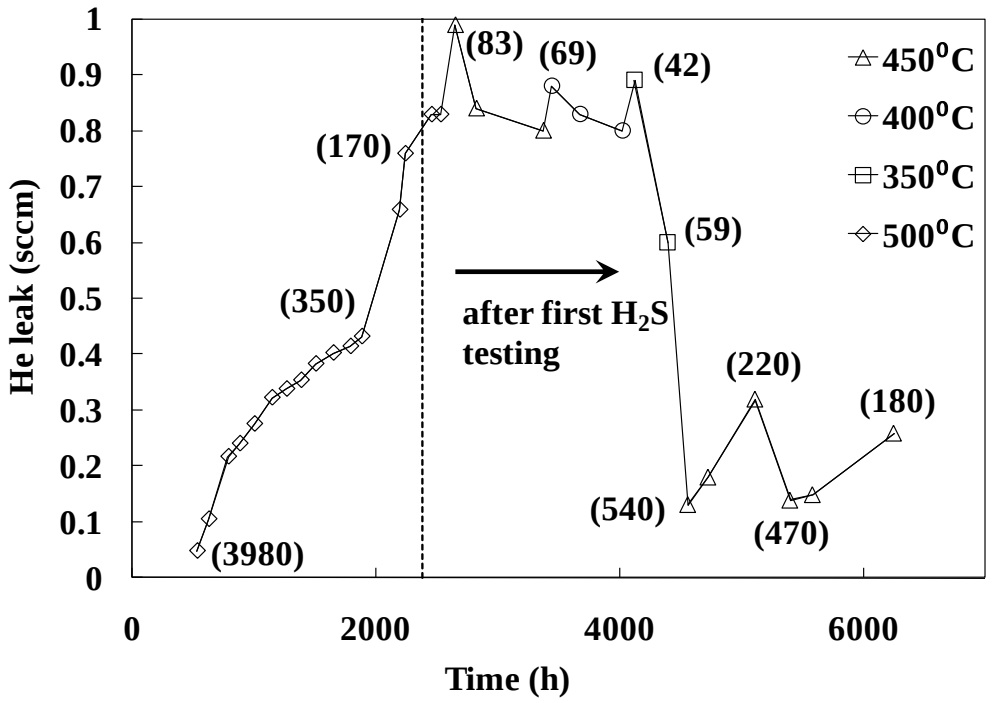

Figure 8-8 He leak as a function of time for membrane N_03. Ideal H_2/He separation factors are shown in parenthesis. The line is for guiding the eye.

Similar to the results of N_03, the leak of N_08a increased at 450ºC from 0.1 to 1.2 sccm (shown in Figure 8-9) over a period of 300 hours and the ideal H_2/He separation factor decreased from 1770 to 220 before the H_2S testing. After the H_2S testing began, the He leak decreased from 1.2 to 1 sccm over a period of 800 hours at 450ºC.

Likewise, the leak of N_02 exhibited a clear upward trend during the long-term testing in H_2 at 500ºC, shown in Figure 8-10. After the poisoning and recovery experiments began, the He leak decreased and the ideal H_2/He separation factor increased until the membrane became dense again, while still being tested. N_02 continued to be dense 200 hours later.

Exposing electroless deposited Pd and Pd alloy membranes, which have not been fabricated to hinder leak development, to elevated temperatures caused leaks to develop over time due to grain coarsening as grain boundaries migrated to equilibrate the surface tensions and reduced the total energy of defects within the Pd lattice. Saini (2006) observed that after annealing at 500ºC in both H_2 and He atmospheres, the grains of electroless deposited Pd grew larger. The grain growth would continue until reaching a static equilibrium where the surface tensions of the adjoining grain boundaries were equal. Guazzone et al. (2006b) observed that microstrains and stresses in the deposit released upon heating caused pinhole formation and growth. Indeed, past research (Saini, 2006, Guazzone et al, 2006b, Guazzone and Ma, 2008) indicated that the He leak of electroless deposited Pd membranes increased during the membrane characterization.

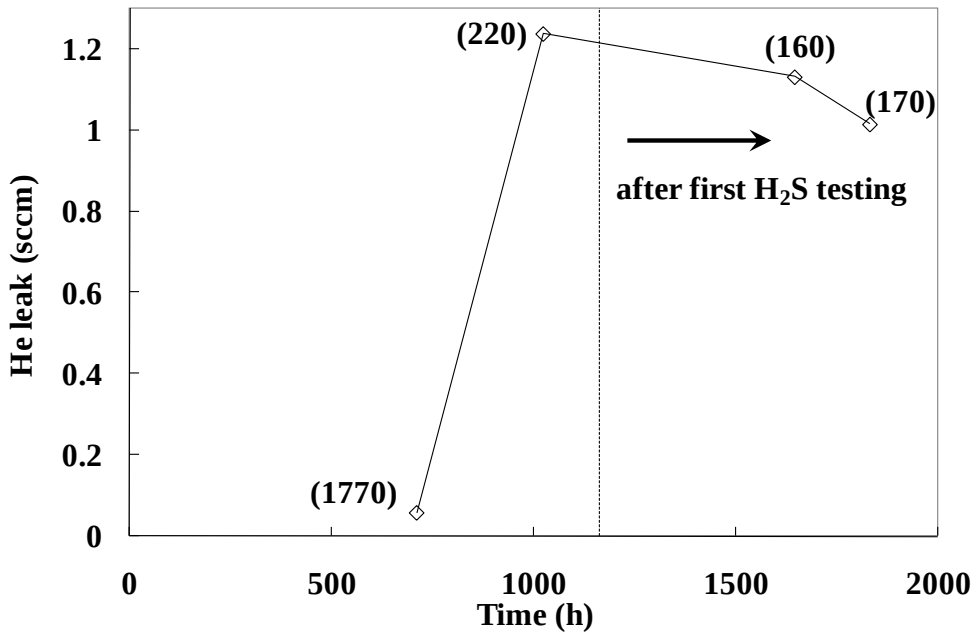

Figure 8-9 He leak as a function of time for N_08a at 450ºC. Ideal H_2/He separation factors are shown in parenthesis. The line is for guiding the eye.

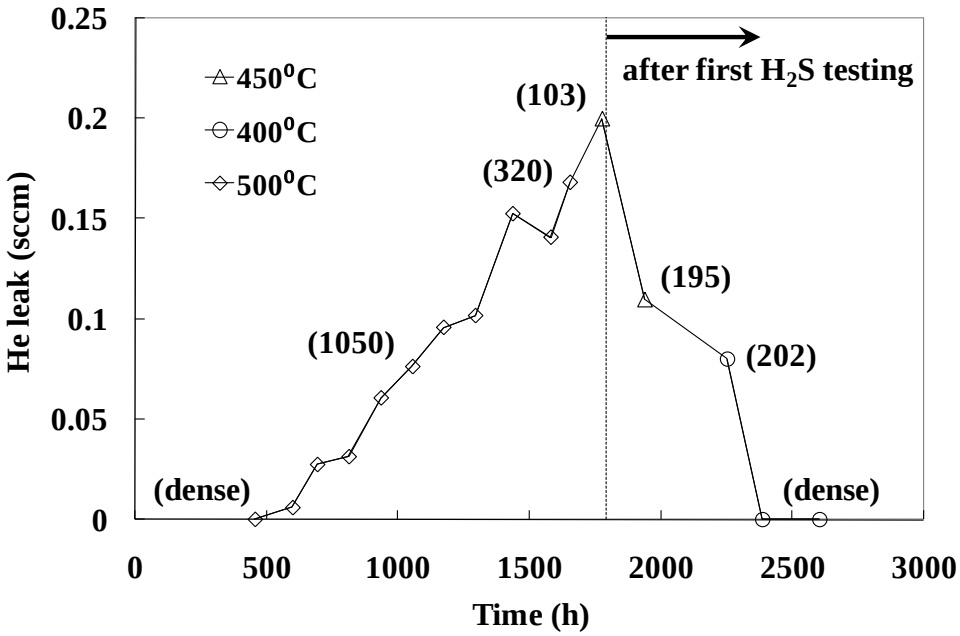

Figure 8-10 He leak as a function of time for N_02. Ideal H_2/He separation factors are shown in parenthesis. The line is for guiding the eye.

Also, according to the dusty gas flow model (Mason and Malinauskas, 1983) the flux of non-permeable gases should increase with decreasing temperature. The work of Mardilovich et al. (1998) showed the increase of the He leak of Pd membranes with decreasing temperature both computationally and experimentally. However, Figure 8-8 shows that the He leak of N_03 decreased from 0.99 sccm at 450ºC to 0.6 sccm at 350ºC. Furthermore, Figure 8-10 shows that N_02 had a He leak of 0.2 sccm at 500ºC and eventually became undetectable during testing at 400ºC.

Since either a small change or a reduction was seen in the He leak after the initiation of the H_2S testing and a decrease in the He leak was observed with a decrease in temperature, it could be concluded that the exposure to the H_2S/H_2 mixture not only prevented the He leak growth but even decreased the leak at times. The reason for the unusual effect that H_2S had on the leak growth could be due to sulfur segregation in the grain boundaries of the membrane. Non-permeable gases could only permeate through grain boundaries, cracks, defects, and pinholes in the membrane layer. It was precisely to these areas that impurities would segregate with sulfur being no exception. Indeed, sulfur was detected by EDX in the grain boundaries of Pd membranes tested with gas mixtures containing H_2S (Iyoha et al, 2007a) and the phenomenon of sulfur segregation in grain boundaries has also been investigated in Fe (Ainslie et al, 1960). If sulfur segregated to the grain boundaries and defects, it would reduce the area of the openings of pathways for non-permeable gases if not blocking them completely.

Furthermore, hydrogen would also be hindered from passing through the pathways between the defects and grain boundaries. A portion of the permeance which

was not recovered with N_03 and N_08a would also be partially due to the blockage of pathways.

8.3.5 Surface morphology

Figure 8-11, Figure 8-12 and Figure 8-13 show respectively the surfaces of N_08a, N_02 and N_03 after testing. No evidence of bulk sulfide formation in the morphology of the Pd/Cu deposit could be seen on N_02, which was exposed to the H_2S/H_2 mixture for a total of 8 hours, N_03, which was exposed to the H_2S/H_2 mixture for a total of 250 hours or N_08 which was exposed to the H_2S/H_2 mixture for a total of 150 hours. The EDX analysis was not able to detect the presence of sulfur on either membrane surface. The only visible peaks in the spectrum in Figure 8-11d were of Pd, Cu, O and C. However, with a penetration depth of 0.2 – 0.8 μm for EDX, the remaining adsorbed sulfur following the permeance recovery would be undetectable by this method of analysis. A more in depth discussion of the adsorption of S to Pd/Cu alloys is discussed in Chapter 9.

EDX spot scans from a magnification of 2 kX showed that the surface Cu content ranged from 10 – 30 wt% for N_02, from 10 – 20 wt% for N_03, and from 20 – 30 wt% for N_08a, confirming that the top layers of the Pd/Cu membranes were indeed in the more sulfur tolerant fcc region of the Pd/Cu phase diagram. However, the composition of the top atomic layer could have a much higher Cu content. Surface studies have shown that heat treated Pd/Cu alloys formed a top atomic layer which had a composition more conducive to the bcc phase (Miller et al., 2008a, Miller et al., 2008b).

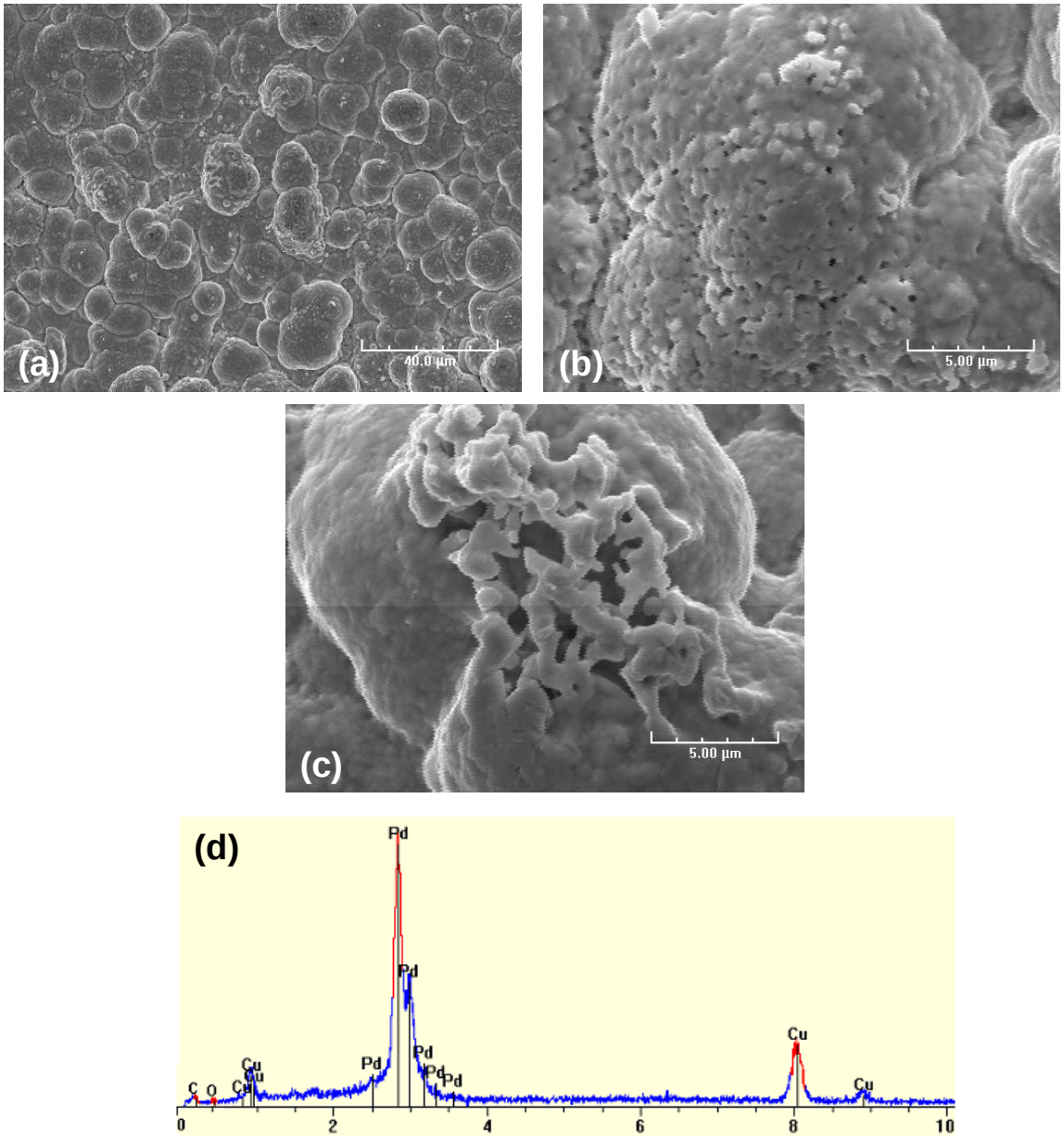

Figure 8-11 SEI micrographs of the surface of N_08a after testing at (a) 1 kX (b) 5 kX and (c) 5 kX and (d) the EDX spectra for the area scan.*

* The EDX spectra were similar for the surfaces of N_08a, N_02 and N_03. Therefore, only the spectrum for N_08 was presented.

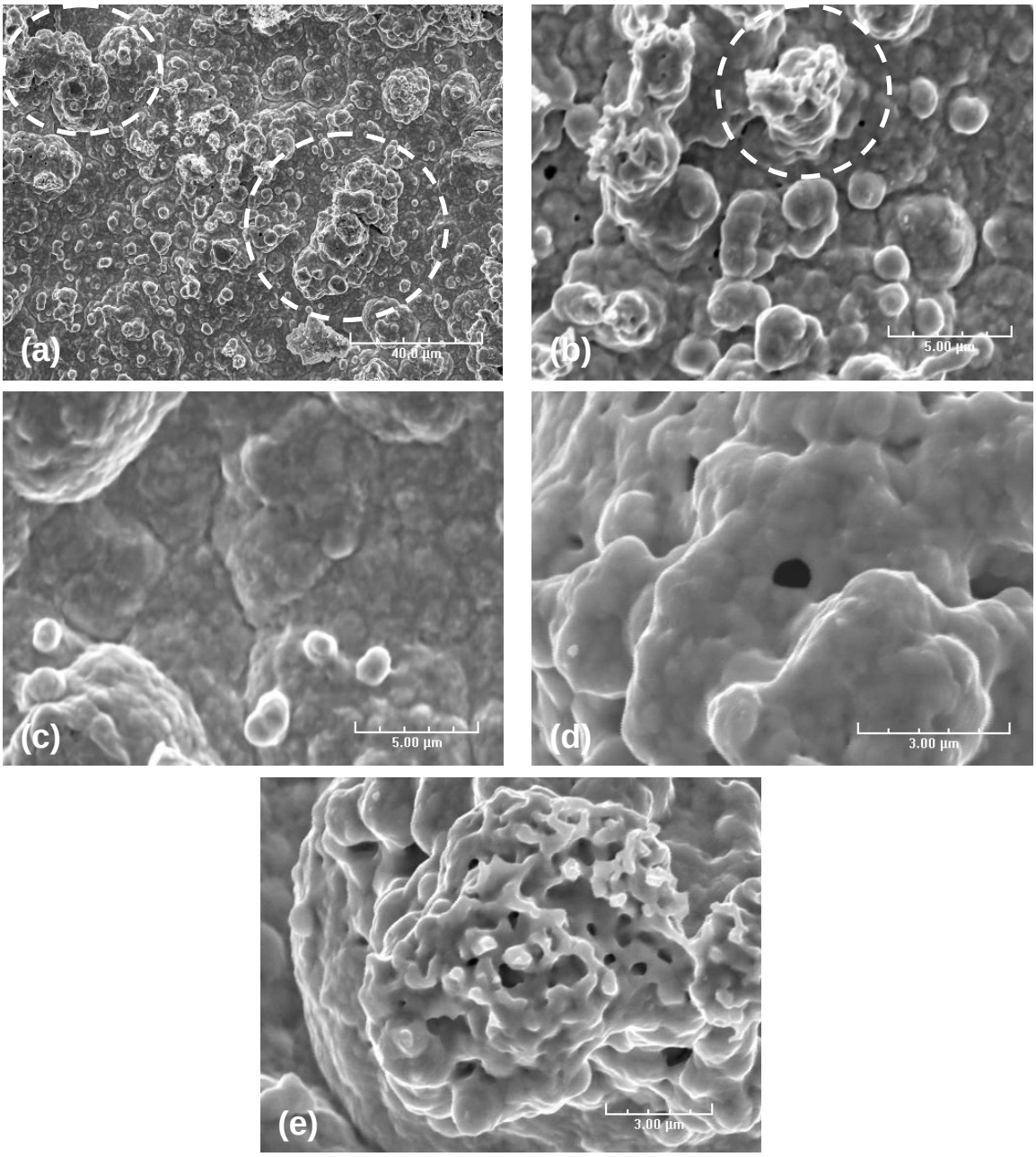

Figure 8-12 SEI micrographs of the surface of N_02 after testing at (a) 1 kX (b) 5 kX (c) 5 kX (d) 7 kX and (e) 7 kX.

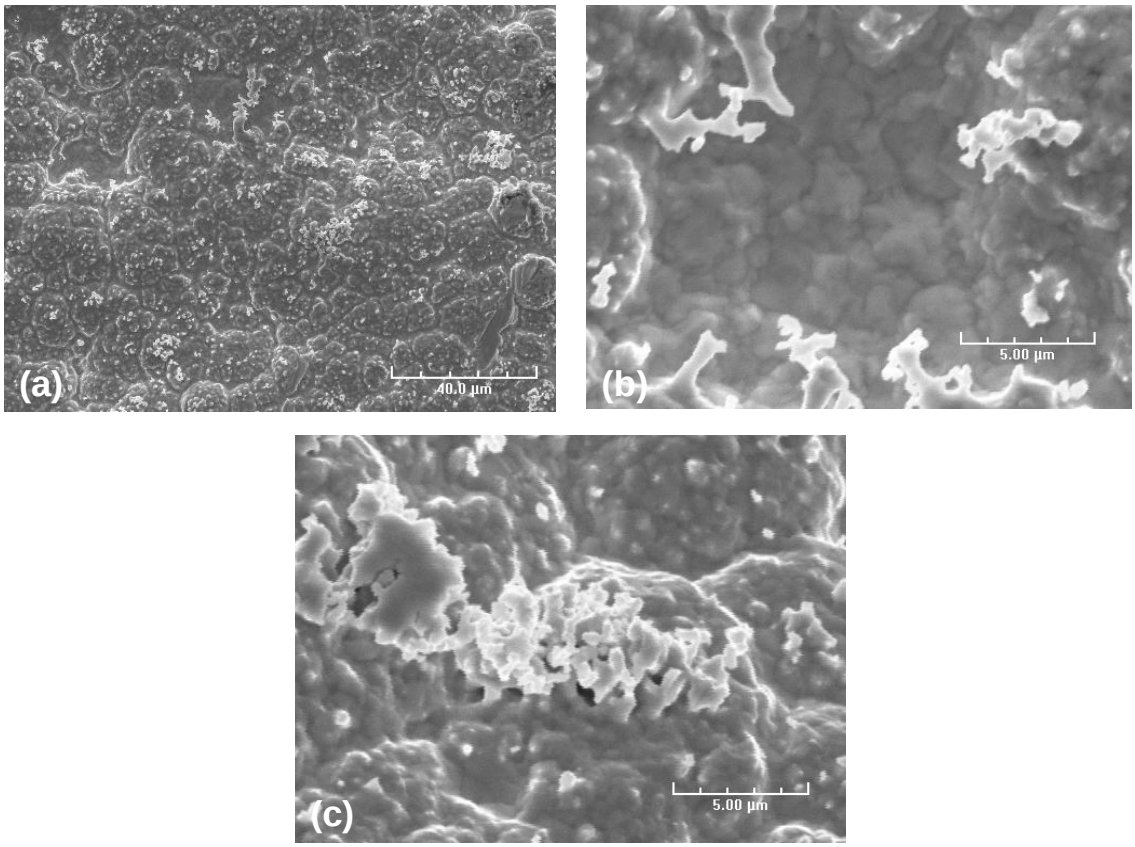

Figure 8-13 SEI micrographs of the surface of N_03 after testing at (a) 1 kX (b) 5 kX and (c) 5 kX.

In addition, the EDX analysis showed that the surface compositions were not uniform. The non-uniformity in Cu surface composition would have caused differing binding energies in the sulfur binding sites (Alfonso et al., 2003). The surface morphologies in Figure 8-11a and Figure 8-13a were more uniform than in Figure 8-12a. N_02 had Cu deposits accumulated one on top of the other whereas the deposits of N_03 and N_08a were much smoother. The accumulated stacks of Cu deposits are circled in Figure 8-12a and b. Some areas of N_02 did have a smoother deposition, as seen in Figure 8-12c. Usually the Cu was plated in one round of plating and the result was a smoother morphology than the morphology of N_02, such as the Cu plated coupons seen in Figure 4-6a. However, the Cu layer of N_02 was plated in two rounds of plating and it is likely that the activation layer for the second round of plating was not uniform, thus causing the accumulation of Cu in stacks.

Additionally, various holes in the membrane surfaces were observed, as seen in Figure 8-12b and d, which appeared to be due to grain coarsening. Sometimes the holes occurred in clusters, as seen in Figure 8-11b, and were likely formed due to the Kirkendall effect, which is explained in more detail in Section 4.3.2. On all three membranes, there were some areas where a porous structure was atop the dense Pd/Cu alloy as seen in Figure 8-11c, Figure 8-12e and Figure 8-13c. Again, the porous alloy was formed due to the Kirkendall effect. Similar porous alloys were seen atop annealed Pd/Cu bi-layers in Figure 4-6b, c and d and by Guazzone (2006). EDX scans did not detect a significant difference in Cu content between the porous and non-porous morphologies.

8.4 Conclusions

The work in this chapter has tested the effect of the H_2S exposure on the long-term stability of Pd membranes with a Pd/Cu top layer in the more H_2S tolerant fcc phase. One of the unique features of the work, but rarely reported in the literature, is the unusually long testing time of thousands of hours, which was necessary to fully understand the characteristics of the poisoning and recovery and their effects on the membrane permeation properties. The exposure of the membranes to approximately 45 – 55 ppm H_2S/H_2 resulted in a significant decrease in hydrogen permeation due to sulfur adsorbing on the membrane surface and blocking hydrogen adsorption sites. The hydrogen permeance could be mostly regenerated in pure H_2 with the amount recovered and rate of recovery increasing with increasing temperature due to the exothermic nature of H_2S adsorption and the increasing rate of desorption with temperature.

The lack of a complete permeance recovery was due to irreducible surface sulfides which reduced the effective membrane area for hydrogen adsorption. The amount of the irreducible surface sulfides increased with increasing exposure time, reaching a limiting value, and also with decreasing temperature. The He leak of the Pd/Cu membranes oscillated and even decreased over time following the initiation of the H_2S testing, most likely due to sulfur segregating to grain boundaries and defects and reducing the area of the pathway for non-permeable gases.

The Pd/Cu membranes showed stability over the period of long-term testing and cycling among H_2, He and H_2S/H_2 mixtures. In the event of approximately 45 – 55 ppm H_2S/H_2 reaching the Pd/Cu membranes, the membranes would not necessitate

replacement since the selectivity would be retained, and might only suffer a minor loss in permeance depending on the length of exposure. Flushing the membrane with pure H_2 at high temperatures would regenerate the majority of the permeance.

9. Surface interactions between sulfur and Pd and Pd/Cu alloys

9.1 Introduction

The results of Chapter 8 showed that only part of the membrane permeance could be recovered with fcc Pd/Cu membranes at the temperatures tested, and that the amount of recoverable permeance decreased with the total exposure time to H_2S. However, while there were surface studies which have investigated the poisoning of both Pd and Pd/Cu surfaces, no one has reported results investigating the recovery of poisoned membranes. Examining poisoned samples which have been recovered could serve to elucidate the cause of the permeance which was not recovered. Furthermore, there were no high resolution XPS surface studies, in the literature to study the nature of the bond between sulfur and the Pd and Pd/Cu surfaces.

The work in this chapter aimed to do two things. The first was to investigate the nature of the sulfur poisoning and recovery of both Pd and Pd/Cu alloys with high resolution XPS studies that have been poisoned and recovered with a broad range of temperatures. The second was to further examine the nature of the permeance of fcc Pd/Cu membranes which was not recovered after long-term poisoning and recovery periods and apply the knowledge gained from the XPS studies to the results of the membrane characterization.

9.2 Experimental

Coupons were oxidized at 700 - 800ºC for 12 hours and plated with approximately 10 – 12 μm of Pd. The Pd samples were plated with an additional 1 – 1.5 μm of Cu. The Pd/Cu samples were annealed for 12 hours in H_2 at 600°C to form the fcc alloy on the surface. The samples were poisoned with concentrations of H_2S varying from approximately 0.5 – 50 ppm between the temperatures of 350 - 500ºC for 12 – 24 hours and recovered in H_2 for 1.5 - 12 hours at temperatures varying between 350 - 500ºC. The Pd coupons were analyzed with the Kratos Axis Ultra XPS at MIT and the Pd/Cu coupons were analyzed with the Thermo Scientific K-alpha at ORNL, as described in Section 3.3.3.

The specifics of the membranes presented in this chapter are listed in Table 9-1. The preparation, characterization and poisoning of N_03 were described in more detail in Chapter 8, the preparation and characterization of N_20 and N_21 are detailed in more Chapter 7 and the poisoning of N_12, N_20 and N_21 is discussed in Chapter 10. The characterization of N_09 and N_12 is briefly discussed in Chapter 7 and the poisoning of N_09 is discussed in this chapter.

Table 9-1 Membranes presented in this chapter.

membrane	intermetallic diffusion barrier	grading	Pd glue (μm)	Pd/Ag barrier (μm)	Pd layer (μm)	Cu layer (μm)	total thickness (μm)	wt% Cu
N_03	air/700ºC/12 h	none	none	none	12.5	1.5	14.0	8
N_09a*	air/700ºC/12 h	Al_2O_3	3.3	4.3	7.9	1.6	17.1	7
N_12	air/700ºC/12 h	Al_2O_3	1.4	2.8	4.7	4.7	13.6	28
N_20	air/700ºC/12 h	Al_2O_3	1.6	6.1	11	0.3	19.0	2
N_21**	air/700ºC/12 h	Al_2O_3	3.7	2.1	3.2	0.6	14.5	5

* N_09a was a Pd membrane that developed a leak of 80 sccm shortly after the characterization. The membrane was replated with Pd and Cu and characterized. Due to the large leak of the membrane before the repairs, the hydrogen permeance results were not presented.

** After annealing N_21 for 12 hours in He during fabrication, a mass loss equal to 4.9 μm of Pd was observed. While a small mass loss was observed after the first annealing step with N_13, N_16 and N_09a, typical values ranged in a mass equivalent from 0.5 – 1.5 μm of Pd and were assumed to be negligible. It is possible that the thickness of N_21 was slightly more than what was recorded here.

9.3 Results and Discussion

9.3.1 Poisoned Pd

To assess the effect of the temperature of H_2S poisoning, the Pd samples were exposed to either a 54.8 ppm H_2S/H_2 mixture or pure H_2 atmosphere for 24 hours for the temperature range of 350ºC to 500ºC. Figure 9-1a shows the EDX spectra of the annealed coupons. The top spectrum was taken from the Pd sample annealed at 350ºC in 54.8 ppm H_2S/H_2 and exhibited a very large sulfur presence with an S/Pd atomic ratio of 0.14. The corresponding XRD pattern in Figure 9-1b shows the presence of both Pd and the bulk sulfide Pd_4S. In contrast, the coupons annealed at 400, 450 and 500ºC in 54.8 ppm H_2S/H_2 had no detectable sulfur (bottom EDX spectrum in Figure 9-1a) and their XRD patterns were similar to the XRD patterns of the Pd coupons annealed in pure H_2 (Figure 9-1b).

Figure 9-2a shows the uniform granular morphology of the deposited Pd annealed in hydrogen. However, the Pd_4S scale formation (Figure 9-2b) caused a smooth coral-like structure to form on top of the Pd clusters of the coupon annealed at 350ºC in 54.8 ppm H_2S/H_2. While Pd has a fcc structure with a lattice parameter of 3.9 Å, Pd_4S has a tetragonal structure with lattice parameters of 5.1 Å and 5.6 Å. The lattice reordering due to the formation of the bulk Pd sulfide caused the drastic change in the morphology. Therefore, the bulk sulfide formation in a membrane would cause such irreparable damage to the selectivity that the membrane would only have Knudsen selectivity towards hydrogen (Kulprathipanja et al., 2005, Chen and Ma, 2010a).

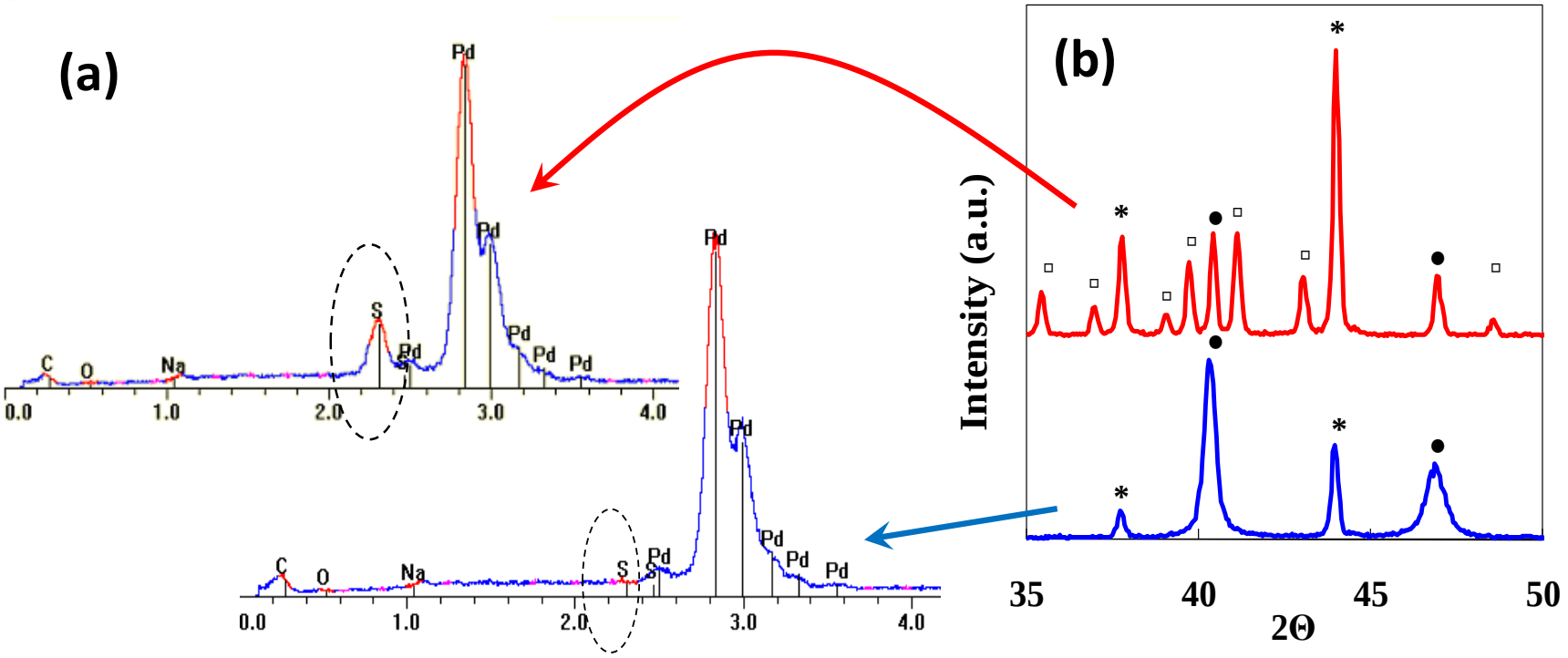

Figure 9-1 (a) EDX spectrum for the Pd coupon annealed at 350ºC in 54.8 ppm H_2S/H_2 (top) and for the remaining annealed Pd coupons (bottom). (b) Corresponding XRD patterns: (*) - Al sample holder, (●) - Pd, (▫) - Pd_4S.

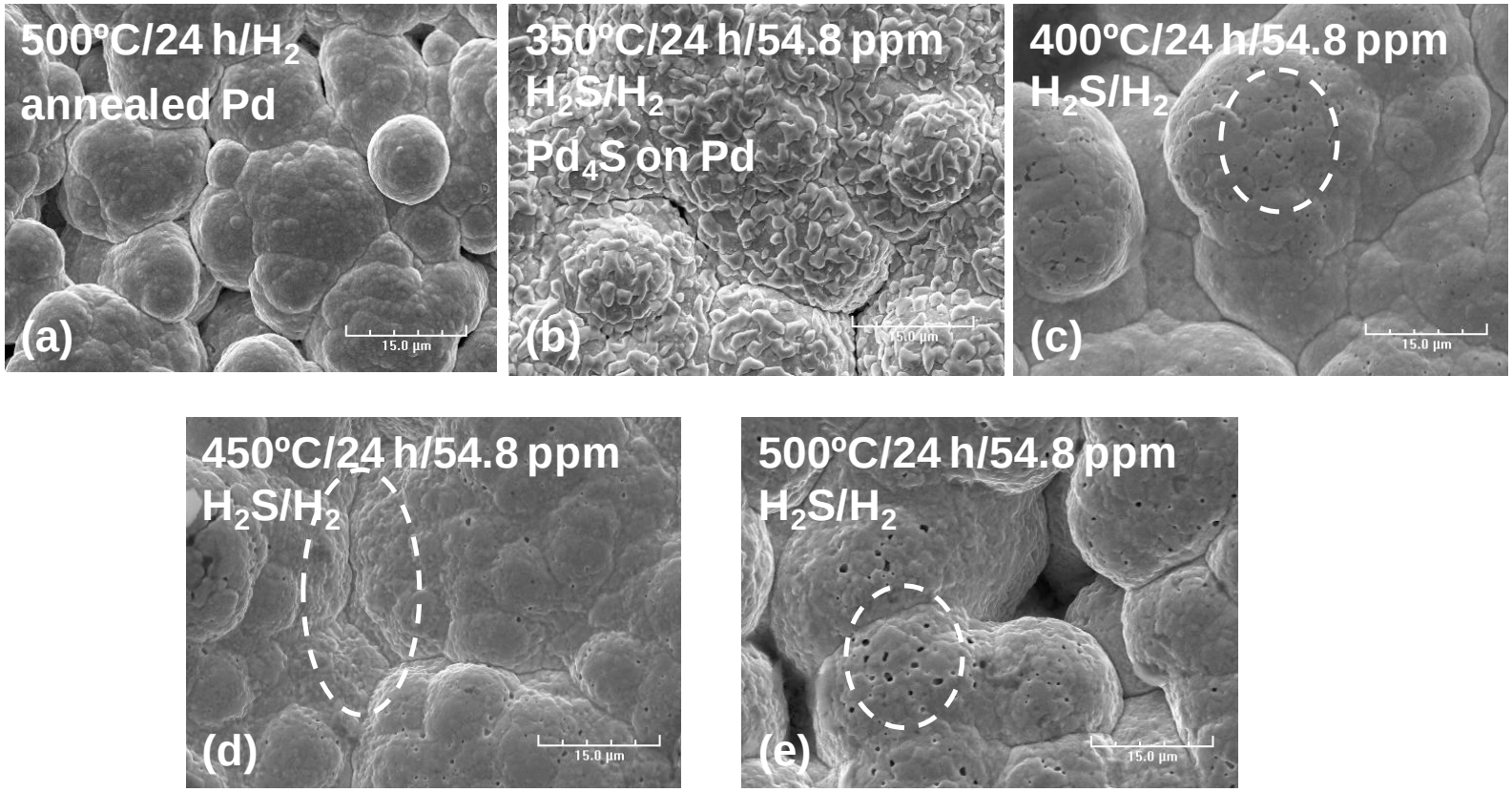

Figure 9-2 SEI micrographs of surfaces of the annealed Pd samples.

While the coupon annealed at 350ºC showed a drastic change in the morphology, the Pd coupons annealed in 54.8 ppm H_2S/H_2 at 400, 450, and 500ºC did not exhibit such drastic changes in the morphology. Rather, they showed a morphology that was somewhat chunkier than unpoisoned Pd samples which is sometimes seen with annealed Pd samples (circled in Figure 9-2d) and pores which formed at the cluster boundaries (circled in Figure 9-2c and Figure 9-2e) due to grain coarsening. Since neither EDX nor XRD could detect the presence of sulfur or a bulk palladium sulfide (Figure 9-1), it appeared that any sulfides on the samples would have been in the form of surface sulfides due to the dissociative chemisorption of H_2S. The performance of a Pd membrane with adsorbed sulfur would deteriorate due to a decrease in the permeance caused by the adsorbed sulfur preventing the H_2 adsorption, and a decrease in the selectivity caused by the pore formation.

To characterize the nature of the adsorbed sulfur on the Pd surface, XPS was used. Figure 9-3a shows the peak fitting of the Pd sample annealed at 400ºC in 54.8 ppm H_2S/H_2. The standards used for the Pd – S and Pd – Pd chemistry shapes were from the samples annealed at 350ºC in 54.8 ppm H_2S/H_2 (shown in Figure 9-3b) and 500ºC in pure H_2 respectively. The areas of the two standards combined to give the measured signal from both Pd – Pd and Pd – S chemistries with the ratio of the peak areas equaling the ratio of each respective chemistry.

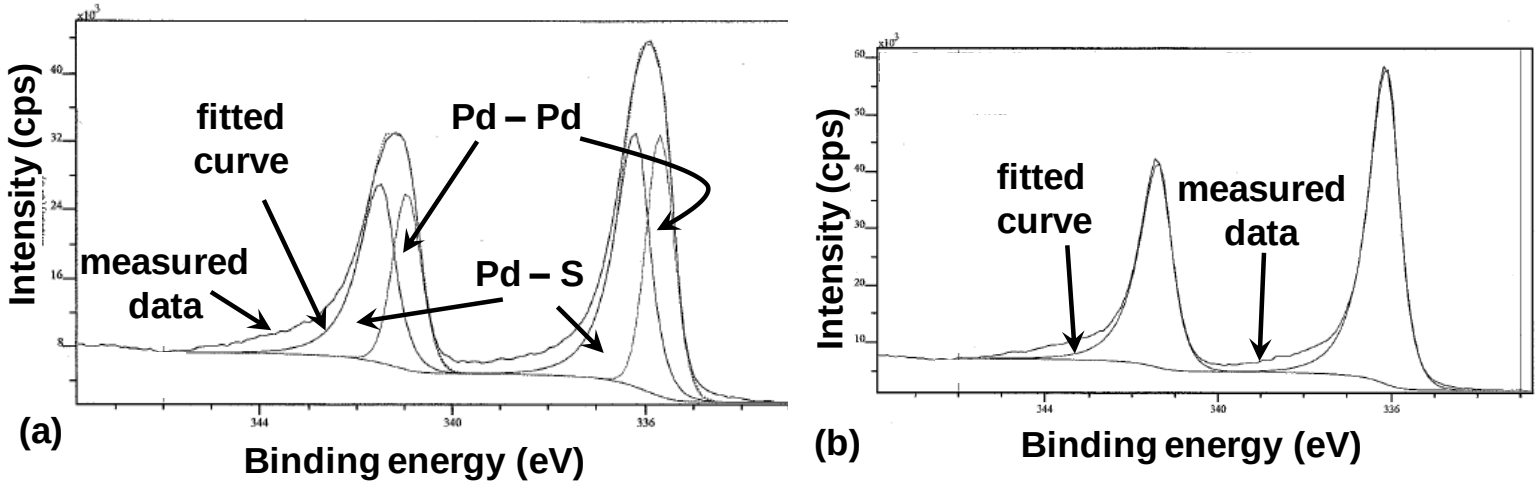

Figure 9-3 Peak fitting of the high resolution XPS data from the Pd coupons annealed at (a) 400ºC in 54.8 ppm H_2S/H_2 for 24 hours and (b) 350ºC in 54.8 ppm H_2S/H_2 for 24 hours.

As can be seen in Figure 9-3a, there was a slight difference between the fitted curve and the measured data where the peaks had tails towards the higher binding energy values. The difference was due to the fact that the Pd – Pd peaks had tails which could not be fitted exactly. This was most likely due to the effect of free electrons in metal bonds on the peak signal, which caused asymmetric peak tails that the CasaXPS software (Fairbanks and Carrick, 2005) was not able to properly fit. The effect on the quantitative analysis would be that the actual amount of the Pd – S chemistry in relation to the Pd – Pd chemistry would be slightly lower than what was calculated.

Figure 9-4 shows the XPS survey spectra for the annealed samples. The top spectrum was for the Pd sample annealed at 500ºC for 24 hours in H_2. The spectrum exhibited the characteristic Pd peaks which were the most prominent, the Auger KLL peak for oxygen, a carbon 1s peak, and a nitrogen 1s peak. The latter three were most likely from the acetone and ethanol used to clean the samples prior to the XPS characterization. The spectra for the samples annealed at 500ºC (middle spectrum) and 350ºC (bottom spectrum) in 54.8 ppm H_2S/H_2 were similar to the spectra of the samples annealed in pure H_2 with the exception of the presence of the 2s and 2p sulfur peaks. The presence of the sulfur peaks showed that sulfur had indeed adsorbed on the Pd surfaces following the exposure to the H_2S/H_2 mixture. Similar results were seen with the Pd samples annealed at 400 and 450ºC in 54.8 ppm H_2S/H_2.

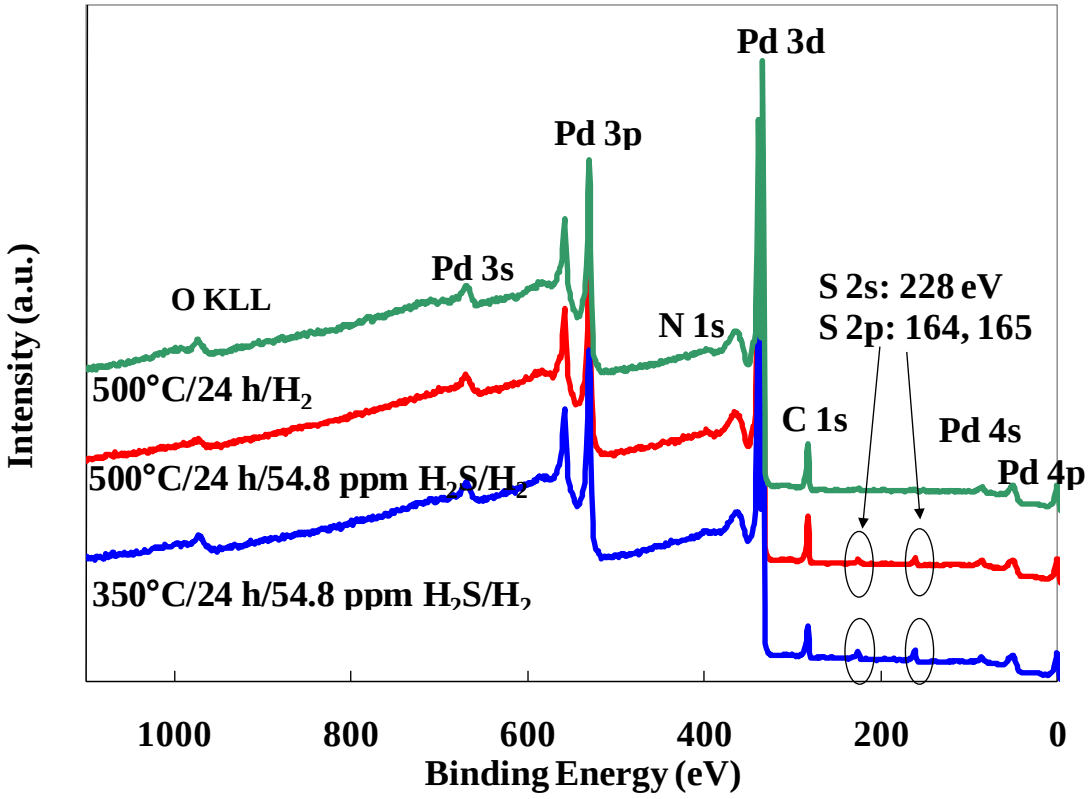

Figure 9-4 XPS survey spectra of the annealed Pd samples.

Figure 9-5 shows the high resolution XPS scans of the $3d_{5/2}$ and $3d_{3/2}$ Pd orbitals. The dotted lines show the placement and shape of the Pd peaks from the samples annealed in H_2. The Pd samples annealed in 54.8 ppm H_2S/H_2 at 400, 450 and 500ºC exhibited peaks which had maximums that had shifted to higher binding energies than the value of the Pd – Pd chemistry. Also, the peak shapes had broadened showing the presence of more than one Pd chemistry.

Peak broadening and shift of the peak maximum to higher binding energies than that of the Pd – Pd peak maximum (dotted lines) at 400, 450 and 500ºC showed that Pd – S bonds had formed on the surface, indicating that H_2S had undergone dissociative chemisorption and formed a surface sulfide with the Pd. Bulk sulfides had not formed as evidenced by the broader peaks between 400 - 500ºC that indicated the presence of the Pd – Pd chemistry near the surface as well as the Pd – S chemistry. However, at 350ºC the 3d Pd peaks were not as broad and the maximum was at the corresponding binding energy of the Pd – S peak maximum. The only chemistry detected at 350ºC was the Pd – S chemistry of the bulk Pd_4S, previously detected by XRD and EDX. The values of the Pd – Pd and Pd – S chemistries were confirmed with the literature (Matsumoto et al., 1980, Endo et al., 2003, Chaplin et al., 2007).

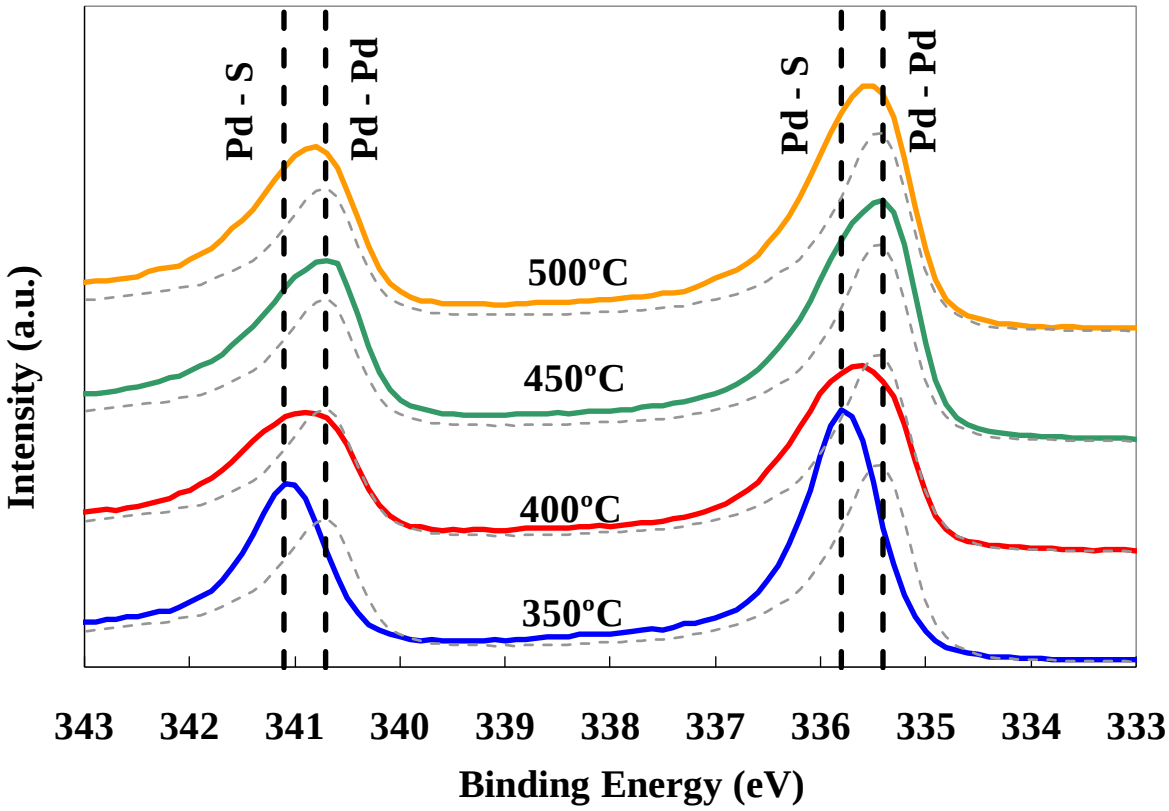

Figure 9-5 High resolution XPS scan of the $3d_{3/2}$ and $3d_{5/2}$ peaks. The solid and dotted lines correspond to the samples annealed in 54.8 ppm H_2S/H_2 and pure H_2, respectively.

The S/Pd atomic ratio was calculated from the survey scans of the Pd samples at each temperature (shown in Figure 9-4) and the amount of the Pd – S and Pd – Pd chemistries were calculated from the high-resolution scans (shown in Figure 9-5) of the Pd samples at each temperature. Figure 9-6 shows the amount of adsorbed sulfur on the Pd surface as a function of temperature. The S/Pd atomic ratio (y-axis on the left) was calculated from an average of three survey scans taken from different locations on each sample. The error bars corresponded to minimum and maximum values of the measurements which were averaged to plot the data points. The fraction of the Pd – S chemistry is shown on the y-axis on the right.

As can be seen, both the amount of sulfur adsorbed and consequently, the amount of sulfur bonded with Pd, increased with decreasing temperature. Sulfur adsorption is an exothermic reaction and higher temperatures would cause less sulfur to adsorb (Bartholomew et al., 1985). A similar trend was seen with bulk Pd sulfides in previous works (Taylor, 1985, Iyoha et al., 2007c) indicating that bulk sulfides would only form at lower temperatures. Indeed, at 350ºC, the S/Pd atomic ratio was close to 0.25, which corresponded to the atomic ratio of Pd_4S. At 400, 450 and 500ºC, only surface sulfides formed from the dissociative chemisorption of H_2S.

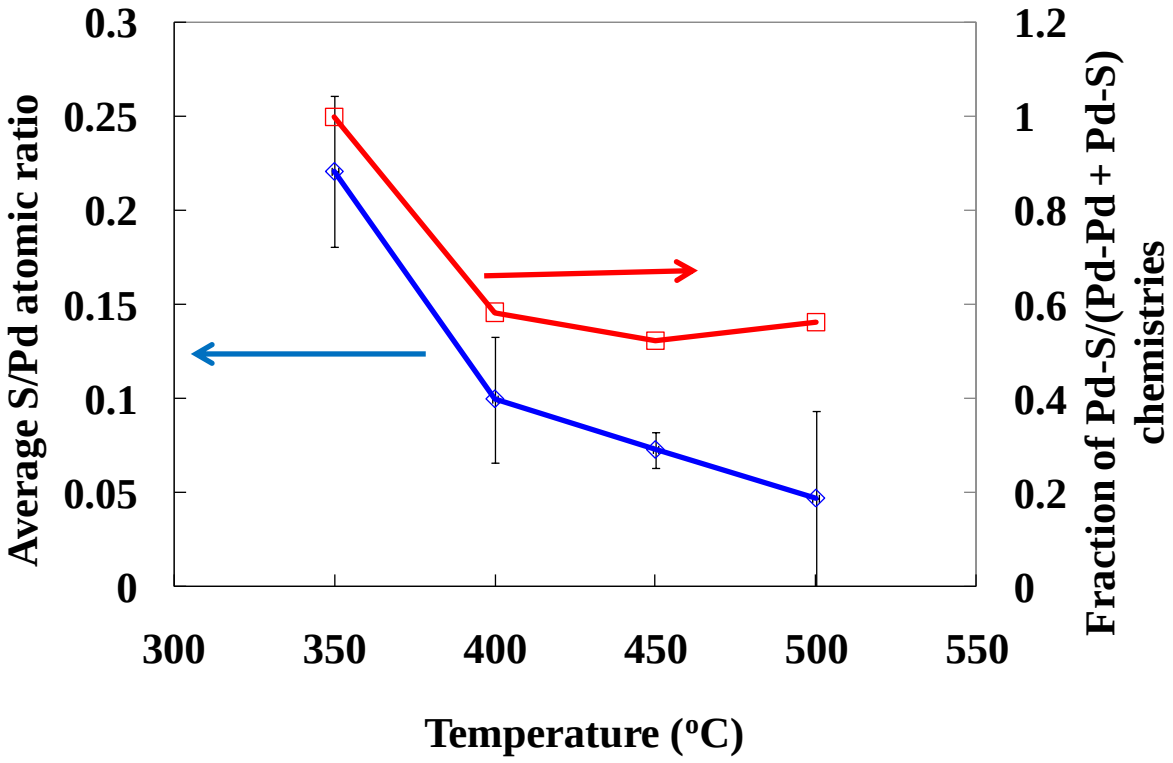

Figure 9-6 Dependence of the amount of adsorbed sulfur on temperature.

A pure Pd membrane was poisoned with 50 ppm and formed the bulk Pd_4S at 400ºC (Chen and Ma, 2010a), rather than up to 350°C, as seen here. The reason for the discrepancy was most likely from temperature gradients within the furnace in which the membrane was tested and the furnace in which the coupons of this work were annealed. Depending on the sample placement, the actual temperature of the samples once exposed to H_2S could be inaccurate. Moreover, failing to flush out the furnaces properly with inert gas before changing the temperature would result in residual H_2S still exposed to the samples below the desired annealing temperature. Indeed, only part of the Pd membrane presented by Chen and Ma (2010a) had formed bulk Pd_4S, showing that the conditions along the axis of the furnace were not uniform. However, since the part of the membrane which had formed bulk Pd_4S was the nearest to the temperature controller of the furnace (Chen and Ma, 2010a), it was likely that the transition temperature from surface to bulk sulfide at 50 ppm H_2S/H_2 was closer to 400ºC, contrary to 350ºC as seen with the results of this work.

9.3.2 Poisoned Pd/Cu alloys

Figure 9-7 shows the high resolution XPS scans of the Pd $3d_{5/2}$ orbital. The unpoisoned Pd sample had a binding energy of 335.8 eV which was roughly 0.7 eV higher than the values found in the literature for the Pd – Pd bond. It was possible that the surface became slightly oxidized to cause a slight peak shift to a slightly higher binding energy. Indeed, the Auger KLL peak for oxygen was seen on the survey spectra for all of the Pd samples. The Pd sample which was poisoned at 350°C in 52.3 ppm H_2S/H_2 for 12 hours exhibited a shift of 0.2 eV to a higher binding energy, caused by the formation of the Pd – S bond. Similar results were seen in Section 9.3.1 and the slight shift is

consistent with the literature (Matsumoto et al., 1980, Endo et al., 2003, Chaplin et al., 2007). The Pd $3d_{5/2}$ peak from the unpoisoned Pd/Cu alloy also exhibited a shift to a higher binding energy which was nearly identical to the shift seen by the poisoned Pd sample. The $3d_{5/2}$ peak has been seen to shift to higher binding energies as a result of Cu alloying (Reyter et al., 2009) with the severity of the shift dependent on the Cu concentration. Lastly, the peak of the poisoned Pd/Cu alloy had the largest shift to a binding energy value of 336.0 eV.

Figure 9-8 shows the high resolution XPS scan of the Cu $2p_{3/2}$ orbital. The Cu peak from the unpoisoned sample had a binding energy of 933.0 eV, which was 0.3 eV higher than the literature values (Liu et al., 1999, Fox et al., 2008). As with the unpoisoned Pd sample, it was possible that the surface of the Cu became slightly oxidized and caused the binding energy shift. The O 1s peak was seen in the survey spectra for all the Cu samples as well. Additionally, a $2p_{3/2}$ peak signal that was purely from the Cu – Cu chemistry would not exhibit the wide peak between 940 – 946 eV, known as a "shake-up satellite" as seen in Figure 9-8, which was caused by the Cu – O chemistry in CuO (Watts and Wolstenholme, 2003). The Cu $2p_{3/2}$ peak from the sample poisoned at 350°C in 52.3 ppm H_2S/H_2 for 12 hours also had a binding energy of 933.0 eV. Even though the S 2p peak clearly showed that sulfur had bonded with the Cu (Figure 9-9), no shift was seen in the binding energy.

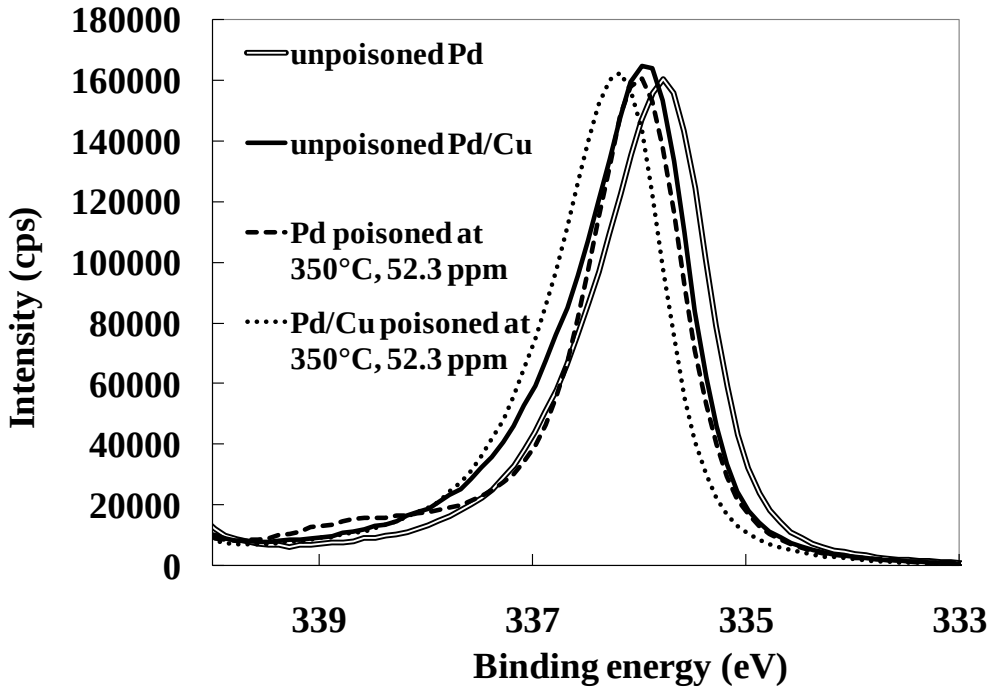

Figure 9-7 High resolution XPS scans of the Pd 3d5/2 peak.

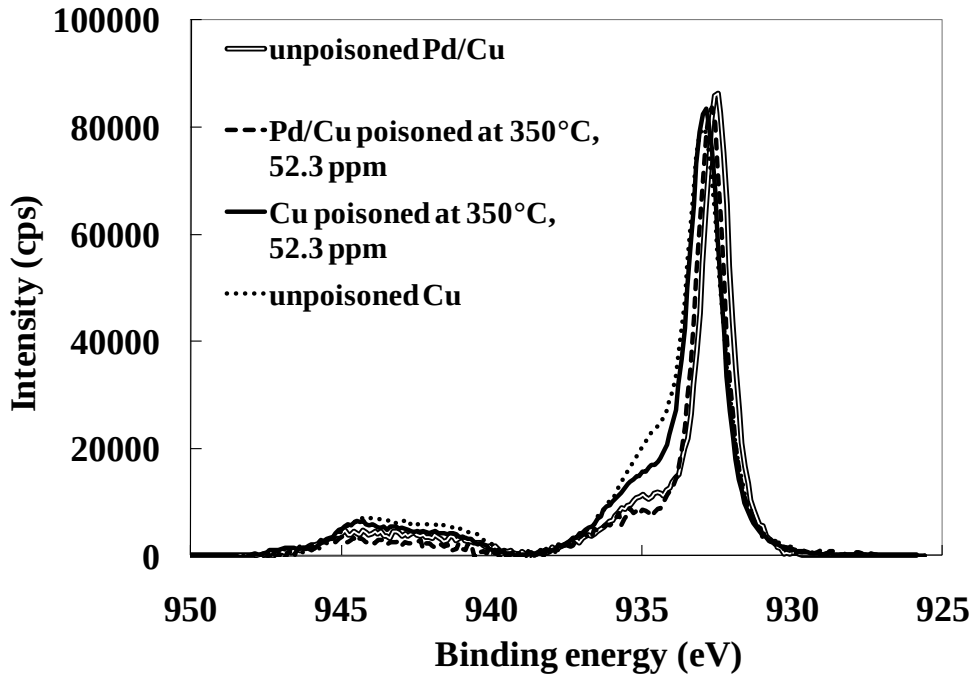

Figure 9-8 High resolution XPS scans of the Cu $2p_{3/2}$ peak.

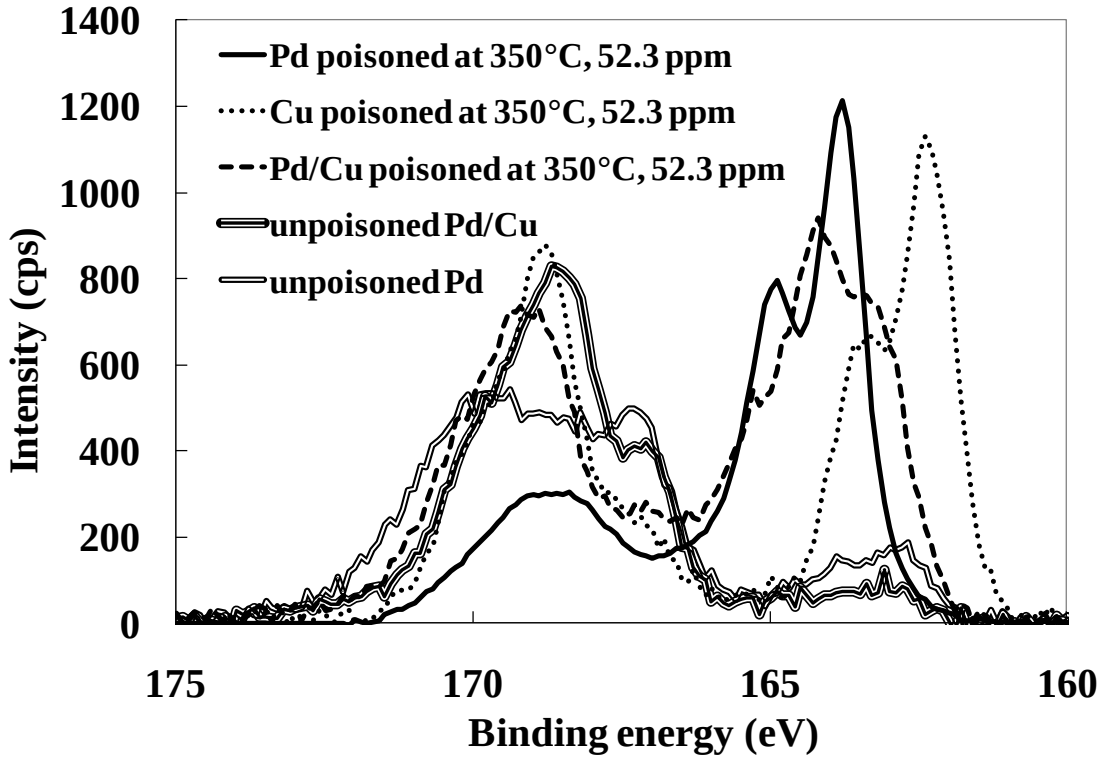

Figure 9-9 High resolution XPS scans of the S 2p peak.

Cu – S values have been seen to range from 931.8 – 933.2 eV (Bhide, et al., 1981). It was possible that the Cu – S bond did not cause a significant shift from the slightly oxidized Cu peak. The unpoisoned Pd/Cu sample yielded a shift to 932.5 eV due to Cu alloying with Pd. Previous studies have shown that Pd/Cu alloys caused a shift in the Cu 2p peak to a lower binding energy (Reyter et al., 2009). Lastly, the binding energy of the Pd/Cu sample poisoned at 350°C in 52.3 ppm H_2S/H_2 for 12 hours had a binding energy of 932.7 eV.

Due to the very small shifts seen in both the Pd $3d_{5/2}$ and Cu $2p_{3/2}$ peaks which were only a few tenths of an eV, it was difficult to deconvolute the different chemistries that comprised each signal, as was done in Figure 9-3 with the Pd $3d_{5/2}$ peak. Indeed, there was no shift at all between the Cu – Cu and Cu – S peak. Furthermore, the amount of possible chemistries and lack of standards made it very difficult to differentiate between the possible chemistries. The Pd peak had possible Pd – Pd, Pd – O, Pd – Cu and Pd – S chemistries while the Cu had possible Cu – Cu, Cu – O, Cu – Pd and Cu – S chemistries.

However, the S 2p peak (shown in Figure 9-9) was much easier to deconvolute due to the large difference in binding energies for the different chemistries. Firstly, any S – O chemistries due to various sulfates and sulfites adsorbing on the surface were clearly distinguishable from the sulfides caused by the sulfur bonding with the Cu and Pd. The sulfides caused a signal which ranged from 161 – 166 eV while the sulfates and sulfites caused a signal which ranged from 166 – 172 eV. Differentiating between the sulfur which had bonded with oxygen to form sulfates and sulfites and the sulfur which had bonded with the Pd and Cu was critical because the sulfur bonded with the metal would

be the cause of the membrane poisoning while the sulfates and sulfites could be found on any sample exposed to the environment. Indeed, the unpoisoned Pd and Pd/Cu samples exhibited a significant peak in the sulfite/sulfate range, showing that some sulfur did indeed adsorb on the surface. The unpoisoned Cu sample did not have any measurable sulfur signal. Furthermore, the unpoisoned samples did not show a significant peak in the sulfide range while all the poisoned samples did. The poisoned samples showed peaks in both the sulfide and sulfate/sulfite regions.

Also, the S – Cu chemistry was clearly distinguishable from the S – Pd chemistry. While the S $2p_{3/2}$ peak of the S – Cu chemistry had a binding energy value of 162.20 eV, the S $2p_{3/2}$ peak of the S – Pd chemistry had a binding energy value of 163.75 eV. There were 1.16 eV between the 3/2 and 1/2 peaks of the 2p orbital split in both cases. The difference between the two sulfides was 1.4 eV, which allowed for the peak deconvolution of the combined sulfide signal to be performed with much more accuracy than with either the Pd $3d_{5/2}$ or Cu $2p_{3/2}$ peaks.

Figure 9-10 shows the peak fitting of the S 2p peak for the sample poisoned at 350°C in 52.3 ppm H_2S/H_2 for 12 hours. The same scan was also shown in Figure 9-9 with the poisoned and unpoisoned Pd, Cu and Pd/Cu samples. All-encompassing sulfate and sulfite peaks for the $2p_{3/2}$ orbital were placed at 169.15 ± 0.2 eV and 166.67 ± 0.2 eV, respectively, with a distance of 1.16 eV given for the 2p orbital split. The values were taken from the unpoisoned samples shown in Figure 9-9. Since the interest of this work was to determine and quantify the sulfides formed, having two all-encompassing sulfate and sulfite peaks rather than separate peaks representing what each sulfate and sulfite was bound to, simplified the quantification process.

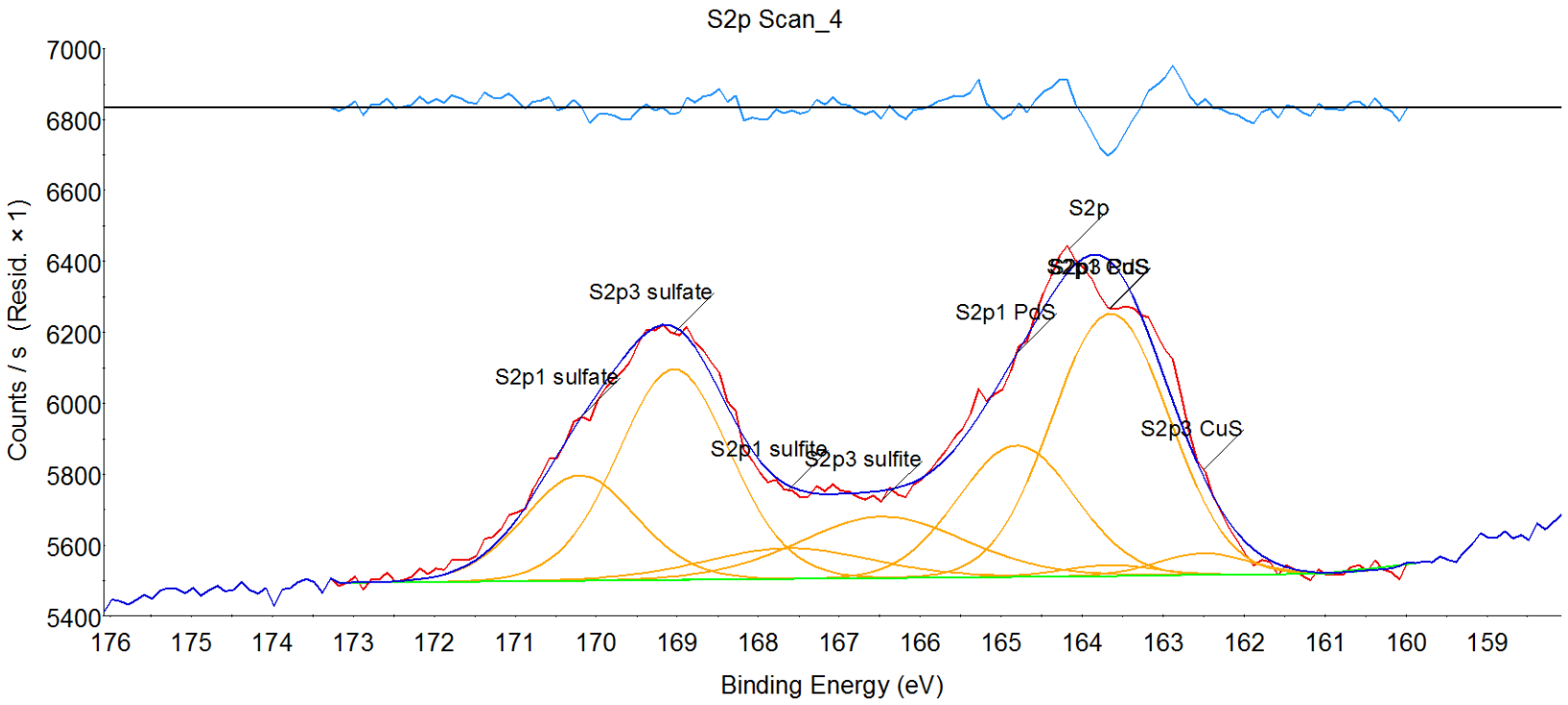

Figure 9-10 Peak fit for the S 2p peak.

The full-width, half-maximum (FWHM) values were constrained between 0.5 – 2.5 and the Lorentzian/Gaussian (L/G) ratio was kept constant at 30%. The S – Cu and S – Pd peaks were taken from the binding energies of the standards shown in Figure 9-9 and constrained to ± 0.2 eV. The distance of the 2p orbital split was also 1.16 eV and the FWHM was constrained between 0.9 – 1.7 and the L/G ratio was constrained between 0 – 50%. All S $2p_{1/2}$ peaks were equal to half the area of the corresponding $2p_{3/2}$ peak, and the FWHM and L/G ratios of the doublets were kept equal. The peak fittings for the rest of the Pd/Cu coupons can be found in Appendix D.

The amount of sulfates and sulfites combined ranged between 35 – 70% of the total S 2p signal. While ion sputtering did eliminate the sulfate and sulfite signal as the adventitious layers of carbon, oxygen and sulfur were burnt off, the underlying sulfide signal did not increase in intensity. Therefore, it was not advantageous to sputter the samples before taking the survey and high resolution spectra since the adventitious sulfur could be easily subtracted from the total sulfur content through peak deconvolution.

Figure 9-11 shows the total amount of sulfides present on the surface of the Pd/Cu samples after being poisoned for 12 hours between the temperatures of 350 - 500°C with 0.5, 5 and 52.3 ppm H_2S/H_2. Unlike with the experiments performed in Section 9.3.1, the Pd, Cu and S content of each sample was measured only once and so there were no error bars to show the data scattering. At a concentration of 52.3 ppm H_2S/H_2, there was a decrease in the amount of sulfides with increasing temperature from roughly 8 at% at 350°C to 3.5 at% at 400°C and 4.5 at% at 500°C. Similarly, the amount of poisoning of Pd/Cu membranes increased with decreasing temperature, although the dependence on temperature was very slight, as shown in Figure 8-2. The decreased sulfide formation

with increasing temperature was due to the exothermic nature of the chemisorption of H_2S on the Pd/Cu surface.

After poisoning with 5 and 0.5 ppm H_2S/H_2, there was a significant drop in the sulfide amount present on the surface. As seen in Figure 10-3, the hydrogen permeance of Pd/Cu membranes decreased much less with smaller H_2S compositions in the feed stream. There was a permeance difference of 20% between exposure to 52.3 and 5 ppm H_2S. Similarly, Barbier et al., (1990) observed that the total sulfur adsorbed on Pt/Al_2O_3 catalysts tripled after being exposed to concentrations of H_2S varying over 4 orders of magnitude at a given temperature (Figure 2-7). Since there was a difference in permeance of 25% between exposure to 0.5 and 5 ppm H_2S at 450°C (see Figure 10-3), one would expect to see a continued decrease in sulfide formation between 5 and 0.5 ppm H_2S. However, it could be that decreasing the amount of H_2S in the feed from 5 to 0.5 ppm resulted in a decrease in sulfides formed which was not as dramatic as with the higher orders of magnitude of feed concentration, as seen in Figure 2-7.

Figure 9-12 shows the percent of palladium sulfides of the total sulfides formed on the Pd/Cu surface. After poisoning with 52.3 ppm H_2S/H_2 for 12 hours, most of the sulfides formed were of the Pd – S chemistry. In fact, the fraction of Pd – S corresponded to the fraction of Pd in the Pd/Cu alloy, as calculated through XPS measurements (overlaid with the grey bar), so it would appear that the sulfur bonded to the available adsorption sites without preference. However, it is not known precisely how the Cu prevented bulk sulfides from being formed, as with the Pd in the study in Section 9.3.1.

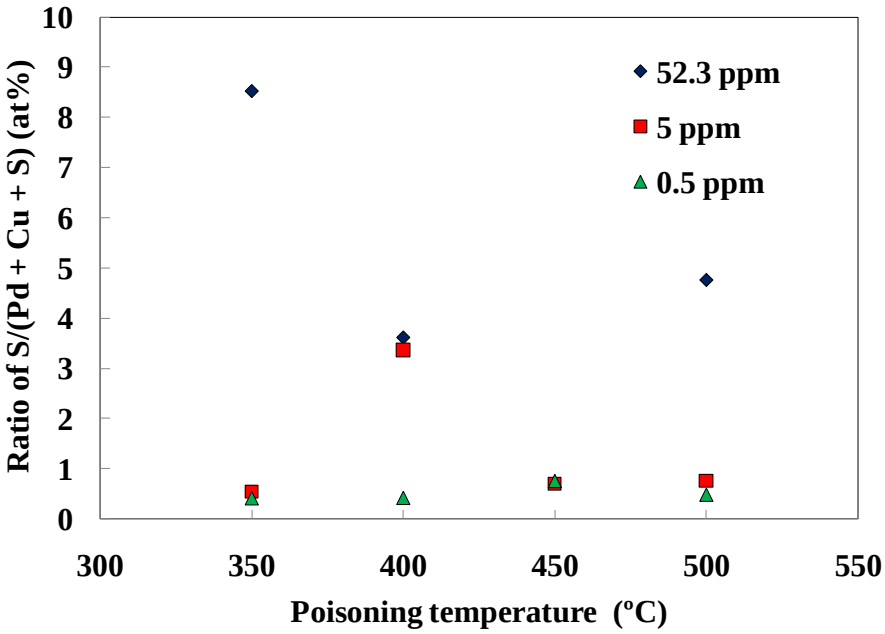

Figure 9-11 Total sulfides formed after poisoning as a function of H_2S concentration and poisoning temperature.

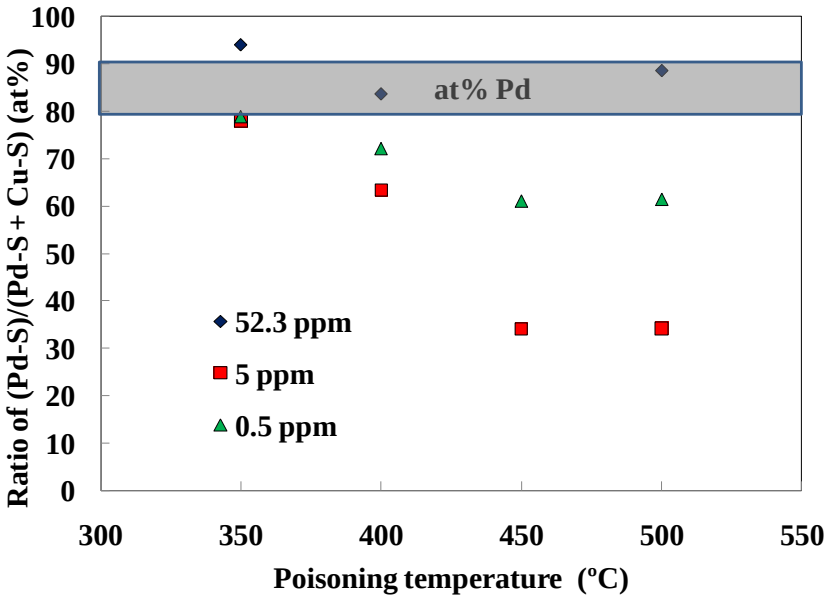

Figure 9-12 Total Pd sulfides formed as a function of H_2S concentration and poisoning temperature. The Pd composition of the Pd/Cu alloy is overlaid in grey.

Miller et al (2008b) observed that exposure to H_2S caused Pd atoms to segregate to the top atomic layer of 20 wt% Cu alloys, and that the Cu concentration was less than the bulk concentration. Increased sulfur surface coverage increased the segregation of Pd atoms to the surface. Their explanation for the migration was the more negative Gibbs' free energy of bulk Pd sulfides in comparison to bulk Cu sulfides. However, the Gibbs' free energies of the surface sulfides were not reported in the literature and the Gibbs' free energies of bulk sulfides could be very different from those of their surface sulfide counterparts.

At lower H_2S concentrations, more Cu sulfides formed so that the amount was disproportionate to the fraction of Cu in the Pd/Cu alloy, especially at higher poisoning temperatures. At decreased sulfur surface coverages, Miller et al (2008b) observed that the Pd segregation to the topmost layer was not as severe. However, as was seen in Figure 9-12, with less H_2S in the feed the sulfur preferentially bonded with the Cu, contradicting the theory put forward by Miller et al. (2008b) with regards to the more negative Gibbs free energy of bulk Pd sulfides. The contradiction between the work presented here and the theory of Miller et al. (2008b) could be due to the difference between the Gibbs free energy of bulk and surface sulfide formation. While there was a correlation between the two energies (Figure 2-6), the correlation did not have a high R^2 value and knowing the value of the Gibbs free energy formation of bulk sulfide formation does not necessarily enable one to predict the Gibbs free energy of surface sulfide formation.

Figure 9-13 shows the total sulfide amount on the Pd/Cu surface as a function of recovery time in H_2 after each sample was poisoned with 52.3 ppm H_2S for 12 hours

between the temperatures of 350 - 500ºC. As can be expected, the total sulfide amount decreased drastically after recovery in pure H_2 due to the sulfur combining with the H_2 in the feed stream and desorbing from the surface. Indeed, from the poisoning and recovery experiments seen in Figure 8-2, a reduction in the sulfide presence on the Pd/Cu surface would be expected as H_2S desorbed from the surface.

Figure 9-14 shows the percent of Pd sulfides and Cu sulfides as a function of recovery time. While the data were somewhat scattered, a reduction in the amount of Pd sulfides could be seen after 1.5 hours of recovery in H_2, and an even larger reduction in Pd sulfides after 12 hours of recovery, showing that the Pd sulfides reduced more readily than the Cu sulfides, thus enabling the increase in permeance seen upon the reintroduction of H_2 to poisoned Pd/Cu membranes. This trend would also correspond to the affinity of H_2S to the Cu upon poisoning, as Cu sulfides formed more readily than Pd sulfides at lower feed concentrations of H_2S, as shown in Figure 9-12. Higher concentrations of H_2S were required in order for Pd sulfides to be formed with the same percent as their presence in the alloy.

When comparing the results of Figure 9-13 and Figure 9-14 to the recovery of Pd/Cu membranes after poisoning (see Figure 8-6), the XPS data at 1.5 hours would place the samples at the beginning of the linear portion of the recovery while the XPS data at 12 hours would place the samples at the end of the linear portion of the recovery at which point most of the permeance had already been recovered. While the different stages of the recovery corresponded to H_2S being flushed out of the system and desorbed from the system at different rates (see Section 9.3.3), the adsorption sites from which the H_2S was first desorbed would be the least energetically favorable.

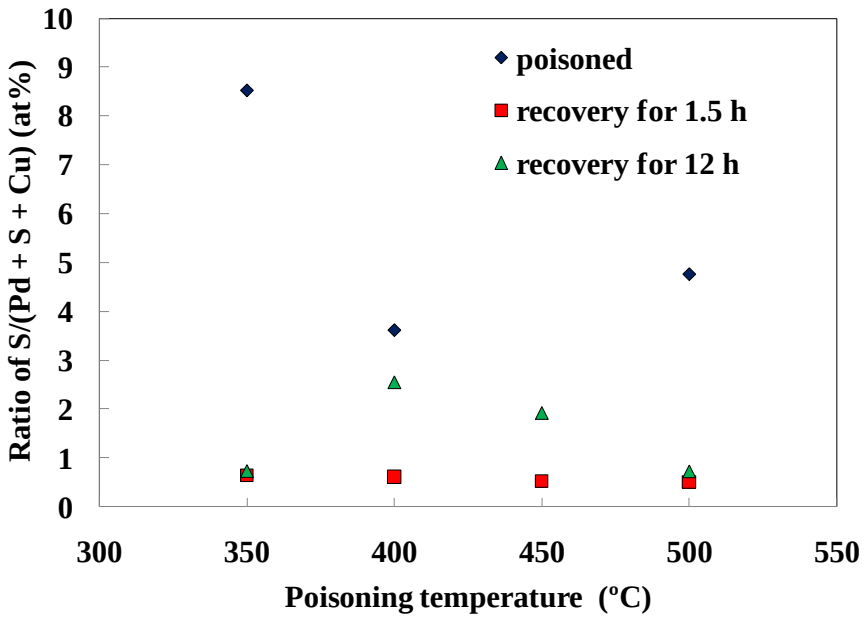

Figure 9-13 Total sulfides formed after poisoning with 52.3 ppm H_2S/H_2 and recovering in H_2 at the poisoning temperature for 12 hours.

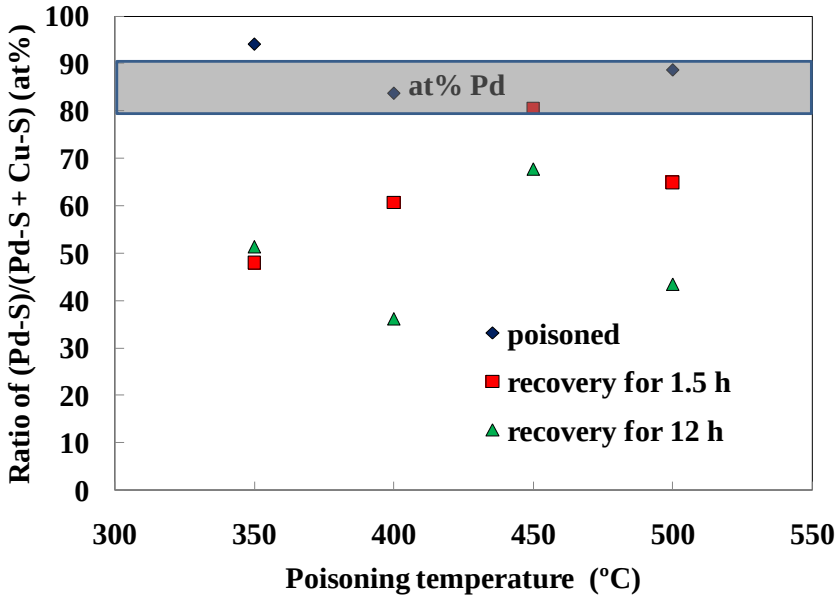

Figure 9-14 Total Pd sulfides formed after poisoning with 52.3 ppm H_2S/H_2 and recovering in H_2 at the poisoning temperature. The Pd composition of the Pd/Cu alloy is overlaid in grey.

From the XPS results, it would appear that the least energetically favorable adsorption sites were those where sulfur was bonded to Pd since increasing the recovery time only increased the ratio of Cu sulfides to Pd sulfides. The sulfur desorption from the Pd adsorption sites would also be accompanied by the largest increase in permeance seen at the beginning of the recovery process.

Figure 9-15 shows the total sulfides formed from samples which were poisoned between the temperatures of 350 - 500ºC for 12 hours with 52.3 ppm H_2S and recovered between the temperatures of 350 - 500ºC for 12 hours in H_2. There did not appear to be a specific pattern with regard to the samples poisoned at varying temperatures. However, an overall reduction in the amount of sulfides which remained after recovery in pure H_2 could be seen with increasing temperature due to the high activation energy of desorption of H_2S from metals and the exothermic nature of the dissociative chemisorption.

Figure 9-16 shows the fraction of Pd sulfides and Cu sulfides as a function of recovery temperature. As with Figure 9-14, the majority of the data points were far below the area of the atomic ratio of Pd to Cu in the alloy showing that the Pd sulfides were reduced preferentially in lieu of the Cu sulfides. However, an increase in recovery temperature showed an increase in the fraction of Pd sulfides. As explained earlier, the Pd sulfides were the least energetically favorable adsorption sites and were reduced in H_2 first. At higher recovery temperatures, the more energetically favorable adsorption sites with Cu were reduced as well, increasing the amount of hydrogen permeance that could be recovered. Also, there was a small amount of Pd sulfides still present at high recovery temperatures, showing that some of the bonding sites of sulfur with Pd were more energetically favorable than the Cu sulfides which were reduced.

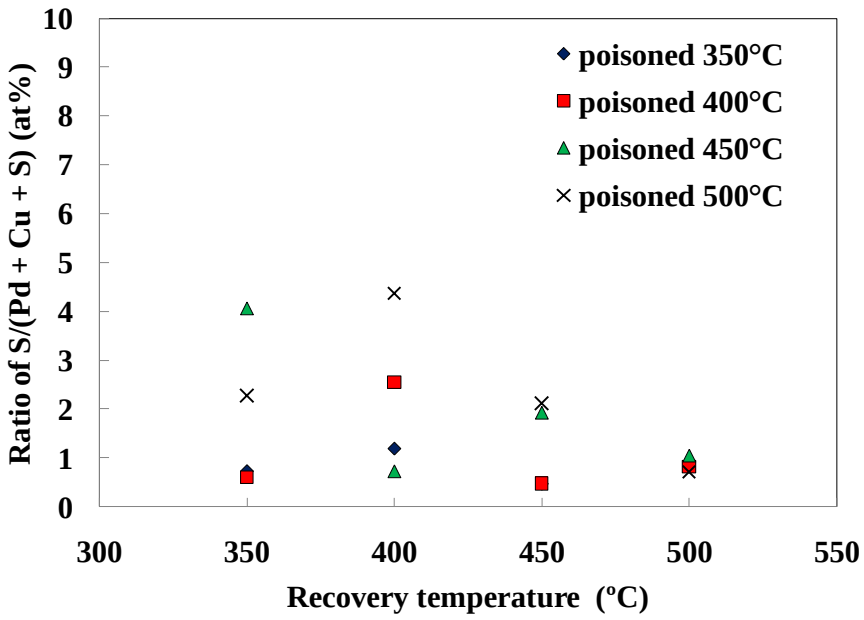

Figure 9-15 Total sulfides formed after poisoning with 52.3 ppm H_2S/H_2 and recovering in H_2 at varying temperatures.

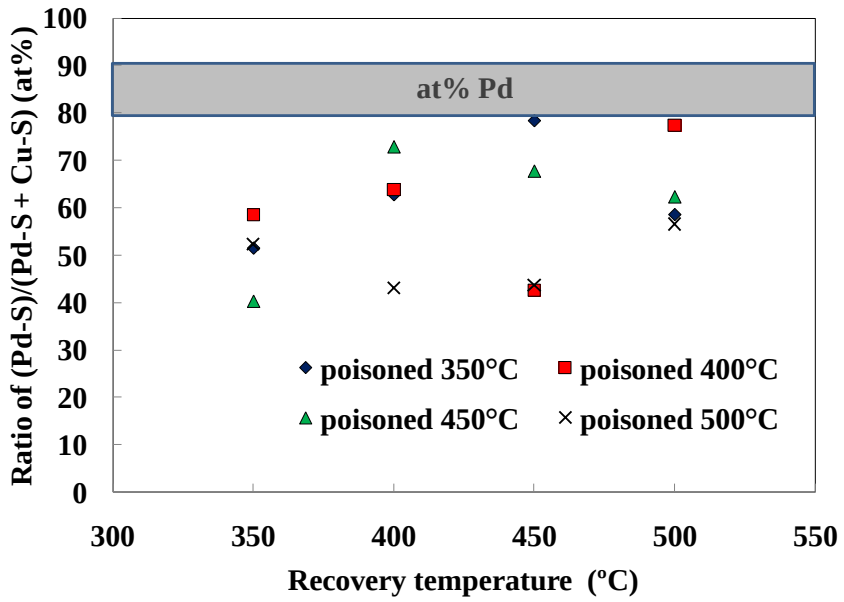

Figure 9-16 Total Pd sulfides formed after poisoning with 52.3 ppm H_2S/H_2 and recovering in H_2 at varying temperatures. The Pd composition of the Pd/Cu alloy is overlaid in grey.

Since the experiments performed in this section did not have extremely long recovery times, only 12 hours at varying temperatures, it was difficult to ascertain precisely what prevented the permeance from being completely recovered at the standard operating temperatures. From the data taken here, it would appear the majority of the recoverable permeance was due to the reduction of Pd sulfides while the Cu sulfides were more difficult to reduce at lower temperatures. Higher temperatures would be needed to reduce both the Pd and Cu sulfides in order to regain the hydrogen permeance.

The steep permeance decline seen at 52.3 ppm was due to a non-preferential binding of the sulfur with both Pd and Cu (Figure 8-6). Furthermore, the biggest increase in recovery seen with Pd/Cu membranes upon the re-introduction of H_2 to the system was caused by the Pd sulfides reducing preferentially. It seems that the tolerance of Pd/Cu membranes in comparison to Pd membranes lies in the preferential adsorption of H_2S on Cu, allowing the H_2 to continue to permeate through the Pd adsorption sites. However, the sulfides formed with the Cu were more difficult to reduce, and prevented the permeance from being completely recovered at the operating temperatures. While increasing the Cu content of the surface to 30 wt% Cu might lessen the permeance decline of the membrane during poisoning by drawing the sulfur away from the Pd, the permeance of the membrane would still decrease due to the additional Cu, and the amount of recoverable permeance at a given temperature might decrease with increased Cu content as well.

9.3.3 Poisoned and recovered Pd/Cu membranes

Figure 9-17 shows the permeance and recovery of N_09. The concentration of H_2S in the retentate flow is shown both by GC measurement and by mass balance

calculation. The membrane was poisoned with 51.4 ppm H_2S/H_2 at 350ºC for 175 hours before undergoing recovery in pure H_2. The poisoning was performed until the concentration of H_2S in the retentate stabilized at the value calculated by the mass balance. The reason that the retentate concentration took such a long time to stabilize was due to the H_2S adsorbing on the tube walls of the system and saturating it over time. On a blank run performed with a shell casing and non-porous stainless steel tube without a Pd membrane, roughly 200 hours were needed for the concentration in the outlet flow to stabilize, showing that the system itself required a long period of time to saturate.

Regardless, the permeance of the membrane stabilized instantaneously. Within several minutes of the introduction of H_2S in the feed, the permeance dropped to roughly 12% of the original permeance at 350ºC and remained stable for the duration of the poisoning experiment, as was seen in previous poisoning experiments at 450ºC (Figure 8-4). Furthermore, after two hours of poisoning at 350ºC, the permeance of N_03 dropped to 13% of the original value at that temperature (Figure 8-2), showing that the time of exposure did not influence the amount that the permeance dropped, as was seen in Chapter 8.

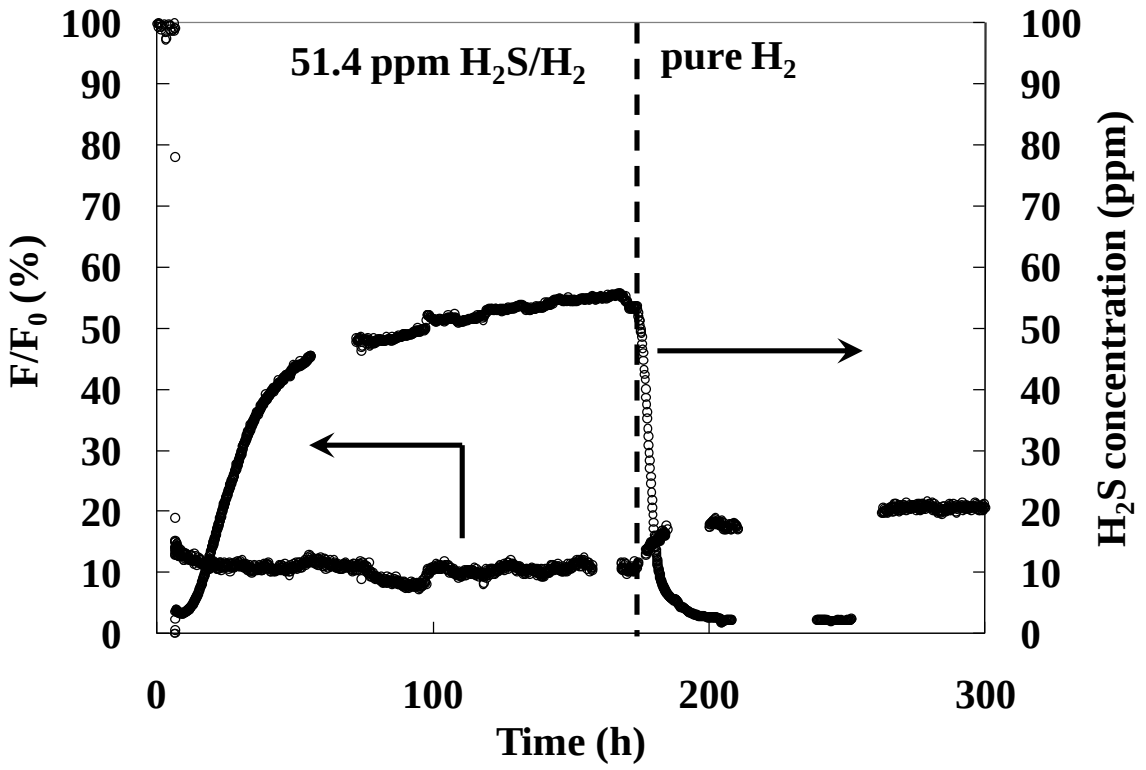

Figure 9-17 Poisoning of N_09a at 350°C with 51.4 ppm H_2S/H_2 and the recovery in pure H_2.

Upon reintroducing pure H_2 to the feed stream, the hydrogen permeance increased in a linear fashion to roughly 17% over a period of 13 hours due to the H_2 flushing out the H_2S from the system, as seen by the corresponding decreasing H_2S concentration in the retentate flow and desorbing sulfur from the membrane. The permeance continued to increase slowly over a period of 100+ hours by another 3% as the H_2S concentration dwindled further until it could no longer be detected. While roughly 76% of the permeance was recovered after poisoning at 350ºC for two hours with N_03 (Figure 8-2), only 20% was able to be recovered after poisoning for 175 hours with N_09. The reason for the drastically decreased recovery was that the amount of recoverable permeance decreased with total exposure time to H_2S, as shown in Figure 8-7 with N_03 and N_08a at 450ºC.

The previous poisoning and recovery experiments performed in Chapter 8 showed three stages of recovery (Figure 8-1 and Figure 8-6) which were thought to correspond to three stages of H_2S desorption from binding sites of differing energetic values. However, in the case of N_09 only two stages were seen. The first stage of instantaneous increase once the H_2S was introduced was not observed. The majority of the permeance was recovered in the first stage as the sulfur which had bonded to the least energetically favorable binding sites recombined with H_2 and desorbed.

The reason that the jump in permeance was not seen with N_09, even on a small scale, was due to the saturation of the system with H_2S as explained in Appendix B.2. After reintroducing H_2, there was still a significant amount of H_2S detected in the retentate for several hours. According to Figure 9-17, the H_2S retentate concentration for a membrane poisoned for two hours would not even reach 5 ppm before H_2 was

reintroduced. Granted, the lack of a permeance change over the time that the retentate flow stabilized showed that the time of exposure had no bearing on the permeance decline, but since the system itself was saturated with H_2S, reintroducing H_2 caused a period of time in which a large amount of H_2S was still present in the bulk flow while desorbing from the system that would not be present in the case of N_03 in Figure 8-1 where the membrane was poisoned for two hours.

The linear, second stage of recovery seen in Figure 8-1 and Figure 8-6 appeared between 175 – 185 hours in Figure 9-17, directly after the reintroduction of H_2 to the system. However, the linear increase corresponded directly to the decrease in H_2S measured in the retentate flow as H_2 flushed the system out. Therefore, the second stage of recovery was due to the decrease in H_2S in the feed flow. In that regard, both the first and second stages of recovery would have been due to the change in gas concentration and the resultant change in the equilibrium condition on the membrane surface, shown in Equation 2.23. The difference between the first and second stages of recovery would simply be the rate at which the gas concentration changed.

The third stage seen in Figure 8-1 and Figure 8-6, which corresponded to the second stage in Figure 9-17, would also be due to the change in the gas concentration, but at a much slower rate due to the fact that the H_2S was not being flushed out of the system by H_2, but being partially desorbed from the walls of the system. It should be noted that the rate of permeance recovery was related to the fluid dynamics of the system, and the speed at which the H_2S was both flushed out and desorbed from the system walls, as shown in Appendix B.2.

Figure 9-14 indicated that the less energetically stable binding sites were those where the sulfur was bonded with Pd since the fraction of Cu sulfides increased after short periods of recovery at the same temperature. Figure 9-16 showed that higher temperatures were needed to further reduce the Cu sulfides, indicating that the lack of a complete permeance recovery was primarily due to sulfur bonding with Cu.

Figure 9-18, Figure 9-19, and Figure 9-20 show the recovery of N_09 in H_2 at 400, 450 and 500ºC, respectively. Since the poisoning of Pd/Cu membranes resulted from the dissociative chemisorption of H_2S which bonded with both the Pd and the Cu to form surface sulfides, the desorption of H_2S from the membrane would be a highly activated process in which high temperatures would be needed to reduce the more energetically favorable Cu sulfides. In each graph, the raising of the temperature (the beginning of the x-axis) was accompanied by a jump in the H_2S measured in the retentate flow which then slowly decreased as time went on. The increase in H_2S seen was caused not only from H_2S desorbing from the membrane, but also from the system itself, as seen in Appendix B.2.

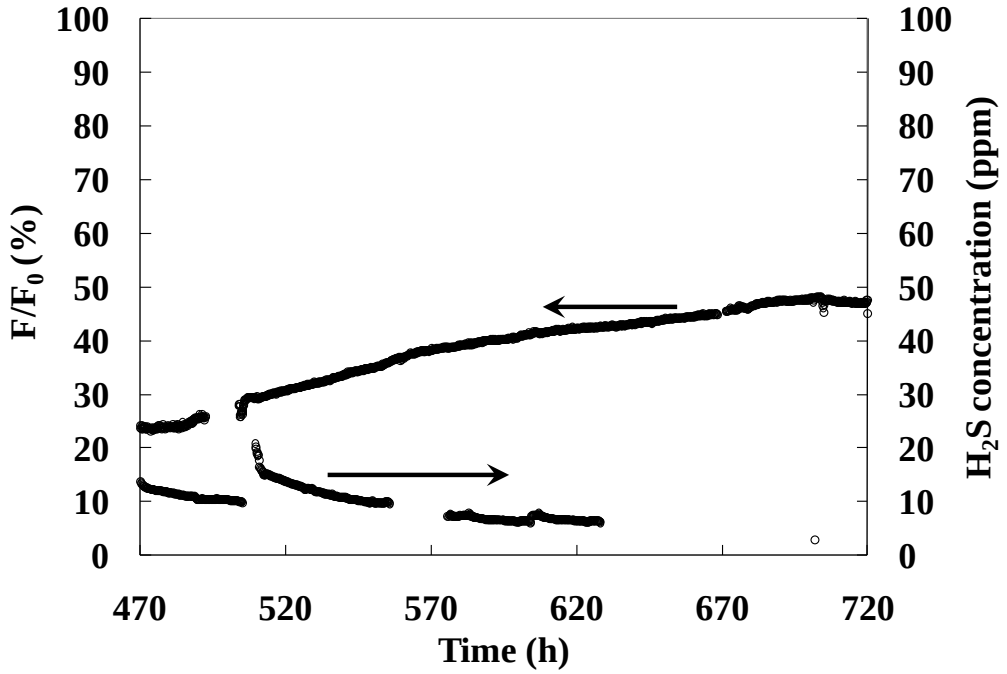

Figure 9-18 Recovery of N_09 at 400°C.

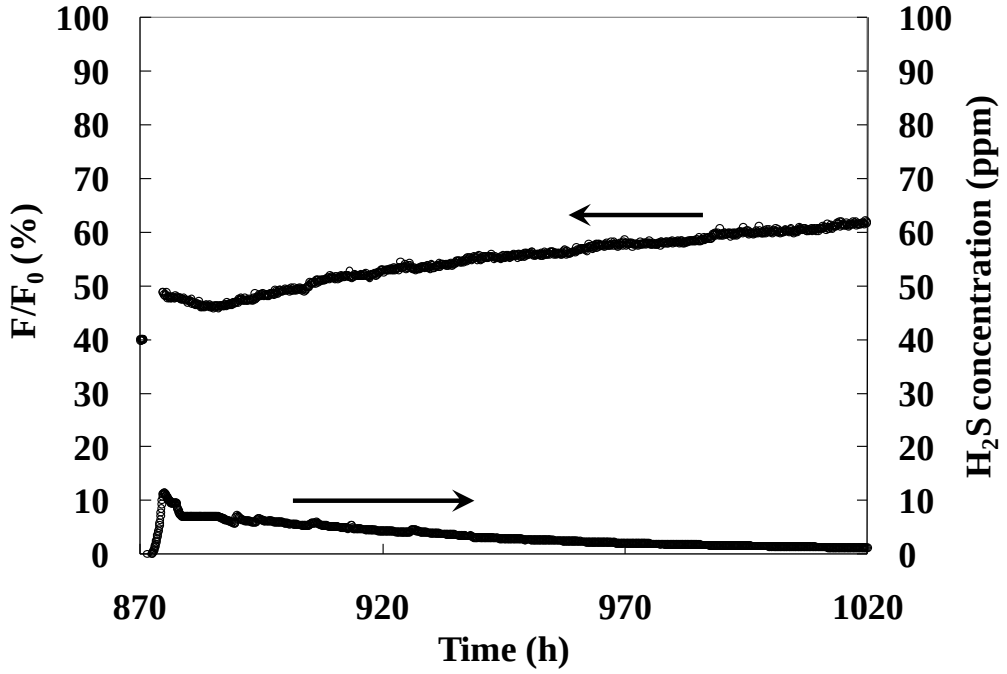

Figure 9-19 Recovery of N_09 at 450°C.

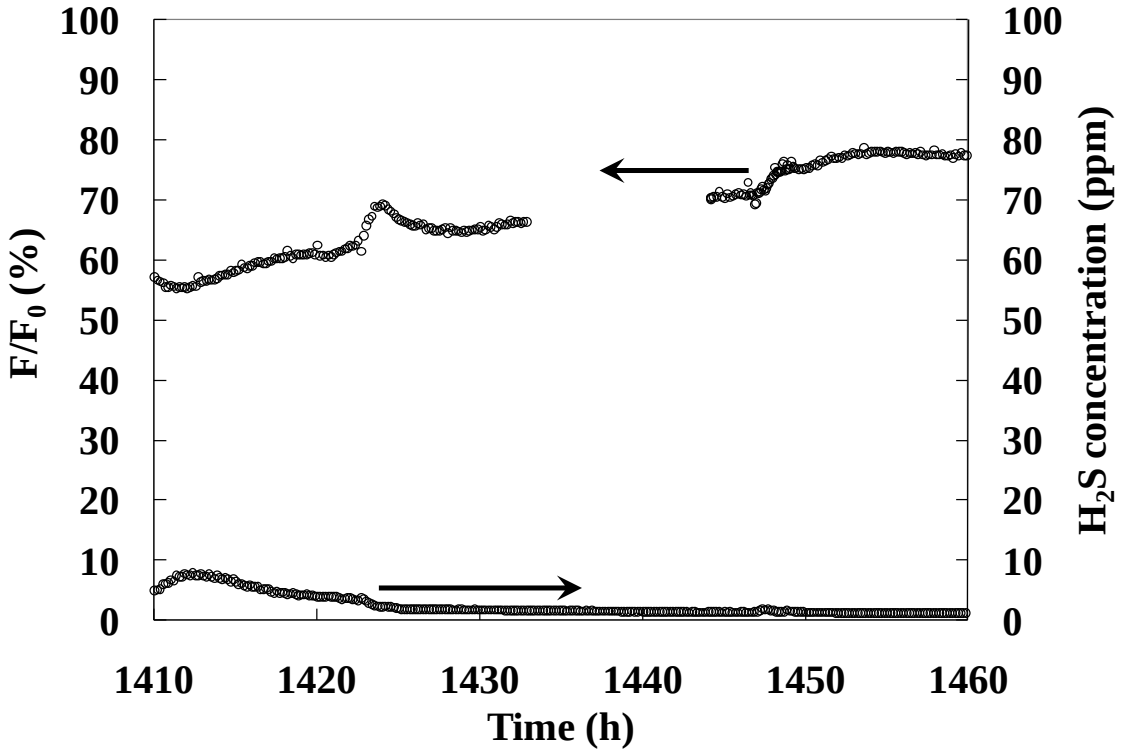

Figure 9-20 Recovery of N_09 at 500°C.

Figure 9-21 shows the Sieverts' Law regressions which were performed at 350ºC after each permeance recovery at a given temperature. The permeance of the membrane increased as the H_2S desorbed from the membrane with higher temperatures resulting in more of the permeance being recovered. As was expected, the linearity of the regressions showed that one dimensional diffusion through the Pd/Cu layer was the rate determining process for hydrogen mass transfer through the composite membrane at each temperature. Even though part of the surface was blocked due to sulfur binding with Pd and Cu and blocking a good portion of the adsorption sites, the dissociative chemisorptions of H_2 continued to be much faster than the diffusion of hydrogen through the membrane.

After the last recovery at 500ºC, the permeance was measured at 500, 350 and 250ºC to calculate the activation energy, shown in Figure 9-22. When comparing the activation energy before and after the poisoning and recovery experiments, there was little change (from 18.5 to 19.3 kJ/mol), showing that the sulfur poisoning did not change the properties of the membrane and the remaining adsorbed sulfur only reduced the effective area for hydrogen dissociative chemisorption, as seen with membrane N_08 in Figure 8-5, membranes N_12, N_20 and N_21 in Figure 10-7.

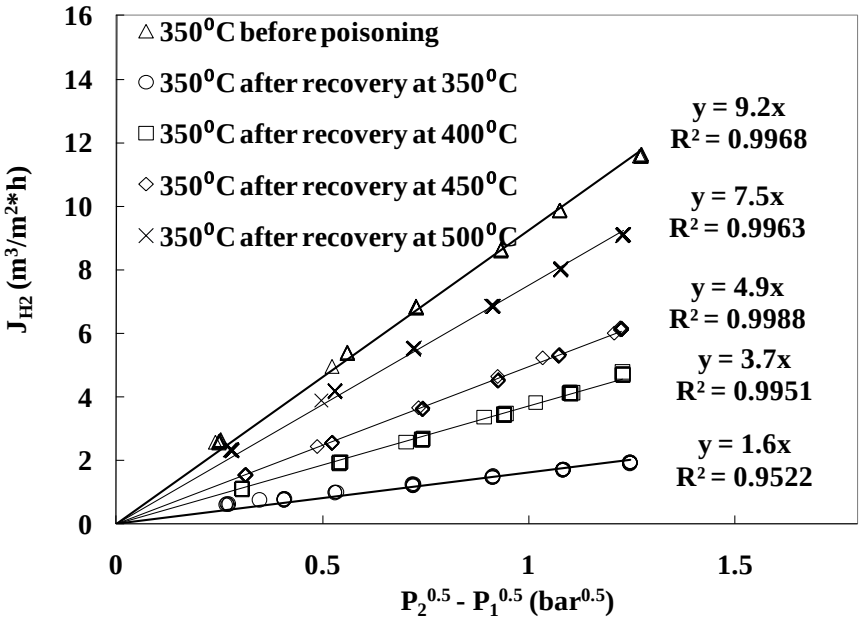

Figure 9-21 Sievert's Law regressions at 350°C before poisoning and after recovery at varying temperatures.

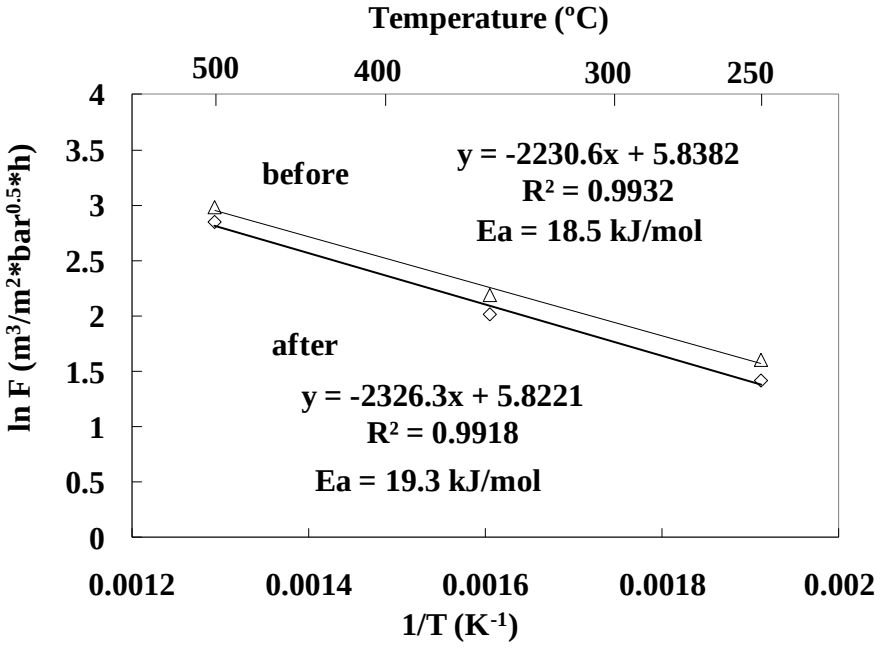

Figure 9-22 Activation energy of N_09 before poisoning and after the final recovery.

Figure 9-23 compiles the recovery data for all of the Pd/Cu membranes tested in this chapter. The five Pd/Cu membranes were made both in the bi-layer fashion as described in Chapter 4 and the tri-layer fashion as described in Chapter 6. The poisoning and recovery data for all of the membranes was summarized in Table 9-2. The membranes compiled in Table 9-2 were poisoned with a range of temperatures and H_2S concentrations. However, the same amount of permeance was recovered at each temperature, regardless of the poisoning concentration or temperature. The commonality of all the membranes was that they had all reached a certain point where the amount of recoverable permeance had reached a limiting value after a lengthy period of poisoning time, as with N_03 in Figure 8-7.

As seen previously in Figure 8-7, the amount of recoverable permeance decreased with exposure time. Furthermore, the slope of the curve showed that the dependence of the recoverable permeance on the total poisoning time stabilized, implying that there was a saturation point where the amount of remaining sulfur reached a limiting value. Figure 9-23 showed that the limiting value was the same at each poisoning temperature regardless of the H_2S concentration in the feed or the poisoning temperature, as long as the saturation point was reached.

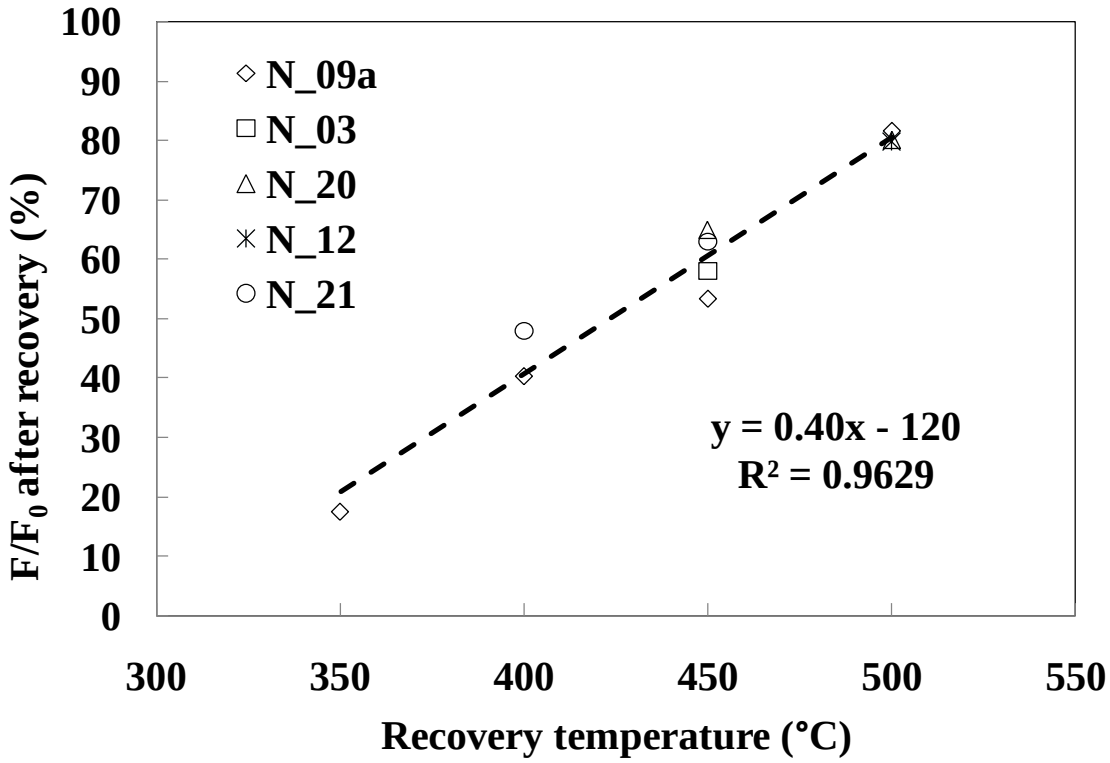

Figure 9-23 Percent recovery as a function of recovery temperature for fcc Pd/Cu membranes.[*]

Table 9-2 Summary of poisoning/recovery experiments.

membrane	H_2S concentration (ppm)	Temperatures poisoned (ºC)	Total time poisoned (h)	Temperatures recovered (ºC)
N_03	50	350 - 500	33.5	32
N_09a	50	350	175	350 - 500
N_12	0.2 - 5	500	120	500
N_20	0.2 - 5	450	120	450 - 500
N_21	0.2 - 5	400	120	400 - 500

[*] The recovery percentage of N_21 at 500°C was not included due to alloying effects on the membrane permeance, as explained in Section 10.3.2.

Fitting a linear regression to the data shows that there was a significant increase in the amount of recoverable permeance with increasing temperature due to more H_2S being desorbed from the surface. The sulfur preferentially desorbed from the Pd, as shown in Figure 9-16. According to Figure 9-23, almost no permeance would be recovered at 300ºC, and nearly all of the permeance would be recovered at 550ºC. If the recovery time were short at 550ºC, the high temperature could be used for Pd/Cu membranes poisoned in the event of a malfunction. However, too long an exposure to high temperatures would result in significant leaks forming in the membrane as a result of grain coarsening (Guazzone and Ma, 2008). The reason for the linearity of the regression is not known at this time.

9.4 Conclusions

While it was clear that pure Pd formed bulk sulfides at 54.8 ppm during the operating temperatures of WGS reactors but the Pd/Cu would not, the XPS studies did not clarify why this was so. However, the increased permeance that fcc Pd/Cu membranes had when compared to Pd membranes when exposed to feed concentrations including H_2S was due to the H_2S preferentially bonding with the Cu rather than the Pd, allowing the H_2 to continue to adsorb on the Pd surface unhindered. It was the Pd sulfides which had reduced more easily and formed the bulk of the reversible poisoning. Ironically, the lack of a complete permeance recovery seen with Pd/Cu membranes at a given temperature was mostly due to the more energetically favorable Cu sulfides formed on the surface.

The partially recoverable permeance of the Pd/Cu membranes was similar for all of the membranes tested in this work, and solely dependent on temperature once the limiting value of recoverable permeance was reached. The permeance decrease both during poisoning and after recovery was deemed to stem from the surface, and not from the formation of bulk sulfides. The rate at which the permeance was recovered was due to the rate at which the H_2S was flushed out from the system, with the rate of desorption being on a time scale much smaller than that of the fluid dynamics of the shell and tube module. While increasing the temperature did increase the amount of recoverable permeance, returning the hydrogen permeance to 82% of the original value at a given temperature at 500ºC, the full permeance would not be able to be recovered at temperatures less than 550ºC.

10. Poisoning with small H_2S concentrations

10.1 Introduction

While Pd/Cu membranes did not suffer irreparable damage as with pure Pd membranes (Chen and Ma, 2010a) upon exposure to roughly 50 ppm H_2S, the Pd/Cu membranes did sustain a significant permeance loss while running continuously in a feed stream with 45 - 55 ppm H_2S. Reducing the concentration of H_2S to the feed stream could show if there was a limiting concentration below which the membranes would not exhibit a permeance decline at all. Furthermore, increasing the H_2S by small increments would show how Pd/Cu membranes would perform at different levels of gas purity following desulfurization stages.

The objective of this chapter was to test both bi-layer and tri-layer Pd/Cu membranes in extremely small concentrations of H_2S by diluting known concentrations of H_2S with H_2, and evaluating their performance during poisoning and recovery. The purpose was to examine their permeation and selectivity characteristics over long periods of time in varying concentrations of H_2S and to better understand the phenomena of the deactivation of Pd/Cu membranes by H_2S.

10.2 Experimental

The membranes tested in this chapter are listed in Table 10-1. The fabrication, characterization, and poisoning of membrane N_03 was described previously in Chapter 8. The fabrication and characterizations of N_12, N_20 and N_21 were described in Chapter 7, while the poisoning of N_12, N_20 and N_21 were described in this chapter. The membranes were all tested in the experimental system described in Section 3.2. The H_2S concentration was varied by diluting a 5 ppm H_2S/H_2 cylinder with pure H_2 in the gas mixer described in Figure 3-4. The H_2S feed concentrations tested ranged between 0.2 – 5 ppm. The feed concentration was measured before entering the membrane shell casing.

Table 10-1 Membranes tested in this chapter.

Membrane	Intermetallic diffusion barrier	grading	Pd glue (μm)	Pd/Ag barrier (μm)	Pd layer (μm)	Cu layer (μm)	wt% Cu
N_03	air/700ºC/12 h	none	none	none	12.5	1.5	8
N_12	air/700ºC/12 h	Al_2O_3 slurry	1.4	2.8	4.7	4.7	28
N_20	air/700ºC/12 h	Al_2O_3 slurry	1.6	6.1	11	0.3	2
N_21*	air/700ºC/12 h	Al_2O_3 slurry	3.1	2.1	3.2	0.6	5

* After annealing N_21 for 12 hours in He during fabrication, a mass loss equal to 4.9 μm of Pd was observed. While a small mass loss was observed after the first annealing step with N_13, N_16 and N_09a, typical values ranged in a mass equivalent from 0.5 – 1.5 μm of Pd and were assumed to be negligible. It is possible that the thickness of N_21 was slightly more than what was recorded here.

10.3 Results

10.3.1 Poisoning the Pd/Cu membranes

Figure 10-1 shows the percent permeance of N_20 as a function of time after 0.2 ppm of H_2S was introduced at 450°C. The right axis shows the H_2S concentration in the retentate stream. As can be seen, the percent permeance started off at 100%, and remained so for five hours after the H_2S was introduced to the feed stream. Shortly after, the percent permeance began to decline slowly until a steady state value was reached at 76%, where the percent permeance remained stable for another 12 hours.

Since no more than two hours were required to completely flush out the system between changing H_2 and He gases, the five hour time lag seen between the introduction of 0.2 ppm H_2S to the feed stream and the decrease in permeance was caused by the H_2S adsorbing onto the walls of the system. The H_2S which deposited on the walls of the tubes and reactor and the non-porous part of the tubular membrane effectively diluted the feed stream which ultimately reached the membrane. As a result, there was not enough H_2S to cause any decrease in the hydrogen permeance. Once the walls of the system neared equilibrium with the H_2S present in the feed and had adsorbed a significant amount of H_2S, the concentration in the bulk flow became high enough to affect the membrane performance and the permeance began to decrease.

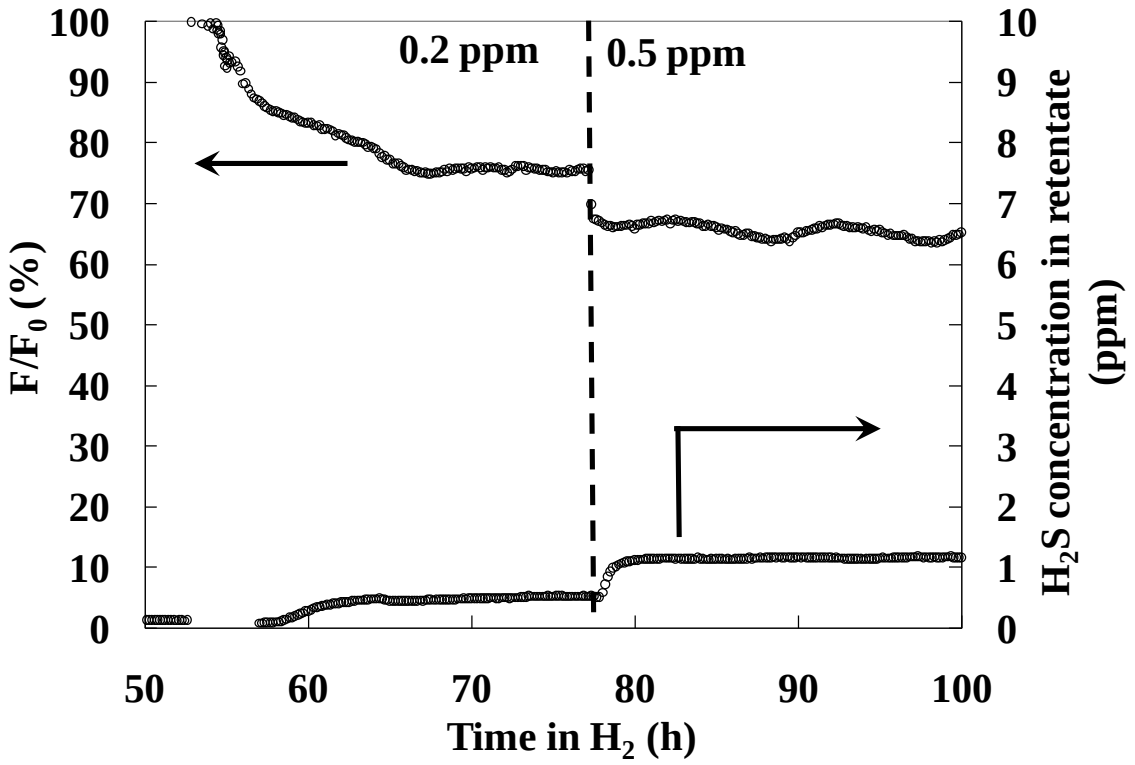

Figure 10-1 Poisoning of N_20 with 0.2 and 0.5 ppm H_2S at 450ºC.

Indeed, the GC did not detect H_2S in the retentate until the permeance began to decrease, showing that the H_2S which had entered the system in the first five hours through the feed had adsorbed without exiting. The concentration of H_2S detected in the retentate was higher than the feed concentration (0.5 and 1.2 ppm with feed concentrations of 0.2 and 0.5 ppm respectively) due to the removal of hydrogen from the flow by the membrane.

However, the system had not yet reached equilibrium with the H_2S in the feed since the H_2S continued to adsorb on the system walls as shown by the increasing concentration of H_2S in the retentate and the decreasing membrane permeance. Indeed, the stabilization of the retentate concentration roughly corresponded with the hydrogen permeance stabilization.

Contrary to the slow decrease in permeance seen upon the introduction of 0.2 ppm, the permeance reached a steady state within 30 minutes after the introduction of 0.5 ppm at 65% of the original permeance at 450ºC. Furthermore, the retentate H_2S concentration stabilized very quickly. Both the relatively fast stabilization of the hydrogen permeance and retentate concentration showed that the system was already covered with adsorbed H_2S and the effects of the change in concentration in the feed were more immediate.

Figure 10-2 shows the continued testing of N_20 at 450ºC with the concentrations of H_2S at 0.2, 0.5, 1, 2 and 5 ppm H_2S and the resulting permeance decline. As expected, increased H_2S in the feed resulted in more H_2S adsorption on the Pd/Cu membrane, which reduced the effective surface area for H_2 adsorption and consequently reduced the permeance further. With each increase in feed concentration, the membrane activity

decreased quickly, reaching a steady state at the new permeance value, showing that enough H_2S had adsorbed onto the system to reach equilibrium and did not influence the permeance decline. The permeance oscillations were caused by oscillations in the temperature by ±5ºC. However, after resetting the constants of the PID controller to new values during the recovery, the oscillations ceased.

The H_2S concentration measured by GC was compared to the concentration as calculated by mass balance. As can be seen, there was little deviation, showing that the calibration curve used in Figure B-3 was accurate. However, during the exposure of the membrane to a feed of 5 ppm, the H_2S retentate flow concentration calculated by mass balance was much higher than the concentration measured by the GC. The reason for the decrease was that the calibration curve shown in Figure B-3 was only accurate for the range of 0.2 – 5 ppm H_2S, and it would be expected to see a large deviation at higher concentrations. Due to H_2 permeating through the membrane and the H_2S remaining, the retentate flow concentration was roughly 2 – 2.5 times higher than the feed flow and at 5 ppm, a retentate concentration of roughly 10 – 11 ppm would be expected.

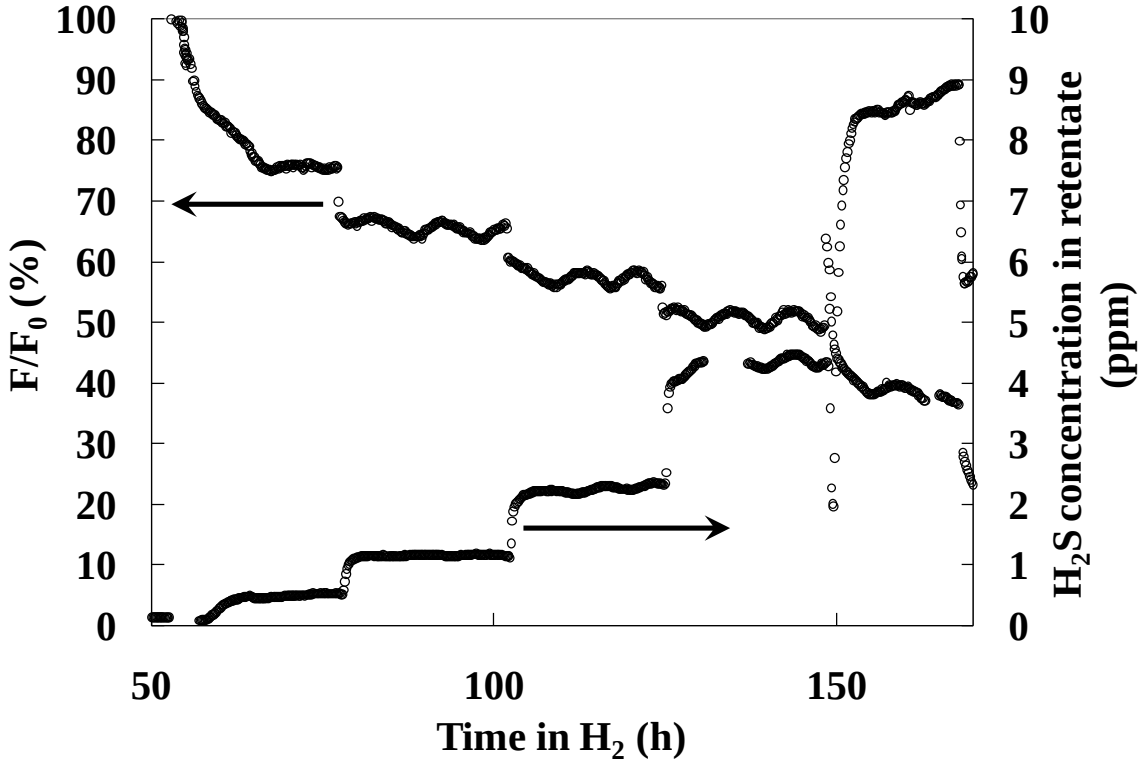

Figure 10-2 Percent permeance as a function of time during the poisoning of N_20 at 450ºC.

Figure 10-3 shows the steady state values for the permeance decline of N_20 at 450ºC as a function of the H_2S feed concentration. The value of permeance decline at 43.7 ppm was taken from the poisoning test of N_03, as shown in Figure 8-1. As can be seen, there was a marketed decrease in the percent permeance with increasing H_2S in the feed stream. However, the slope of the decrease lessened in severity with increased concentration, almost reaching a limit in the amount of adsorption sites that were blocked to H_2 adsorption. Since a similar permeance decline was seen with N_08a with 54.2 ppm at 450ºC in Figure 8-4, it was unclear whether or not feed concentrations of H_2S higher than roughly 50 ppm would result in a slightly more of a permeance decrease, or if the permeance would remain at roughly 20% of the original value at 450ºC. Still, the same experiment performed at 400 and 500ºC (Figure 10-4) showed decrease patterns that were indicative of a limiting value of roughly 20%, even more so than the experiment performed at 450ºC.

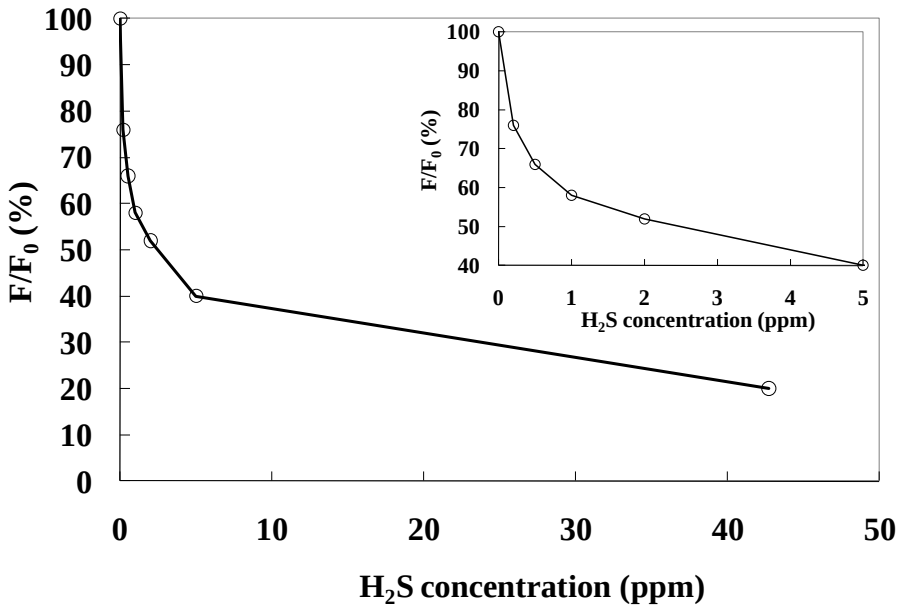

Figure 10-3 Percent permeance decline as a function of H_2S feed concentration at 450°C.

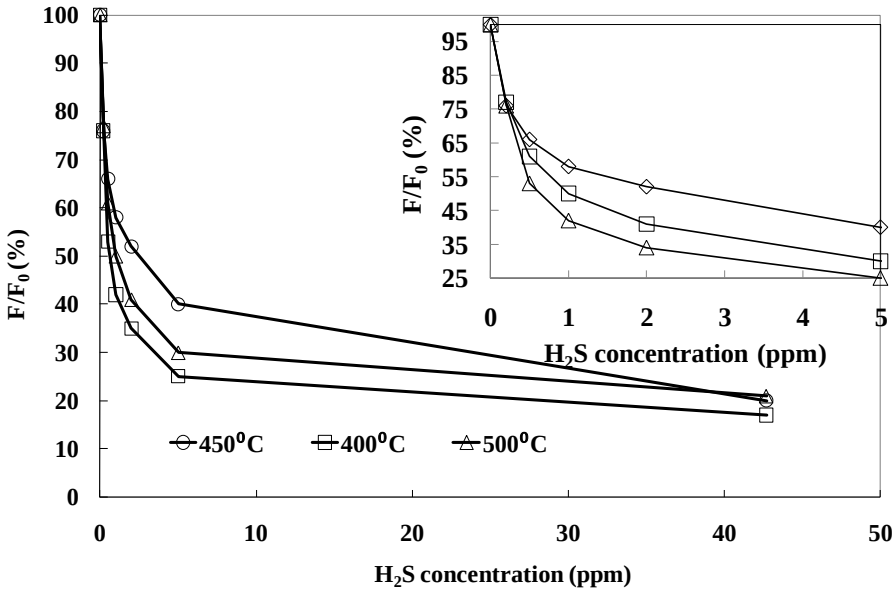

Figure 10-4 Summary of the percent permeance decline as a function of H_2S concentration and temperature.

The permeance decline pattern indicated that H_2S underwent dissociative chemisorption and adsorbed as a monolayer. While Type I* adsorption isotherms from monolayer adsorption have one limiting value of surface coverage as a function of adsorbate pressure, multi-layer isotherms (such as the Type IV isotherm) where the adsorbate species interact with one another can include interim limiting values before reaching a final limiting value, or continuing on to infinity as with Type II and III isotherms (Thomas and Thomas, 1997). In a case where there was not monolayer adsorption, the permeance decline would not follow a smooth curve to a limiting value, but either continue until all available sites were covered and the permeance reached zero, or have a disjointed permeance decline curve corresponding to several interim limiting values of surface coverage.

It was difficult to determine the sulfur surface coverage on the Pd/Cu surface as a function of permeance decline due to the lack of data available in the literature. Studies of pure Pd have indicated that the sulfur atom not only blocked hydrogen adsorption sterically by taking up adsorption sites, but also electronically, creating a repulsion force that decreased the sticking probability of hydrogen to an empty adsorption site (Burke and Madix, 1990). The repulsion force decreased with distance from the sulfur atom resulting in one sulfur atom blocking between 2 – 4 adsorption sites for H_2 (Peden et al., 1986, Burke and Madix, 1990, Alfonso, 2005).

Assuming that the same was true for Pd/Cu as for pure Pd, the permeance decline of 24% at a feed concentration of 0.2 ppm would indicate that the sulfur surface coverage varied between 0.06 – 0.12 ML based on the geometric area of the membrane. Similarly,

* From the Brunauer classification (Thomas and Thomas, 1997).

at approximately 50 ppm the permeance decline of 80% would indicate a sulfur surface coverage of 0.2 – 0.4 ML. Clearly, the poisoning process did not require a large sulfur coverage to hamper the membrane performance. For Pd(1 0 0), it was found that hydrogen adsorption was completely blocked at a value of 0.28 ML (Burke and Madix, 1990).

Figure 10-4 shows the results of the permeance decline between the feed concentrations of 0.2 – 42.7 ppm at 400, 450 and 500ºC. Due to the fact that the permeance of N_20 could not be fully recovered (see Section 10.3.2), fresh Pd/Cu membranes were prepared for the poisoning runs at 400 and 500ºC. Since the poisoning mechanism between the temperatures of 350 – 500ºC was the same, as shown in Chapter 8, it was expected that the permeance decline patterns would be the same at all three temperatures. Again, the permeance decline values at 42.7 ppm for 400 and 500ºC were taken from N_03 in Figure 8-2. As seen previously in Figure 8-1, the values in the remaining permeance between 350 - 500ºC did not differ greatly, although there was a slight increase with temperature due to the exothermic nature of H_2S adsorption on metals. Similarly, there was not a large difference in remaining permeance between the three temperatures upon exposure to 0.2 ppm. However, the rest of the curve of the remaining permeance as a function of H_2S concentration at 450ºC was higher than the curve at 400ºC.

Figure 10-4 appears to show that the adsorption of H_2S on Pd/Cu followed the Type I adsorption isotherm with small differences in permeance loss at very low H_2S concentrations. At high H_2S concentrations, the plots in Figure 10-4 all approached a limiting value depending on the poisoning temperature. Figure 10-4 also shows that at

very low H_2S concentrations, the adsorption isotherm may be approximated by Henry's Law.

The curve of the remaining permeance taken at 450ºC was higher than the curve at 400ºC, due to the exothermic nature of H_2S adsorption. However, what was unexpected was that the curve at 500ºC was also lower than the curve at 450ºC when the curve at 500ºC should have been higher. The reason for the anomaly was most likely due to residual bcc left on the surface of the membrane, and the fcc phase only partially covering the surface. The bi-layer membrane N_12 had a relatively large amount of Cu (28 wt% Cu) in comparison to the other bi-layer membranes made with the same method of support modification (see Table 7-2).

Membranes N_20 and N_21 were both made with the tri-layer method described in Chapter 6 and N_12, the membrane poisoned at 500ºC, was made with the bi-layer method described in Chapter 4. Although the membrane was annealed for the required amount of time as prescribed in Table 4-2, N_12 had a slightly higher Cu composition than the coupons used in the study in Chapter 4 and it was possible that there were residual patches of the bcc phase on the surface, decreasing the sulfur tolerance of the membrane. Also, the highest concentration of the tri-layer membranes would be below the surface. Accordingly, any residual bcc phase would not necessarily come into contact with the feed stream. The bi-layer membranes would have the highest concentration on the surface and consequently, any residual bcc phase would decrease the sulfur tolerance.

Nevertheless, the significance of Figure 10-4 is that it enables process design engineers to calculate how much of a decrease in permeance they are willing to sustain and compensate for in membrane reactor length in comparison to how much it would cost

to desulfurize the feed stream to smaller and smaller concentrations. Finding the most cost effective solution will require an optimization of the two factors.

The advantage of the optimization with the membranes presented here is that even at a concentration of 5 ppm, the tri-layer membranes would outperform homogeneous fcc membranes with 20 wt% Cu, even if the homogeneous membranes did not exhibit a permeance decline during poisoning, which would not necessarily be the case. The tri-layer membranes have a permeance conducive to pure Pd membranes before they suffer the decrease in permeance caused by the H_2S adsorption as seen in Table 7-3 and Table 7-4. The 20 wt% Cu homogeneous membranes would already be performing at roughly 20% of the permeance of pure Pd membranes before the introduction of H_2S (McKinley, 1966), showing that the tri-layer membranes would be the most cost-effective solution.

The increase in H_2S seen between the feed flow and the retentate flow in Figure 10-2 will also have a greater significance when H_2S is introduced to a CMR. The increase in H_2S across the length of the membrane reactor was caused by H_2 permeating through the membrane, increasing the H_2S retentate concentration in the axial direction. In a CMR, the retentate concentration of the H_2S would be much less than with the ideal testing state presented here because the feed flow would consist of a mixed gas with a fraction of H_2. Because there would be less H_2 in the mixed gas feed than with the pure gas test system, the increase of H_2S along the length of the reactor would not be as steep, resulting in less of a permeance decline.

However, it was unclear if it was the concentration of H_2S or the H_2S/H_2 ratio in the feed which dictated the permeance decline seen by the Pd/Cu membranes. If it was the ratio, then the effect on the membrane would be far more severe in a mixed gas

system. In a pure gas system as was tested in this work, a feed concentration of 0.5 ppm H_2S would correspond to a H_2S/H_2 ratio of $5 * 10^{-7}$. The concentration which increased to 1.2 ppm towards the retentate would result in a H_2S/H_2 ratio of $1.2 * 10^{-6}$.

In a mixed gas system with 27% H_2 (balance CO_2, H_2O, CO), as is common with syngas feeds (Augustine et al., 2010), a feed flow with 0.5 ppm H_2S would have a corresponding H_2S/H_2 ratio of $1.9 * 10^{-6}$, four times higher than the case with the pure gas feed. Depending on the hydrogen recovery of the mixed gas system, the concentration in the retentate would increase along the length of the membrane as H_2 permeated through, and the H_2S/H_2 ratio would increase even more. In the mixed gas system with 27% H_2 in the feed and an 80% hydrogen recovery (Augustine et al., 2010), the retentate H_2S concentration would only be increased from 0.5 ppm in the pure gas scenario to 0.6 ppm. However, the H_2S/H_2 ratio would increase to $0.9 * 10^{-5}$, almost an order of magnitude higher than the H_2S/H_2 ratio of the retentate flow of the pure gas system. Increasing the H_2 recovery would result in an even larger H_2S/H_2 ratio at the exit. The higher H_2S/H_2 ratio could place the membrane at a point on the Type I adsorption curve much closer to the saturation level of the monolayer, resulting in more of a permeance decline. The worst case scenario would be the possible formation of bulk sulfides, as seen with pure Pd in Section 8.3.1, which would render the membrane useless.

10.3.2 Recovering the Pd/Cu membranes

Figure 10-5 shows the recovery of N_20 in pure H_2. The permeance stabilized after 50 hours at 450ºC with about 65% of the original permeance recovered, indicating an permeance loss of 35% at 450ºC. The H_2S concentration in the retentate flow swiftly

dropped upon the re-introduction of H_2, as could be expected, and then tapered off to roughly 0.8 ppm. It could be concluded that the residual H_2S detected in the retentate flow was desorbing from the walls of the reactor and the non-porous part of the tube (as seen in Appendix B.2) because the permeance of the membrane did not increase any further even though the H_2S continued to be detected in the retentate.

Interestingly enough, the H_2S desorbing from the walls of the reactor had little to no influence on the permeance of the membrane. While 0.8 ppm was detected in the retentate, the permeance after the recovery at 450ºC was at 65%. According to Figure 10-3, a permeance decline of 65% was seen with a feed of 0.5 ppm with 1.2 ppm in the retentate (Figure 10-1). Clearly, it was not the H_2S in the retentate stream which was the cause of the cause of the lack of recovery, but the remaining surface sulfides described in Chapters 8 and 9. Due to the Reynold's number being so low (Re = 0.35 with a retentate flow of 35 sccm and a pressure difference of 1 atm) and the flow being laminar, the H_2S desorbing from the walls of the reactor did not mix well enough in the bulk of the stream to reach the membrane surface. Furthermore, the H_2S desorbing from the non-porous part of the tube would not reach the membrane since the non-porous part lies between the membrane and the shell casing exit (see Appendix B.2).

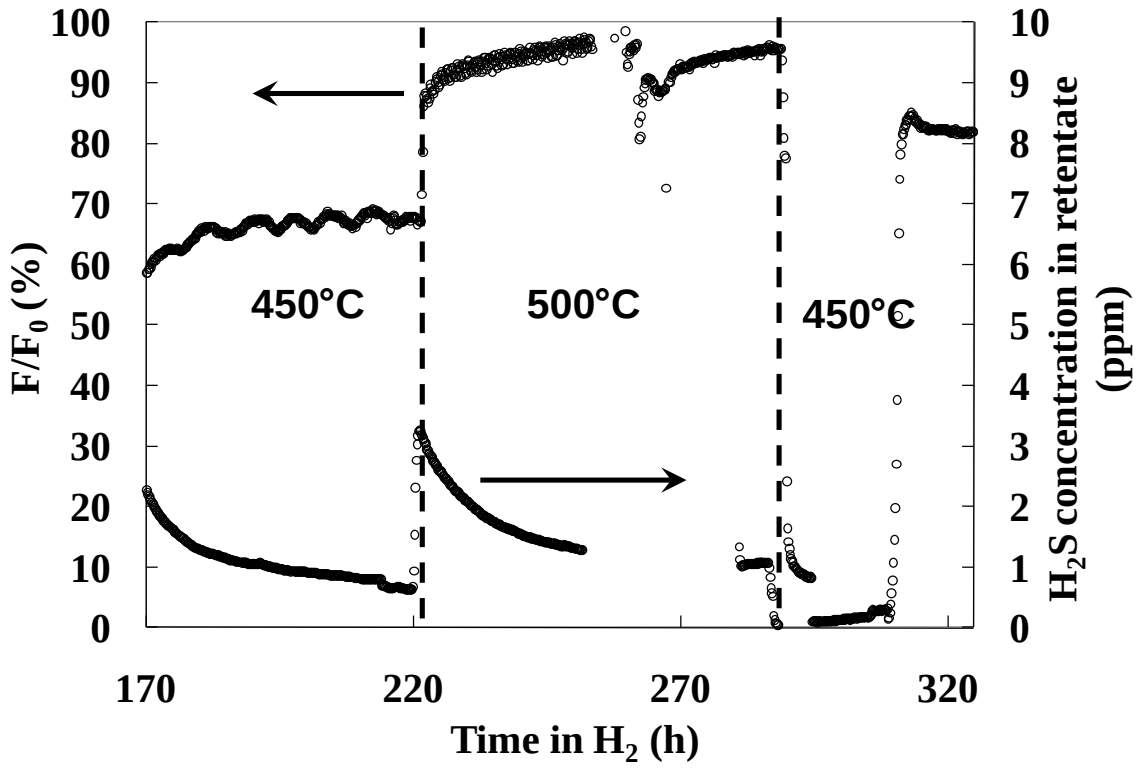

Figure 10-5 Recovery of N_20 at 450 and 500°C.*

* The percent permeance is relative to the original permeance of N_20 at 450ºC.

Following the stabilization of the permeance at 450ºC, the temperature was increased to 500ºC (at 220 hours in Figure 10-5) in an effort to recover more of the permeance. Increasing the temperature resulted in a greater amount of H_2S desorbing from both the system and the membrane, as seen by the increase in concentration of the retentate flow. After the permeance stabilized at 500ºC, the temperature was decreased to 450ºC to see the effect of the higher recovery temperature on the H_2 permeance.

As with the re-introduction of N_20 to H_2 at 450ºC, the permeance increased and stabilized. Upon decreasing the temperature to 450ºC, the permeance had increased to a value roughly 82% of the original permeance. Increasing the temperature to 500ºC had increased the amount of recoverable permeance, as seen in Chapter 9. Again, H_2S could be clearly seen in the retentate flow at a value of 1.2 ppm even though the permeance was at 82%. According to Figure 10-4, 76% of the permeance should remain at a concentration of 0.2 ppm in the feed and 0.5 ppm in the retentate. Clearly, the H_2S detected in the retentate flow continued to come from the system and had little to no effect on the permeance of the membrane due to the laminar nature of the reactor flow.

Figure 10-6 shows the Sieverts' Law regressions at 450ºC for the membranes poisoned in this chapter both before the poisoning and after the final recovery at 500ºC. As with the results of N_02, N_03 and N_08a in Chapter 8 and N_09a in Chapter 9, the membranes all had linear slopes showing that one dimensional diffusion continued to be the rate limiting step of hydrogen permeation through the composite membranes, and that the remaining surface sulfides on each membrane had merely reduced the effective area for H_2 adsorption. Furthermore, as shown in Figure 9-23, the permeance reduction for N_12 and N_20 was roughly 18 – 20% for each membrane regardless of poisoning

temperature, after they had all been recovered at 500ºC since they had reached the limiting value of recoverable permeance, as described in Section 9.3.3. N_21 was the exception in that the permeance reduction was by 35% after recovering at 500°C, seemingly not improving the recovery seen at 450°C.

The reason for the discrepancy was that N_21 had slightly more Cu (shown in Table 10-1) than N_20 and had not yet been annealed at 500°C. While the recovery at 500°C did not affect the permeance of N_20, N_21 continued to anneal, and the Cu diffused further into the membrane layer, decreasing the permeance further and preventing an accurate assessment of the recoverable permeance at 500°C. Since N_20 saw no permeance decrease after the dwell time at 500ºC, limiting the Cu thickness to 0.3 µm or less should prevent the decrease in permeance seen by N_21 even though the Cu would most certainly continue to diffuse.

Figure 10-7 shows the activation energy regression calculated from the Sieverts' Law permeance taken at each temperature both before the poisoning and after the final recovery at 500ºC. As with N_08a in Figure 8-5 and N_09a in Figure 9-22, the activation energy of permeation did not change significantly for N_12 and N_20, showing that neither the mechanism nor the bulk structure of the membranes had changed from the remaining surface sulfides. The lack of change in activation energy further confirmed that the sulfide formation merely reduced the effective area for H_2 adsorption, and did not interact with the bulk of the membrane. N_21 did see an increase in the activation energy, however the increase would be expected from further diffusion of the Cu into the Pd layer and thus increasing the mass transfer resistance to H_2.

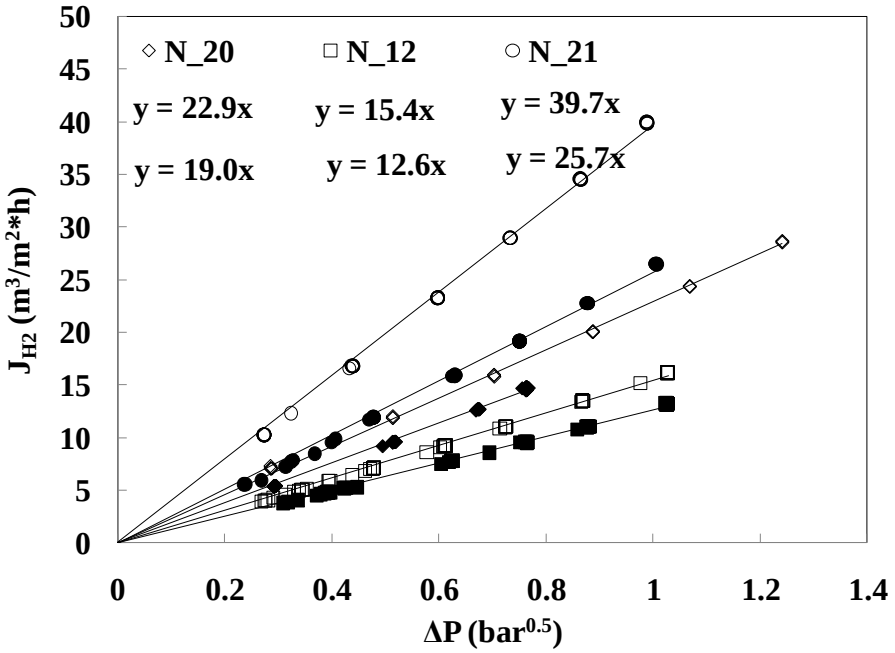

Figure 10-6 Sieverts' Law at 450°C for the Pd/Cu membranes before poisoning (open marker, top value) and after recovery at 500°C (closed marker, bottom value).

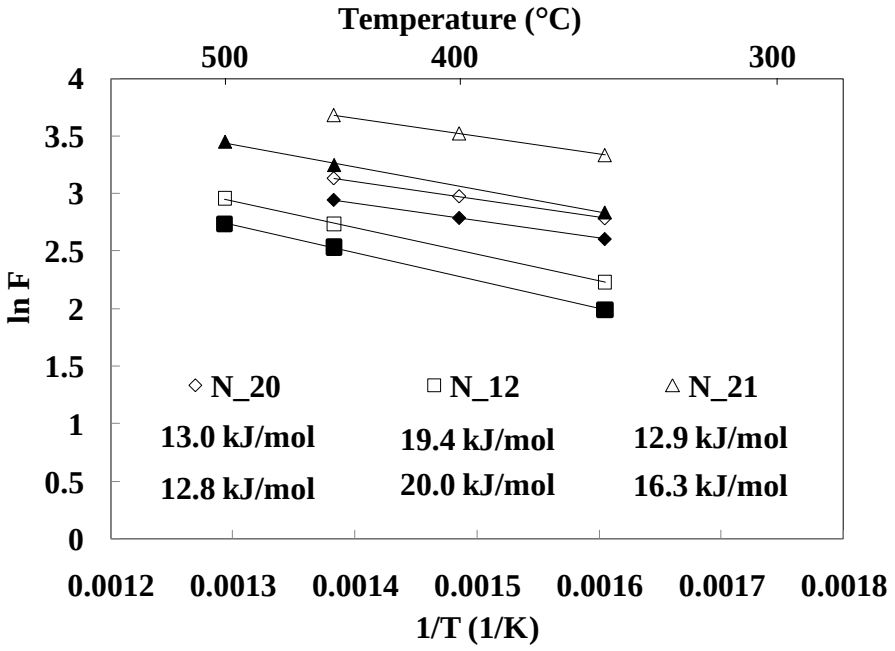

Figure 10-7 Activation energy of the Pd/Cu membranes before poisoning (open marker, top value) and after recovery at 500°C (closed marker, bottom value).

10.4 Conclusions

The study performed in this chapter showed that if there was a limiting concentration of H_2S below which the permeance of Pd/Cu membranes would not be affected, it was outside the limits of the GC to detect accurately. Both bi-layer Pd/Cu membranes and tri-layer Pd/Cu/Pd membranes lost a portion of their permeance during continuous exposure to H_2S due to adsorption of sulfur on the membrane surfaces. However, the hydrogen permeance stabilized quickly. The permeance decreased with increasing H_2S feed concentration due to the equilibrium between the ambient H_2S concentration and the adsorbed sulfur surface coverage being shifted towards more sulfur adsorption. The permeance decline increased with increasing H_2S concentration towards a limiting value of roughly 20% at roughly 42.7 ppm without bulk sulfides forming indicating a monolayer type adsorption.

Furthermore, the permeance decline increased with decreased temperature due to the exothermic nature of H_2S adsorption on metals. However, the percent decline of the bi-layer membrane was greater than that of the tri-layer membrane even though the poisoning temperature was higher indicating the possibility of patches of the less sulfur tolerant bcc phase on the surface of the bi-layer Pd/Cu membrane.

All of the membranes were recovered in pure H_2 with part of the permeance being recoverable and part being irrecoverable at a given recovery temperature. The irrecoverable portion of the permeance decreased with increasing temperature.

11. Overall Conclusions

- High-temperature, X-ray diffraction was successfully employed to investigate the kinetics of the fcc Pd/Cu membrane fabrication. The formation of the fcc alloy on the surface of the Pd/Cu layer was found to be one dimensional and controlled by the interdiffusion of Pd and Cu.
- Forming the fcc Pd/Cu alloy on the membrane surface from bi-layers would either require high annealing temperatures for short annealing times which would be detrimental to membrane selectivity, or low annealing temperatures with high annealing times which would be less cost effective for membrane production.
- Bath agitation enabled uniform, ultra-thin layers of Cu to be deposited on Pd surfaces in a consistent manner, and uniform, ultra-thin Pd layers to be deposited on the Cu layers through displacement, forming a Pd/Cu/Pd tri-layer.
- Depositing a Pd/Cu/Pd tri-layer drastically reduced both the annealing time and temperature needed for the fcc alloy formation on membrane surfaces.
- Stable, high permeance fcc Pd/Cu membranes were fabricated with the tri-layer that performed on par with the Pd membranes fabricated in this work due to the confinement of the Pd/Cu alloy to the surface, thus minimizing the disadvantage inherent with fcc Pd/Cu alloys of a decreased permeance.
- The poisoning of Pd/Cu membranes was found to have caused a partially non-recoverable permeance loss at lower temperatures. XPS results showed that the recoverable permeance was mostly due to the formation of less energetically

favorable Pd sulfides and the unrecoverable permeance was mostly due to the formation of Cu sulfides. For the conditions tested in this work, the membrane poisoning was caused by surface sulfide formation rather than bulk sulfide formation.

- The enhanced tolerance of fcc Pd/Cu membranes in comparison to Pd membranes was due to the preferential adsorption of sulfur on Cu adsorption sites, allowing H_2 to continue to be adsorbed on Pd adsorption sites and to permeate through the layer.
- The recoverable permeance of Pd/Cu membranes decreased with increased exposure time to H_2S, reaching a limiting value that increased with temperature due to the exothermic nature of H_2S chemisorption on metals.
- Both bi-layer and tri-layer Pd/Cu membranes showed decreases in permeance at small concentrations of H_2S. The permeance declines increased with H_2S concentration, reaching a limiting value at roughly 20% of the original permeance. However, given that there was no permeance loss due to Pd/Cu alloying, the tri-layer membranes would outperform homogeneous fcc Pd/Cu membranes even if the homogeneous membranes retained the original permeance.

12. Recommendations

- Tri-layer Pd/Cu membranes should be tested in WGS CMR's both with and without H_2S as it is not known how the H_2S adsorption on the Pd/Cu surface would change in the presence of the WGS components. Homogeneous 20 wt% Cu membranes have previously been tested in WGS CMR's at 900°C and resulted in lower CO conversions than pure Pd MR's due to the decrease in hydrogen permeance (Iyoha et al., 2007b). Tri-layer fcc Pd/Cu membranes would have both the high permeance associated with pure Pd membranes enabling a high CO conversion to be attained, and the sulfur resistance of fcc Pd/Cu membranes. Care should be maintained at high H_2 recoveries as the H_2S/H_2 ratio will increase along the length of the CMR and could not only deactivate the surface of the membrane, but destroy it by forming bulk sulfides as seen with CMR's including 2000 ppm H_2S in the feed flow (Iyoha et al., 2007a).
- Previous work (Zhang et al., 2007) has indicated that the presence of CO_2 and H_2O decreases the permeance of Pd/Cu membranes (the composition of the alloy was not reported) in the temperature range of 250 - 500°C. However, it was not clear if the decrease was due to surface adsorption or mass transfer effects within the gas flow. The effect of WGS gases on Pd/Cu membranes should also be explored.
- To further increase the permeance of the tri-layer fcc Pd/Cu composite membranes, a larger amount of silver can be deposited within the layer before adding the sub-micron Pd/Cu alloy layer. However, it is likely that a Pd composite membrane with a

larger amount of Ag within the bulk of the layer would develop more leaks over time due to the Kirkendall effect.

- Another way of increasing the permeance of the tri-layer Pd/Cu alloys would be to employ a more effective method of support grading which does not cause the Pd to penetrate so deeply into the pores of the support, such as activating the Al_2O_3 grading particles as presented by Guazzone (2006). The thin, dense Pd membrane could then be modified for sulfur resistance with the sub-micron Pd/Cu alloy presented in this work.
- Since the XPS was unable to differentiate between sulfides formed on and just below the surface, LEIS would be an ideal tool to further analyze the surface sulfides which prevented the complete permeance recovery. LEIS could determine if the sulfides formed solely on the top atomic layer or within the layers beneath, similarly to how Miller et al (2008a) determined the top atomic layer composition of annealed Pd/Cu alloys.

Nomenclature

Latin letters

A	area	cm^2
A	absorbance, pre-exponential factor	
b	path length of the sample	cm
C	concentration	mol/L or mol/m^3
D	diffusion coefficient	m^2/s
E	activation energy	kJ/mol
E_0	incident electron beam energy	keV
E_C	energy above which characteristic X-rays are produced	keV
F	permeance	$m^3/(m^2*h*bar^{0.5})$ or $m^3/(m^2*h*bar)$
f	weight fraction	
G	Gibb's free energy	kJ/mol
G_x	fraction of diffracted intensity	
H	enthalpy	kJ/mol
h	mass transfer coefficient	$m/(s*bar^{0.5})$
J	flux	$m^3/(m^2*h)$
K_s	Sieverts' constant	$bar^{0.5}$
k	Avrami rate constant, reaction rate constant	
k_a	adsorption rate constant	$m^3/(m*h*bar)$
k_d	desorption rate constant	$m^3/(m^2*h)$
k_i	rate constant into Pd lattice	$m^3/(m^2*h)$
k_o	rate constant exiting Pd lattice	$m^3/(m^2*h)$
l	membrane thickness	m
M	molecular weight	g/mol

m	mass	g
$n_{H/Pd}$	molar H/Pd ratio	
n	n-value exponent, Avrami exponent	
P	pressure	bar
Q	permeability	$m^3/(m*h*bar^{0.5})$
R	universal gas constant	J/(mol*K)
R_{tot}	resistance of composite membrane	$(h*bar^{0.5})/m$
R_x	depth of X-ray production	µm
r	reaction rate	mM/min
r	tube radius	m
r_p	pore radius	m
S	solubility	mol/m^3
s(θ)	sticking coefficient	
T	temperature	°C or K
t	time	h or min
w	weight fraction	
X	volume adsorbed/volume of krypton in monolayer	
x	penetration depth	m
z	direction of membrane thickness	m

Greek letters

α	reaction order for Cu^{2+}	
β	reaction order for H_2CO	
Γ	rate of molecular bombardment	mol/m^2*h
γ	reaction order for OH^-	
Δ	difference	
δ	reaction order for $EDTA^{4-}$	
θ	fractional surface coverage	

θ	half of the diffraction angle	
κ	hydrogen solubility coefficient	mol/m^3
ε	porosity	
ε	molar absorbtivity	L/mol*cm
μ	linear adsorption coefficient	1/m
μ_k	geometric factor for Knudsen diffusion	
μ_v	geometric factor for viscous flow	
η	viscosity	m^2/s
π	pi constant	
ρ	density	g/cm^3, kg/m^3

subscripts

0	value before sulfur poisoning
1	low pressure side of membrane
2	high pressure side of membrane
a	of adsorption
d	of desorption
D	of diffusion
H	of hydrogen
H_2	of hydrogen gas
k	of Knudsen diffusion
Q	of permeability
S	of solubility
v	of viscous flow
X	of the volume adsorbed

References

Agnew, W.G., ed. The Hydrogen Economy: Opportunities, Costs, Barriers, and Research and Development Needs. National Academies Press, Washington D.C., 2004.

Ainslie, N.G.; Hoffman, R.E. and Seybolt, A.U. "Sulfur Segregation at [α]-iron grain boundaries--I." *Acta Metallurgica.* **8**(8) (1960) 523.

Akis, B.C.; Engwall, E.E.; Mardilovich, I.P. and Ma, Y.H. "Effects of the *in-situ* formation of an intermetallic diffusion barrier layer on the properties of composite palladium membranes." *Preprints of Symposia - ACS.* **48**(1) (2003) 337 - 338.

Alefeld, G. and Volkl, J., EDX. Hydrogen in Metals. Springer – Verlag, Berlin, 1978.

Alfonso, D.R. "First-principles study of sulfur overlayers on Pd(111) surface." *Surface Science.* **596** (2005) 229 – 241.

Alfonso, D.R. "Initial incorporation of sulfur into the Pd(1 1 1) surface: a theoretical study." *Surface Science.* **600** (2006) 4508 – 4516.

Alfonso, D.R.; Cugini, A.V. and Sorescu, D.C. "Adsorption and decomposition of H_2S on Pd(1 1 1) surface: a first-principles study." *Catalysis Today.* **99** (2005) 315 – 322.

Alfonso, D. R.; Cugini, A. V. and Sholl, D. S. "Density functional theory studies of sulfur binding on Pd, Cu and Ag and their alloys." *Surface Science*. **546**(1) (2003) 12.

Ali, J.K.; Newson, E.J. and Rippin, D.W.T. "Deactivation and regeneration of Pd-Ag membranes for dehydrogenation reactions." *Journal of Membrane Science*. **89** (1994) 171 – 184.

Al-Kassab, T.; Macht, M. and Wollenberger, H. "FIM/AP analysis of Cu-Pd multilayers." *Appied Surface Science.* **87 - 88** (1995) 329-336.

Antoniazzi, A.B.; Haasz, A.A. and Stangeby, P.C. "The effect of adsorbed carbon and sulfur on hydrogen permeation through palladium." *Journal of Nuclear Materials.* **162 – 164** (1989) 1065 – 1070.

Athayde A.L.; Baker, R.W. and Nguyen, P. "Metal composite membranes for hydrogen separation." *Journal of Materials Science*. **94** (1994) 299 – 311.

Averback, R.S.; Hofler, H.J.; Hahn, H. and Logas, J.C. *Nanostructured Materials*, **1** (1992) 173.

Avrami, M. “Kinetics of phase change. I. General theory.” *Journal of Chemical Physics*. **7** (1939) 1103 – 1112.
Avrami, M. “Kinetics of phase change. II. Transformation-time relations for random distribution of nuclei.” *Journal of Chemical Physics*. **8** (1940) 212 – 224.

Avrami, M. “Granulation, phase change and microstructure. Kinetics of phase change. III.” *Journal of Chemical Physics*. **9** (1941) 177 – 184.

Augustine, A.; Ayturk, M.E.; Kazantzis, N. and Ma, Y.H. “Composite palladium membrane reactor for the water-gas shift reaction.” Presented at the 2009 AIChE Annual Meeting, Nashville, TN, November 8 – 13, 2009.

Augustine, A.; Ayturk, M.E.; Kazantzis, N. and Ma, Y.H. “Palladium membrane reactor for water gas shift reaction.” In Press, *Catalysis Today*, (2010).

Ayturk, M.E. “Synthesis, annealing strategies and in-situ characterization of thermally stable composite thin Pd/Ag alloy membranes for H_2 separation.” PhD thesis, Worcester Polytechnic Institute, 2007.

Ayturk, M.E.; Engwall, E.E. and Ma, Y.H. “Microstructure analysis of intermetallic diffusion-induced alloy phases in composite Pd/Ag/porous stainless steel membranes.” *Industrial Engineering and Chemical Research*. **46** (2006a) 4265 – 4306.

Ayturk, M.E.; Mardilovich, I.P.; Engwall, E.E. and Ma, Y.H. “Synthesis of composite Pd-porous stainless steel (PSS) membranes with a Pd/Ag intermetallic diffusion barrier.” *Journal of Membrane Science*. **285** (2006b) 385 – 394.

Ayturk, M.E.; Payzant, E.A.; Speakman, S.A. and Ma, Y.H. “Isothermal nucleation and growth kinetics of Pd/Ag alloy phase via *in situ* time-resolved high-temperature X-ray diffraction (HTXRD) analysis.” *Journal of Membrane Science*. **316** (2008) 97 – 111.

Ayturk, M.E. and Ma, Y.H. “Electroless Pd and Ag deposition kinetics of the composite Pd and Pd/Ag membranes synthesized from agitated plating baths.” *Journal of Membrane Science*. **330** (2009) 233 – 245.

Badia, M. “Interdiffusion of Fe and the transition metals.” PhD thesis, University of Nancy, 1969.

Balachandran, U.; Lee, T.H.; Chen, L.; Song, S.J.; Picciolo, J.J. and Dorris, S.E. "Hydrogen separation by dense cermet membranes." *Fuel*. **85** (2006) 150 – 155.

Barbier, J.; Lamy-Pitara, E.; Marecot, P.; Boitiaux, J.P.; Cosyns, J. and Verna, F. “Role of sulfur in catalytic hydrogenation reactions.” *Advances in Catalysis*. **39** (1990) 279 – 318.

Barrer, R.M. “Stationary and nonstationary states of flow of hydrogen in palladium and iron.” *Transactions of the Faraday Society.* **36** (1940) 1235 - 48.

Bartholomew, C.H.; Agrawal, P.K. and Katzer, J.R. “Sulfur poisoning of Metals.” *Advances in Catalysis.* **31** (1982) 135 – 242.

Bhide, V.G.; Salkalachen, S.; Rastogi, A.C.; Rao, C.N.R. and Hegde, M.S. “Depth profile composition studies of thin film CdS: Cu_2S solar cells using XPS and AES.” *Journal of Physics D: Applied Physics*. **14** (1981) 1647 – 1656.

Biswas, J.; Bickle, G.M. and Gray, P.G. “The role of deposited poisons and crystallite surface structure in the activity and selectivity of reforming catalysts.” *Catalysis Reviews – Science and Engineering.* **30**(2) 161 – 247.

Bitler, W.R.; Pickering, H.W. and Kaja, S. “Interdiffusion kinetics of copper with palladium.” *Platinum Surface Finishings*. **72** (1985) 60 - 63.

Bomermann, J.; Huck, M.; Kuntze, J.; Rauch, T.; Speller, S. and Heiland, W. “An STM, AES and LEED study of the segregated sulfur on Pd(111).” *Surface Science.* **357 – 358** (1996) 849 – 854.

Borovskii, I.B.; Marchukova, I.D. and Ugaste, Y.E. “Interdiffusion in binary systems forming a continuous series of solid solution by using a local x-ray spectral analysis. The iron-palladium, cobalt-palladium, nickel-palladium, and copper-palladium systems.” *Fiz. Met. Metalloved*. **22** (1966) 849-858.

Bredesen, R.; Jordal, K. and Bolland, O. “High-temperature membranes in power generation with CO_2 capture.” *Chemical Engineering and Processing.* **43** (2004) 1129 – 1158.

Bryden, K.J. and Ying, J.Y. "Nanostructured palladium membrane synthesis by magnetron sputtering." *Materials Science and Engineering*. **A204** (1995) 140 – 145.

Bryden, K.J. and Ying, J.Y. "Nanostructured palladium-iron membranes for hydrogen separation and membrane hydrogenation reactions." *Journal of Membrane Science*. **203** (2002) 29 – 42.

Burke, M.L. and Madix, R.J. “Hydrogen on Pd (100) – S: the effect of sulfur on precursor mediated adsorption and desorption.” *Surface Science.* **237** (1990) 1 – 19.

Butrymowicz, Manning and Read. “Diffusion in copper and copper alloys.” *Journal of Physical Chemistry Reference Data.* **4**(1) (1976) 201 – 213.

Buxbaum, R.E. and Kinney, A.B. “Hydrogen transport through tubular membranes of palladium-coated tantalum and niobium.” *Industrial and Engineering Chemistry Research*. **35** (1996) 530 – 537.

Chaplin, B.P.; Shapley, J.R. and Werth, C.J. “Regeneration of Sulfur-Fouled Bimetallic Pd-Based Catalysts.” *Environmental Science and Technology*. **41** (2007) 5491- 5497.

Chen, C.-H. and Ma, Y.H. “The effect of H_2S on the performance of Pd and Pd/Au composite membranes.” In Press, *Journal of Membrane Science*, (2010a)

Chen, C.-H. and Ma, Y.H. “The effect of H_2S concentration on hydrogen permeance of a composite Pd/Au hydrogen separation membrane prepared by galvanic displacement.” Presented at the ACS 239th National Meeting and Exposition, San Francisco, CA, USA, March 21 – 26, 2010b.

Chen, L.C.; Spaepen, F.; Robertson, J.L.; Moss, S.C. and Hiraga, K. *Journal of Materials Research*, **5** (1990) 1871.

Cheng, Y.S. and Yeung, K.L. "Effects of electroless plating chemistry on the synthesis of palladium membranes." *Journal of Membrane Science*. **182** (2001) 195 - 203.

Chow, K.M.; Ng, W.Y. and Yeung, L.K. “Barrier properties of Ni, Pd and Pd-Fe for Cu diffusion.” *Surface Coating Technology*. **105** (1998) 56-64.

Christian, J.W. Theory of Transformations in Metals and Alloys, Part 1: Thermodynamics and General Kinetic Theory. Pergamon, New York, 1978.

Cicero, D.C. and Jarr, L.A. "Application of ceramic membranes in advanced coal-based power generation systems." *Separation Science and Technology*. **25** (1990) 1455 - 1472

Collins, J.P. and Way, J.D. "Preparation and characterization of a composite palladium - ceramic membrane." *Industrial and Engineering Chemistry Research*. **32** (1993) 3006 - 3013.

Cullity, B. D. and Stock, S. R. Elements of X-ray Diffraction. Prentice Hall: New Jersey, USA, 2001.

“Hydrogen from Coal Program: Development, and Demonstration Plan for the period 2009 through 2016”, Office of Fossil Energy, National Energy Technology Laboratory, US Department of Energy, 2009.

Deville, H. St C. *C.r. hebd. Seanc. Acad. Sci.,* Paris **59** (1864) 965 – 967.

Donahue, F.M. “Kinetics of electroless copper plating. III. Mass transport effects.” *Journal of the Electrochemical Society.* **127**(1) (1980) 51 – 55.

Donahue, F.M. “Kinetics of electroless copper plating. V. Mass transport at cylindrical surfaces.” *Journal of the Electrochemical Society.* **128**(11) (1981) 2366 – 2367.

Donahue, F.M. and Shippey, F.L. “Kinetics of electroless copper plating. II. Mixed potential analysis.” *Plating.* **60** (1973) 135 – 137.

Donahue, F.M.; Wong, K.L.M. and Bhalla, R. “Kinetics of electroless copper plating. IV. Empirical rate law for H_2CO-EDTA baths.” *Journal of the Electrochemical Society.* **127**(11) (1981) 2340 – 2342.

Dumesic, J.; Koutsky, J.A. and Chapman, T.W. “The rate of electroless copper deposition by formaldehyde reduction.” *Journal of the Electrochemical Society.* **121**(11) (1974) 1405 – 1412.

Edlund, D.J. and Pledger, W.A. "Thermolysis of hydrogen sulfide in a metal-membrane reactor." *Journal of Membrane Science*. **77** (1993) 255 – 264.

Edlund, D.J. and Pledger, W.A. "Catalytic platinum-based membrane reactor for removal of H_2S from natural gas streams." *Journal of Membrane Science*. **94** (1994a) 111 – 119.

Edlund, D.J.; Friesen, D.; Johnson, B. and Pledger, W.A. “Hydrogen-permeable metal membranes for high-temperature gas separations.” *Gas Separation and Purification.* **8**(3) (1994b) 131 – 136.

Edlund, D.J. and McCarthy, J. "The relationship between intermetallic diffusion and flux decline in composite-metal membranes: implications for achieving long membrane lifetime." *Journal of Membrane Science*. **107** (1995) 147 – 153.

El-Raghy, S.M. and Abo-Salama, A.A. “The electrochemistry of electroless deposition of copper.” *Journal of the Electrochemical Society.* **126** (1979) 171 – 176.

Endo, K.; Ohno, H.; Matsuda, K. and Asakura, S. “Electrochemical and surface studies on the passivity of a dental Pd-based casting alloy in alkaline sulphide solution.” *Corrosion Science*. **45** (2003) 1491 - 1504.

Fairbanks, N. and Carrick, A. The Casa Cookbook. Acolyte Science, 2005.

Feldstein, N. and Weiner, J.A. "The effectiveness of tin sensitizer solutions." *Plating*. **59**(2) (1972) 140 – 141.

Fox, E.B.; Velu, S.; Engelhard, M.H.; Chin, Y-H.; Miller, J.T.; Kropf, J. and Song, C. “Characterization of CeO_2-supported Cu-Pd bimetallic catalyst for the oxygen-assisted water-gas shift reaction.” *Journal of Catalysis*. **260** (2008) 358 – 370.

Frieske, H. and Wicke, E. “Magnetic susceptibility and equilibrium diagram of palladium hydride.” *Berichte der Bunsen-Gesellschaft.* **77** (1973) 48-52.

Gao, H.; Lin, Y.S.; Li, Y. and Zhang, B. "Chemical stability and its improvement of palladium-based metallic membranes." *Industrial and Engineering Chemistry Research*. **43** (2004) 6920 - 6930.

Geilin, P.; Urfels, L.; Primet, M. and Tena, E. "Complete oxidation of methane at low temperature over Pt and Pd catalysts for the abatement of lean-burn natural gas fuelled vehicles emissions: influence of water and sulfur containing compounds." *Catalysis Today*. **83** (2003) 45 – 57.

Goldstein, J.; Newbury, D.; Joy, D.; Lyman, C.; Echlin, P.; Lifshin, E.; Sawyer, L. and Michael, J. Scanning Electron Microscopy and X-Ray Microanalysis. 3rd edition. Springer Science and Business Media, Inc., USA, 2003.

Graham, T. "On the adsorption and dialytic separation of gases by colloid septa." *Philosophical Transactions of the Royal Society of London.* **156** (1866) 399 – 439.

Gryaznov, V.M. "Metal containing membranes for the production of ultrapure hydrogen and the recovery of hydrogen isotopes." *Separation and Purification Methods*. **29**(2) (2000) 171 – 187.

Gryaznov, V.M.; Serebryannikova, O.S.; Serov, Y.M.; Ermilova, M.M.; Karavanov, A.N.; Mischenko, A.P. and Orekhova, N.V. "Preparation and catalysis over palladium composite membranes." *Applied Catalysis A: General.* **96** (1993) 15 – 23.

Guazzone, F. "Engineering of substrate surface for the synthesis of ultra-thin composite Pd and Pd-Cu membranes for H_2 separation." PhD thesis. Worcester Polytechnic Institute, 2006.

Guazzone, F.; Engwall, E.E. and Ma, Y.H. "Effects of surface activity, defects and mass transfer on hydrogen permeance and n-value in composite palladium-porous stainless steel membranes." *Catalysis Today.* **118** (2006a) 24 – 31.

Guazzone, F. and Ma, Y.H. "Leak growth mechanism in composite Pd membranes prepared by the electroless deposition method." *AICHE Journal*. **54**(2) (2008) 487.

Guazzone, F.; Payzant, E.A.; Speakman, S.A. and Ma, Y.H. "Microstrains and stresses analysis in electroless deposited thin Pd films." *Industrial Engineering and Chemical Research.* **45**(24) (2006b) 8145.

Henis, J.M.S. and Tripodi, M.K. "Composite hollow fiber membranes for gas separation: the resistance model approach." *Journal of Membrane Science.* **8** (1981) 233 – 246.

Horanyi, G. and Rizmayer, E. M. "Radiotracer study of the adsorption of hydrogen sulfide by a platinized platinum electrode." *Journal of Electroanalytical Chemistry and Interfacial Electrochemistry.* **206**(1-2) (1986) 297.

Howard, B.H.; Killmeyer, R.P.; Rothenberger, K.S.; Cugini, A.V.; Morreale, B.D.; Enick, R.M. and Bustamante, F. “Hydrogen permeance of palladium-copper alloy membranes over a wide range of temperatures and pressures.” *Journal of Membrane Science*. **241** (2004) 207 – 218.

Hulbert, S.F. “Models for solid-state reactions in powdered compacts.” *Journal of the British Ceramic Society.* **6** (1969) 11-20.

Hurlbert, R.C. and Konecny, J.O. “Diffusion of hydrogen through palladium.” *The Journal of Chemical Physics.* **34**(2) (1961) 655 – 658.

Hurtado, P.; Ordonez, S.; Vega, A. and Diez, F. "Catalytic combustion of methane over commercial catalysts in presence of ammonia and hydrogen sulfide." *Chemosphere.* **55** (2004) 681 - 689.

Itoh, N.; Wu, T. and Haraya, K. “Two and three dimensional analysis of diffusion through a dense membrane supported on a porous material.” *Journal of Membrane Science.* **99** (1995) 175 – 183.

Iyoha, O.; Enick, R.; Killmeyer, R.; Howard, B.; Ciocco, M. and Morreale, B. “H_2 production from simulated coal syngas containing H_2S in multi-tubular Pd and 80wt% Pd-20wt% Cu membrane reactors at 1173K.” *Journal of Membrane Science*. **306** (2007a) 103 – 115.

Iyoha, O.; Enick, R.; Killmeyer, R.; Howard, B.; Ciocco, M. and Morreale, B. “Well-catalyzed water-gas shift reaction in multi-tubular Pd and 80wt% Pd-20wt% Cu membrane reactors at 1173K.” *Journal of Membrane Science*. **298** (2007b) 14 – 23.

Iyoha, O.; Enick, R.; Killmeyer, R. and Morreale, B. “The influence of hydrogen sulfide-to-hydrogen partial pressure ratio on the sulfidization of Pd and 70 mol% Pd-Cu membranes.” *Journal of Membrane Science*. **305** (2007c) 77 - 92.

Jemaa, N.; Shu, J.; Kaliaguine, S. and Grandjean, B.P.A. "Thin palladium film formation on shot peening modified porous stainless steel substrates." *Industrial and Engineering Chemistry Research.* **35** (1996) 973 - 977.

Jost, W. and Widman, A. “Diffusion of hydrogen and deuterium in palladium.” *Zhurnal Physik Chemie.* **B45** (1940) 285-96.

Kajiwara, M.; Uemiya, S. and Kojima, T. "Stability and hydrogen permeation behavior of supported platinum membranes in the presence of hydrogen sulfide." *International Journal of Hydrogen Energy*. **24** (1999) 839 - 844.

Kamakoti, P.; Morreale, B.D.; Ciocco, M.V.; Howard, B.H.; Killmeyer, R.P.; Cugini, A.V.; and Sholl, D.S. "Prediction of hydrogen flux through sulfur-tolerant binary alloy membranes." *Science*. **307** (2005) 569 - 573.

Kessler, G. “Requirements for nuclear energy in the 21st century: Nuclear energy as a sustainable energy source.” *Progress in Nuclear Energy*. **40**(3 – 4) (2002) 309 – 325.

Klette, H. and Bredesen, R. “Sputtering of very thin palladium-alloy hydrogen separation membranes.” *Membrane Technology.* May 2005, 7 – 9.

Knapton, A.G. “Palladium alloys for hydrogen diffusion membranes: A review of high permeability materials.” *Platinum Metal Reviews*. **21** (1977) 44 – 50.

Kulprathipanja, A.; Alptekin, G.O.; Falconer, J.L. and Way, J.D. "Effects of water gas shift gases on Pd-Cu alloy membrane morphology and separation properties." *Industrial Engineering and Chemical Research*. **43** (2004) 4188 – 4198.

Kulprathipanja, A.; Alptekin, G.O.; Falconer, J.L. and Way, J.D. "Pd and Pd-Cu membranes: inhibition of H_2 permeation by H_2S." *Journal of Membrane Science*. **254** (2005) 49 – 62.

Kusakabe, K.; Yokoyama, S.; Morooka, S.; Hayashi, J. and Nagata, H. “Development of supported thin palladium membrane and application to enhancement of propane aromatization on Ga-silicate catalyst.” *Chemical Engineering Science*. **51** (1996) 3027 – 3032.

Latyshev, V.V. and Gur’yanov, V.G. “The interaction of hydrogen with palladium-based alloy membranes.” *Russian Journal of Physical Chemistry*. **62**(2) (1988) 220 – 224.

Lewis, F.A. The Palladium-Hydrogen System. Academic Press, London, New York, 1967.

Li, A.; Liang, W. and Hughes, R. "Characterization and permeation of palladium/stainless steel composite membranes." *Journal of Membrane Science*. **149** (1998) 259 - 268.

Li, A.; Liang, W. and Hughes, R. "Fabrication of dense palladium composite membranes for hydrogen separation." *Catalysis Today*. **56** (2000) 45 - 51.

Li, Z.Y.; Maeda, H.; Kusakabe, K.; Morooka, S.; Anzai, A. and Akiyama, S. "Preparation of palladium-silver alloy membranes for hydrogen separation by the spray pyrolysis method." *Journal of Membrane Science*. **78** (1993) 247 - 254.

Li-Dun, A. and Quan, D.Y. “Mechanism of sulfur poisoning of supported $Pd(Pt)/Al_2O_3$ catalysts for H_2-O_2 reaction.” *Applied Catalysis*. **66** (1990) 219 – 234.

Liu, G.; St. Clair, T.P. and Goodman, D.W. “An XPS study of the interaction of ultrathin Cu films with Pd(1 1 1).” *Journal of Physical Chemistry B*. **103** (1999) 8578 – 8582.

Lu, K.; Wei, W.D. and Wang, J.T. *Journal of Applied Physics*, **69** (1991) 7395.

Ma, Y.H.; Akis, B.C.; Ayturk, M.E.; Guazzone, F.; Engwall, E.E. and Mardilovich, I.P. "Characterization of intermetallic diffusion barrier and alloy formation for Pd/Cu and Pd/Ag porous stainless steel composite membranes." *Industrial Engineering and Chemistry Research.* **43** (2004a) 2936 – 2945.

Ma, Y.H.; Engwall, E.E. and Mardilovich, I.P. "Method for fabricating composite gas separation modules." US Patent 2004085044, 2004b.

Ma, Y.H.; Mardilovich, I.P. and Engwall, E.E. "Composite gas separation modules having intermediate porous metal layers." US Patent 7,175,694, 2007.

Ma, Y.H.; Mardilovich, I.P. and Engwall, E.E. "Thin composite palladium and palladium/alloy membranes for hydrogen separation." *Annals of the New York Academy of Sciences*. **984** (2003) 346 – 360.

Ma, Y.H.; Mardilovich, P.P. and She, Y. "Hydrogen gas-extraction module and method of fabrication." US Patent 6,152,987, 2000.

Mallory, G.O. and Hajdu, J.B., ed. Electroless Plating: Fundamentals and Applications. American Electroplaters and Surface Finishers Society, Orlando, 1990.

Mardilovich, I.P.; Engwall, E. and Ma, Y.H. "Dependence of hydrogen flux on the pore size and plating surface topology of asymmetric Pd-porous stainless steel membranes." *Desalination.* **144** (2002) 85 - 89.

Mardilovich, P.P.; She, Y.; Ma, Y.H. and Rei, M. "Defect free palladium membranes on porous stainless steel support." *AiChE Journal*. **44**(2) (1998) 310 - 322.

Mason, E.A. and Malinauskas, A.P. Gas Transport in Porous Media: The Dusty-gas Model. Elsevier, Amsterdam, 1983.

Matsumoto, Y.; Soma, M.; Onishi, T. and Tamaru, K. "State of sulfur on the palladium surface studied by Auger electron spectroscopy, electron energy loss spectroscopy, ultraviolet photoelectron spectroscopy, and x-ray photoelectron spectroscopy*." Journal of the Chemical Society, Faraday Transactions I*. **76** (1980) 1122 - 1130.

McKinley, D.L. "Metal alloy for hydrogen separation and purification." US Patent 3,350,845, 1967.

McKinley, D.L. "Method for hydrogen separation and purification." US Patent 3,247,648, 1966.

McKinley, D.L. "Method for hydrogen separation and purification." US Patent 3,439,474, 1969.

Miller, J.B.; Alfonso, D.R.; Howard, B.H.; O'Brien, C.P. and Morreale, B.D. "Hydrogen dissociation on Pd_4S surfaces." *J. Phys. Chem. C*. **113** (2009) 18800 – 18806.

Miller, J.B.; Matranga, C. and Gellman, A.J. "Surface segregation in a polycrystalline $Pd_{70}Cu_{30}$ alloy hydrogen purification membrane." *Surface Science.* **602**(1), (2008a) 375.

Miller, J.B.; Morreale, B.D. and Gellman, A.J. "The effect of adsorbed sulfur on surface segregation in a polycrystalline $Pd_{70}Cu_{30}$ alloy." *Surface Science*. **602**(10) (2008b) 1819.

Molenaar, A.; Holdrinet, M.F.E. and Van Beek, L.K.H. "Kinetics of electroless copper plating with EDTA as the complexing agent for cupric ions." *Plating.* **61**(3) (1974) 238 - 242.

Morreale, B.D.; Ciocco, M.V.; Howard, B.H.; Killmeyer, R.P.; Cugini, A.V. and Enick, R.M. "Effect of hydrogen-sulfide on the hydrogen permeance of palladium-copper alloys at elevated temperatures." *Journal of Membrane Science*. **241** (2004) 219 – 224.

Morreale, B.D.; Howard, B.H.; Iyoha, O.; Enick, R.M.; Ling, C. and Sholl, D.S. "Experimental and computational prediction of the hydrogen transport properties of Pd_4S." *Industrial Engineering and Chemistry Research*. **46**(19) (2007) 6313.

Mundschau, M.V.; Xie, X.; Evenson IV, C.R.; and Sammells, A.F. "Dense inorganic membranes for production of hydrogen from methane and coal with carbon dioxide sequestration." *Catalysis Today*. **118** (2006) 12 – 23.

Musket, R.G. "Effects of contamination on the interaction of hydrogen gas with palladium: a review." *Journal of the Less Common Metals*. **45**(2) (1976) 173 - 183.

Nam, S. and Lee, K. "Hydrogen separation by Pd alloy composite membranes: introduction of diffusion barrier" *Journal of Membrane Science*. **192** (2001) 177 – 185.

O'Brien, C.P.; Howard, B.H.; Miller, J.B.; Morreale, B.D. and Gellman, A.J. "Inhibition of hydrogen transport through Pd and $Pd_{47}Cu_{53}$ membranes by H_2S at 350°C." *Journal of Membrane Science*. **349** (2010) 380 – 384.

Oudar, J. "Sulfur-metal interactions." *Materials Science and Engineering.* **42** (1980) 101 – 109.

Paglieri, S.N.; Foo, K.Y.; Way, J.D.; Collins, J.P. and Harper-Nixon, D.L. "A new preparation technique for Pd/alumina membranew with enhanced high-temperature stability." *Industrial Engineering and Chemistry Research*. **38** (1999) 1925 – 1936.

Pan, X.; Kilgus, M. and Goldbach, A. "Low-temperature H_2 and N_2 transport through thin $Pd_{66}Cu_{34}H_x$ layers." *Catalysis Today*. **104** (2005) 225 – 230.

Paunovic, M. and Vitkavage, D. “Determination of electroless copper deposition rate from polarization data in the vicinity of the mixed potential.” *Journal of the Electrochemical Society.* **126** (1979) 2282 - 2284.

Pawelec, B.; Cano-Serrano, E.; Campos-Martin, J.M.; Navarro, R.M.; Thomas, S. and Fierro, J.L.G. "Deep aromatics hydrogenation in the presence of DBT over Au-Pd/γ-alumina catalysts." *Applied Catalysis A: General*. **275** (2004) 127 - 139.

Peden, C.H.F.; Kay B.D. and Goodman, D.W. “Kinetics of hydrogen adsorption by chemically modified Pd(1 1 0).” *Surface Science.* **175** (1986) 215 – 225.

Philofsky, E.M. and Hilliard, J.E. “Effect of coherency strains on diffusion in copper-palladium alloys.” *Journal of Applied Physics*. **40** (1969) 2198-2205.

Pick, M.A. “The dependence of the hydrogen concentration in metals on the surface impurities.” *Journal of Nuclear Materials*. **145 – 147** (1987) 297 – 300.

Piper, J. “Diffusion of hydrogen in copper-palladium alloys.” *Journal of Applied Physics*. **37** (1966) 715 – 721.

Porter, D.A. and Easterling, K.E . Phase Transformation in Metals and Alloys. Chapman and Hall, London,1981.

Reyter, D.; Belanger, D. and Roue, L. “Elaboration of Cu-Pd films by coelectrodeposition: Application to nitrate electroreduction.” *Journal of Physical Chemistry C*. **113** (2009) 290 – 297.

Rhoda, R.N. and Madison, A. "Palladium plating by chemical reduction" US Patent 2,915,406, 1959.

Roa, F.; Block, M.J. and Way, J.D. “The influence of alloy composition on the H_2 flux of composite Pd-Cu membranes.” *Desalination*. **147** (2002) 411 – 416.

Roa, F. and Way, J.D. “Influence of alloy composition and membrane fabrication on the pressure dependence of the hydrogen flux of palladium-copper membranes.” *Industrial Engineering and Chemistry Research.* **42** (2003) 5827 – 5835.

Roa, F.; Way, J.D.; McCormick, R.L. and Paglieri, S.N. “Preparation and characterization of Pd-Cu composite membranes for hydrogen separation.” *Chemical Engineering Journal*. **93** (2003) 11 – 22.

Rodriguez, J.A.; Chaturvedi, S. and Jirsak, T. “The bonding of sulfur to Pd surfaces: photoemission and molecular-orbital studies.” *Chemical Physics Letters.* **296** (1998) 421 – 428.

Rosenqvist, T. “A thermodynamic study of iron, cobalt, and nickel sulfides.” *Journal of the Iron and Steel Institute.* **176** (1954) 37 – 57.

Ryu, C.K.; Ryoo, M.W.; Ryu, I.S. and Kang, S.K. "Catalytic combustion of methane over supported bimetallic palladium catalysts: Effects of Ru or Rh addition." *Catalysis Today.* **47** (1999) 141 – 147.

Saini, A. “An investigation of the cause of leak formation in palladium composite membranes.” MS thesis, Worcester Polytechnic Institute, 2006.

Saint-Claire Deville, H.E. “Over the permeability of iron at high temperature.” *Annalen der Physik.* **198**(6) (1864) 331 – 333.

Saleh, J.M. “Interaction of sulfur compounds with palladium.” *Transactions of the Faraday Society.* **66**(1) (1970) 242 – 250.

Saleh, J.M.; Kemball, C. and Roberts, M.W. “Interaction of hydrogen sulfide with nickel, tungsten and silver films.” *Transactions of the Faraday Society.* **57** (1961) 1771 – 1780.

Samsonov, G.V. The Oxide Handbook. IFI/Plenum, New York, 1973.

Shirasaki, Y.; Tsuneki, T.; Ota, Y.; Yasuda, I.; Tachibana, S.; Nakajima, H. and Kobayashi, K. “Development of membrane reformer system for highly efficient hydrogen production from natural gas.” *International Journal of Hydrogen Energy*. **34** (2009) 4482 – 4487.

Shu, J.; Grandjean, B.P.A. and Kaliaguine, S. "Morphological study of hydrogen permeable palladium membranes." *Thin Solid Films*. **252** (1994) 26-31.

Shu, J.; Grandjean, B.P.A.; Kaliaguine, S.; Giroir-Fendler, A. and Dalmon, J. "Hysteresis in hydrogen permeation through palladium membranes." *Journal of the Chemical Society, Faraday Transactions*. **92**(15) (1996) 2745-2751.

Shu, J.; Grandjean, B.P.A.; Van Neste, A. and Kaliaguine, S. “Catalytic palladium - based membrane reactors: A review.” *The Canadian Journal of Chemical Engineering.* **69** (1991) 1036 – 1060.

Silberg, P.A. and Bachman, C.H. “Diffusion of hydrogen in palladium.” *The Journal of Chemical Physics.* **29**(4) (1958) 777 – 781.

Smithell, C.J. ed. Smithell’s Metals Reference Book. 6th edition. Butterworth and Co. Ltd. United Kingdom, 1983.

Souleimanova, R.S.; Mukasyan, A.S. and Varma, A. "Pd membranes formed by electroless plating with osmosis: Hydrogen permeation studies." *AIChE Journal*. **48**(2) (2002) 262 – 268.

Speller, S.; Rauch, T.; Bomermann, J.; Borrmann, P.; and Heiland, W. “Surface structures of S on Pd (111).” *Surface Science.* **441** (1999) 107 – 116.

Subramanian, P.R. and Laughlin, D.E. “Copper-palladium.” *Journal of Phase Equilibria.* **12**(2) (1991) 231 – 243.

Taylor, J.R. “Phase relationships and thermodynamic properties of the Pd-S system.” *Metallurgical Transactions B.* **16B** (1985) 143 – 148.

Thoen, P.M.; Roa, F. and Way, J.D. “High flux palladium-copper composite membranes for hydrogen separations.” *Desalination*. **193** (2006) 224 – 229.

Thomas, J.M. and Thomas, W.J. Principles and Practice of Heterogeneous Catalysis. VCH Verlagsgesellschaft mbH, Weinheim, 1997.

Tong, J.; Kashima, Y.; Shirai, R.; Suda, H. and Matsumura, Y. “Thin defect-free Pd membrane deposited on asymmetric porous stainless steel substrate.” *Industrial Engineering and Chemical Research.* **44** (2005) 8025 – 8032.

Tong, J. and Matsumura, Y. "Thin Pd membrane prepared on macroporous stainless steel tube filter by an in-situ mulit-dimensional plating mechanism." *Chemical Communications*. (2004) 2460 – 2461.

Torikai, E.; Kawami, Y. and Takenaka, K. Japanese Patent 84-80766, 1984.

Uemiya, S.; Kajiwara, M. and Kojima, T. "Composite membranes of group VIII metal supported on porous alumina." *AIChE Journal*. **43**(11A) (1997) 2715 – 2723.

Uemiya, S.; Sato, N.; Ando, H.; Kude, Y.; Matsuda, T. and Kikuchi, E. “Separation of hydrogen through palladium thin film supported on a porous glass tube.” *Journal of Membrane Science*. **56** (1991) 303 - 313.

Wang, D.; Tong, J.; Xu, H. and Matsumura, Y. “Preparation of palladium membrane over porous stainless steel tube modified with zirconium oxide.” *Catalysis Today.* **93 – 95** (2004) 689 – 693.

Wang, N.; Wang, Z.; Aust, K.T. and Erb, U. “Isokinetic analysis of nanocrystalline nickel electrodeposits upon annealing.” *Acta Materialia*, **45**(4) (1997) 1655 – 1669.

Ward, T.L.; and Dao, T. "Model of hydrogen permeation behavior in palladium membranes." *Journal of Membrane Science*. **153** (1999) 211 - 231.

Watts, J.F. and Wolstenholme, J. An Introduction to Surface Analysis by XPS and AES. John Wiley and Sons, Ltd., England, 2003.

Way, J.D.; Lusk, M.; and Thoen, P. “Sulfur-resistant composite metal membranes.” US Patent Application 20080038567, 2008.

Wicke, E. and Nernst, G. “Phase diagram and thermodynamic behavior of the system Pd/H_2 and Pd/D_2 at normal temperatures; H/D separations effects.” *Berichte der Bunsen-Gesellschaft fur Physikalische Chemie*. **68** (1964) 224 – 235.

Wijmans, J.G. and Baker, R.W. "The solution-diffusion model: a review." *Journal of Membrane Science*. **107** (1995) 1 - 21.

Wilke, S. and Scheffler, M. “Mechanism of poisoning the catalytic activity of Pd(1 0 0) by a sulfur adlayer.” *Physical Review Letters.* **76** (1996) 3380 – 3383.

Wilke, S. and Scheffler, M. “Poisoning of Pd(1 0 0) for the dissociation of H_2: a theoretical study of co-adsorption of hydrogen and sulfur.” *Surface Science.* **329** (1995) L605 – L610.

Wu, L.; Xu, N. and Shi, J. "Preparation of a palladium composite membrane by an improved electroless plating technique." *Industrial Engineering and Chemistry Research*. **39** (2000) 342 - 348.

Yeung, K.L.; Christiansen, S.C. and Varma, A. "Palladium composite membranes by electroless plating technique: Relationships between plating kinetics, film microstructure and membrane performance." *Journal of Membrane Science*. **159** (1999) 107 - 122.

Yeung, K. L. and Varma, A. “Novel preparation techniques for thin metal-ceramic composite membranes.” *AIChE Journal.* **41(**9) (1995) 2131-2139.

Yuan, L.; Goldbach, A.; and Xu, H. “Permeation hysteresis in PdCu membranes.” *Journal of Physical Chemistry B.* **112** (2008) 12692 – 12695.

Zhang, X.; Wang, W.; Liu, J.; Sheng, S.; Xiong, G. and Yang, W. “Hydrogen transport through thin palladium-copper alloy composite membranes at low temperatures.” *Thin Solid Films.* **516** (2008) 1849 – 1856.

Zhang, X.; Xiong, G. and Yang, W. “Hydrogen separation from the mixtures in a thin Pd-Cu alloy membrane reactor.” *Natural Gas Conversion VII: Proceedings of the 8th Natural Gas Symposium.* **167** (2008) 219 – 224.

Zhao, H.B.; Pflanz, K.; Gu, J.H.; Li, A.W.; Stroh, N.; Brunner, H. and Xiong, G.X. "Preparation of palladium composite membranes by modified electroless plating procedure." *Journal of Membrane Science*. **142** (1998) 147 - 157.

Appendix A: AAS calibration

Calibration curves were constructed before each use of the Perkin Elmer AAnalyst 300 Spectrometer. The calibration was carried out with three sample concentrations. For the concentrated Cu plating solution, the concentrations of 5, 15 and 30 mg Cu/l were used to build the calibration curve. A typical calibration curve for the concentrated Cu plating solution is shown in Figure A-1. The burner head was tilted slightly to reduce the absorbance of the 30 ppm sample to shorten the path of the sample through the flame and prevent the highest measured concentration from saturating the signal.

For the dilute Cu plating solution, concentrations of 1, 3 and 5 mg Cu/l were used for building the calibration curve. The burner head was not tilted so that the path of the sample through the flame could be maximized and the full absorbance of the Cu could be detected. The slope for the calibration curve of the dilute Cu bath was larger than the slope of the concentrated Cu bath due to the tilt of the burner head during the acquisition of data for the concentrated Cu bath.

For the Pd displacement solution, concentrations of 2.5, 5 and 10 mg Pd/l were used for building the calibration curve. A typical calibration curve for the Pd displacement solution is shown in Figure A-2.

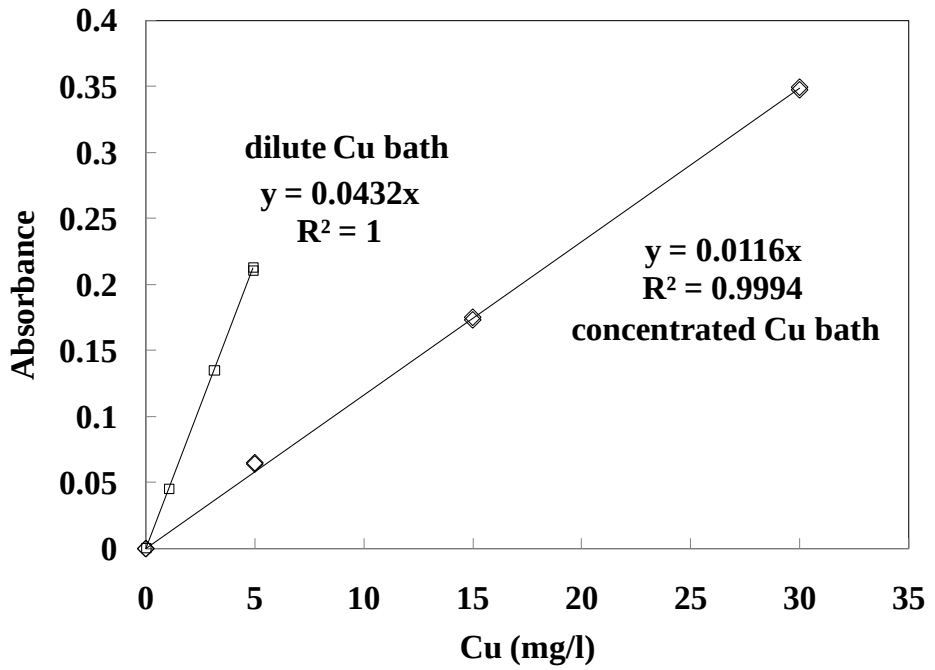

Figure A-1 Typical calibration curves for the Cu plating solution.

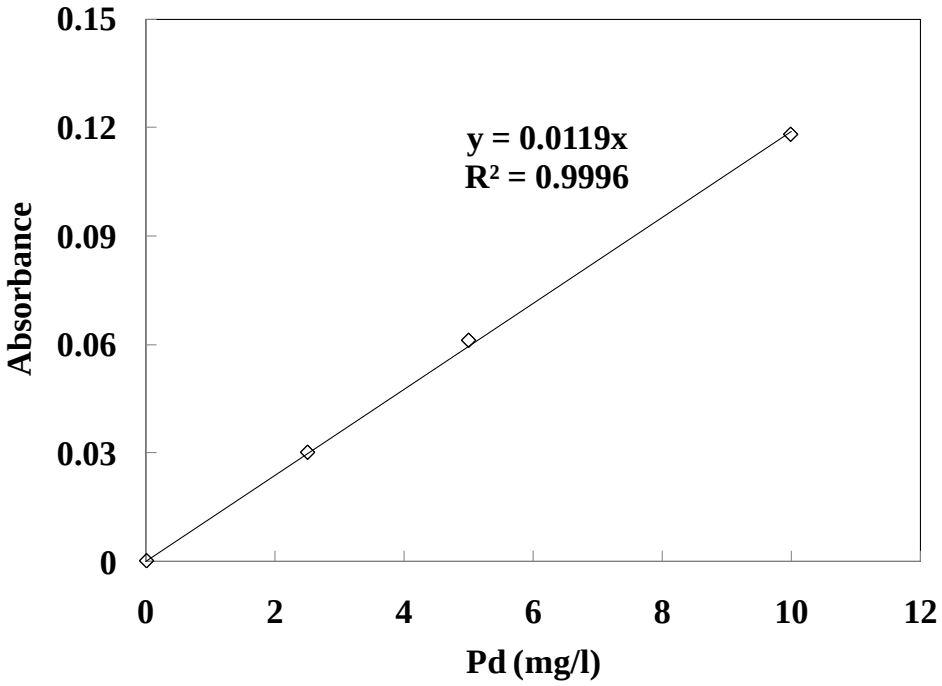

Figure A-2 Typical calibration curve for the Pd displacement solution.

All three calibration curves show that the dependence of the absorbance on the sample concentration was linear in accordance with Beer's Law (Equation A.1) where A is the absorbance of the sample, ε is the molar absorbtivity in L/(mol*cm), b is the path length of the sample in cm and C is the concentration of the sample in mol/L. In the absence of interference, linear dependences are usually observed for low concentrations.

$$A = \varepsilon \cdot b \cdot C \tag{A.1}$$

The error in the absorbance readings from a single sample was negligible and only two repeats of each sample were necessary in the calibration curves. To determine the error of the sample concentration, ten identical samples of Pd and Cu were prepared and measured. The error bars shown in the results of Chapter 6 represent the 95% confidence interval calculated from the standard deviation. Further details on the use of the AAS can be found in Section 3.3.4.

Appendix B: GC methodology

B.1. Calibration

Figure B-1 shows the dependence of the peak area on the flow rate of roughly 50 ppm H_2S/H_2 to the GC. Increasing the flow rate to the GC resulted in an increase in signal at lower flow rates due to the loop not being completely filled which resulted in a large error in the peak area and unrepeatable results. After 30 sccm, the peak area ceased to increase and for all experiments, a flow rate of 35 – 40 sccm was used.

For the testing of 50 ppm H_2S/H_2, the GC was calibrated for detecting concentrations in the range of 1 – 200 ppm. The calibration was carried out by flowing 55.6 and 213.4 ppm H_2S/H_2 directly towards the GC through a bypass in the system (Figure 3-3). The gain was set to medium. The loop sizes were varied using 500 μl as the full concentrations of the cylinders and 10, 25, 50, 100 and 250 μl as fractions of the concentrations. Ten repetitions were used at each loop size.

Figure B-2 shows the calibration curve for the GC for running a feed gas of 50 ppm H_2S/H_2. The span of the curve was for three orders of magnitude and a second order polynomial regression was used. For the calibration curve for dilute concentrations of H_2S, a high gain was used and the PMT voltage was adjusted to give the maximum signal at 5 ppm. The calibration curve for the dilute concentrations below 5 ppm as formed by the gas mixer is shown in Figure B-3. The insets of Figure B-2 and Figure B-3 show the smaller concentrations on the calibration curves.

Before performing a test run, a feed mixture of a known H_2S/H_2 concentration was run through the bypass. The signal of the mixture was attenuated to fall on the calibration curve by adjusting the voltage of the PMT. After the known concentration was sufficiently close to the calibration curve, the gas flow from the permeation system was sent to the GC for continuous analysis.

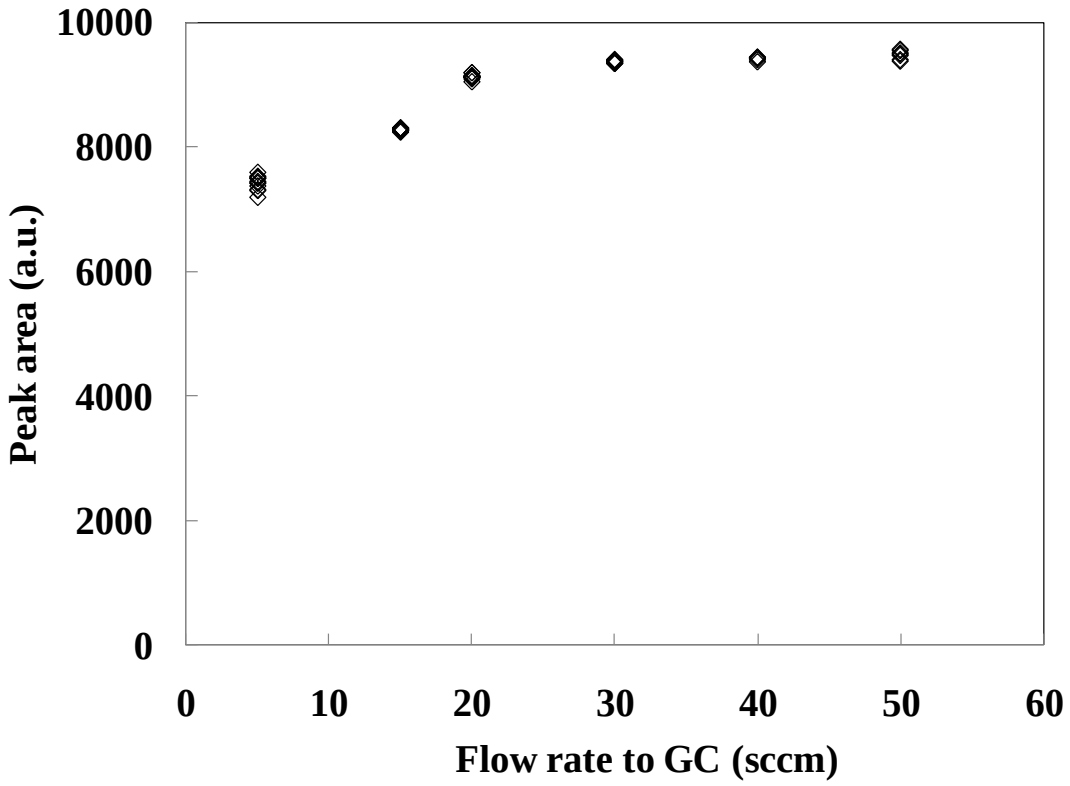

Figure B-1 Dependence of the GC signal on the flow rate.

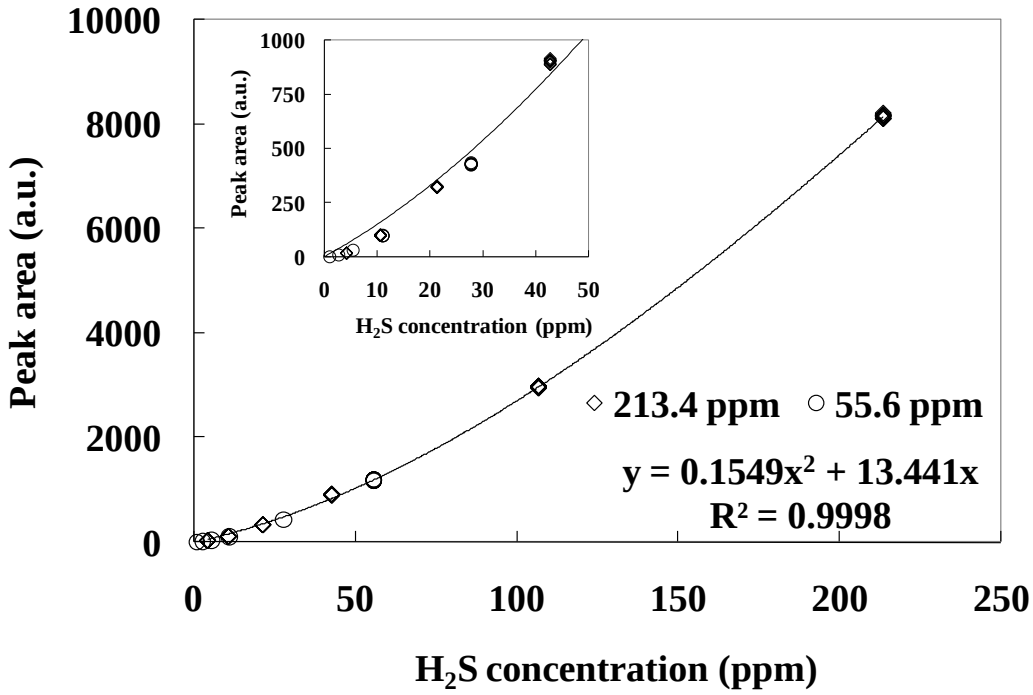

Figure B-2 Typical calibration curve for the GC for running 50 ppm H_2S/H_2.

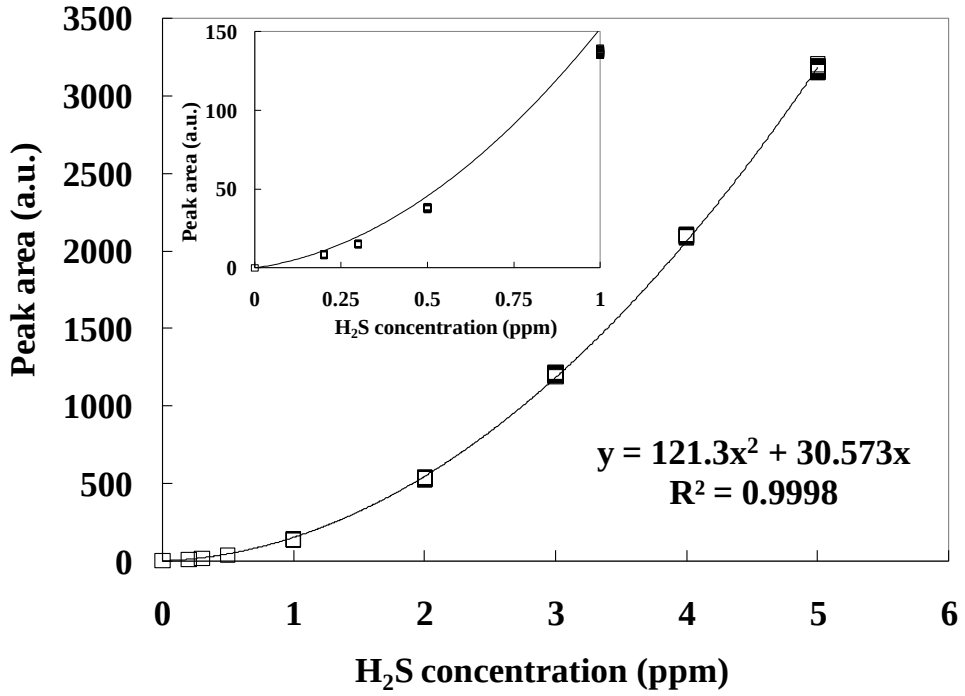

Figure B-3 Typical calibration curve for the GC for running 5 ppm H_2S/H_2.

B.2. Test run with non-porous tube

To isolate the effect of H_2S on the system from the effect of H_2S on the membrane, a blank run was performed by inserting a non-porous 310 SS tube of the same dimensions as the composite membrane tubular support into the shell casing. The system was heated to 450°C in H_2 and a 45 ppm H_2S/H_2 mixture was introduced with a feed flow of 50 sccm, which was a typical volumetric flow rate for the retentate stream in the membrane permeation experiments. The Reynold's number was 0.4 and the residence time was 3.7 minutes.

Figure B-4 shows the change in the H_2S concentration of the shell casing outlet as a function of time where C_0 was equal to 45 ppm. As can be seen, nearly 275 hours was needed for the concentration to level out. Since roughly two hours were needed to completely flush the system out between changes of H_2 and He gases, the reason for the lengthy time was due to the adsorption of H_2S on the system walls and the non-porous stainless steel tube. The amount of the sulfur adsorbed on the system, as calculated from the area under the curve of the left side of the graph in Figure B-4, was 0.018 g H_2S total.

After the outlet concentration stabilized, pure H_2 was reintroduced with a flow rate of 35 sccm. As with the introduction of the H_2S/H_2 mix, the outlet concentration required a lengthy time to stabilize as the H_2S desorbed from the system walls. Over 300 hours passed before the H_2S stabilized at roughly 1 ppm. As with the amount of sulfur adsorbed, the amount of sulfur desorbed from the system was calculated from the area under the curve on the right side of the graph in Figure B-4. The amount of H_2S which desorbed from the system totaled 0.013 g.

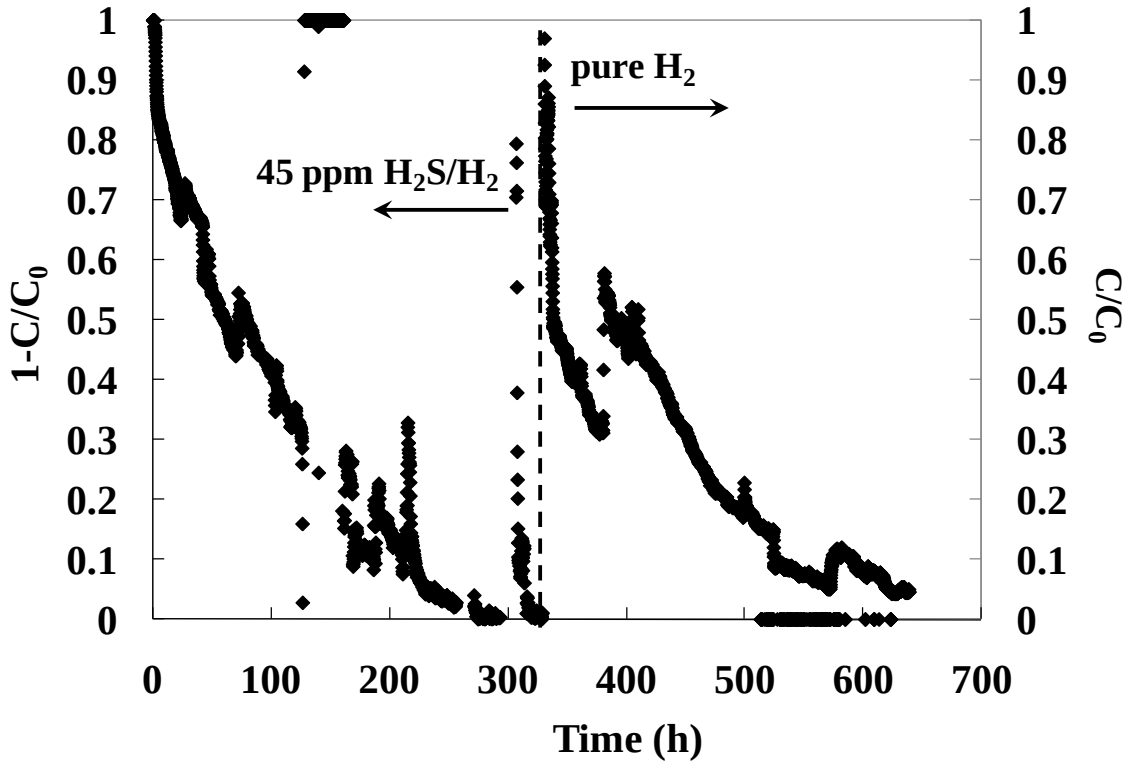

Figure B-4 H_2S concentration in outlet as a function of time for a non-porous 310 SS tube.

Assuming the calculations were accurate, 0.005 g of H_2S had accumulated on the walls of the system after purging with H_2. The accumulated sulfur could clearly be seen on the non-porous tube used in place of a membrane, as seen in Figure B-5 which shows the tube after the test run in the furnace. The right side of the tube remained shiny, showing the 310 SS which was not inside the shell casing. The middle part of the tube was a darker color and typical of the effect of oxidation and deposited carbon, also seen on the non-porous parts of the membrane tubes after runs which did not include H_2S. However, the left side of the tube, circled in Figure B-5, showed a grayish deposit

which rubbed off easily and was not seen on non-porous tubes exposed only to H_2 and He atmospheres. It was this grey deposit which was the sulfur and would most likely be found on the walls of the shell casing if the casing were to be taken apart. Clearly, the system accumulated large amounts of sulfur during poisoning experiments.

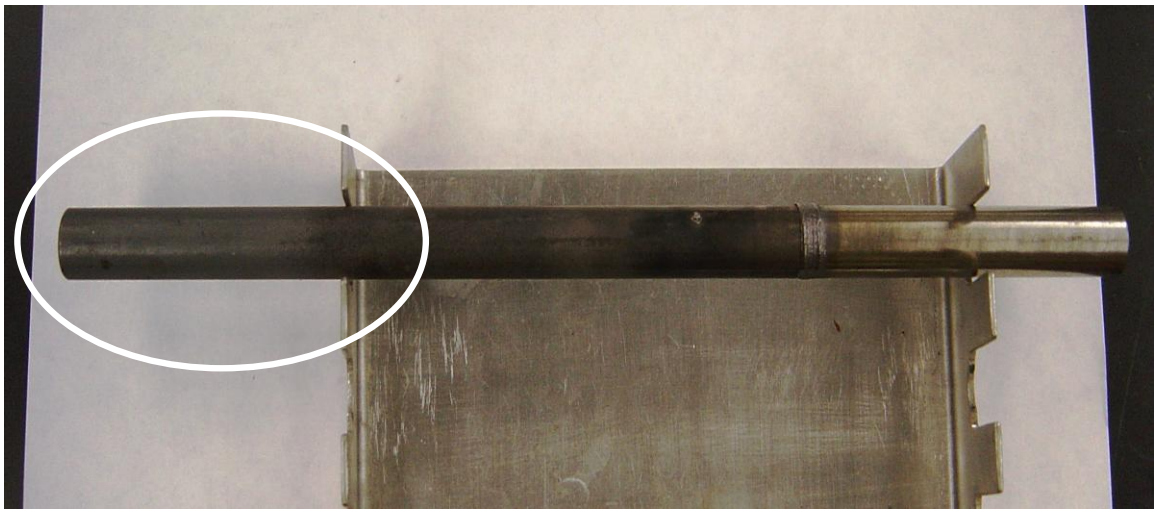

Figure B-5 Non-porous 310 SS tube after the blank run.

Appendix C: HT-XRD scans

Many HT-XRD scans were taken while at ORNL, however, not all were used or shown in Chapter 4. Figure C-1 shows the phase transformation of the Pd/Cu bi-layer into the various Pd/Cu alloys over time while annealed at 400°C in H_2. The data from the scan at 400°C was not included in the kinetics calculations due to the uncertainty of the phase(s) present. The broad peak which lay between the Pd (1 1 1) and Pd rich fcc (1 1 1) peaks would have belonged to any one, or a combination of, the Pd/Cu phases to the left of the fcc/bcc miscibility gap in Figure 1-1 (referred to as $L1_2$, 1D LPS and 2D LPS). The ordered phases were tetragonal in structure and varied in their respective Pd/Cu atomic ratios (Subramanian and Laughlin, 1991). Figure C-2 shows the phase transformation at 450°C in which the same problem occurred and it was difficult to identify and differentiate between the various Cu rich phases. Furthermore, the Cu rich phases were bunched together at 2θ values slightly higher than the 2θ value of the Pd (1 1 1) peak and could not be differentiated from the Pd rich fcc phase.

It was only at annealing temperatures at 500°C and above that the many Cu rich phases were no longer present and were replaced by a single Cu rich fcc phase. At temperatures above 600°C, the bcc phase would no longer present (Figure 1-1). Figure C-3 and Figure C-4 show the phase transformations at 500 and 600°C, respectively. The peak areas of the phases in Figure C-3 and Figure C-4 were used to calculate the weight fractions in Figure 4-8 and Figure 4-10, respectively.

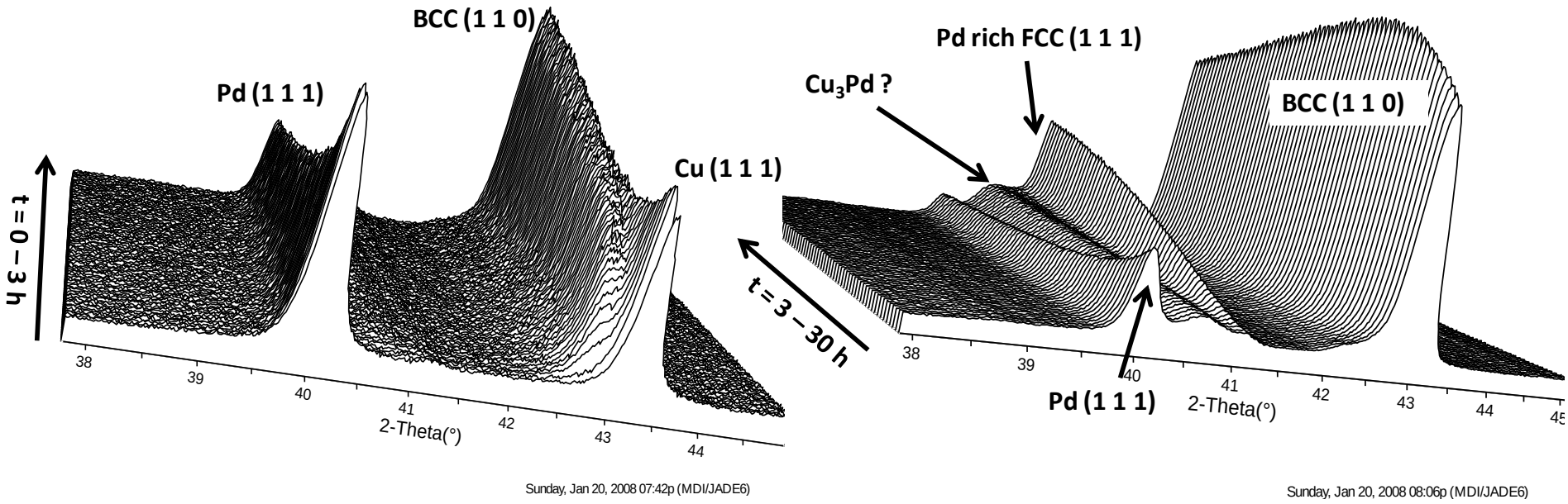

Figure C-1 HT-XRD scans as a function of time at 400°C.

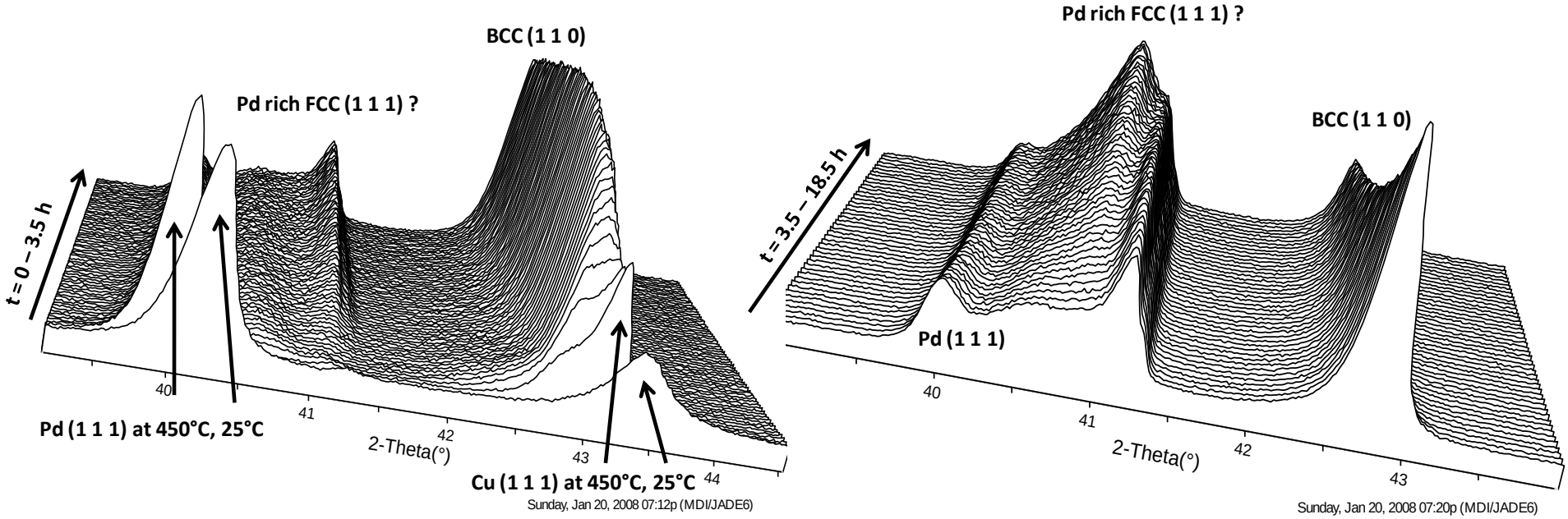

Figure C-2 HT-XRD scans as a function of time at 450°C.

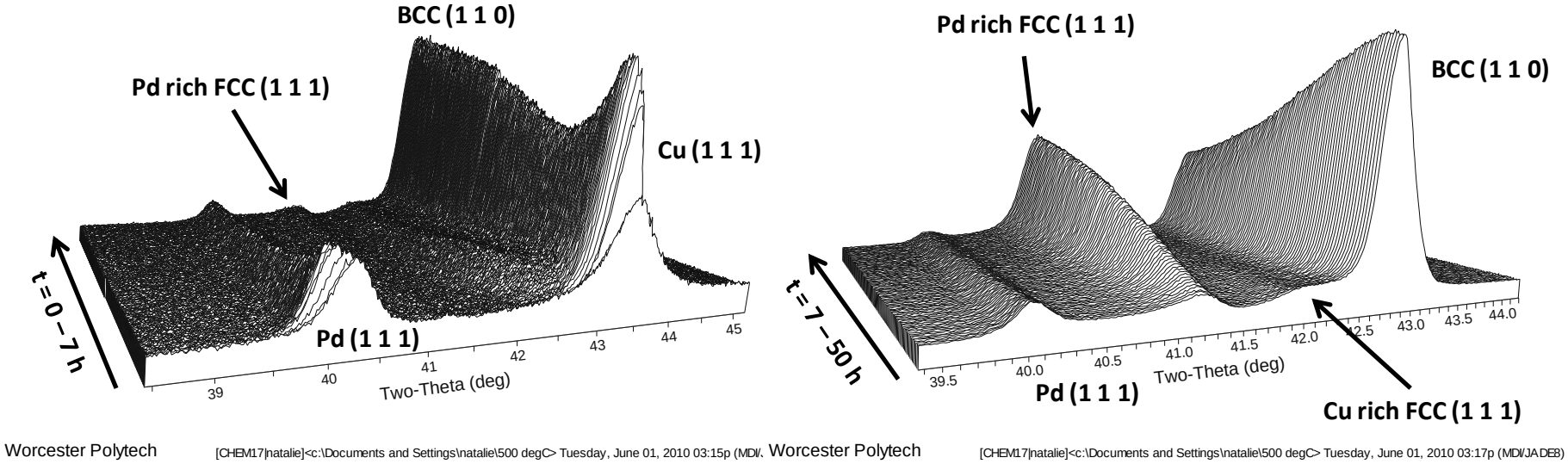

Figure C-3 HT-XRD scans as a function of time at 500°C.

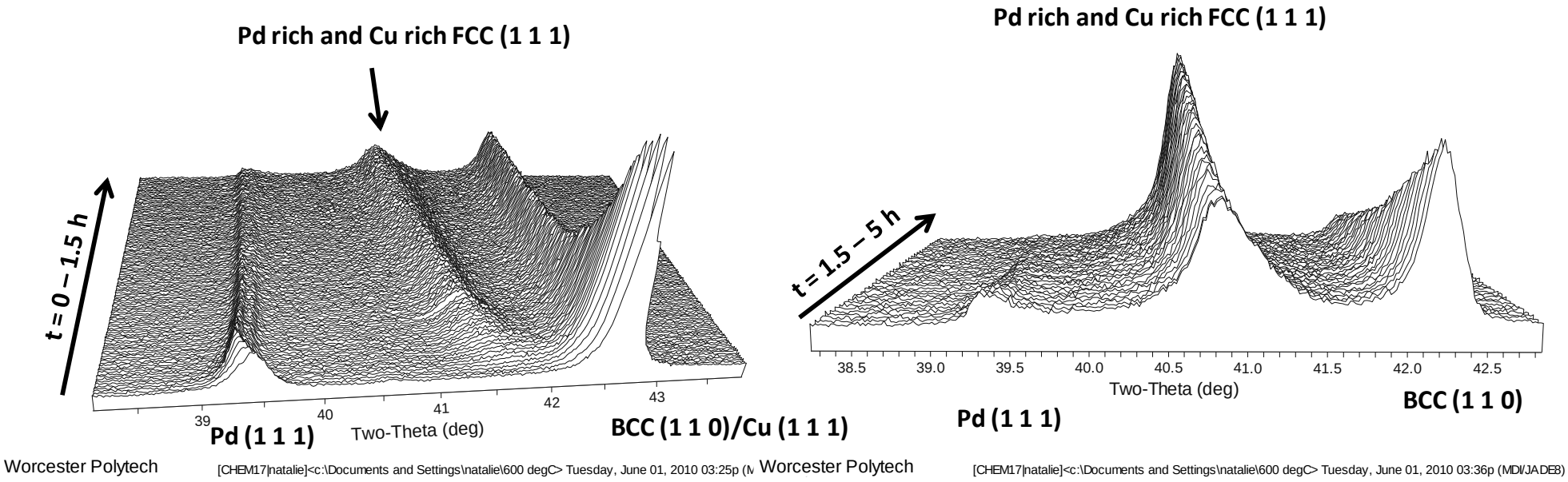

Figure C-4 HT-XRD scans as a function of time at 600°C.

Appendix D: XPS scans

The peak fitting for the 2p S orbital was performed on numerous Pd/Cu samples that were poisoned in H_2S. In Chapter 9 only one peak fitting was shown, that of the Pd/Cu sample exposed to 52.3 ppm H_2S/H_2 at 350ºC. Here, the peak fittings for all of the poisoned Pd/Cu samples are presented.

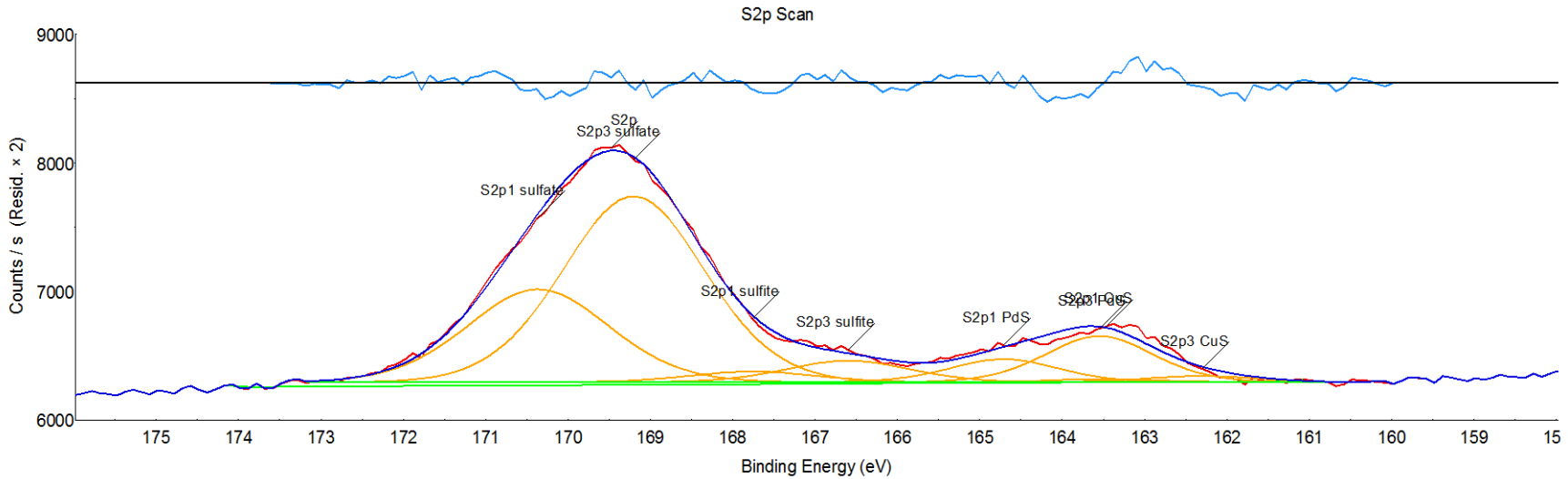

Figure D-1 Pd/Cu coupon poisoned at 400ºC for 12 hours in 50 ppm H_2S.

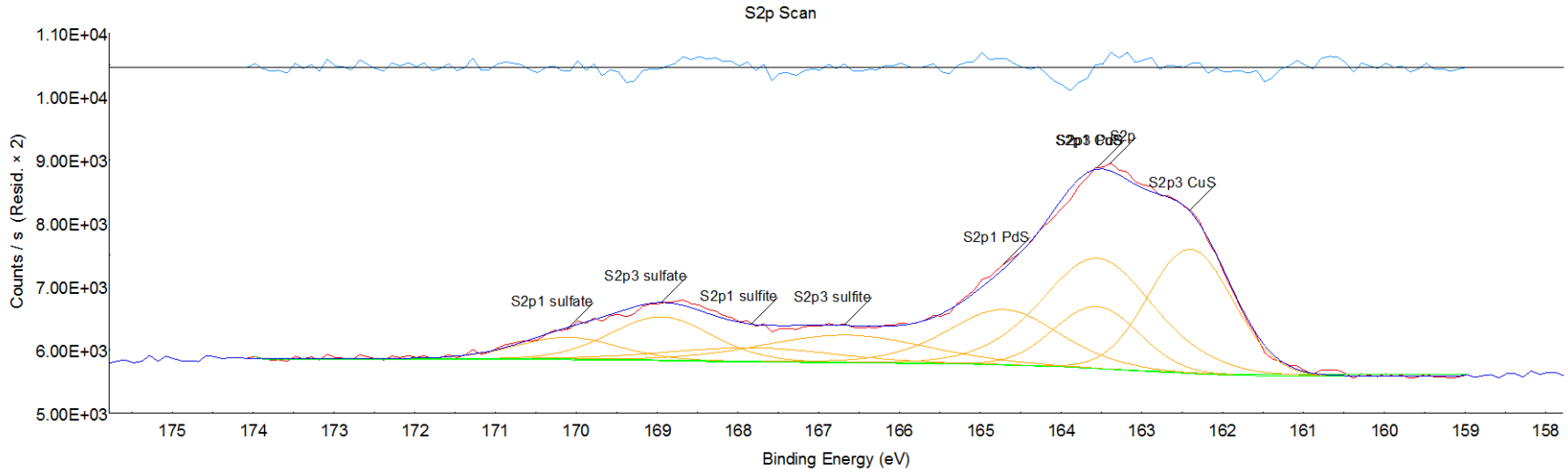

Figure D-2 Pd/Cu coupon poisoned at 450ºC for 12 hours in 50 ppm H_2S.

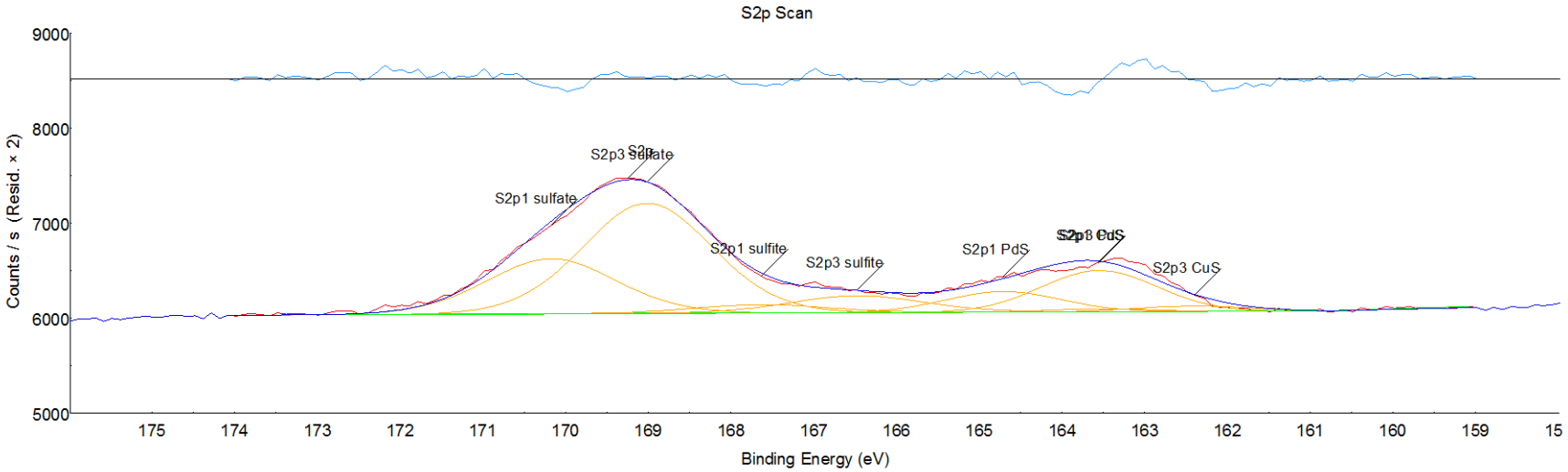

Figure D-3 Pd/Cu coupon poisoned at 500ºC for 12 hours in 50 ppm H_2S.

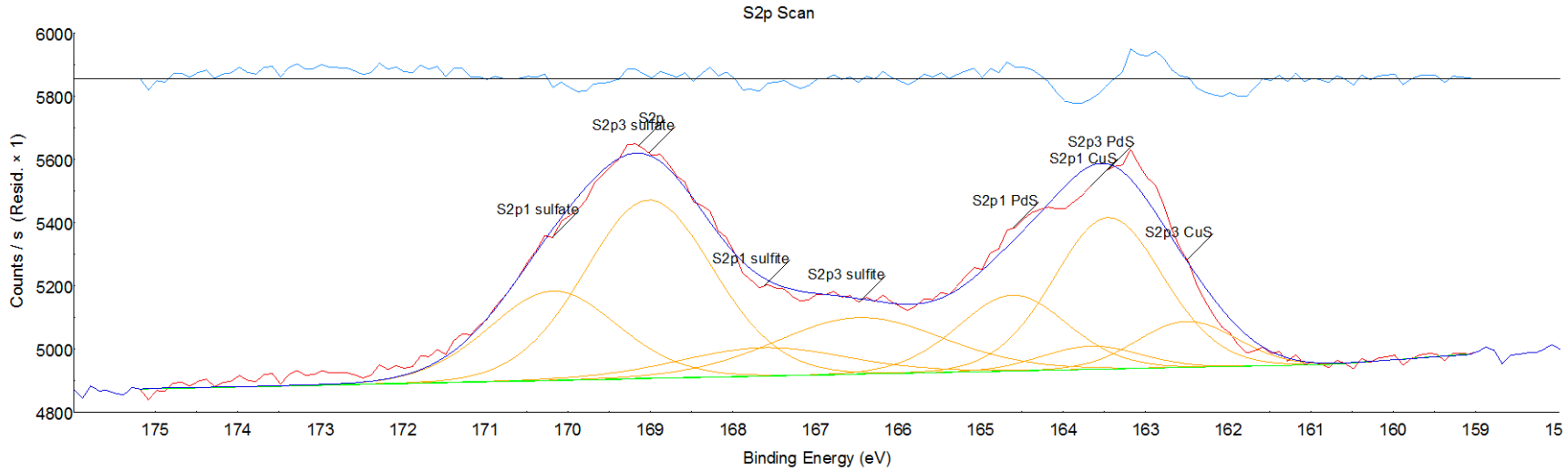

Figure D-4 Pd/Cu coupon poisoned at 350ºC for 12 hours in 0.5 ppm H_2S.

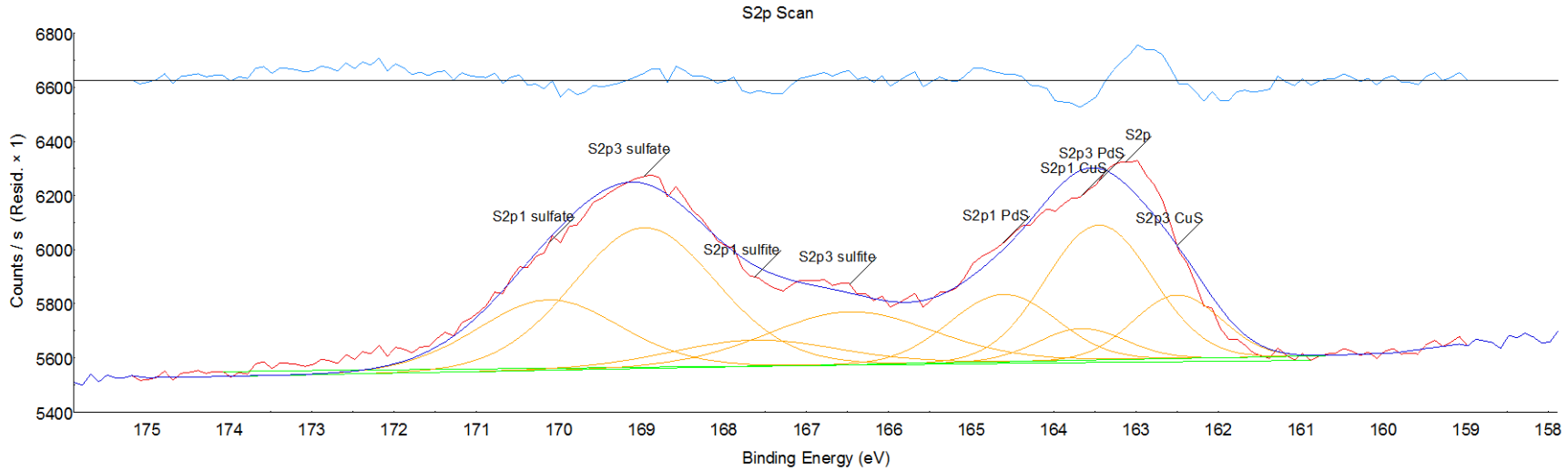

Figure D-5 Pd/Cu coupon poisoned at 400ºC for 12 hours in 0.5 ppm H_2S.

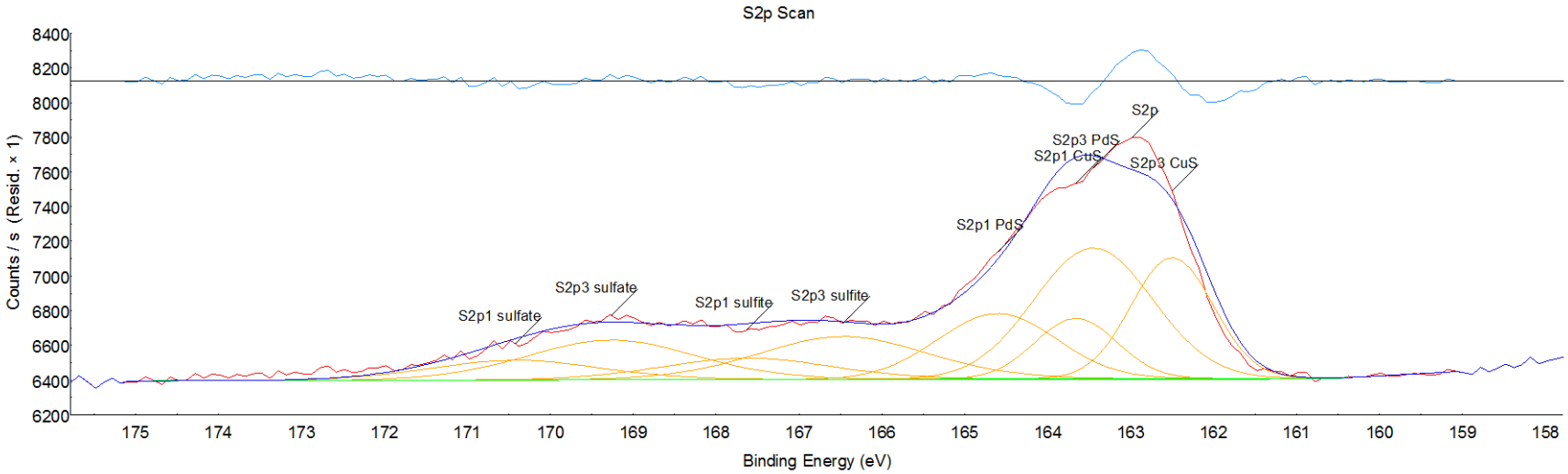

Figure D-6 Pd/Cu coupon poisoned at 450ºC for 12 hours in 0.5 ppm H_2S.

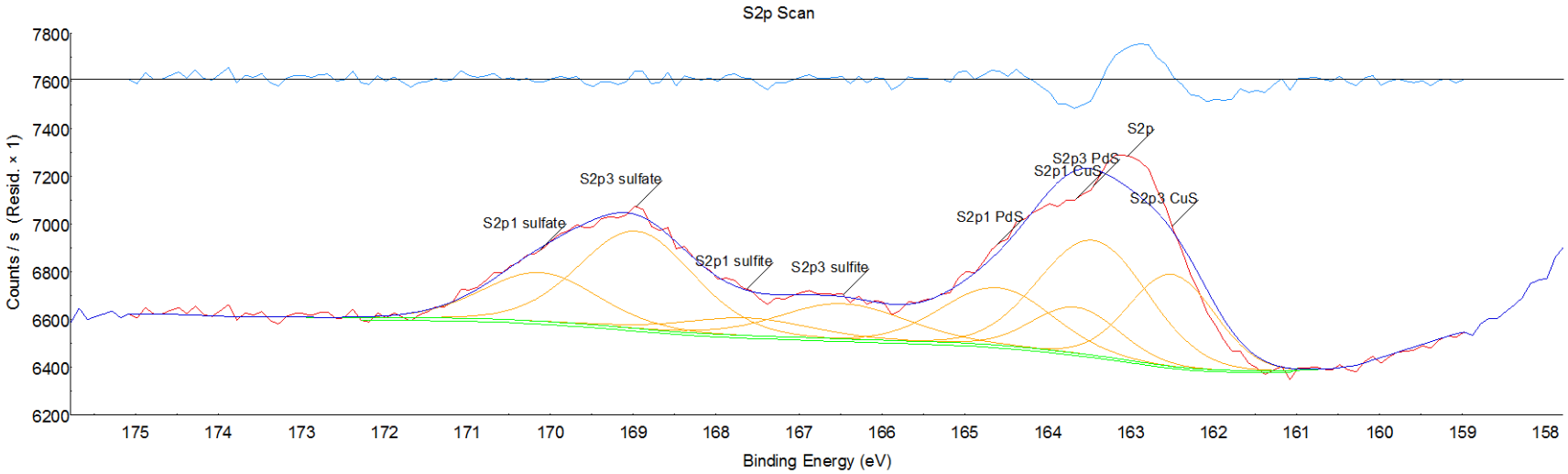

Figure D-7 Pd/Cu coupon poisoned at 500ºC for 12 hours in 0.5 ppm H_2S.

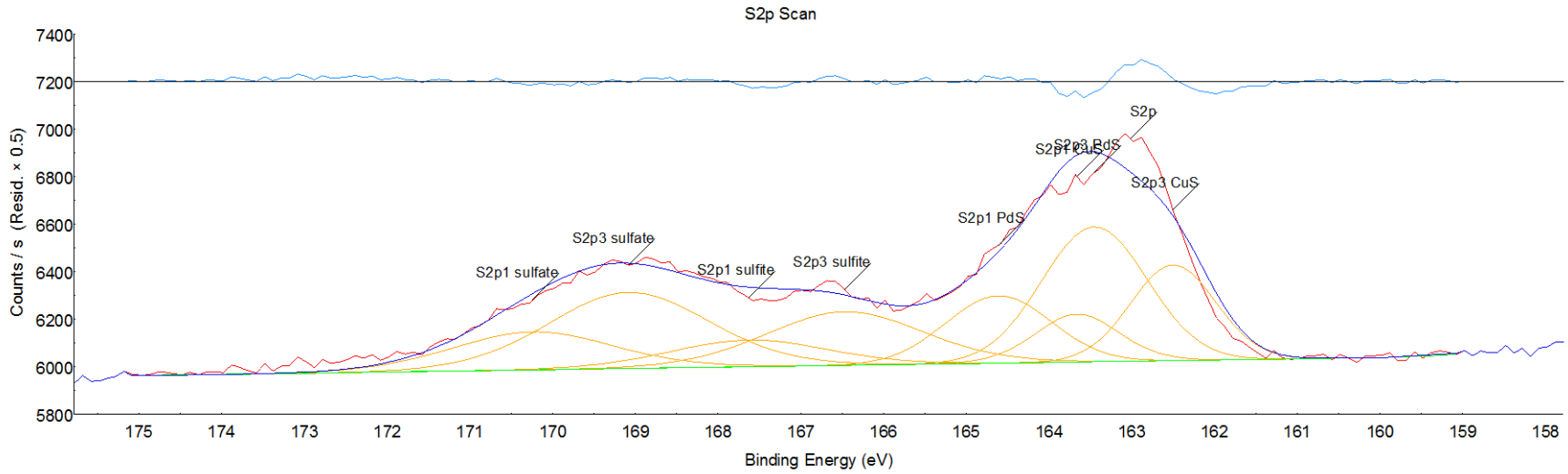

Figure D-8 Pd/Cu coupon poisoned at 350ºC for 12 hours in 50 ppm H_2S and recovered in H_2 at 500ºC for 12 hours.

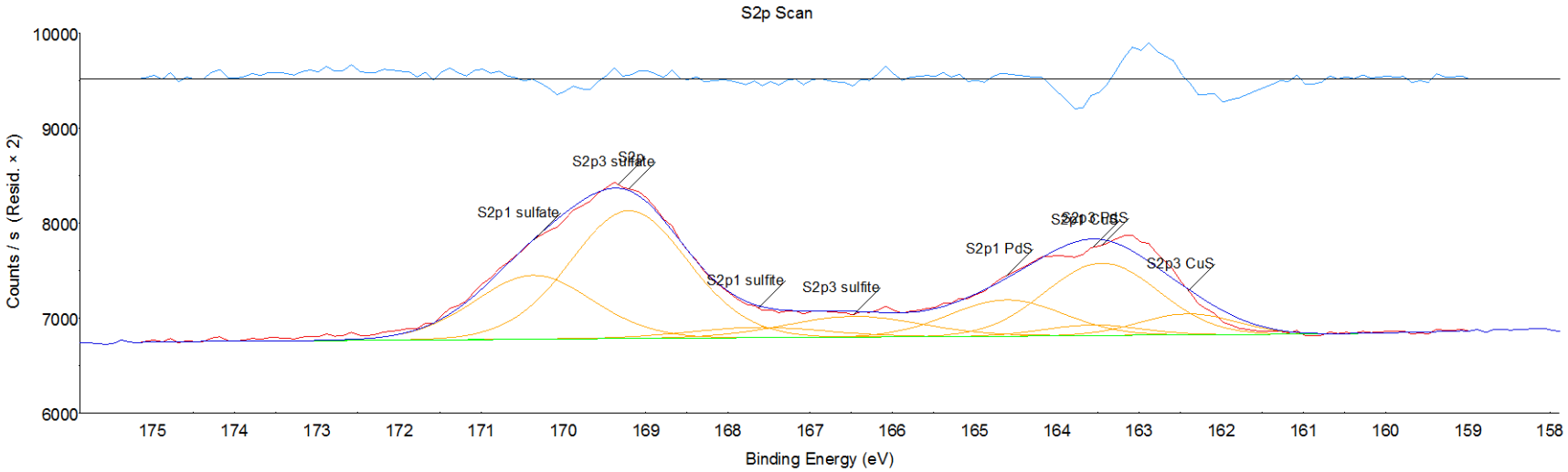

Figure D-9 Pd/Cu coupon poisoned at 400ºC for 12 hours in 50 ppm H_2S and recovered in H_2 at 500ºC for 12 hours.

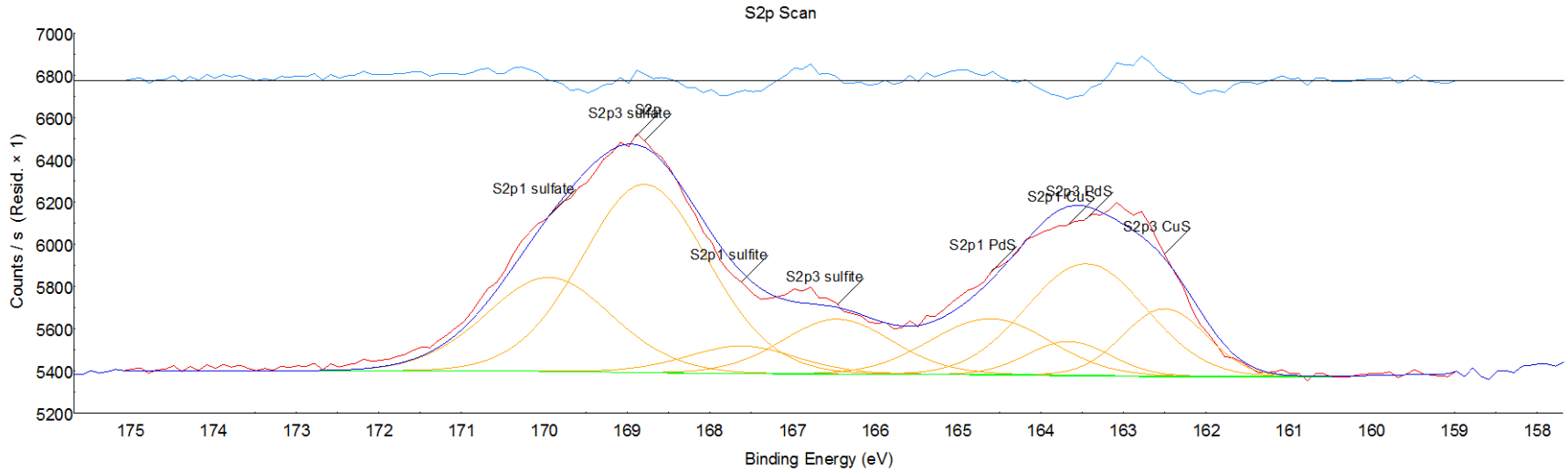

Figure D-10 Pd/Cu coupon poisoned at 450ºC for 12 hours in 50 ppm H_2S and recovered in H_2 at 500ºC for 12 hours.

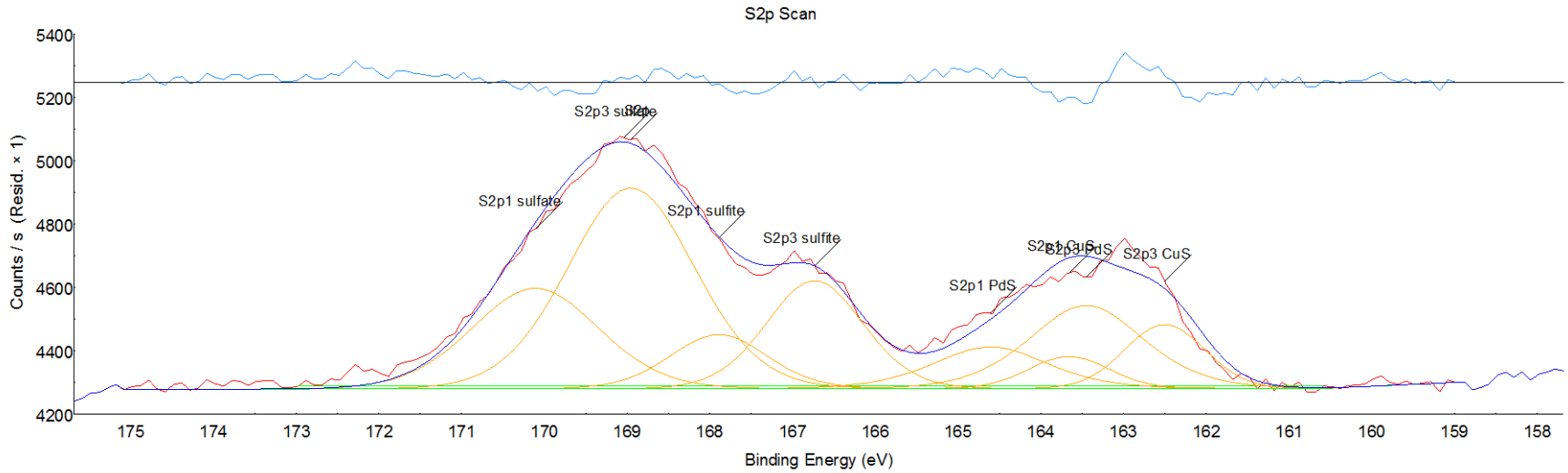

Figure D-11 Pd/Cu coupon poisoned at 500ºC for 12 hours in 50 ppm H_2S and recovered in H_2 at 500ºC for 12 hours.

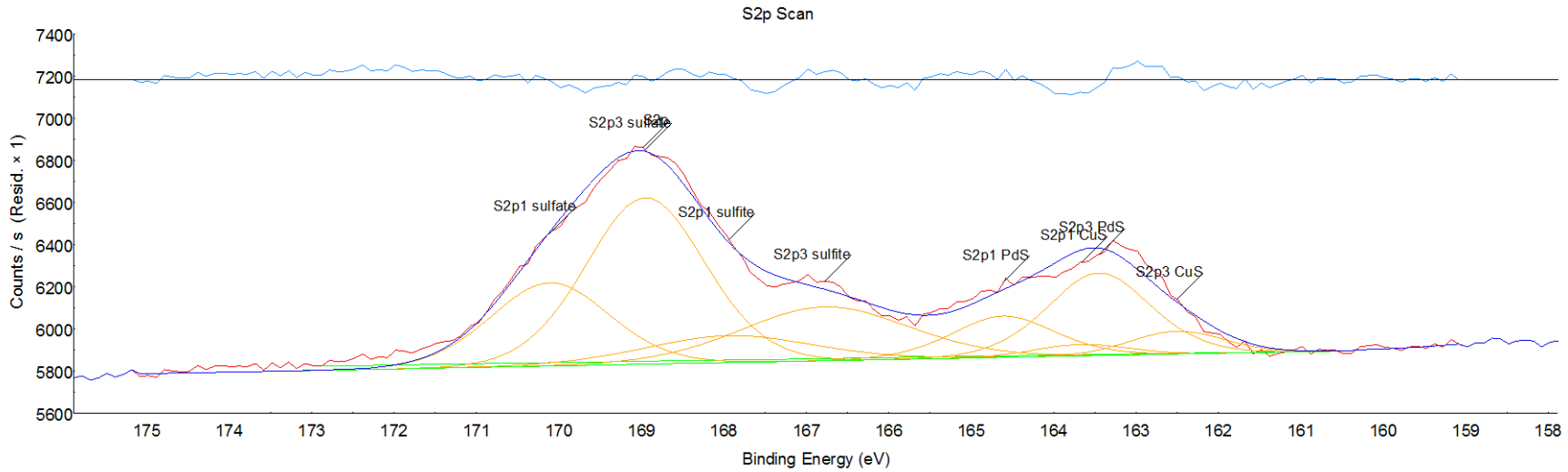

Figure D-12 Pd/Cu coupon poisoned at 350ºC for 12 hours in 50 ppm H_2S and recovered in H_2 at 450ºC for 12 hours.

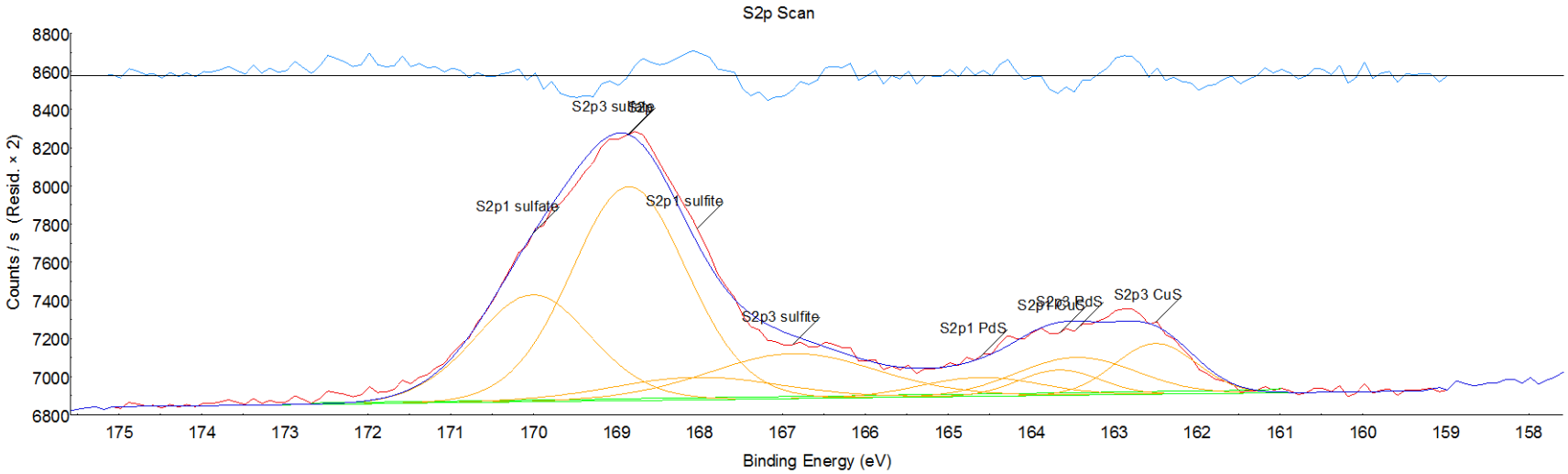

Figure D-13 Pd/Cu coupon poisoned at 400ºC for 12 hours in 50 ppm H_2S and recovered in H_2 at 450ºC for 12 hours.

.

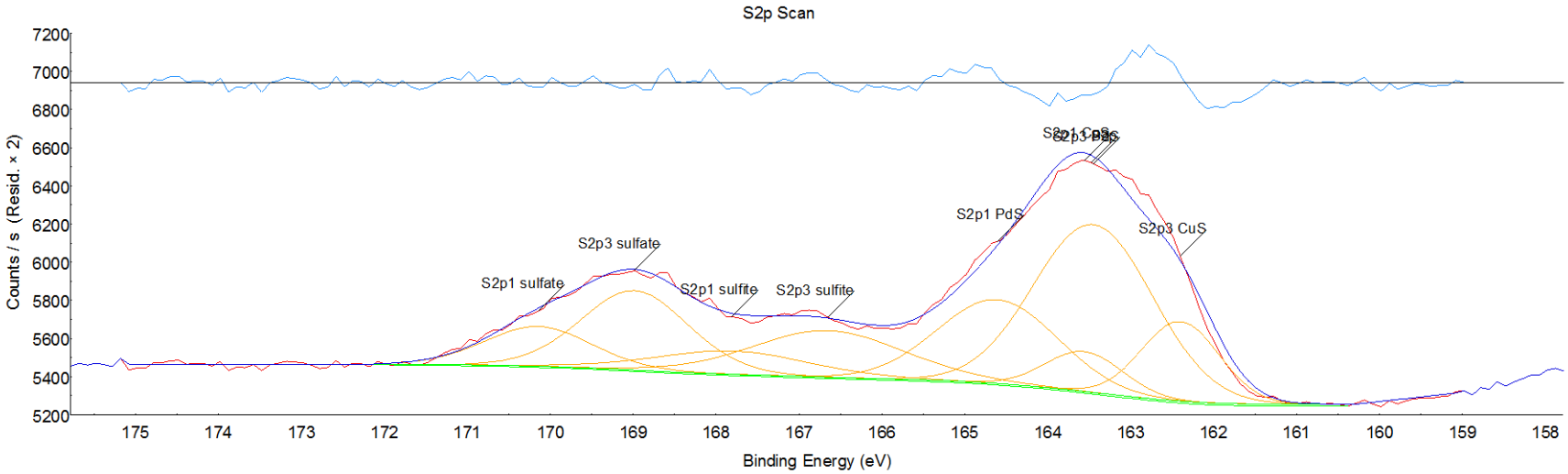

Figure D-14 Pd/Cu coupon poisoned at 450ºC for 12 hours in 50 ppm H_2S and recovered in H_2 at 450ºC for 12 hours.

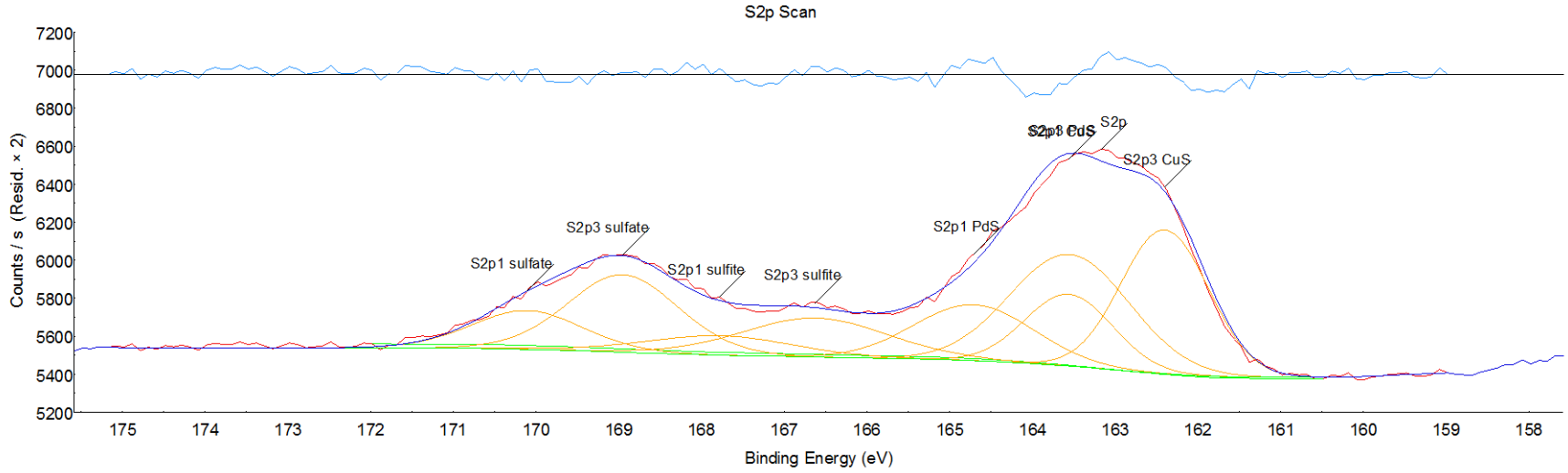

Figure D-15 Pd/Cu coupon poisoned at 500ºC for 12 hours in 50 ppm H_2S and recovered in H_2 at 450ºC for 12 hours.

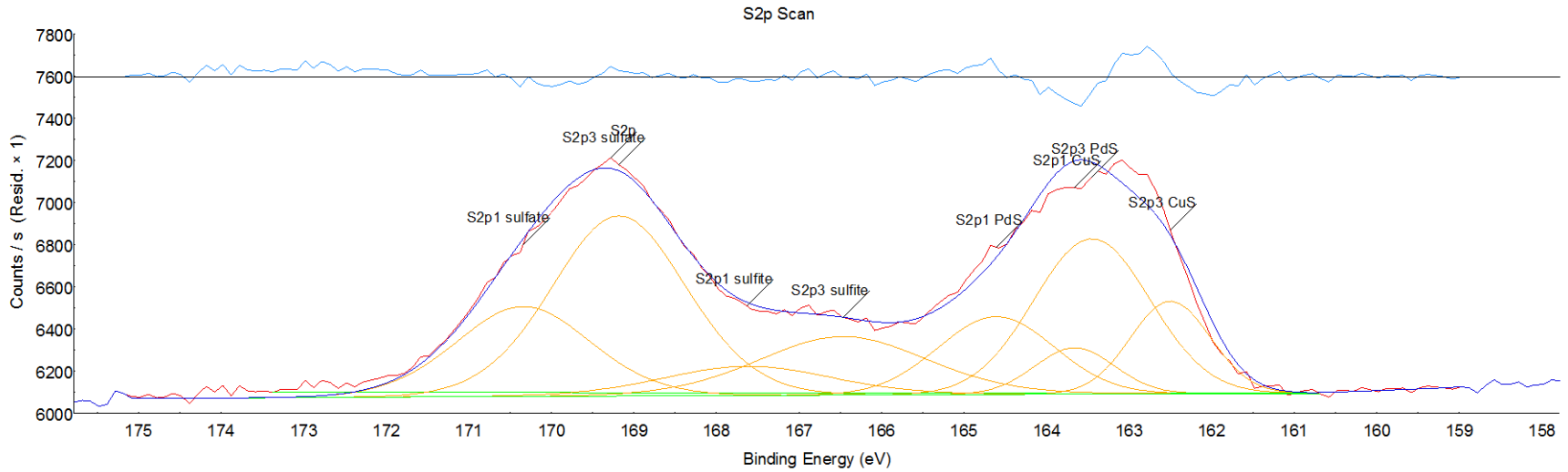

Figure D-16 Pd/Cu coupon poisoned at 350ºC for 12 hours in 50 ppm H_2S and recovered in H_2 at 400ºC for 12 hours.

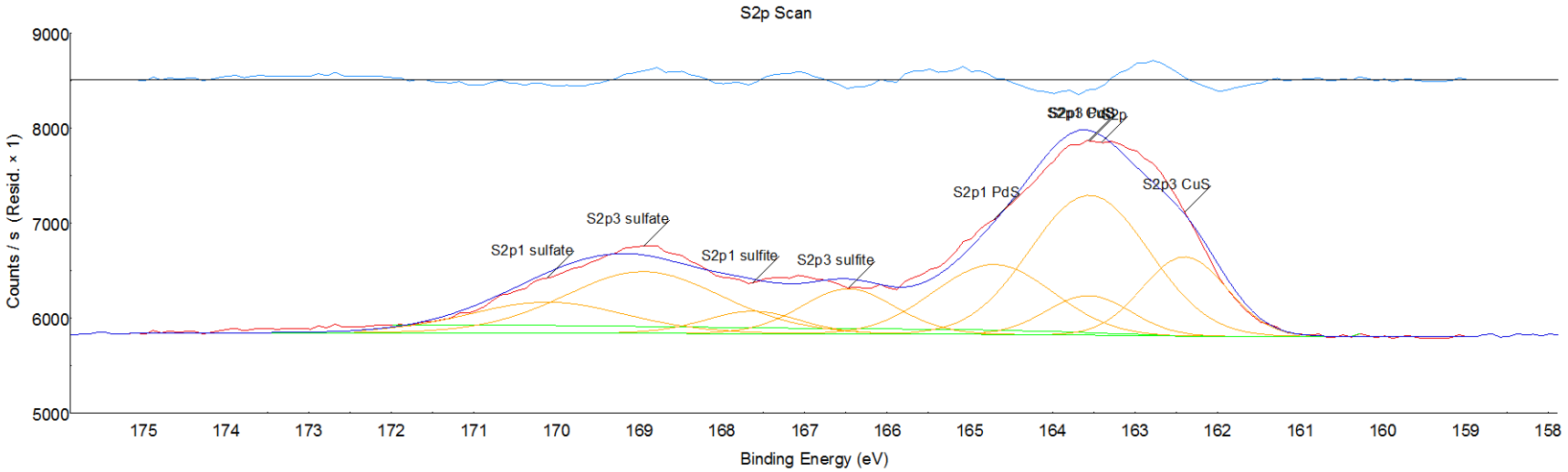

Figure D-17 Pd/Cu coupon poisoned at 400ºC for 12 hours in 50 ppm H_2S and recovered in H_2 at 400ºC for 12 hours.

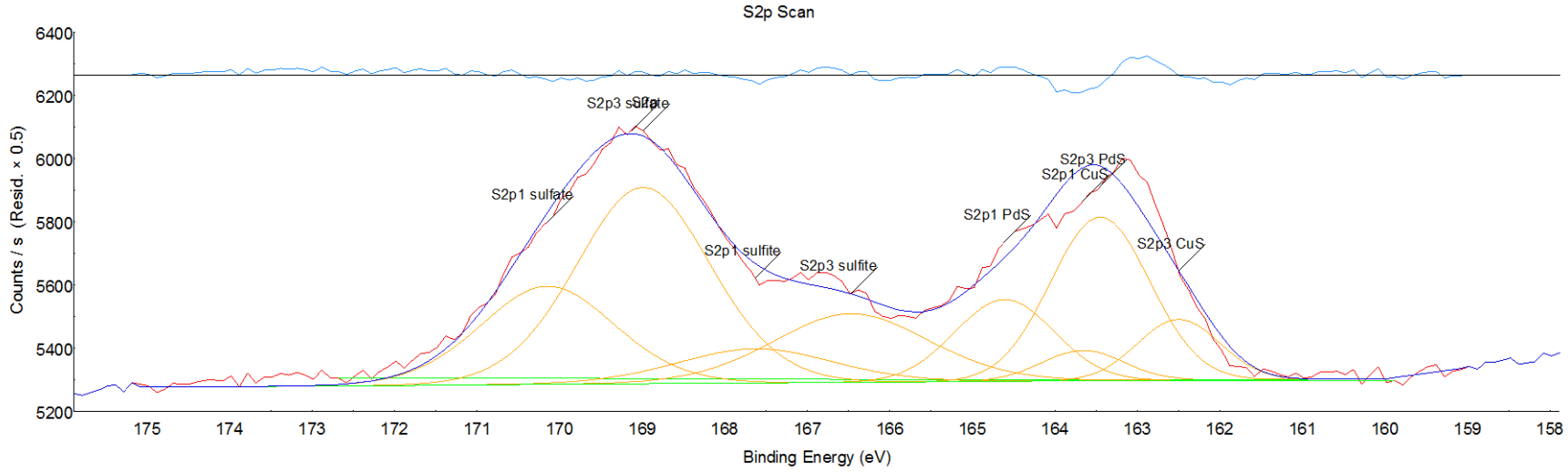

Figure D-18 Pd/Cu coupon poisoned at 450ºC for 12 hours in 50 ppm H_2S and recovered in H_2 at 400ºC for 12 hours.

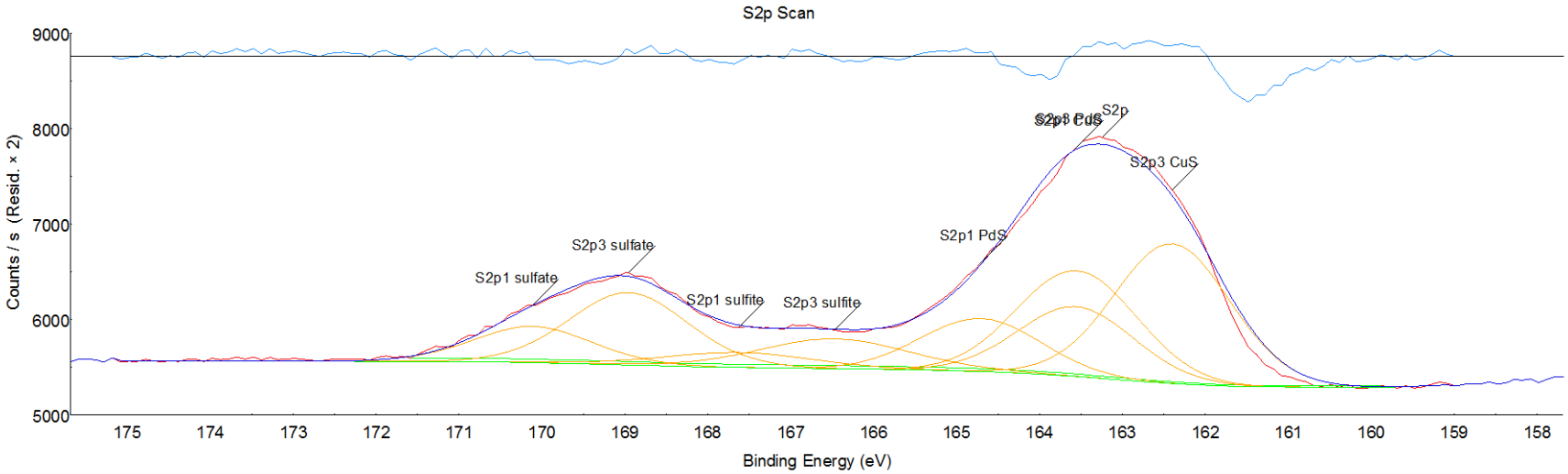

Figure D-19 Pd/Cu coupon poisoned at 500ºC for 12 hours in 50 ppm H_2S and recovered in H_2 at 400ºC for 12 hours.

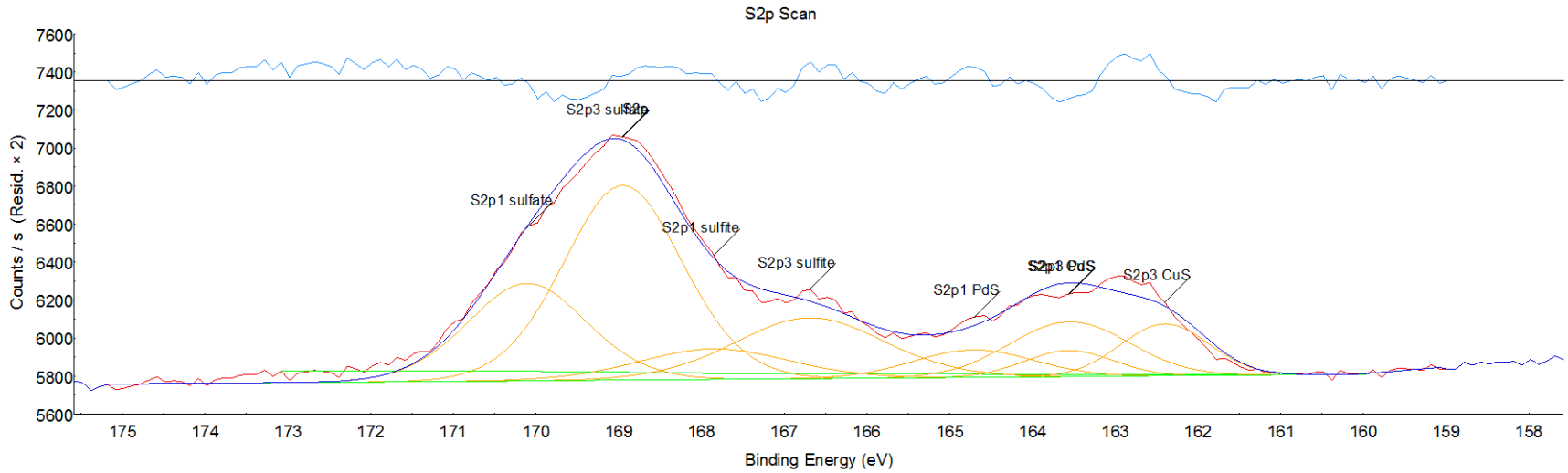

Figure D-20 Pd/Cu coupon poisoned at 350ºC for 12 hours in 50 ppm H_2S and recovered in H_2 at 350ºC for 12 hours.

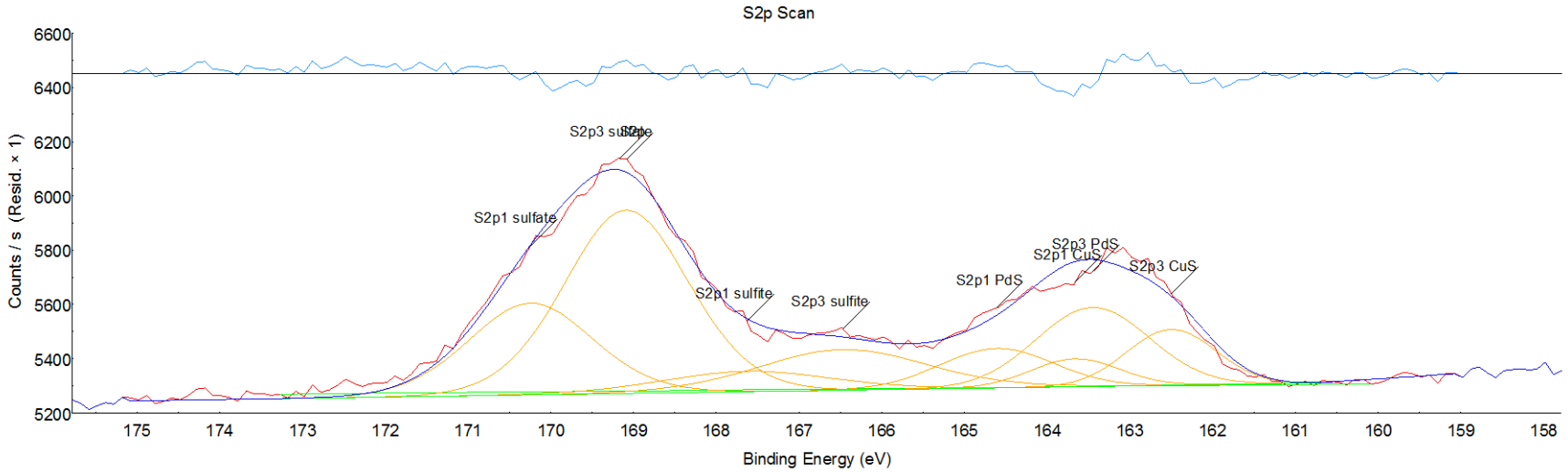

Figure D-21 Pd/Cu coupon poisoned at 400ºC for 12 hours in 50 ppm H_2S and recovered in H_2 at 350ºC for 12 hours.

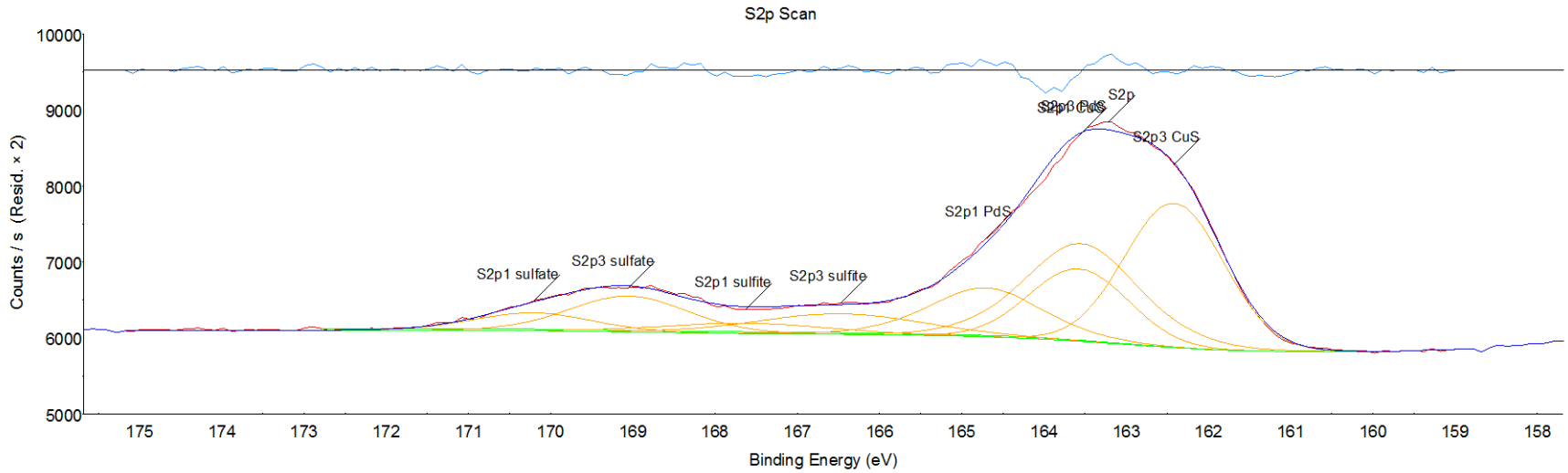

Figure D-22 Pd/Cu coupon poisoned at 450ºC for 12 hours in 50 ppm H_2S and recovered in H_2 at 350ºC for 12 hours.

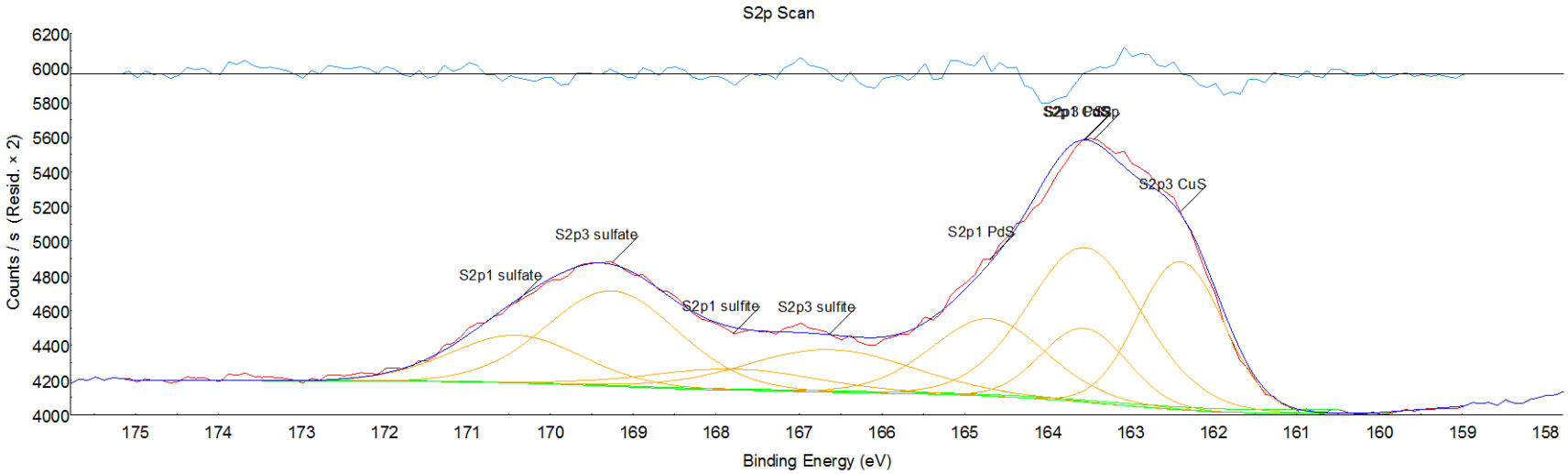

Figure D-23 Pd/Cu coupon poisoned at 500ºC for 12 hours in 50 ppm H_2S and recovered in H_2 at 350ºC for 12 hours.

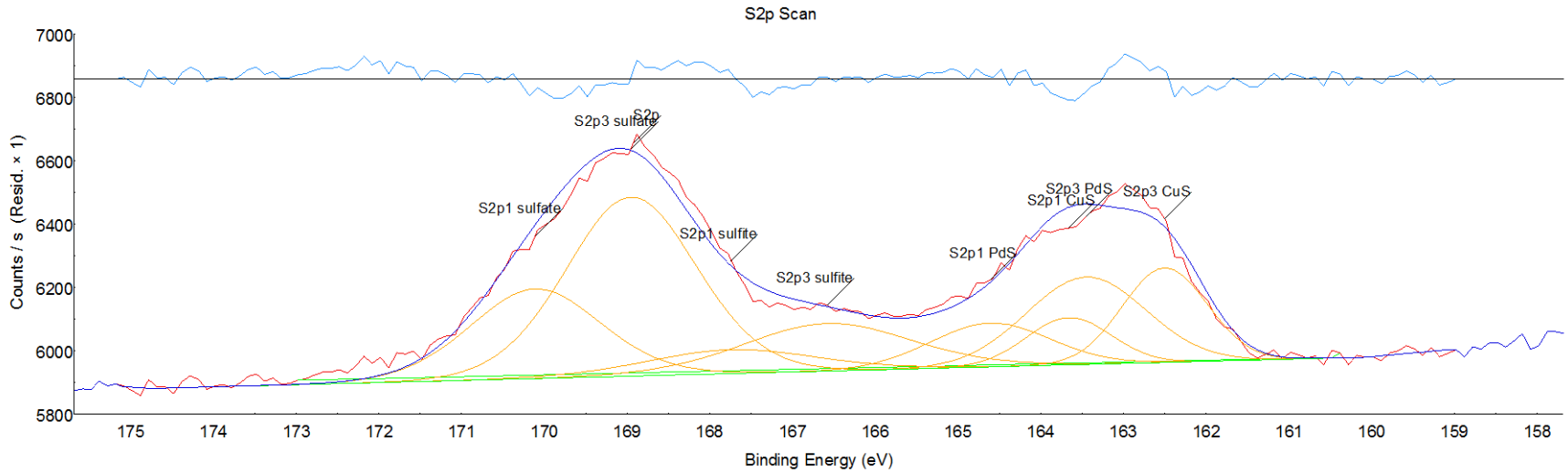

Figure D-24 Pd/Cu coupon poisoned at 350ºC for 12 hours in 50 ppm H_2S and recovered in H_2 at 350ºC for 1.5 hours.

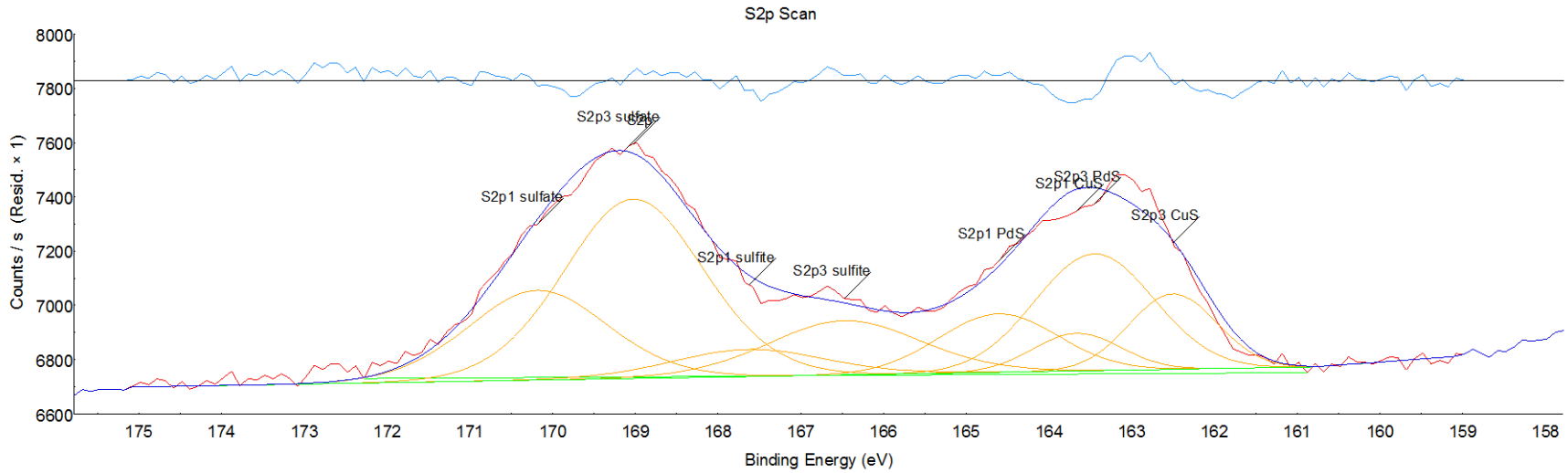

Figure D-25 Pd/Cu coupon poisoned at 400ºC for 12 hours in 50 ppm H_2S and recovered in H_2 at 400ºC for 1.5 hours.

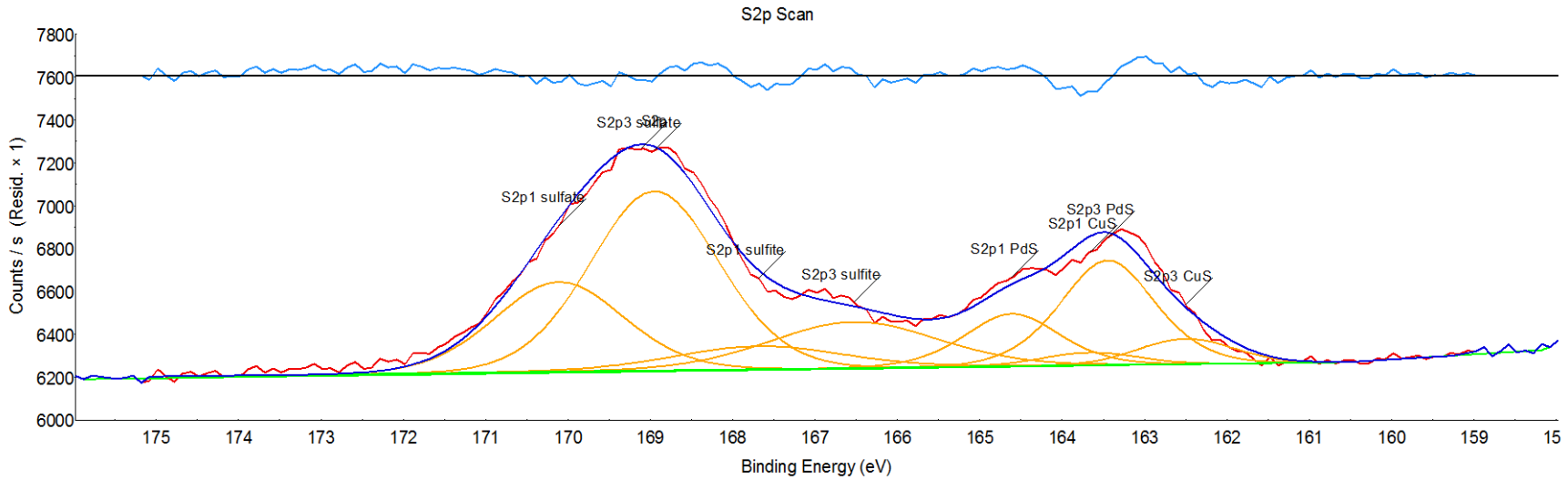

Figure D-26 Pd/Cu coupon poisoned at 450ºC for 12 hours in 50 ppm H_2S and recovered in H_2 at 450ºC for 1.5 hours.

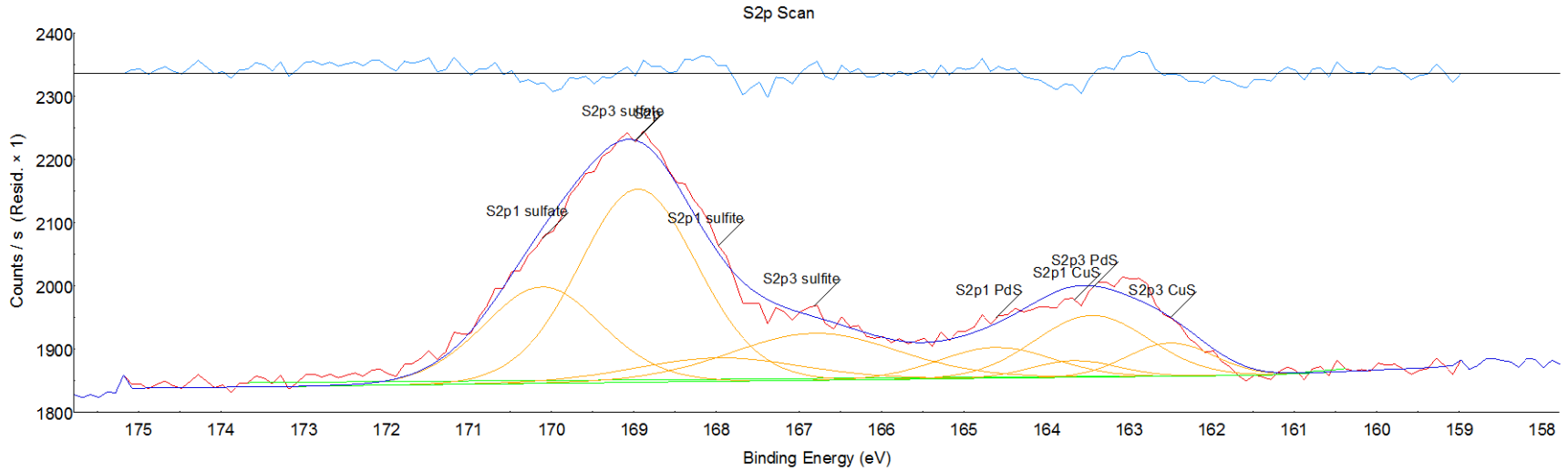

Figure D-27 Pd/Cu coupon poisoned at 500ºC for 12 hours in 50 ppm H_2S and recovered in H_2 at 500ºC for 1.5 hours.

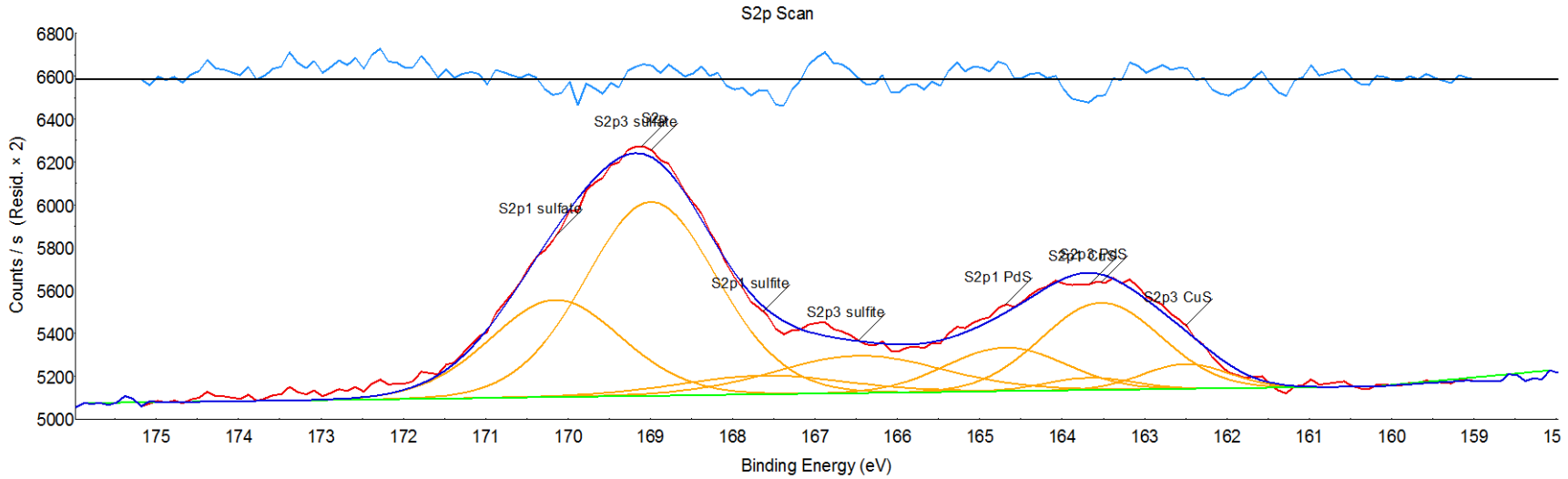

Figure D-28 Pd/Cu coupon poisoned at 350ºC for 12 hours in 5 ppm H_2S.

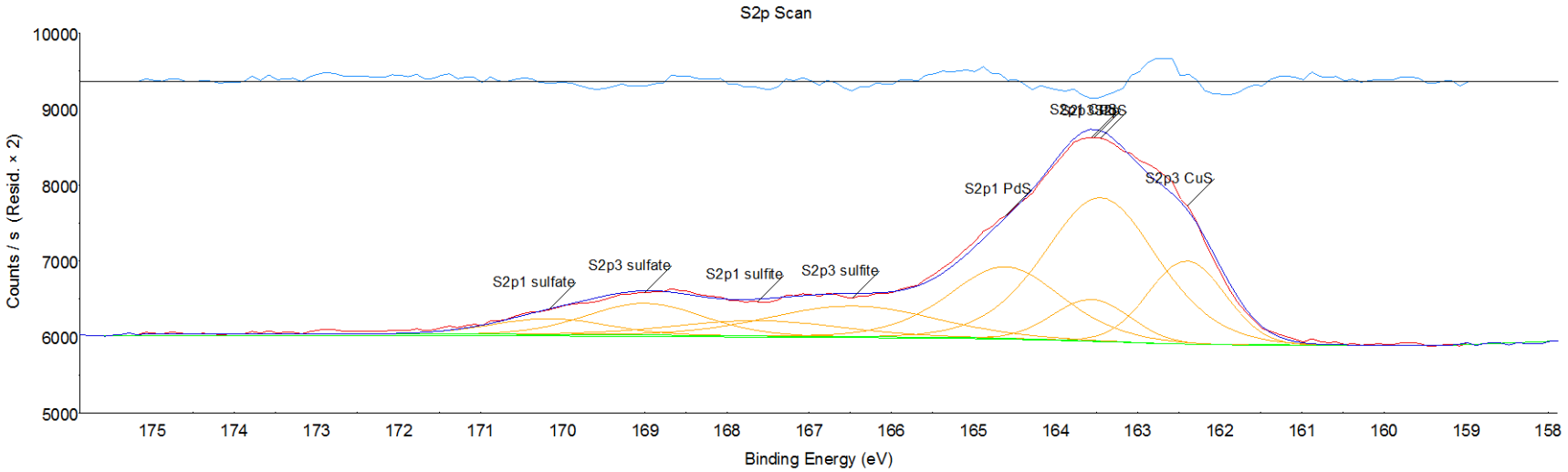

Figure D-29 Pd/Cu coupon poisoned at 400ºC for 12 hours in 5 ppm H_2S.

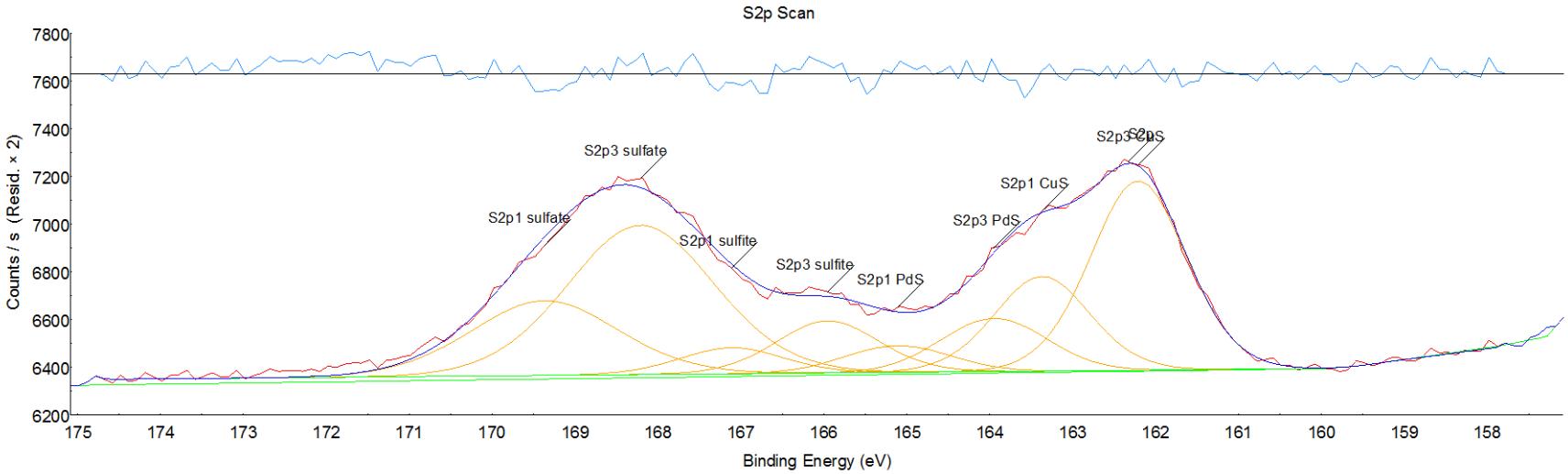

Figure D-30 Pd//Cu coupon poisoned at 450ºC for 12 hours in 5 ppm H_2S.

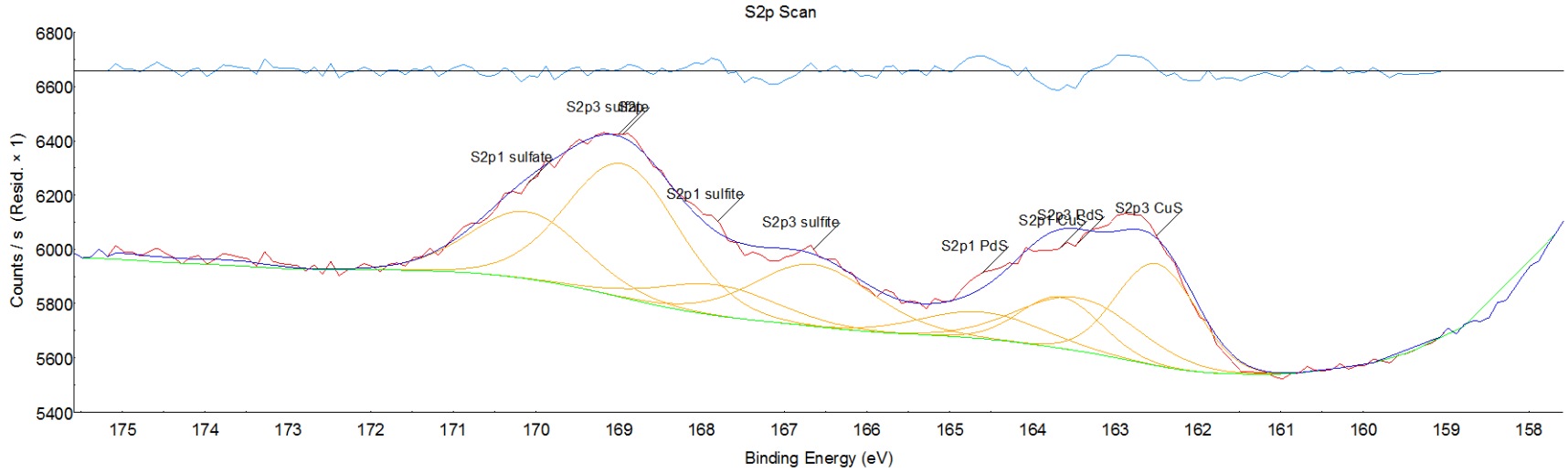

Figure D-31 Pd/Cu coupon poisoned at 500ºC for 12 hours in 5 ppm H_2S.